Circumstellar Disk Structure and Evolution through Resolved Submillimeter Observations

A dissertation presented

by

Alanna Meredith Hughes

to

The Department of Astronomy

in partial fulfillment of the requirements

for the degree of

Doctor of Philosophy

in the subject of

Astronomy

Harvard University

Cambridge, Massachusetts

May 2010

Thesis Advisor: David J. Wilner Alanna Meredith Hughes

Circumstellar Disk Structure and Evolution through Resolved Submillimeter Observations

Abstract

Circumstellar disks provide the reservoirs of raw material and determine conditions for the formation of nascent planetary systems. This thesis presents observations from millimeter-wavelength interferometers, particularly the Submillimeter Array, that address the following outstanding problems in the study of protoplanetary disks: (1) constraining the physical mechanisms driving the viscous transport of material through the disk, and (2) carrying out detailed studies of "transitional" objects between the gas-rich protoplanetary and tenuous, dusty debris disk phases to better understand how gas and dust are cleared from the system. We study accretion processes in three complementary ways: using spatially resolved observations of molecular gas lines at high spectral resolution to determine the magnitude and spatial distribution of turbulence in the disk; using polarimetry to constrain the magnetic properties of the outer disk in order to evaluate whether the MRI is a plausible origin for this turbulence; and investigating the gas and dust distribution at the outer disk edge in the context of self-similar models of accretion disk structure and evolution. The studies of transition disks use spatially resolved observations to study the detailed structure of the gas and dust in systems that are currently in the process of clearing material. We obtain snapshots of the inside-out clearing of gas and dust in several systems, and compare our observations with the theoretical predictions generated for different disk clearing mechanisms. Our observations are generally consistent with the characteristics predicted for viscous transport driven by the magnetorotational instability and disk clearing accomplished through the dual action of giant planet formation and photoevaporation by energetic radiation from the star.

Contents

Acknowledgments

I can't possibly say enough to thank David Wilner for the guidance and support that have made this thesis possible. I have never wanted for data, resources, opportunities, feedback, or attention as his student. I am grateful for his responsiveness in part because it has meant that my only limitations have been my own, which seems to be a rare and valuable experience in grad school. I am also thankful that fate and the Hubble fellowship brought Sean Andrews to the CfA two years after I arrived. He has made my experience here better in every way, as a valuable resource and a shining example to (try to) live up to, and by always being willing to talk about whatever's on my mind. I am also grateful for Charlie Qi's quiet support in helping me work with RATRAN and dealing with the weirder SMA issues we've encountered over the years.

The contributions of many wonderful collaborators are represented in this thesis. I'm particularly grateful to Inga Kamp, Jungyeon Cho, and Michiel Hogerheijde for letting me mess with their wondrously complex codes, as well as Antonio Hales, Simon Casassus, and Michael Meyer for providing opportunities to work with new kinds of data. Dan Marrone and Ram Rao kindly taught me to use the SMA polarimeter and have helped me deal with its quirks. At the CfA, I've enjoyed rare but beneficial conversations with Ruth Murray-Clay, Alyssa Goodman, and Ramesh Narayan, and I thank Jim Moran for providing me with a thorough grounding in the fundamentals of radio astronomy. The mostly invisible work of the SMA staff also forms the backbone of this thesis, and I am particularly grateful to the schedulers, the operators, the TAC, and Taco for helping me to get such great data out of the telescope. Long nights at the summit were shortened by Shelbi's wacky movies and Erin's guitar.

Life at the CfA has been immeasurably enriched by my fellow grad students. I'm not sure what I'd have done without the opportunity to talk through ideas and presentations, rant, or go for afternoon cookie or frisbee walks with Stephanie Bush, Joey Muñoz, and Ryan O'Leary. I also don't think I could have worked back-to-back for five years with anyone other than Gurtina Besla. I'm grateful for the advice and encouragement of Antonella Fruscione, and to Jean Collins, Peg Herlihy, and Jennifer Barnett for cheerfully practicing their administrative magic. The observatory night bunch and the Friday afternoon EHI crew at the Museum of Science have provided a friendly atmosphere in which to play with science and remember how exciting it is. I thank Christine Pulliam and David Aguilar for opportunities to share my enthusiasm for my work with non-astronomers, particularly short and noisy ones.

I am, as always, grateful to my family for their love and support, and for their excitement and pride in what I'm doing even when they're not quite sure what it is. I thank my grandfather for introducing me to my first computer program and for showing me that logic puzzles were fun long before I found out they were uncool. I am grateful to my mother for everything and more. I absolutely could not have done this without her.

Chapter 1

Introduction

Circumstellar disks provide the reservoirs of raw material and initial physical conditions for the formation of nascent planetary systems. Studies of their structure and evolution therefore hold the potential to reveal much about the planet formation process in all of its most important stages: the growth of submicron-sized, primordial interstellar grains into larger particles; the agglomeration of these particles into planetesimals; and the growth and orbital evolution of these planetary embryos into the mature systems observed around our own star and dozens of others. The variety of extrasolar planetary properties and system architectures observed over the past 15 years is staggering (e.g., Butler et al. 2006) and largely unexplained. Attention is increasingly focused on unraveling the origins of these planetary systems and the role of the disk in shaping their properties. This thesis uses spatially resolved observations at millimeter wavelengths to study circumstellar disks in their planet-forming stages, with the aim of constraining the basic physical processes that determine their structure and evolution.

Circumstellar disks pass through several discernible stages on their way to becoming planetary systems. While the terminology describing these disks is a matter of some discussion[1], we use the following terms to refer to the major stages of evolution of circumstellar disks:

- **protoplanetary** disks retain a substantial and largely primordial reservoir of gas and dust, massive enough to imply planet-forming potential
- **transition** disks have properties intermediate between protoplanetary and

[1]See the Diskionary at http://arxiv.org/abs/0901.1691

debris disks, exhibiting substantial clearing of gas and/or dust from the system

- **debris** disks have little or no gas, tenuous dust disks, and dust lifetimes shorter than the age of the system, indicating that the disk is second-generation rather than primordial

This thesis focuses on the first two stages of evolution, which necessarily include the epoch of planetesimal growth and giant planet formation as large planets must form before gas is dissipated from the disk.

The time-dependent structure of a protoplanetary disk tells us where, when, and how much material is available for planet formation. We measure the gas and dust distribution in protoplanetary and transition disks in order to (1) characterize their planet-forming potential, (2) determine the conditions under which planets may form, and (3) constrain the physical processes that drive disk evolution and dispersal. The major questions in the study of disk evolution are how and why the radial distribution of gas and dust changes with time, and when and how gas and dust are cleared from the system. The former question is laid out in more detail in Section 1.2, and the latter in Section 1.3.

1.1 Why Millimeter Interferometry?

Current millimeter interferometers provide spatial resolution from several arcseconds to a few tenths of an arcsecond. With the nearest star-forming regions at distances of order $\sim$100 pc, this resolution corresponds to radial scales of tens to hundreds of astronomical units, just outside the orbit of Saturn in our own solar system. This is sufficient to substantially resolve circumstellar disks, which typically span several hundreds of AU in radius (e.g. Dutrey et al. 1996; Kitamura et al. 2002; Andrews & Williams 2007).

The millimeter region of the spectrum provides access to important diagnostics of gas and dust content. The millimeter-wavelength dust continuum emission is generally optically thin, even for protoplanetary disks. It therefore traces the mass distribution rather than surface features, and is weighted towards the dense midplane where most of the mass is located. Furthermore, the stellar photosphere is very faint at long wavelengths compared to the dust emission, which has low surface brightness but subtends a large solid angle, so that the contrast between star and disk is quite low. The primary challenge associated

with interpreting millimeter-wavelength continuum observations is the unknown opacity of the dust grains. Various *ad hoc* estimates of mass opacity are used (the most common being Beckwith et al. 1990), but they depend sensitively on the currently unknown size distribution of grains in each system. Most of the mass is in gas, and much of the mass in solids could be locked up in larger particles, implying that measurements of disk mass from millimeter continuum observations may represent lower limits. Since the millimeter flux is the product of temperature, surface density, and opacity, it can be particularly difficult to disentangle these properties without complementary constraints on one or more of the parameters, for example gas tracers, resolved observations at multiple radio frequencies, or broadband photometry across the spectrum.

This millimeter-wavelength spectral region is also rich with rotational transitions of small molecules that provide access to dynamical and chemical information about the gas disk. The dominant mass constituent of protoplanetary disks is thought to be H_2, due to the high elemental abundance of hydrogen and its resistance to depletion onto dust grains. Its lack of a dipole moment makes it all but unobservable, with the exception of some measurements of infrared and fluorescent ultraviolet H_2 lines originating in the warm inner disk (e.g., Beckwith et al. 1978; Brown et al. 1981; Carr 1990). Other small molecules are readily observable at millimeter wavelengths, however, including CO, which is the next most abundant molecule after H_2 (with a nominal abundance of 10^{-4}). The primary complications associated with deriving information about the gas content from millimeter-wavelength observations are the high optical depth of abundant molecules, which makes the line flux largely insensitive to density, and the chemistry, which affects the relative abundances of different molecules (as a function of radius, scale height, or even azimuth), and can also include freeze-out of molecules from gaseous to solid phase onto grain surfaces in low-temperature regions of the disk.

Despite the complications, the combination of spatial resolution and sensitivity provided by millimeter-wavelength interferometers makes an important contribution to the study of protoplanetary disks. The constraints provided at millimeter wavelengths, including dust grain sizes, the surface density of solids, gas content, and temperatures from gas lines, complement diagnostics from observations across the spectrum. The integration of spectral energy distribution (SED) modeling with spatially resolved observations at millimeter wavelengths has provided important constraints on the temperature and surface density structure of circumstellar disks (e.g. Calvet et al. 2002; Andrews & Williams 2007; Andrews et al. 2009). While measurements of the sizes of inner holes in

transition disks are best accomplished using millimeter-wavelength (or longer) observations to trace the location of large dust grains (see discussion in Hughes et al. 2007), critical information about the properties of gas and dust in the inner disks of these systems is provided by gas and dust tracers at shorter wavelengths and higher spatial resolution (see e.g. Ratzka et al. 2007; Salyk et al. 2007, 2009; Eisner et al. 2006; Pontoppidan et al. 2008). Multiwavelength constraints are crucial for understanding the structure and evolution of circumstellar disks, and millimeter wavelengths play an important role in that process.

1.2 Protoplanetary Disks as Accretion Disks

Since the seminal work by Lynden-Bell & Pringle (1974), the photospheric excess and optical and UV variability exhibited by many pre-main sequence stars has been attributed to emission from an accreting disk. Steady accretion from the disk to the star requires some form of viscous angular momentum transport through the disk. The molecular viscosity in a protoplanetary disk implies a disk evolution timescale much too long to account for the observed evolution of disks: an additional source of viscosity is therefore required. As conjectured by Shakura & Syunyaev (1973), turbulence can provide an "anomalous" viscosity large enough to account for accretion and disk evolution on the appropriate time scales. However, while turbulence is commonly invoked as the source of viscosity in disks, its physical origin, magnitude, and spatial distribution are largely unconstrained.

The mechanism most commonly invoked as the source of turbulence providing viscous transport in circumstellar disks is the magnetorotational instability (MRI), in which magnetic interactions between fluid elements in the disk combine with an outwardly decreasing velocity field to produce torques that transfer angular momentum from the inner disk outwards (Balbus & Hawley 1991, 1998). A cartoon of the elements of this instability, adapted from Balbus & Hawley (1998), is included in Figure 1.1. The conditions for the instability are satisfied over much of the extent of a typical primordial circumstellar disk: there must be a subthermal magnetic field ($B^2/8\pi\rho < c_s^2$); the ionization fraction must be high enough for the elements to interact via the magnetic field; and the velocity field must decrease outwards, a condition easily satisfied in any Keplerian disk (Gammie & Johnson 2005, and references therein). Where these conditions are satisfied, the instability will operate and the disk will become turbulent.

The importance of MRI turbulence to circumstellar disks is manifold. It drives the viscous evolution that determines the global structure of the accretion

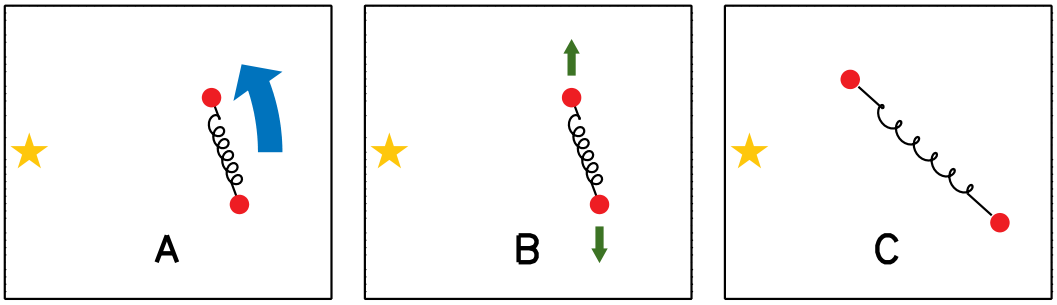

Figure 1.1.— Cartoon of the magnetorotational instability, adapted from Balbus & Hawley (1998). The left panel (*A*) shows two elements of material (red circles) orbiting counterclockwise around a star (yellow), interacting via a magnetic field (black line). In the center panel (*B*), the same arrangement is shown in the rotating frame, with the relative velocity of the two pieces of material, due to the Keplerian shear and the slight difference in radii, indicated by the green arrows. The right panel (*C*) shows the result of the magnetic interaction in the Keplerian disk: due to the tension created by the magnetic field in the presence of the velocity shear, the inner particle loses angular momentum and spirals towards the star while the outer particle gains angular momentum and spirals away from the star. This runaway process generates turbulence and transfers angular momentum through the disk. Chapters 6-8 look for observable features of this process, including magnetic fields, turbulence, and the global disk structure.

disk with time, and is commonly invoked in a wide range of smaller-scale processes leading to the formation of planets within the disk. It is thought to aid in the aggregation of planetesimals by creating local pressure maxima towards which larger solids will migrate and collect, aiding in the initiation of gravitational collapse (e.g. Johansen et al. 2007). Turbulence may also play an important role in lengthening the lifetime of protoplanets undergoing type I migration, by causing fluctuations in the gravitational torque of the disk on the planet (e.g. Nelson & Papaloizou 2003). It is also invoked in regulating the settling of solids from the disk atmosphere to the midplane (e.g. Ciesla 2007) and explaining mixing in meteoritic composition (Boss 2004).

Measurements that constrain the magnitude and physical origin of disk turbulence therefore promise to provide important insight into the physics of planet formation on many different physical and temporal scales. We approach this problem from several directions, seeking observable elements of MRI-driven viscous transport including the large-scale density profile, magnetic fields, and

turbulence. In Chapter 6, we investigate how the global structure of gas and dust, particularly at the disk outer edge, can reflect viscous accretion processes operating on small scales. In Chapter 7 we use polarimetry to seek evidence of large-scale magnetic fields in the outer disk, with the aim of providing observational support for the magnetic origin of disk turbulence. In Chapter 8, we use high spectral resolution observations to measure the nonthermal widths of molecular lines in order to the turbulent linewidth in the outer disk.

1.3 Disk Dissipation

The dissipation of material from low- and intermediate-mass systems seems to occur by ages of around 10 Myr (e.g. Mamajek 2009), and the correlation between dust tracers at many different wavelengths implies that the process occurs nearly simultaneously across the radial extent of the disk (Skrutskie et al. 1990; Wolk & Walter 1996; Andrews & Williams 2005). Similarly, the low fraction of systems observed in the transitional stage in any given star-forming region implies that this stage is either rapid or rare (e.g. Cieza et al. 2007; Uzpen et al. 2008). Because transition disks are rare and difficult to identify, they have only recently begun to be studied in detail.

Transition disks were first classified more than 20 years ago (Strom et al. 1989), and are generally identified observationally by a deficit of mid-infrared flux in their SED relative to stars of comparable ages. Figure 1.2 illustrates the basics of how SED modeling is used to derive spatial information from unresolved spectra: because wavelength is associated with temperature, and temperature decreases monotonically with distance from the star, wavelength can serve as a proxy for distance from the star. SED modeling has undergone numerous advances over the past few decades, increasing in sophistication as the quality and quantity of data have increased, particularly with the advent of the *Spitzer Space Telescope*. Some highlights include the addition of a flared disk geometry (Adams et al. 1987; Kenyon & Hartmann 1987), the introduction of hydrostatics and distinct surface and interior layers (Chiang & Goldreich 1997; Chiang et al. 2001), and the inclusion of a self-consistent temperature structure, heating by accretion, two-dimensional radiative transfer, realistic dust composition and opacities, and shadowing by an inner rim (D'Alessio et al. 1999, 2001, 2006; Dullemond et al. 2001, 2002). The interpretation of a mid-IR deficit as an inner hole is not unique, however. Boss & Yorke (1996) showed that the signature of an inner hole could alternatively be attributed to variations of opacity and geometry in the unresolved

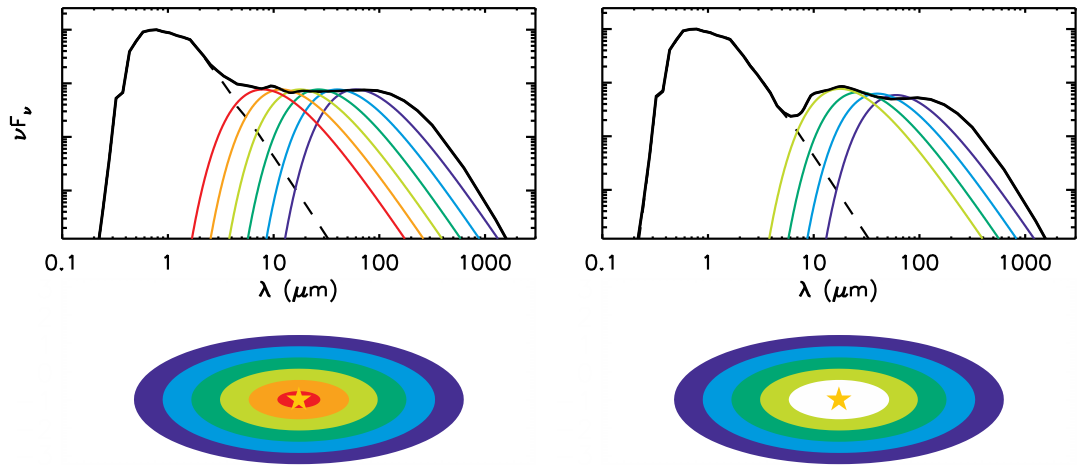

Figure 1.2.— Cartoon illustrating SED modeling and the association between mid-IR deficits and inner holes in transition disks. The black solid line shows a model of a T Tauri star surrounded by a disk that (*left*) extends in to the dust destruction radius or (*right*) is truncated at 1 AU from the star. The dashed line marks the SED contribution from the stellar photosphere. The colored lines are blackbody curves showing the contribution of dust at different temperatures to the excess over the photosphere: curves with peaks at shorter wavelengths originate from hotter dust. The mid-IR deficit in the figure on the right corresponds to missing emission from the hottest dust. The illustration below each plot shows how the temperature of the dust is related to distance from the star, and highlights the idea that missing short-wavelength emission from the SED corresponds to missing dust close to the star. Chapters 2-5 include detailed studies of individual transition disks and seek clues to the physical processes underlying the clearing of gas and dust from the disk.

system, and healthy skepticism about the inner hole interpretation was also expressed by other authors, including Chiang & Goldreich (1999). These studies highlight the necessity of using spatially resolved observations to test the inferred characteristics of disk structure from models of spatially unresolved SEDs.

The processes determining the amount and distribution of gas and dust in transition disks are the same processes that shape the features of emergent planetary systems around young stars. Many basic questions about transition disks remain unaddressed: when in the lifetime of the star does the disk clear? Does the dust clear before the gas, or vice versa? Does the disk clear from the inside out or in a radially invariant manner? These questions address the larger problem of when and how in the lifetime of a star planets are formed. Detailed

studies of transitional objects can also help to distinguish the physical mechanisms responsible for the clearing of gas and dust from the system. Several different mechanisms have been proposed to drive the dispersal of gas and dust from protoplanetary disks, including decreasing dust opacity due to grain growth (e.g. Strom et al. 1989), photophoretic effects of gas on dust grains (Krauss & Wurm 2005), photoevaporation of material by x-ray or UV photons from the central star (e.g., Clarke et al. 2001; Owen et al. 2010), or the dynamical influence of a giant planet forming within the disk (e.g., Lin & Papaloizou 1986; Bryden et al. 1999). Each makes distinct predictions for the observable disk features, although more than one mechanism may come into play over the lifetime of the disk.

We use millimeter-wavelength interferometry to study several transitional objects in order to characterize their structure and constrain the physical mechanisms responsible for the dissipation of the gas and dust disk. Chapters 2 and 3 describe observations of the disks around the prototypical transitional systems TW Hya and GM Aur, designed to test the paradigm that mid-IR SED deficits are associated with the clearing of dust from the inner disk. These chapters also explore the multiwavelength constraints on the properties of these systems and how they compare to proposed theoretical mechanisms for disk clearing. Chapter 4 provides spatially resolved observations of the disk around 49 Ceti, which represents a rare example of a system in which the dust distribution resembles a debris disk but with a substantial reservoir of molecular gas remaining. Chapter 5 combines SED modeling with millimeter-wavelength constraints on gas and dust content to model the structure and composition of two old transitional systems in Corona Australis.

Chapter 2

An Inner Hole in the Disk around TW Hydrae Resolved in 7 millimeter Dust Emission

A. M. Hughes, D. J. Wilner, N. Calvet, P. D'Alessio, M. J. Claussen, & M. R. Hogerheijde 2007, *The Astrophysical Journal*, Vol. 664, pp. 536-542

Abstract

We present Very Large Array observations at 7 millimeters wavelength that resolve the dust emission structure in the disk around the young star TW Hydrae at the scale of the ∼4 AU (∼0.″16) radius inner hole inferred from spectral energy distribution modeling. These high resolution data confirm directly the presence of an inner hole in the dust disk and reveal a high brightness ring that we associate with the directly illuminated inner edge of the disk. The clearing of the inner disk plausibly results from the dynamical effects of a giant planet in formation. In an appendix, we develop an analytical framework for the interpretation of visibility curves from power-law disk models with inner holes.

2.1 Introduction

The TW Hya system is thought to be a close analog of the early Solar nebula. At a distance of 51±4 pc (Mamajek 2005), it is the closest known classical

T Tauri star, and a suite of observational studies have shown that TW Hya harbors a massive disk of gas and dust. Scattered light observations at optical and near-infrared wavelengths reveal a surface brightness profile consistent with a nearly face-on, optically thick, flared disk extending to ∼200 AU in radius (Roberge et al. 2005; Weinberger et al. 2002; Krist et al. 2000; Trilling et al. 2001). Observations at millimeter wavelengths have detected thermal dust emission and a variety of molecular species, including ^{13}CO, ^{12}CO, CN, HCN, HCO$^+$, and DCO$^+$ (Weintraub et al. 1989; Zuckerman et al. 1995; Kastner et al. 1997; van Dishoeck et al. 2003; Wilner et al. 2003; Qi et al. 2004). The dust also displays signatures of grain growth up to centimeter scales (Wilner et al. 2005), and perhaps substantially larger sizes.

Detailed models of the TW Hya spectral energy distribution (SED) provide constraints on many aspects of the disk structure (Calvet et al. 2002), including the radial dependence of outer disk surface density and temperature, and a clearing of the inner disk within ∼4 AU radius. Resolved interferometric observations of millimeter and submillimeter dust emission are in good agreement with the structure inferred from the irradiated accretion disks models that match the SED (Qi et al. 2004; Wilner et al. 2000), though the resolution and sensitivity at these wavelengths have not been sufficient to address the presence of the inner hole.

The inner hole is indicated by two features of the SED (Calvet et al. 2002): (1) a flux deficit from ∼2-20μm, indicative of low (dust) surface density in the inner disk, and (2) a flux excess at ∼20-60 μm, thought to originate from the truncated inner edge of the disk, directly illuminated by the star. Similar spectral features have been recognized in other T Tauri star SEDs (e.g. GM Aurigae and DM Tauri; see Calvet et al. 2005) and may signify an important phase in the evolution of circumstellar disks. One exciting possibility is that a discontinuity in the inner disk is a consequence of the perturbative gravity field of a giant planet. Theories of planet-disk interaction predict the opening of gaps in a disk as a result of the formation of massive planets (e.g. Lin & Papaloizou 1986; Bryden et al. 1999). However, Boss & Yorke (1993, 1996) show that the interpretation of infrared flux deficits as central clearings is not unique and reproduce SEDs of accreting disks around low-mass, pre-main sequence stars with a combination of opacity and geometry effects in the unresolved system. Spatially resolved observations of disk structure are required to confirm the inference from spectral deficits of inner disk clearing.

To probe the disk morphology on size scales commensurate with the 4 AU

transitional radius of Calvet et al. (2002), we have used the Very Large Array[1] to observe thermal dust emission from TW Hya at a wavelength of 7 millimeters. These observations show clearly a deficit of dust emission in the inner disk consistent with the predicted hole.

2.2 Observations

We used the Very Large Array to observe TW Hya at 7 millimeters in the most extended (A) configuration. The observations used 23 VLA antennas (several were unavailable due to eVLA upgrades) that gave baseline lengths from 130 to 5200 kλ. The observations were conducted for four hours per night on 10, 11 February 2006 and 7 March 2006, from 7 and 11 UT (0 to 4 MST), during the late night when atmospheric phases on long baselines are most likely to be stable. Both circular polarizations and two 50 MHz wide bands were used to obtain maximum continuum sensitivity. The calibrator J1037-295 was used to calibrate the complex gains, using an 80-second fast switching cycle with TW Hya. The calibrator J1103-328, closer to TW Hya in the sky, was also included in a few minutes of fast switching each hour to test of the effectiveness of the phase transfer from J1037-295. The phase stability was good during the observations of 11 February, worse on 10 February, and much worse on 7 March. Using the AIPS task SNFLG, we pruned the data with phase jumps of more than 70° between phase calibrator scans. This procedure passed about 80% of the data from the night of 11 February but substantially less from the other nights. Therefore, in the subsequent analysis we have used data only from 11 February, the most stable night. The calibrator 3C286 was used to set the absolute flux scale (adopting 1.45 Jy, from the AIPS routine SETJY), and we derived 1.95 Jy for J1037-295. The uncertainty in the flux scale should be less than 10%.

[1]The National Radio Astronomy Observatory is a facility of the National Science Foundation operated under cooperative agreement by Associated Universities, Inc.

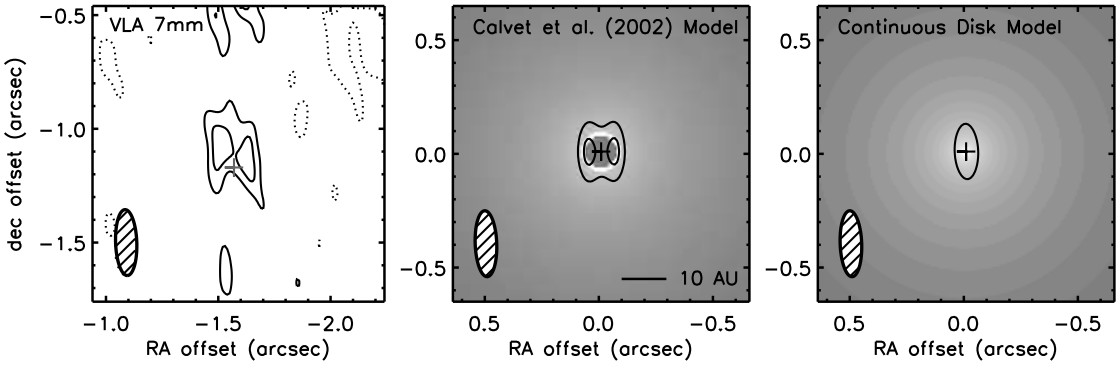

Figure 2.1.— The TW Hya 7 millimeter continuum emission observed with the VLA *(left)* compared to simulated images generated from the Calvet et al. (2002) model of an irradiated accretion disk, truncated at the 4 AU radius indicated by the SED and including the directly illuminated inner edge *(center)*, or extending in to the 0.01 AU dust destruction radius *(right)*. The contour levels are $-2, 2, 3\times0.23$ mJy (the rms noise). In each panel, the ellipse in the lower left corner indicates the $0\farcs29 \times 0\farcs09$, PA 2.1° synthesized beam. The cross marks the derived position of the central star (see text). The center and right panels also show the disk models at full resolution, in a logarithmic grayscale to display the range of intensities in the fainter, outer regions of the disk and the bright, thin wall at the inner edge of the canonical model.

2.3 Results

2.3.1 7 mm Image

Figure 2.1 shows an image of the TW Hya 7 millimeter emission, where a Gaussian taper (FWHM 2000 kλ) has been used in the imaging process to obtain an angular resolution matched to the surface brightness sensitivity. The rms noise level in this image is 0.23 mJy, and the peak flux of 0.88 mJy corresponds to a brightness temperature of 46 K. Because of the southern declination of TW Hya and the VLA antenna geometry, the beam is elliptical and the resolution is higher east-west than north-south. Inspection of Figure 2.1 shows that the 7 millimeter emission is clearly not centrally peaked, as would be expected for a disk that extends continuously inwards towards the central star. Instead, the image exhibits a double-peaked morphology, consistent with a nearly face-on disk with a central hole observed with an elliptical beam. An image of the test calibrator J1103-328 made with the same parameters is point-like, as expected.

2.3.2 Radially Averaged 7 mm Visibilities

The central hole in the TW Hya emission may be identified even more clearly in the visibility domain, free from the effects of the Fourier transform process and non-linear deconvolution. To better show the brightness distribution, we averaged the visibility data in concentric annuli of deprojected (u,v) distance, $\mathcal{R}_{uv}$, as described in Lay et al. (1997). We use the TW Hya disk position angle and inclination found by Qi et al. (2004) from CO line imaging of the outer disk (-45° and 7°, respectively). These values may not be valid in the inner disk, if e.g. the disk warps in the interior. However, as long as the disk remains close to face-on at all radii, the deprojection correction is small and therefore insensitive to the exact values of these parameters.

For each visibility, the coordinates were redefined in terms of $\mathcal{R} = \sqrt{u^2 + v^2}$, the distance from the origin of the (u,v) plane, and $\phi = \arctan\left(\frac{v}{u} - PA\right)$, the polar angle from the major axis of the disk (defined by the position angle, PA, measured east of north). Assuming circular symmetry and taking into account the disk inclination i, the deprojected (u,v) distances parallel to the major and minor axes of the disk, are $d_a = \mathcal{R}\sin\phi$, $d_b = \mathcal{R}\cos\phi\ \cos i$, respectively, and the deprojected (u,v) distance is $\mathcal{R}_{uv} = \sqrt{d_a^2 + d_b^2}$.

An important parameter in the averaging process is the position of the star, or the center of the disk. To examine the radial distribution of flux at the smallest scales permitted by the data, particularly in the east-west direction of highest resolution, we must know the phase center to within a fraction of the radius set by the resolution, i.e., the position of the star must be specified to within a few hundredths of an arcsecond, which is better than the absolute astrometric accuracy of the data (typical positional accuracies in the A array are $\sim 0\farcs1$ due to baseline uncertainties and uncorrected tropospheric phase fluctuations; see, e.g. the 2004 VLA Observational Status Summary). To the extent that the disk is symmetric, the process of deprojecting and averaging at the correct star position will minimize the scatter within each deprojected radial bin and bring the average of the imaginary parts of the visibilities (the average phase) to zero. Therefore, we chose the star position to be that which minimized the absolute value of the mean of the imaginary visibility bins. This position is indicated by the cross in the left panel of Figure 2.1.

Figure 2.2 shows the annularly averaged visibility amplitude as a function of $\mathcal{R}_{uv}$. The width of each bin is 430 kλ, chosen to be narrow enough to sample the shape of the visibility function and also wide enough to have sufficient signal-to-noise ratio. Although the visibility data are still noisy when divided up

in this way, it is evident that the visibility function passes through a null near $\mathcal{R}_{uv}$ of $\sim$1000 kλ, indicative of a sharp edge in the emission.

2.4 Discussion

The most striking feature of the new 7 millimeter observations is the central depression in the image, which is also indicated by the presence of the null in the deprojected visibility function. We identify this feature with a clearing of the inner dust disk. A continuous disk that extends inward to the dust destruction radius at $\sim$0.01 AU would show sharply centrally peaked emission and would not show a null at the observed baselines. Figure 2.1 compares the 7 millimeter image (left panel) with an image generated for a model with a continuous disk (right panel). Figure 2.2 also shows the visibility function of continuous disk (dashed line); this is clearly not compatible with the 7 mm observations (or the infrared SED).

Independent of detailed modeling, the size scale of this inner hole can be estimated simply from the separation of the peaks in the image. These peaks are sensitive primarily to inner edge of the disk, where the 7 millimeter brightness is highest. The separation of the peaks is $\sim$0.″14, or $\sim$ 7 AU. This separation is slightly smaller than the diameter of the inner hole, since the bright emission from the inner edge to the north and to the south of the star, combined with the lower angular resolution in the north-south direction, tend to draw the image peaks together. This effect is evident in the right panel of Figure 2.1, in which the contoured peaks can be seen to lie interior to the inner edge of the disk. The null in the visibility function provides a corroborating estimate of the size of the inner hole in the disk. In appendix A, we show how the angular scale of the null in the visibility function of a power law disk depends on the density and temperature power law indices and the radius of the inner hole. If we assume that the outer disk emission contributes little on these long baselines, and that the total emission is dominated by a bright, thin ring associated with the inner edge of the disk, as discussed in §2.4.1 below, then we can estimate the radius of the inner hole hole with equation A.11. A linear fit to the binned visibilities gives a null position of 930$\pm$60 kλ and implies an inner hole radius 4.3$\pm$0.3 AU. Thus the resolved dust emission shows an inner hole in the disk at a size scale very similar to that inferred from SED modeling.

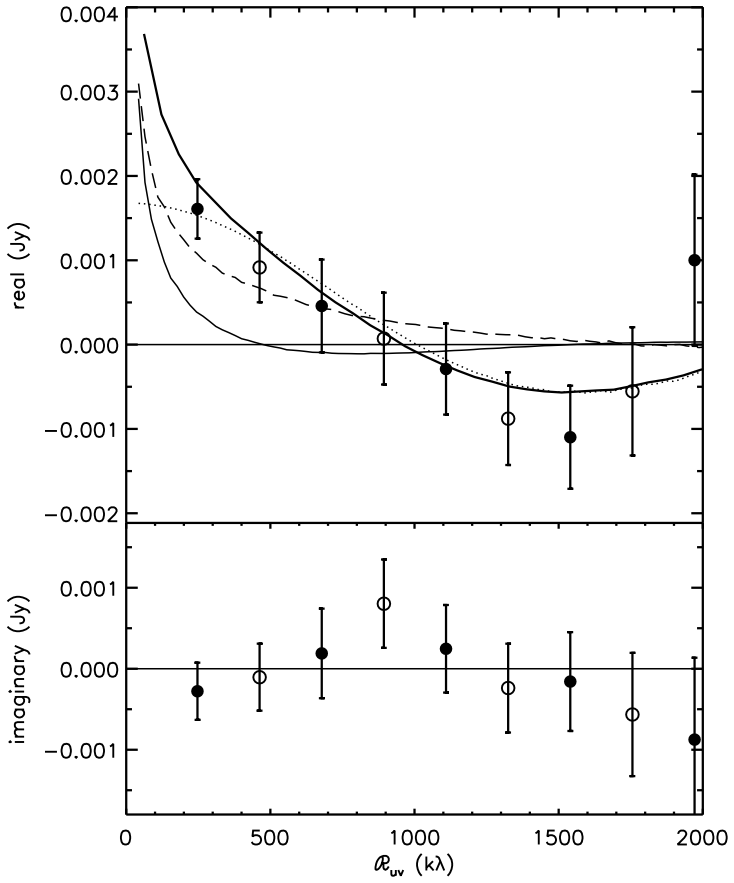

Figure 2.2.— TW Hya real and imaginary 7 millimeter visibilities, in 430-kλ bins of deprojected u-v distance from the center of the disk. Error bars represent the standard error of the mean in each bin. Note that bins represented by open and filled circles are not independent: the bins are overlapping, i.e., the domain of each open circle extends to the neighboring filled circles. The calculated visibility functions for the best fit irradiated accretion disk model is indicated by the heavy solid line and is composed of contributions from an outer disk (solid line) with an inner hole of radius 4.5 AU and a bright, thin wall (dotted line). For comparison, the visibility function for a disk model that extends in to the dust destruction radius at $\sim$0.01 AU is also shown (dashed line). To the extent that the disk is radially symmetric, the imaginary part of the visibility (the average phase) should be zero for all models.

2.4.1 Comparison with Disk Models

Power Law Disk Models

The dust emission from the outer disk of TW Hya has been shown to be a good match to the structure of an irradiated accretion disk model, approximated by power laws in temperature and surface density with indices $q \sim 0.5$ and $p \sim 1.0$, respectively, over a wide range of radii. However, an extrapolation of this very simple power law model to an inner disk truncated at $\sim$ 4 AU radius is not compatible with the new long-baseline 7 millimeter data. For these power laws, the null in the visibility function of the 4 AU hole should appear at $\sim$ 500 kλ, which is a factor of two smaller than observed (equation A.9). In order for a 4 AU hole to be consistent with a $\sim$1000 kλ null, the power law model requires a much steeper emission gradient, with the sum of the radial power law indices $p + q$ approaching 5. Such steep power laws are inconsistent with observations of the outer disk. In addition, this power law model fails to reproduce the flux in the image peaks by nearly an order of magnitude. Another possibility is that the radius of the hole is smaller than that predicted by the SED. A power law disk with $p + q = 1.5$ and radius 2 AU does reproduce the 1000 kλ null and observed peak separation; however, this model still fails to reproduce the observed peak flux by more than a factor of five. These discrepancies indicate that a more complex model of the disk is needed. In general, reproducing the observed peak flux in the new high resolution observations requires a greater concentration of material at the inner edge of the disk than that of power-law disk models.

A natural modification to the power law disk model with an inner hole is the addition of a bright, thin, inner edge, or "wall" component. This "wall" component corresponds to the frontally illuminated inner edge of the disk in the calculations of Calvet et al. (2002), who show that a small range of temperatures is required to reproduce the narrow spectral width of the mid-infrared excess. The presence of this additional compact component to the model shifts the angular scale of the null in the visibility function to larger $\mathcal{R}_{uv}$ and raises the flux at long baselines. In this composite model, for a given power law description, the angular scale of the null in the composite "disk+wall" visibility function depends on (1) the radius of the inner hole, and (2) the relative brightness of the disk and wall. The effect of the second dependency is to move the angular scale of the null between the limiting positions from the "disk" alone and from the "wall" alone. In fact, the position of the null in the 7 millimeter data is close to that expected from an infinitesimally thin ring of $\sim$4 AU radius (equation A.11). A bright, thin ring also reproduces the $\sim 0\farcs14$ separation of the image peaks. Thus it appears

that the high resolution observations show primarily the directly illuminated wall at the inner edge of the disk. At these long baselines, the extended emission from the outer disk that dominates at larger size scales is weak and effectively not detected.

Irradiated Accretion Disk Model

The irradiated accretion disk model of Calvet et al. (2002) provides a more realistic description of disk structure than a simple power-law model. To compare the data to this more sophisticated disk model, we simulate numerically the expected emission at 7 millimeters, including the detailed visibility sampling of the Very Large Array observations.

For the frontally illuminated component of the inner edge of the disk, we follow the prescription of Calvet et al. (2002), adopting a shape given by

$$z_s = z_0 \exp\left[(R - R_0)/\Delta R\right] \tag{2.1}$$

and temperature

$$T_{phot}(R) \approx T_* \left(\frac{R_*}{R}\right)^{1/2} \left(\frac{\mu_0}{2}\right)^{1/4} \tag{2.2}$$

where R is the radius from the star, z_s is the height of the wall, subscript 0 refers to the boundary between the wall and the outer disk, $\mu_0 = \cos\theta_0$ and $\theta_0 = \pi/2 - \tan^{-1}(dz_s/dR)$, and we assume that at 7 millimeters the radial brightness tracks the temperature. To set the absolute flux of this component, we normalized the intensity distribution to match the peak flux of the image and the total flux of the disk determined from previous, lower resolution imaging (Wilner et al. 2000). Since ΔR is not well constrained by our data, except that the wall must be narrow compared to the size of the hole ($\Delta R \ll R$) and the resolution of the data ($\Delta R \ll 0\farcs09$, or 4.6 AU at 51 pc), we use the value $\Delta R = 0.5$ AU which Calvet et al. (2002) find to be consistent with the shape of the mid-IR SED. We choose R_0 to be 4.5 AU so that the peak of the wall emission occurs near 4.0 AU, causing the null of the model to match the position indicated by the data. For the dust mass opacity, we use the power law form $\kappa = \kappa_0(\frac{\nu}{\nu_0})^\beta$ where $\kappa_0 = 1.8$, $\nu_0 = 1.0 \times 10^{12}$, and $\beta = 0.8$ (D'Alessio et al. 2001).

We used the Monte Carlo radiative transfer code RATRAN (Hogerheijde & van der Tak 2000) to calculate a sky-projected image from the model continuum emission, with frequency and bandwidth appropriate for the observations, and the miriad task *uvmodel* to simulate the observations, using the appropriate antenna

positions and visibility weights. Figure 2.2 shows the visibility function from this model (heavy solid line), which matches well the observations. The light solid line shows the contribution from the outer disk, which accounts for only a small fraction of the flux observed at long baselines, and the dotted curve shows contribution from the thin wall component, which dominates the outer disk at $\mathcal{R}_{uv}$ beyond $\sim$ 100 kλ. The long baseline data are sensitive to the total flux and thin width of the wall, and are compatible with the assumptions of the wall structure used in the previous SED modeling. In the image domain, we have compared the 7 millimeter data to the Calvet et al. (2002) model using RATRAN to generate images of a disk with an inner hole of radius 4.5 AU and a bright wall of width 0.5 AU and total flux 1.7 mJy (Figure 2.1, center panel), which Calvet et al. (2002) find to be consistent with the mid-infrared SED. For comparison, we also generate an image of a continuous disk extending inward to the dust destruction radius at 0.01 AU (Figure 2.1, right panel). The data are inconsistent with this continuous disk model, while the SED-based model of Calvet et al. (2002) with an inner hole and bright wall matches the observed structure well.

In short, the 7 millimeter data suggest an outer dust disk extending inward to $\sim$ 4.5 AU, where there is wall of radial extent $\sim$0.5 AU that is much brighter than the surrounding disk on account of direct illumination by the star. Interior to the wall, a sharp transition occurs to a region of lower dust surface density and correspondingly weak or absent 7 millimeter emission.

2.4.2 Disk Clearing

The resolved observations bolster the inference from SED models that the TW Hya disk has an inner hole of much reduced dust column density of radius $\sim$ 4 AU. Theories of disk-planet interaction have long predicted the opening of gaps in circumstellar disks as a consequence of the formation of giant planets (e.g. Lin & Papaloizou 1986; Bryden et al. 1999), and numerical simulations of such interactions produce these gaps in a consistent way across differing architectures and computational algorithms (de Val-Borro et al. 2006). Recent work by Varnière et al. (2006) has shown that in turbulent disks with α-viscosity, inner holes are in fact more likely than gaps as a consequence of the formation of Jupiter-mass planets around solar mass stars, as the process of outward angular momentum transfer mediated by spiral density waves can cause clearing of the inner disk on time scales an order of magnitude shorter than the viscous timescale.

While the inner disk is largely cleared, it is not entirely devoid of gas and dust. Optical emission lines indicate gas accretion (Muzerolle et al. 2000), albeit

at the low rate of 4×10^{-10} $M_\odot$ yr^{-1}. Rettig et al. (2004) detect $\sim 6 \times 10^{21}$ g of warm CO at distances of 0.5-1 AU from the star, and Herczeg et al. (2004) infer the presence of warm H_2 within 2 AU of the star by modeling the HST and FUSE H_2 emission spectrum. The 10 μm silicate feature (Sitko et al. 2000; Uchida et al. 2004) indicates that there must be at least a few tenths of a lunar mass of dust grains present in the otherwise largely cleared inner disk (Calvet et al. 2002). The region within $\sim$0.3 AU has been spatially resolved by Eisner et al. (2006) at 2 μm using the Keck interferometer, detecting emission from optically thin, submicron-sized dust populating the inner regions. This small amount of material may be the result of a restricted flow through the transition region at $\sim$ 4 AU from the massive reservoir of the outer disk. A population of micron-sized grains in the inner disk is consistent with the predictions of Alexander & Armitage (2007), who show that planet-induced gaps tend to filter out and confine large grains at the gap edge while allowing small grains to migrate across the gap with accreting gas and populate the inner disk. Our data are consistent with an inner region devoid of 7mm dust emission; however, the degree of clearing is difficult to constrain due to both the low signal-to-noise ratio at long baselines and the dependence on the wall model adopted.

The dynamical effect of a planet is not the only possible explanation for the observed central flux deficit at millimeter wavelengths. Photoevaporation of gas by ultraviolet radiation has also been invoked to explain inner disk clearing (Clarke et al. 2001), if the evaporation rate at the gravitational radius dominates the accretion rate. As discussed by Alexander et al. (2006), TW Hya is at best marginally consistent with a photoevaporation scenario, since the outer disk mass is larger than predicted for photoevaporation, and the observed accretion should occur only for the brief period while the inner disk is draining onto the star. In contrast with the case of a planet-induced gap, photoevaporation should also clear the inner disk of all but the largest grains, as noted by Alexander & Armitage (2007). Other mechanisms, such as photophoretic effects (Krauss & Wurm 2005), could also aid in clearing the inner disk region, if gas densities are high enough.

2.5 Conclusions

We present new, spatially resolved observations of the TW Hya disk at 7 millimeters that provide direct evidence for a sharp transition in dust surface density at $\sim$ 4 AU radius, a feature consistent with the inner hole inferred from SED modeling by Calvet et al. (2002). The interpretation of the mid-infrared flux

deficit as a central clearing of material is robust. The TW Hya system is ideally suited to future observations that will be able to distinguish between the various scenarios invoked to explain central clearing in the disks around young stars. Signatures diagnostic of planets in formation, in particular spiral density waves in the disk and thermal emission from circumplanetary dust, should be within the detection capabilities of the Atacama Large Millimeter Array operating at the shortest submillimeter wavelengths (300 μm) and at the longest baselines ($>$ 10 km) to achieve the necessary angular resolution (Wolf & D'Angelo 2005). Such observations will benefit from the close proximity of TW Hya, the nearly face-on viewing geometry, and the size scale of the inner hole now confirmed by direct observation at millimeter wavelengths.

Chapter 3

A Spatially Resolved Inner Hole in the Disk around GM Aurigae

A. M. Hughes, S. M. Andrews, C. C. Espaillat, D. J. Wilner, N. Calvet, P. D'Alessio, C. Qi, J. P. Williams, & M. R. Hogerheijde 2009, *The Astrophysical Journal*, Vol. 698, pp. 131-142

Abstract

We present 0.″3 resolution observations of the disk around GM Aurigae with the Submillimeter Array (SMA) at a wavelength of 860 μm and with the Plateau de Bure Interferometer at a wavelength of 1.3 mm. These observations probe the distribution of disk material on spatial scales commensurate with the size of the inner hole predicted by models of the spectral energy distribution. The data clearly indicate a sharp decrease in millimeter optical depth at the disk center, consistent with a deficit of material at distances less than $\sim$20 AU from the star. We refine the accretion disk model of Calvet et al. (2005) based on the unresolved spectral energy distribution (SED) and demonstrate that it reproduces well the spatially resolved millimeter continuum data at both available wavelengths. We also present complementary SMA observations of CO J=3$-$2 and J=2$-$1 emission from the disk at 2″ resolution. The observed CO morphology is consistent with the continuum model prediction, with two significant deviations: (1) the emission displays a larger CO J=3$-$2/J=2$-$1 line ratio than predicted, which may indicate additional heating of gas in the upper disk layers; and (2) the position angle of the kinematic rotation pattern differs by 11° $\pm$ 2° from that

measured at smaller scales from the dust continuum, which may indicate the presence of a warp. We note that photoevaporation, grain growth, and binarity are unlikely mechanisms for inducing the observed sharp decrease in opacity or surface density at the disk center. The inner hole plausibly results from the dynamical influence of a planet on the disk material. Warping induced by a planet could also potentially explain the difference in position angle between the continuum and CO data sets.

3.1 Introduction

Understanding of the planet formation process is intimately tied to knowledge of the structure and evolution of protoplanetary disks. Of particular importance is how and when in the lifetime of the disk its constituent material is cleared, which provides clues to how and when planets may be assembled. While observations suggest that the inner and outer dust disk disperse nearly simultaneously (e.g. Skrutskie et al. 1990; Wolk & Walter 1996; Andrews & Williams 2005), it is not clear which physical mechanism(s) drives this process, or the details of how it progresses. Possible dispersal mechanisms, of which several may come into play over the lifetime of a disk, include a drop in dust opacity due to grain growth (e.g. Strom et al. 1989; Dullemond & Dominik 2005), photoevaporation of material by energetic stellar radiation (e.g. Clarke et al. 2001), photophoretic effects of gas on dust grains (Krauss & Wurm 2005), inside-out evacuation via the magnetorotational instability (Chiang & Murray-Clay 2007), and the dynamical interaction of giant planets with natal disk material (e.g. Lin & Papaloizou 1986; Bryden et al. 1999). Observing the distribution of gas and dust in disks allows us to evaluate the roles of these disk clearing mechanisms.

One particular class of systems, those with "transitional" disks (e.g. Strom et al. 1989; Skrutskie et al. 1990), have become central to our understanding of disk clearing. These disks exhibit a spectral energy distribution (SED) morphology with a deficit in the near- to mid-infrared excess over the photosphere consistent with a depletion of warm dust near the star. The advent of the *Spitzer* Space Telescope has allowed detailed measurement of mid-infrared spectra with unprecedented quality and quantity. Combined with simultaneous advances in disk modeling that can now reproduce in detail the SED features (e.g. D'Alessio et al. 1999, 2001; Dullemond et al. 2002; D'Alessio et al. 2006), these observations have revolutionized the study of disk structure. However, such studies rely entirely on SED deficits whose interpretations are not unique, since effects of

geometry and opacity can mimic the signature of disk clearing (Boss & Yorke 1996; Chiang & Goldreich 1999).

Spatially resolved observations are crucial for confirming the structures inferred from disk SEDs. High resolution imaging at millimeter wavelengths is especially important because dust opacities are low, and the disk mass distribution can be determined in a straightforward way for an assumed opacity. Millimeter observations also avoid many of the complications present at shorter wavelengths, including large optical depths, spectral features, and contrast with the central star. Several recent millimeter studies have resolved inner emission cavities for disks with infrared SED deficits through direct imaging observations, e.g. TW Hya (Calvet et al. 2002; Hughes et al. 2007), LkHα 330 (Brown et al. 2007, 2008), and LkCa 15 (Piétu et al. 2007; Espaillat et al. 2008). These observations unambiguously associate infrared SED deficits with a sharp drop in millimeter optical depth in the disk center. More information is needed to determine whether the low optical depth is a result of decreased surface density or opacity.

GM Aurigae is a prototypical example of a star host to a "transitional" disk. The ∼1-5 Myr old T Tauri star (Simon & Prato 1995; Gullbring et al. 1998) of spectral type K5 is located at a distance of 140 pc in the Taurus-Auriga molecular complex (Bertout & Genova 2006), and its brightness and relative isolation from intervening cloud material have enabled a suite of observational studies of its disk properties. The presence of circumstellar dust emitting at millimeter wavelengths was first inferred by Weintraub et al. (1989), and the disk structure was subsequently resolved in the ^{13}CO J=2–1 transition by Koerner et al. (1993). Their arcsecond-resolution mapping of the gas disk revealed gaseous material in rotation about the central star. Assuming a Keplerian rotation pattern allowed a determination of the dynamical mass for the central star of 0.8 $M_\odot$. Further modeling of the structure and dynamics of the disk was carried out by Dutrey et al. (1998), using higher-resolution ^{12}CO J=2–1 observations. Scattered light images revealed a dust disk inclined by 50-56° extending to radii ∼ 300 AU from the star (Stapelfeldt & The WFPC2 Science Team 1997; Schneider et al. 2003).

Efforts to model the SED of GM Aurigae have long indicated the presence of an inner hole, and estimates of its size have grown over the years as the quality of data and models have improved. In the early 1990s, the low 12 μm flux led to ∼ 0.5 AU estimates of the inner disk radius (Marsh & Mahoney 1992; Koerner et al. 1993). That value was later increased to 4.8 AU by Chiang & Goldreich (1999) in the context of hydrostatic radiative equilibrium models, and a putative planet at a distance of 2.5 AU from the star was shown to be capable of clearing an inner hole of this extent using simulations of the relevant hydrodynamics

(Rice et al. 2003). With the aid of a ground-based mid-IR spectrum, Bergin et al. (2004) increased the gap size estimate to 6.5 AU, and subsequently Calvet et al. (2005) inferred an inner hole radius of 24 AU using a *Spitzer* IRS spectrum in combination with sophisticated disk structure models. Recently, Dutrey et al. (2008) have argued for a 19±4 AU inner hole in the gas distribution, using combined observations of several different molecular line tracers. Like the SED-based measurements, their method is indirect: they use a model of the disk in Keplerian rotation to associate a lack of high-velocity molecular gas with a deficit of material in the inner disk.

We present interferometric observations at 860 μm from the Submillimeter Array[1] and 1.3 mm from the Plateau de Bure Interferometer[2] that probe disk material on scales commensurate with the 24 AU inner disk radius inferred from the SED. These data allow us to directly resolve the inner hole in the GM Aur disk for the first time. We describe the observations in §3.2 and present the dual-wavelength continuum data in §3.3.1. We also present observations of the molecular gas disk in the CO J=3–2 and J=2–1 lines that allow us to study disk kinematics in §3.3.2. We use these data to investigate disk structure in the context of the SED-based models of Calvet et al. (2005), described in §3.4. Implications for the disk structure and evolutionary status are discussed in §3.5.

3.2 Observations and Data Reduction

The GM Aur disk was observed with the 8-element (each with a 6 m diameter) Submillimeter Array (SMA; Ho et al. 2004) in the very extended (68-509 m baselines) and compact (16-70 m baselines) configurations on 2005 November 5 and 26, respectively. Observing conditions on both nights were excellent, with ∼1 mm of precipitable water vapor and good phase stability. Double sideband receivers were tuned to a central frequency of 349.935 GHz (857 μm), with each 2 GHz-wide sideband centered ±5 GHz from that value. The SMA correlator was configured to observe the CO J=3−2 (345.796 GHz) and HCN J=4−3 (354.505 GHz) transitions with a velocity resolution of 0.18 km s^{-1}. No HCN

[1]The Submillimeter Array is a joint project between the Smithsonian Astrophysical Observatory and the Academica Sinica Institute of Astronomy and Astrophysics and is funded by the Smithsonian Institution and the Academica Sinica.

[2]Based on observations carried out with the IRAM Plateau de Bure Interferometer. IRAM is supported by INSU/CNRS (France), MPG (Germany) and IGN (Spain).

was detected, with a 3σ upper limit of $0.9\,\mathrm{Jy\,beam^{-1}}$ in the $2\farcs2\times1\farcs9$ synthesized beam. The observing sequence alternated between GM Aur and the two gain calibrators 3C 84 and 3C 111. The data were edited and calibrated using the MIR software package.[3] The passband response was calibrated using observations of Saturn (compact configuration) or the bright quasars 3C 273 and 3C 454.3 (very extended configuration). The amplitude scale was determined by bootstrapping observations of Uranus and these bright quasars, and is expected to be accurate at the $\sim$10% level. Antenna-based gain calibration was conducted using 3C 111, while the 3C 84 observations were used to check on the quality of the phase transfer. We infer that the "seeing" induced on the very extended observations by phase noise and small baseline errors is small, $\lesssim0\farcs1$. Wideband continuum channels from both sidebands and configurations were combined. The derived $870\,\mu$m flux of GM Aur is $640\pm60\,$mJy.

Additional SMA observations in the extended (28-226 m) and sub-compact (6-69 m baselines) configurations were conducted on 2006 December 10 and 2007 September 14, respectively, with a central frequency of 224.702 GHz ($1335\,\mu$m). While the sub-compact observations were conducted in typical weather conditions for this band (2.5 mm of water vapor), the extended data were obtained in better conditions similar to those for the higher frequency observations described above. The correlator was configured to simultaneously cover the J=2−1 transitions of CO (230.538 GHz), ^{13}CO (220.399 GHz), and C^{18}O (219.560 GHz) with a velocity resolution of $\sim0.28\,\mathrm{km\ s^{-1}}$. The calibrations were performed as above.

GM Aurigae was also observed with the 6-element (each with a 15 m diameter) Plateau de Bure Interferometer (PdBI) in the A configuration (up to 750 m baselines) on 2006 January 15. Observing conditions were excellent, with atmospheric phase noise generating a seeing disk of $\lesssim0.2''$. The PdBI dual-receiver system was set to observe the 110.201 GHz (2.7 mm) and 230.538 GHz (1.3 mm) continuum simultaneously. As with the SMA data, observations alternated between GM Aur and two gain calibrators, 3C 111 and J0528+134. The data were edited and calibrated using the GILDAS package (Pety 2005). The passband responses and amplitude scales were calibrated with observations of 3C 454.3 and MWC 349, respectively. The derived 1.3 and 2.7 mm fluxes of GM Aur are 180 ± 20 and $21\pm2\,$mJy.

The standard tasks of Fourier inverting the visibilities, deconvolution with the CLEAN algorithm, and restoration with a synthesized beam were conducted with the MIRIAD software package. A high spatial resolution image of the

[3]See http://cfa-www.harvard.edu/∼cqi/mircook.html.

860 μm continuum emission from the SMA data was created with a Briggs robust = 1.0 weighting scheme for the visibilities, excluding projected baselines $\leq 70\,\mathrm{k}\lambda$, resulting in a synthesized beam FWHM of $0\farcs30 \times 0\farcs24$ at a position angle of 34°. A similar image of the 1.3 mm continuum emission with a synthesized beam FWHM of $0\farcs43 \times 0\farcs30$ at a position angle of 35° was generated from the PdBI data using natural weighting (robust = 2.0). Table 3.1 summarizes the line and continuum observational parameters.

3.3 Results

3.3.1 Millimeter Continuum Emission

Figure 3.1 shows the results of the SMA and PdBI continuum observations in both the image and Fourier domains. The presence of an inner hole in the GM Aur disk, as predicted by models of the SED, is clearly indicated both by the double-peaked emission structure in the image and by the null in the visibility data. The double-peaked emission structure points to a deficit of flux near the disk center; the null in the visibility function, or the location at which the real part of the visibilities change sign, similarly reflects a decrease in flux at small angular scales. The resolution of the 2.7 mm data from the PdBI was insufficient to provide information about the inner hole.

The maps in the left panel of Fig. 3.1 show a double-peaked brightness distribution at both wavelengths, with peak flux densities of 59 ± 4 mJy beam^{-1} at 860 μm and 16.6 ± 0.3 mJy beam^{-1} at 1.3 mm. For all but the most edge-on viewing geometries (e.g. Wolf et al. 2008), a continuous density distribution extending in to the dust destruction radius (∼0.05-0.1 AU; Isella et al. 2006) would be expected to result in a centrally-peaked brightness distribution. In the

Table 3.1: Observational parameters for GM Aur

			Continuum		
Parameter	^{12}CO J=3–2	^{12}CO J=2–1	860 μm	1.3 mm	2.7 mm
Rest Frequency (GHz)	345.796	230.538	349.935	230.538	110.201
Channel Width	0.18 km s^{-1}	0.28 km s^{-1}	2 × 2 GHz	2 × 548 MHz	548 MHz
Beam Size (FWHM)	$2\farcs2 \times 1\farcs9$	$2\farcs1 \times 1\farcs4$	$0\farcs30 \times 0\farcs24$	$0\farcs43 \times 0\farcs30$	$0\farcs93 \times 0\farcs60$
PA	14°	56°	34°	35°	31°
RMS noise (mJy beam^{-1})	310	90	3.5	0.75	0.25
Peak Flux Density (mJy beam^{-1})	6700 ± 300	2400 ± 100	59 ± 4	16.6 ± 0.8	10.3 ± 0.3
Integrated Continuum Flux (mJy)	–	–	640 ± 60	180 ± 20	21 ± 2
Integrated Line Intensity (Jy km s^{-1})	29	37	–	–	–

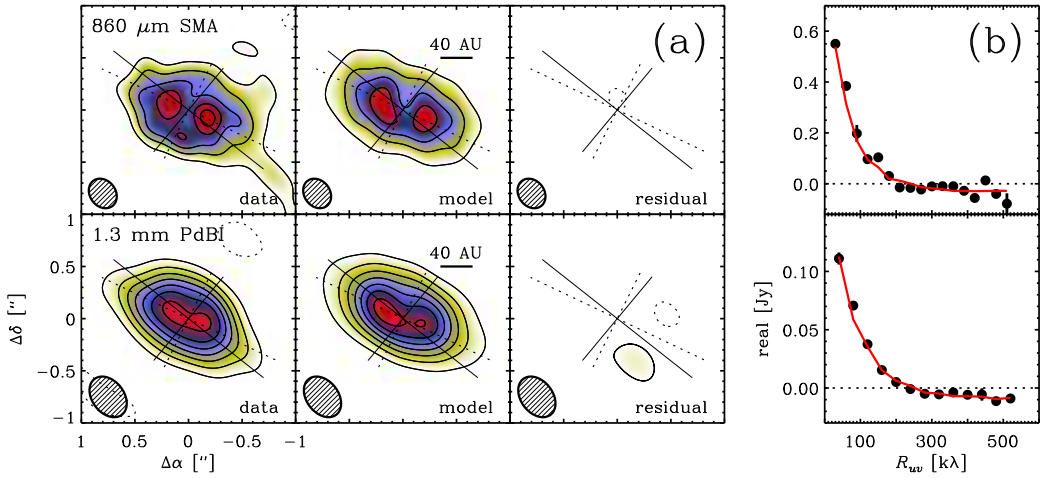

Figure 3.1.— Continuum emission from the disk around GM Aur at wavelengths of 860 μm observed with the SMA (*top*) and 1.3 mm observed with PdBI (*bottom*). The data are displayed in both the image (*a*) and Fourier (*b*) domains. In the image domain (*a*), the observed brightness distribution at each wavelength (*left*) is compared with the model prediction (*center*; see §3.4.1 for model details), and the residuals are also shown (*right*). In the data and model frames, the contours are $[3, 6, 9, ...]\times$ the rms noise (3.5 mJy beam^{-1} at 860 μm and 0.75 mJy beam^{-1} at 1.3 mm). In the residual frame, the contours start at 2σ and are never greater than 3σ. The synthesized beam sizes and orientations for the two maps are, respectively, $0\farcs30\times0\farcs24$ at a position angle of 34° and $0\farcs43\times0\farcs30$ at a position angle of 35°. Two sets of axes are shown: the dotted line indicates the position angle of the double-peaked continuum emission, while the solid line indicates the best-fit position angle of the CO emission (see §3.3.2 for details). In the Fourier domain (*b*), the visibilities are averaged in bins of deprojected u-v distance from the disk center, and compared with the model prediction (red line). The inner hole in the GM Aur disk is clearly observed at both wavelengths, as a double-peaked emission structure in the image domain or as a null in the visibility function in the Fourier domain.

case of GM Aurigae, the double-peaked emission structure is a geometric effect due to the truncation of disk material at a much larger radius, viewed at an intermediate inclination of 50-56° (Dutrey et al. 1998, 2008): the region of highest density is near the inner disk edge, with a large column density of optically thin material in this ring effectively generating limb brightening at the inner edge of the outer disk, at two points along the disk major axis.

The size of the inner hole can be roughly estimated by the separation of the emission peaks, although the peak separation will also depend on the brightness of the directly-illuminated inner edge of the outer disk relative to the extended disk component (Hughes et al. 2007). The separation of the peaks in the 860 μm image is $0\farcs38 \pm 0\farcs03$, corresponding to a physical diameter of 53 ± 4 AU (radius 27 ± 2 AU) at a distance of 140 pc. A position angle of 66° is estimated by the orientation of a line that bisects the two peaks, although a more robust value of $64° \pm 2°$ is derived in §3.4.1 below. Since the peaks are not distinctly separated in the 1.3 mm image, the same estimate cannot be made, but the position angle is clearly consistent with that derived from the 860 μm visibilities and indicated by the perpendicular dashed lines in Fig. 3.1.

The presence of an inner hole is also evident from the visibilities displayed in the right panel of Fig. 3.1. The real part of the complex visibilities have been averaged in concentric annuli of deprojected (u, v) distance from the disk center. For details of the deprojection process, see Lay et al. (1997). As discussed in the appendix of Hughes et al. (2007), the presence of a null in the visibility function indicates a sharp decrease in flux at a radius corresponding roughly to the angular scale of the null position. The precise position of the null depends primarily on the angular size of the inner hole, but also on the radial gradients of the surface density and temperature distribution and the relative brightness of the directly illuminated wall at the inner edge of the outer disk. In a standard power-law parameterization, the disk temperature T and surface density Σ vary inversely with radius as $\Sigma \propto R^{-p}$ and $T \propto R^{-q}$. Neglecting the emission from the wall and assuming standard values of $p = 1.0$ and $q = 0.5$, expected for a typical viscous disk with constant α (Hartmann et al. 1998) and consistent with previous studies of the GM Aur disk (Dutrey et al. 1998; Andrews & Williams 2007; Hughes et al. 2008b), we may obtain a rough estimate of the size of the inner hole using the observed null position and Eq. A9 from Hughes et al. (2007): $\mathcal{R}_{\rm null}({\rm k}\lambda) = (1\ {\rm AU}/R_{\rm hole})(D_{\rm source}/100\ {\rm pc})[2618 + 1059(p+q)]$. A polynomial curve fit to the visibilities yields a null position of 190 kλ at 860 μm and 224 kλ at 1.3 mm, which correspond to inner hole radii of 31 and 26 AU, respectively. However, these estimates are uncertain to within ∼30%, as the data are consistent

with a broad range of null positions. We therefore turn to a more sophisticated modeling procedure described in §3.4.1 below.

3.3.2 CO Channel and Moment Maps

Figures 3.2–3.4 display the new SMA observations of CO emission from the GM Aur disk. Figures 3.2 and 3.3 show channel maps with contours starting at twice the rms noise level and increasing by factors of $\sqrt{2}$, while Figure 3.4 displays the zeroth (contours) and first (color) moments of the data: these are the velocity-integrated intensity and intensity-weighted velocities, respectively. The peak flux density is $6.7 \pm 0.3\,\mathrm{Jy\,beam^{-1}}$ in the CO J=3–2 line and $2.4 \pm 0.1\,\mathrm{Jy\,beam^{-1}}$ in the CO J=2–1 line, with integrated fluxes of $9.4\,\mathrm{Jy\,km\,s^{-1}}$ and $21.2\,\mathrm{Jy\,km\,s^{-1}}$, respectively (although emission from extended ambient cloud material is likely to increase the CO J=2–1 integrated flux over that originating from the disk alone). The channel and moment maps are broadly consistent with the expected kinematic pattern for material in Keplerian rotation about the central star, substantially inclined to our line of sight (as in Dutrey et al. 1998; Simon et al. 2000).

The short-baseline spatial frequencies in the (u, v) plane provided by the subcompact configuration of the SMA during our observations of the J=2−1 transition are sensitive to emission on the largest spatial scales. These short antenna spacings reveal the severity of the cloud contamination to an extent not possible with previous data. The contamination is evident as an extended halo around the disk emission in the central channels of the J=2−1 channel maps near LSR velocities of 5-6 $\mathrm{km\,s^{-1}}$ (Fig. 3.3). It is also evident in the moment map (Fig. 3.4) as an elongation of emission near the systemic velocity (green-yellow) to the northwest along the disk minor axis. This contamination indicates that caution must be exercised when deriving kinematic information from the CO lines, particularly the central channels. Spatial filtering by the interferometer does not ameliorate cloud contamination in an abundant, easily-excited, high-optical depth tracer like COJ=2–1. The J=3−2 line appears less contaminated than J=2−1 (Figs. 3.2 and 3.4), although similarly short antenna spacings (8-43 m) are not present in this data set. Nevertheless, we expect less cloud contamination in the J=3−2 transition, since the temperature of the cloud will be lower than that of the disk and will therefore populate the upper rotational levels of the CO molecule less efficiently. The cloud contamination prevents detection of self-absorption in the central channels of the CO J=2–1 channel maps along the near (northwest) edge of the disk (as determined by scattered light observations;

see Schneider et al. 2003). Dutrey et al. (1998) report self-absorption along the southeast edge, but our observations suggest that this brightness asymmetry may be due to cloud contamination. It is also possible that the contamination is due to a residual envelope, although we are unable to determine the large-scale structure of the extended line emission with our interferometric data.

In all figures, the disk orientation based on the position angle of 64° derived from the continuum emission (Fig. 3.1 and §3.4.1) is plotted over the CO emission as a set of crossed dashed lines, with the relative extent of the major and minor axes (based on the inclination angle of 55°) indicated by the length of the perpendicular lines. The position angle of 51° derived by Dutrey et al. (1998) from fitting the CO J=2−1 emission, consistent with our own J=3−2 and J=2−1 observations, is illustrated by the solid line. Note that the position angle of the CO emission differs slightly from the position angle of the continuum emission, by $11° \pm 2°$ (see §3.4.1). The trend is clear for both transitions, but more obvious in the less-contaminated J=3−2 transition. Note that the position angle for the CO emission is derived entirely from the rotation pattern (evident in the isovelocity contours) and not from the geometry of the integrated CO emission: the integrated emission appears to match the position angle from the continuum emission reasonably well. We do not observe the isophote twisting in integrated CO emission seen by Dutrey et al. (1998). The cloud contamination and differences in antenna spacings may play a role.

3.4 Disk Structure Models

3.4.1 Updated SED Model

Here we revisit the broadband SED modeling of GM Aur presented by Calvet et al. (2005). Taking into consideration new observational constraints at sub-millimeter and millimeter wavelengths, we use the irradiated accretion disk models of D'Alessio et al. (2005, 2006) to re-derive the properties of the outer disk of GM Aur and its inner, truncated edge or "wall." Our grain-size distribution follows a power-law of $a^{-3.5}$, where a is the grain radius. We assume ISM-sized grains in the upper layers of the disk and accordingly adopt a_{min}=0.005 μm and a_{max}=0.25 μm (Draine & Lee 1984). Closer to the disk midplane grains have a maximum size of 1 mm. Input parameters for the outer disk include the stellar properties, the mass accretion rate, the viscosity parameter (α), and the settling parameter (ϵ) which measures the dust-to-gas mass ratio in the upper layers of

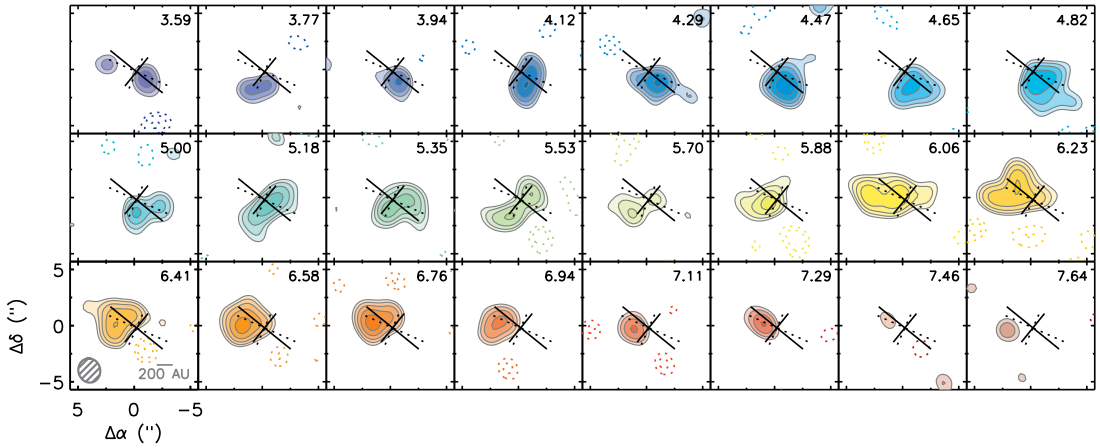

Figure 3.2.— Channel maps of CO J=3−2 emission from the GM Aur disk. Contour levels start at 0.61 Jy (2 times the rms noise) and increase by factors of $\sqrt{2}$. LSR velocity is indicated by color and quoted in the upper right of each panel. The synthesized beam (2.″2×1.″9 at a PA of 14°) and physical scale are indicated in the lower left panel. Two sets of axes are shown: the dotted line indicates the position angle of the double-peaked continuum emission, while the solid line indicates the best-fit position angle of the CO emission.

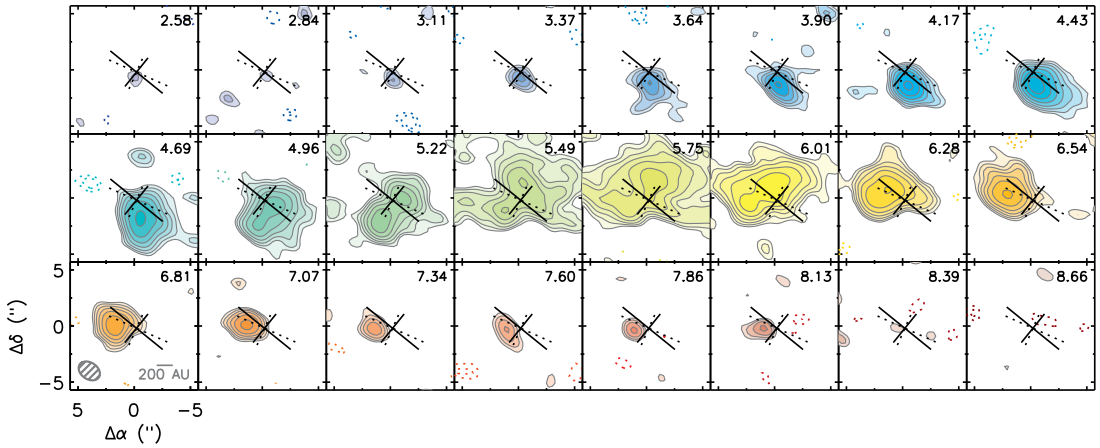

Figure 3.3.— Channel maps of CO J=2−1 emission from the GM Aur disk. Contour levels start at 0.17 Jy (2 times the rms noise) and increase by factors of $\sqrt{2}$. LSR velocity is indicated by color and quoted in the upper right of each panel. The synthesized beam (2.″1×1.″4 at a PA of 56°) and physical scale are indicated in the lower left panel. Two sets of axes are shown: the dotted line indicates the position angle of the double-peaked continuum emission, while the solid line indicates the best-fit position angle of the CO emission. Cloud contamination is evident in at least the central four channels.

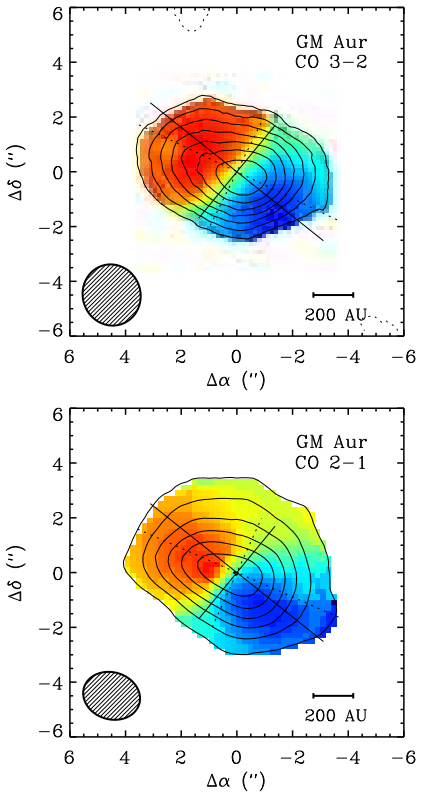

Figure 3.4.— Zeroeth (*contours*) and first (colors) moment map of the CO J=3−2 (*top*) and J=2−1 (*bottom*) data in Figs. 3.2 and 3.3. The dotted line indicates the position angle of the double-peaked continuum emission, while the solid line indicates the best-fit position angle of the CO emission. The zeroth moment contours are well aligned with the latter, while the isovelocity contours of the first moment map are more consistent with the former. Cloud contamination is evident in the CO J=2−1 map in the northwest region along the disk minor axis.

the disk relative to the standard dust-to-gas mass ratio. Following Calvet et al. (2005), we adopt the same extinction, distance, inclination, dust grain opacities, and stellar properties (i.e. luminosity, radius, and temperature; see Table 3.2). We use a mass accretion rate of $7.2{\times}10^{-9}\,M_{\odot}\,yr^{-1}$ which was derived using *HST* STIS spectra by Ingleby & Calvet (2009), in contrast to the value of $10^{-8}\,M_{\odot}\,yr^{-1}$ derived from veiling measurements in Calvet et al. (2005). We assume an outer disk radius of 300 AU, which matches the observed extent of scattered light from the dust disk (Schneider et al. 2003) and previous fits to the continuum emission (Hughes et al. 2008b), as well as the short-baseline data presented here.

In order to reproduce the outer disk component of the SED, we vary ϵ and α (Figure 3.5). As described in (Calvet et al. 2005), α effectively determines

the mass surface density distribution and therefore the disk mass, which is best reflected by the longest-wavelength SED points. The value of ϵ has the greatest effect on the slope of the SED beyond 100 μm. With the new millimeter data we find ϵ=0.5, indicating less settling than reported previously. We also find α=0.002 and a more massive outer disk of 0.16 $M_\odot$. This mass is significantly larger than an estimate based on the 860 μm and 1.3 mm flux measurements using opacities from Beckwith et al. (1990), which yields $\sim$0.04 $M_\odot$, and is only marginally Toomre stable at 300 AU (Q$\sim$1.1). The outer disk model uses an opacity of $\sim$0.1 cm^2 g^{-1} at 1 mm (D'Alessio et al. 2001) which is about four times lower than that derived from the Beckwith et al. (1990) opacities, accounting for the discrepancy in mass. Within the inner disk hole, there are 1.1×10^{-11} $M_\odot$ of optically thin small dust grains, which account for the 10 μm emission and the near-IR excess. The mass in solids could be much larger than this mass if pebbles, rocks, or even planetesimals have grown in the inner disk, since they would have a negligible opacity in the near-IR. We note that Calvet et al. (2005) reports the mass of the dust as 7×10^{-10} $M_\odot$; this is actually the mass of the gas within the hole, assuming the standard dust to gas mass ratio. The gas mass could be significantly larger, depending on the total amount of solids and the actual ratio, but these are poorly constrained by existing data.

We vary the temperature of the wall to best reproduce the data. The radius of the wall is set by the temperature and dust composition, and the wall's height is set by the disk scale height. We assume that the wall is axisymmetric and composed of relatively small grains, as well as vertically flat in order to reproduce the rapid rise of the mid-IR excess at wavelengths beyond 10 μm. We adopt the dust composition used in D'Alessio et al. (2005) and Calvet et al. (2005). The maximum grain size is adjusted from ISM sizes to reproduce the shape of the IRS spectrum as necessary. At short wavelengths, larger grains have smaller opacities than ISM-sized grains. Therefore, at a given temperature large grains will be at smaller radii than ISM-sized grains as per Eqn. 12 of D'Alessio et al. (2005). The derived size of the inner hole varies somewhat depending on whether the SED or the resolved millimeter visibilities are included. Fitting only the broadband SED and neglecting the resolved millimeter-wavelength data, the wall is located at 26 AU and has a temperature of 130K and a height of $\sim$2 AU with maximum grain size a_{max}=0.25 μm (Fig. 3.5, left panel). The radius of the wall differs by $\sim$2 AU from Calvet et al. (2005), since here we take $L_{acc} \sim GM\dot{M}/R$ assuming magnetospheric accretion while Calvet et al. (2005) uses $L_{acc} \sim GM\dot{M}/2R$ as per the boundary layer model. We also adopt a different mass accretion rate.

In order to compare the SED model with the resolved continuum data, it is

necessary to fix the disk geometry. As listed in Table 3.2, we adopt an inclination of 55°, in order to maintain consistency with Calvet et al. (2005). However, the position angle is poorly reproduced by the value of $53.4° \pm 0.9°$ that is the weighted average of fits to the CO emission (Dutrey et al. 1998, 2008, see Fig. 3.1). To derive a more appropriate position angle, we generate a sky-projected image from the disk model and use the MIRIAD task uvmodel to sample the image at the same spatial frequencies as the data. We compare these model visibilities with the observed 860 μm visibilities (which have the finest resolution). We repeat this process for a range of position angles and calculate a χ^2 value comparing each set of model visibilities with the data. Using this method, we fit a position angle of $64° \pm 2°$, which differs by $11° \pm 2°$ from the position angle of the CO disk derived by Dutrey et al. (1998, 2008).

When considering the resolved millimeter-wavelength visibilities, a disk with a 20 AU hole reproduces the emission much better (Fig. 3.5, right panel, and Fig. 3.1, center panels). Using the same χ^2 comparison of visibilities as described in the previous paragraph, the 20 AU model represents a 3σ improvement over the 26 AU model, which significantly underpredicts the amount of flux produced close to the star. This 20 AU hole has a wall with a temperature of 120 K, a height of 1.4 AU, and maximum grain size a_{max}=5 μm. For neither the 20 AU nor the 26 AU model does the wall contribute significant continuum emission at the wavelengths and spatial scales probed by our data. The main discrepancy between the fits to the SED and the millimeter visibilities occurs between wavelengths of ~20–40 μm where the 20 AU hole model overpredicts the flux. However, the SED morphology in this region is likely sensitive to the properties of the wall at the inner disk edge, which are not well known and are not constrained by our data. It is also possible that the composition of the grains, particularly whether the silicate and graphite form composite grains or are separated, can affect the temperature and therefore the mid-IR morphology of the wall component of the SED (D'Alessio 2009). Since our focus is on the interferometric millimeter-wavelength data, we adopt the model with a 20 AU inner hole for the remainder of the analysis. Figure 3.1 compares this model with the data in the image plane (center panel) and in the visibility domain (red line in the right panel). The agreement is excellent, and the residuals are less than 3σ within the $2''$ box shown.

The flux density of the eastern peak of the 860 μm image is 50 mJy beam^{-1}, while that of the western peak is 59 mJy beam^{-1}. The corresponding peaks in the model images are 49 and 50 mJy beam^{-1}, respectively. Given the rms noise of 3.5 mJy beam^{-1}, these values are consistent with no flux difference and hence axially symmetric emission from the inner disk edge. The positional accuracy of

the data and knowledge of the stellar proper motion are insufficient to determine whether or not the emission peaks are equally offset from the star. This result may be contrasted with the strong asymmetries observed by Brown et al. (2008) in their observations of the inner hole in LkHα 330, although these data are missing short antenna spacings present in the GM Aur data that may dilute asymmetries. However, as in the case of LkHα 330, we find that the GM Aur continuum presents a sharp contrast in brightness between the inner and outer disk, reflected by the null in the visibility function and the strong agreement between the data and the model containing an inner hole. The $1.1 \times 10^{-11}\,M_\odot$ of dust within the central hole in the model implies a reduction in the mass surface density of small grains of at least 6 orders of magnitude at 1 AU relative to a continuous model of the dust disk, indicating that the data are consistent with an inner disk region that is essentially completely evacuated of small grains.

3.4.2 Comparison with CO Observations

In order to compare the gas and dust properties of the GM Aur disk, we used the SED-based model described above to generate predicted CO J=3−2 and J=2−1 emission. We assume that gas and dust are well mixed, with a uniform gas-to-dust mass ratio of 100 (neglecting the complication of dust settling) and a constant CO abundance relative to H_2 of 10^{-6}, which is required to reproduce the peak CO J=2−1 flux. We also add microturbulence with a FWHM of $0.17\,\mathrm{km\,s^{-1}}$ throughout the outer disk, as derived by Dutrey et al. (1998). This is comparable to the 0.18 $\mathrm{km\,s^{-1}}$ spectral resolution of the data and does not affect our determination of the disk geometry. Due to the position angle differences evident between the continuum emission in Fig. 3.1 and the central channels in Fig. 3.2, we also adjust the position angle to 51° (as in Dutrey et al. 1998). Finally, we note that with an outer radius of 300 AU, the continuum model severely underpredicts the CO emission at large radii, as expected for a model with a sharp cutoff at its outer edge (Hughes et al. 2008b). We therefore extrapolate the model to 525 AU to match the spatial extent of the CO emission (Dutrey et al. 1998). While this larger CO model no longer matches perfectly the continuum emission for the shortest baselines, based on the prediction assuming a constant gas-to-dust mass ratio, it retains the kinematic and thermal structure of the small-scale continuum model. In order to consistently solve for the level populations and generate sky-projected images in the CO lines, we use the Monte Carlo radiative transfer code RATRAN (Hogerheijde & van der Tak 2000). We then use the MIRIAD task uvmodel to sample the model image at identical

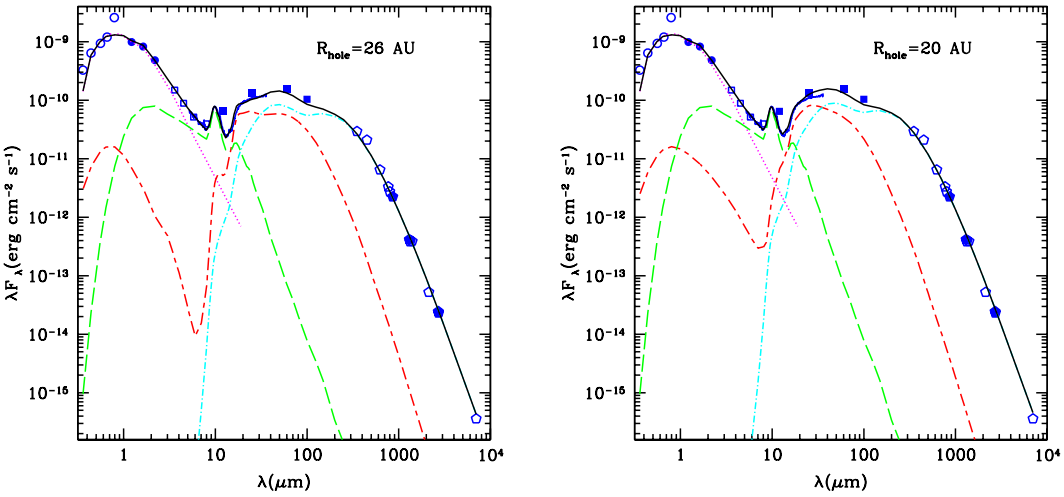

Figure 3.5.— Model of the SED of GM Aur using the method of D'Alessio et al. (2005, 2006). Final model of SED alone has an inner disk hole of 26 AU (*left*), while the model that best reproduces the resolved millimeter visibilities has a hole of radius 20 AU (*right*). See §3.4 for model details. We show optical (open circles; Kenyon & Hartmann 1995), 2MASS (closed circles), IRAC (open squares; Hartmann et al. 2005), and IRAS (closed squares; Weaver & Jones 1992) data and a *Spitzer* IRS spectrum (Calvet et al. 2005). Open pentagons represent millimeter observations (Andrews & Williams 2005; Beckwith & Sargent 1991; Dutrey et al. 1998; Kitamura et al. 2002; Koerner et al. 1993; Looney et al. 2000; Rodmann et al. 2006; Weintraub et al. 1989). Closed pentagons are from this work. The final model (solid line) includes the following components: stellar photosphere (dotted line), optically thin dust region (long-dashed line), disk wall (short-long dashed line), outer disk (dot-dashed line). The peak at $\sim$1μm from the wall emission is due to scattered light. While the 20 AU model does not fit the IRS spectrum as well between $\sim$20–40 μm as the 26 AU model, it reproduces the millimeter continuum emission very well at both 860 μm and 1.3 mm (Fig. 3.1).

Table 3.2: Stellar and Model Properties

Property	Value
L_* ($L_\odot$)	1.1
R_* ($R_\odot$)	1.5
T_* (K)	4730
$\dot{\mathrm{M}}$ ($M_\odot yr^{-1}$)	7.9×10^{-9}
Distance (pc)	140
A_V	1.2
Inclination ($^\circ$)	55
R_{wall} (AU)	20 (26)
a_{min} (μm)[1]	0.005
a_{max} (μm)[3]	5 (0.25)
T_{wall} (K)[3]	120 (130)
z_{wall} (AU)[3,4]	1.4 (2)
$R_{d,out}$ (AU)[1].....	300
ϵ[3].....	0.5
α[3].....	0.002
M_d ($M_\odot$).....	0.16

[1]These values are adopted. Refer to text for references.

[2]Values in parenthesis refer to parameters in the case that the hole is 26 AU.

[3]These are free parameters that are constrained by the SED.

[4]z_{wall} is the height of the wall above the midplane

spatial frequencies to those present in our interferometric CO data set.

Figure 3.6 compares the predicted CO emission from the extended SED model (right) with the observed emission from the GM Aur disk (left) for the J=2−1 (top) and J=3−2 transitions. It is clear that the velocity pattern in the disk is consistent with Keplerian rotation (as previously noted by Koerner et al. 1993; Dutrey et al. 1998), and that the SED-based model is capable of reproducing the basic morphology of the CO emission.

The primary difference between data and model is the CO J=3–2/J=2–1 line ratio: the disk structure model that reproduces the peak flux density of the J=2−1 transition underpredicts the peak J=3−2 flux by 30%. This difference may be attributed to a ∼10 K difference in temperature between the gas and dust in the upper layers of the GM Aur disk that are probed by these optically

thick CO lines. While the vertical temperature gradient of the dust in the model is fixed by the SED, a relative increase in gas temperature would populate the upper rotational transition of the molecule more efficiently and produce more J=3−2 emission relative to J=2−1. The temperature and the CO abundance are also somewhat interdependent, since the CO abundance sets the vertical location, and therefore the temperature, of the τ=1 surface from which most of the line emission originates. An increase in temperature would therefore also vary the anomalously low CO/H_2 ratio necessary to reproduce the J=2−1 flux. Such line ratio differences have been previously observed in the disk around TW Hya (Qi et al. 2004, 2006), and may be due to additional heating of gas in the upper disk by such processes as x-ray and UV irradiation, dissociative or mechanical heating (e.g. Glassgold et al. 2004; Kamp & Dullemond 2004; Nomura et al. 2007)

Nevertheless, while the flux levels vary between the data and model prediction, the similarity in morphology makes it clear that the overall disk structure is consistent between the molecular gas traced by CO and the model based on dust traced by continuum emission and the SED. The only other significant difference between the two is in the position angle of the emission, which differs by ∼11°. The implications of this result are discussed in §3.5.2 below.

3.5 Discussion

3.5.1 Inner Disk Clearing

The resolved millimeter continuum observations of the GM Aur system are consistent with the prediction from the SED model. Models of the observed 860 μm and 1.3 mm maps in conjunction with the SED and *Spitzer* IRS spectrum, give a value of ∼20 AU for the extent of this inner cleared region. The inference of an inner hole of this size from the SED and resolved millimeter visibilities is consistent with recent millimeter-wave observations of rotational transitions of CO isotopologues from the GM Aur disk that provide spectroscopic evidence for a diminished density of cold CO within 20 AU (Dutrey et al. 2008). However, other observations indicate that this region cannot be entirely devoid of gas. Salyk et al. (2007) detect CO rovibrational emission originating from hot gas at radii near ~ 0.5 AU, from which they infer a total gas mass in the inner disk of ~ 0.3 $M_\oplus$. Measurements of the Hα linewidth imply an accretion rate of $\sim 10^{-8}$ $M_\odot$ yr^{-1} (White & Ghez 2001; Ingleby & Calvet 2009); accretion at this rate requires a

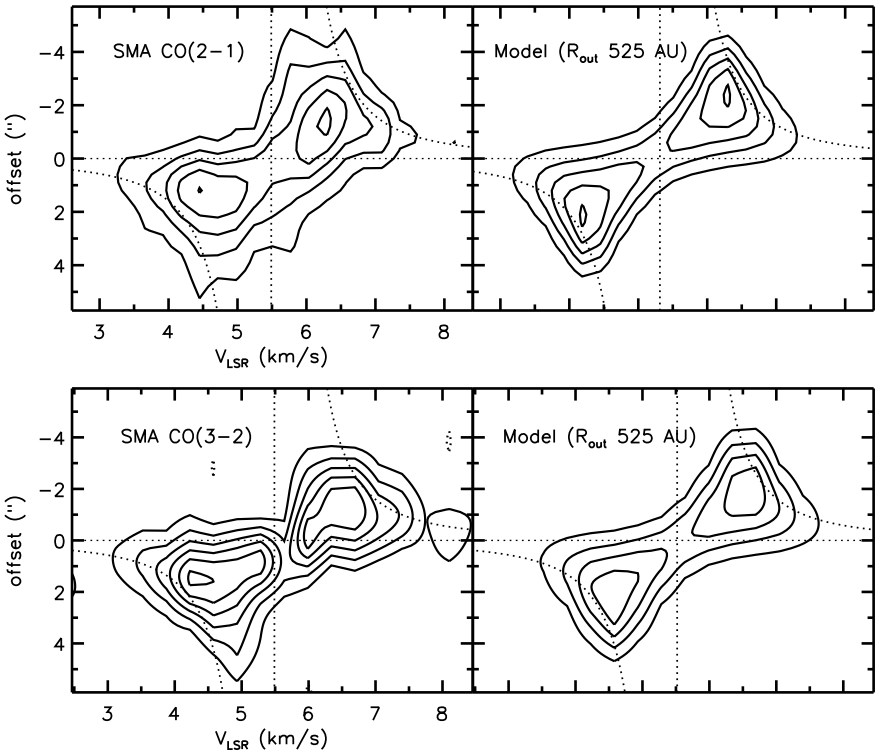

Figure 3.6.— Position-velocity diagram comparing the molecular line observations (*left*) with the predicted (*right*) CO J=2–1 (*top*) and CO J=3–2 (*bottom*) emission from the GM Aur disk, assuming a standard gas-to-dust mass ratio of 100. The plots show the brightness as a function of distance along the disk major axis, assuming a position angle of 51°. Contours are [2,4,6,...] times the rms flux density in each map (0.17 and 0.61 Jy beam^{-1}, respectively). The dotted line shows the expected Keplerian rotation curve for a star of mass $0.84\,M_{\odot}$. The outer radius of the model has been extended to 525 AU to reproduce the extent of the molecular gas emission (see §3.4.2 for details). The CO morphology is consistent with the SED-based model, with the exception of the line ratio: the model that best reproduces the peak flux of the CO J=2–1 line underpredicts the CO J=3–2 brightness by 30%.

steady supply of gas from the inner disk. The SED model also requires 3×10^{-4} lunar masses of dust in the inner disk, to account for the 10 μm silicate feature and slight near- to mid-IR excess (Calvet et al. 2005).

A wide variety of mechanisms has been invoked to explain the low optical depth of the central regions of transition disks (see e.g. Najita et al. 2007, and references therein), each with different implications for planet formation and the process of evolution between the primordial and debris disk stages. The available measurements of properties of the inner hole in the GM Aur disk allow us to evaluate the plausibility of each mechanism as the driver of disk clearing in this system.

Grain Growth – The agglomeration of dust into larger particles should proceed faster in central regions where relative velocities of particles are faster and surface densities are higher. This would produce a drop in opacities associated only with the inefficiency of emission of large grains at the observed wavelengths (e.g. Strom et al. 1989; Dullemond & Dominik 2005). However, this process is inconsistent with the clearing of CO from the central region observed by Dutrey et al. (2008), as grain growth should proceed without diminishing the gas density. Grain growth is also somewhat inconsistent with the steep submillimeter slope observed by Rodmann et al. (2006) for the GM Aur system. The value inferred for the millimeter wavelength slope α of 3.2 is the steepest in their sample of ten T Tauri stars, and is typical of a grain population that has undergone little growth, with grain size $a_{max} \leq 1$ mm. Furthermore, the original SED model and the submillimeter visibilities both independently indicate a *sharp* decrease in surface density or opacity near 24 AU, while grain growth and dust settling are predicted to be a continuous process and so should display a more gradual transition between the inner and outer disk (Weidenschilling et al. 1997; Dullemond & Dominik 2005).

Photoevaporation – Another proposed process to generate inside-out clearing of protoplanetary disks is photoevaporation via the "UV switch" mechanism (Clarke et al. 2001). In this scenario, high-energy photons from the star heat the upper disk layers, allowing material to escape the system at a rate that gradually diminishes the disk mass, while most of the disk mass drains onto the star via viscous accretion (e.g. Hartmann et al. 1998). Once the photoevaporation rate matches the accretion rate near 1 AU and prevents resupply of material from the outer disk, the inner disk will decouple and drain onto the star within a viscous timescale, leaving an evacuated central region surrounded by a low-mass outer disk that will then rapidly disperse. As noted by Alexander & Armitage (2007), the properties of the GM Aur system are inconsistent with a photoevaporative

scenario because the large mass of the outer disk should still be sufficient to provide a substantial accretion rate to counteract the photoevaporative wind. Furthermore, the measured accretion rate is high enough that within the framework of the photoevaporation scenario, it would only be observed during the brief period of time when the inner disk was draining onto the star. Photoevaporation may yet play a role in clearing the outer disk of its remaining gas and dust, but it cannot explain the current lack of inner disk material.

Inside-Out MRI Clearing – The magnetorotational instability operating on the inner disk edge may also drive accretion and central clearing, although it should be noted that this is purely an evacuation mechanism: it can only take hold after the generation of a gap by some other means. Nevertheless, given the creation of a gap, MRI clearing is predicted to operate in systems like GM Aur whose outer disks are still too massive for photoevaporation to dominate (Chiang & Murray-Clay 2007). The observed depletion of CO interior to 20 AU radius (Dutrey et al. 2008) is consistent with this theory, which predicts a total gas mass depletion of order 1000× interior to the rim radius relative to the extrapolated value from the outer disk power law fit, normalizing to the total disk mass of $0.16 M_{\odot}$. This theory is consistent with the substantial accretion rate of the GM Aur system, yielding a value of α of 0.005, only slightly greater than the derived value of 0.002 from the model. Salyk et al. (2007) estimate a gas-to-dust ratio of ~ 1000 in the inner disk, roughly 10 times greater than that of the outer disk, which is consistent with the prediction of the inside-out MRI evaporation scenario that flux from the star should promote blowout of small dust grains by radiation pressure, substantially clearing the inner disk of dust even as the gas continues to accrete onto the star. However, it is difficult to reconcile this with the substantial population of μm-size grains that must be present in the inner disk to account for the $10\,\mu$m silicate feature in the IRS spectrum. It is also important to consider the source of the requisite initial gap in the disk.

Binarity – The dynamical influence of an unseen stellar or substellar companion would also cause clearing of the inner disk. A notable example is the recent result by Ireland & Kraus (2008) demonstrating that the inner hole in the transition disk around CoKu Tau/4 is caused by a previously unobserved companion. There are relatively few constraints on the multiplicity of GM Aur at the $< 20\,$AU separations relevant for the inner hole. Radial velocity studies with $\mathrm{km\,s^{-1}}$ precision do not note variability (Bouvier et al. 1986; Hartmann et al. 1986), ruling out a close massive companion. As Dutrey et al. (2008) discuss, the stellar temperature and dynamical mass from the disk rotation combined with the H-band flux place an upper limit of $\sim$0.3 $M_{\odot}$ on the mass of a companion.

Interferometric aperture-masking observations with NIRC2 that take advantage of adaptive optics on the Keck II telescope place an upper limit of ∼40 times the mass of Jupiter on companions with separations between 1.5 and 35 AU from the primary (A. Kraus and M. Ireland, private communication). The presence of hot CO in the central 1 AU of the system (Salyk et al. 2007) and the high accretion rate, undiminished relative to the Taurus median, also argue against the presence of a massive close companion. A stellar companion is therefore an unlikely origin for the central clearing in the GM Aur system.

Planet-Disk Interaction – Perhaps the most compelling mechanism for producing a transition disk is the dynamic clearing of material by a giant planet a few times the mass of Jupiter. The opening of gaps and holes in circumstellar disks has long been predicted as a consequence of giant planet formation (e.g. Lin & Papaloizou 1986; Bryden et al. 1999). Some simulations have shown that inner holes may in fact be a more common outcome than gaps as angular momentum transfer mediated by spiral density waves can clear the inner disk faster than the viscous timescale (Varnière et al. 2006; Lubow & D'Angelo 2006). The planet-induced clearing scenario was considered in detail for GM Aur by Rice et al. (2003) and found to be globally consistent with the observed properties of the system (although their estimate of the inner hole radius is based on pre-*Spitzer* SED information). This mechanism naturally explains the diminished but persistent accretion rates and presence of small dust grains through two predictions of models of planet-disk interaction: (1) filtration of dust grains according to size is expected at the inner disk edge, leading to a dominant population of small grains in the inner disk (Rice et al. 2006); and (2) a sustained reduction in accretion rate to $\sim 10\%$ of that through the outer disk is predicted as the giant planet begins to intercept most of the accreting material (Lubow & D'Angelo 2006). These effects combined may also explain the enhanced gas-to-dust ratio in the inner disk. A planet-induced gap could also serve as a catalyst for inside-out MRI clearing Chiang & Murray-Clay (2007).

Given the observed 20 AU inner disk radius and the scenario of clearing via dynamical interaction with a giant planet, it is possible to make a simple estimate of the distance of the planet from the star. The width of a gap opened by a planet is approximately $2\sqrt{3}$ Roche radii (Artymowicz 1987), and simulations show that the minimum mass necessary to open a gap is of order 1 Jupiter mass (e.g. Lin & Papaloizou 1993; Edgar et al. 2007). If the outer edge of the planet-induced gap coincides with the 20 AU inner disk radius (with the portion of the disk interior to the planet cleared via spiral density waves or the MRI), then a companion between 1 and 40 times the mass of Jupiter would be located between 11 and

16 AU from the star. The influence of a planet carving out an inner cavity in the dust distribution is therefore a plausible scenario, bolstered by recent results demonstrating that a planet is responsible for dynamical sculpting of dust in the much older Fomalhaut system (Kalas et al. 2008).

3.5.2 Evidence for a Warp?

While the model comparison in §3.4 above shows that CO emission from the disk is globally consistent with Keplerian rotation, the 11° difference in position angle between the continuum data and the two CO data sets is significant at the $\sim 5\sigma$ level, and may indicate some kinematic deviation from pure Keplerian rotation in a single plane. Changes in position angle with physical scale are commonly interpreted as warps in the context of studies of galaxy dynamics (e.g. Rogstad et al. 1974); it may be that the change in position angle in the GM Aur disk indicates a kinematic warp.

The possibility of a warp or other deviation from Keplerian rotation was discussed by Dutrey et al. (1998), although their discussion was based on possible isophote twisting observed in integrated CO J=2−1 contours. We observe no such isophote twisting in the integrated CO J=2–1 or J=3–2 emission presented here (Fig. 3.4), although this determination may be influenced by the differing baseline lengths and beam shapes in the respective interferometric data sets. Instead, we observe deviations from the expected position angle only in the rotation pattern of the resolved CO emission, which is reflected in the isovelocity contours of Fig. 3.4. This position angle change does not appear to be related to the cloud contamination, as it is more clear in the less-contaminated CO J=3−2 data set. In order to test whether the position angle of the true brightness distribution might have been altered by incomplete sampling of the data in the Fourier domain, we generated a model of the disk at a position angle of 64°, consistent with that measured independently for the two continuum data sets. We then fit the position angle by χ^2 minimization as in §3.4.1 above. With this method, after sampling with the response at the spatial frequencies in the CO J=3–2 data set, we recover the position angle to within less than a degree of the input model. This is to be expected, since the χ^2 fitting procedure takes into account the interferometer response when fitting for the position angle. The position angle change is therefore robust independent of beam convolution effects.

In order to cause a change in position angle on physical scales between those probed by the continuum ($\sim$ 30 AU) and the CO ($\sim$ 200 AU), a warp would have to occur at a size scale of order 100 AU. The most natural explanations

for the presence of a warp in a gas-rich circumstellar disk include flybys and perturbations by a planet or substellar companion. A simple estimate of the timescale of flyby interactions is $\tau = 1/(N\pi b^2\sigma)$, where N is the number density of stars, b is the approach distance, and σ is the velocity dispersion. Assuming typical values for Taurus, including a stellar density of $\sim$10 pc^{-3} (e.g. Gomez et al. 1993) and velocity dispersion of 0.2 km s^{-1} (Kraus & Hillenbrand 2008), the timescale for interactions at distances of $\sim$1000 AU, sufficient to cause significant perturbations at Oort Cloud radii (Scholl et al. 1982), is of order 1 Gyr. Since the results of a one-time perturbation would likely damp in a few orbital periods (10^3 yr at a distance of 100 AU), such an interaction is statistically unlikely. However, it should be noted that a recent interaction might have been capable of producing an extended feature like the "blue ribbon" observed in scattered light by Schneider et al. (2003).

The influence of a massive planet or substellar companion has been investigated as the origin of warps observed in gas-depleted debris disks, including β Pic (Mouillet et al. 1997) and HD 100546 (Quillen 2006). However, there is a dearth of theoretical investigation into the plausibility of warps caused by planetary systems in gas-rich disks more closely analogous to the GM Aur system. Since the warp in the GM Aur disk must occur between the Hill sphere of the putative planet and the $\sim$200 AU resolution of the CO line observations, it is plausible that the warp could be due to the gravitational influence of the same body responsible for evacuating the inner disk. A theoretical inquiry into this possibility would be useful, but is beyond the scope of this paper.

3.6 Conclusions

Spatially resolved observations in millimeter continuum emission, obtained using the SMA at 860 μm and PdBI at 1.3 mm, reveal a sharp decrease in optical depth near the center of the GM Aur disk. Simple estimates of the extent of this region, based on the separation of peaks in the continuum images and the position of the null in the visibility functions in Fig. 3.1, are consistent with the inner hole radius of 24 AU derived by Calvet et al. (2005) using disk structure models to fit the SED. No significant azimuthal asymmetry is detected in the continuum emission.

Refined versions of the SED-based model of Calvet et al. (2005) show that the data are very well reproduced by a disk model with an inner hole of radius 20 AU. This model overpredicts the broadband SED flux in the 20–40 μm wavelength regime, but this region of the spectrum likely depends on the properties of the

wall at the inner disk edge, which are poorly constrained by available data.

CO emission in the J=3−2 and J=2−1 transitions confirms the presence of a disk with kinematics consistent with Keplerian rotation about the central star, but at a position angle offset from the continuum by $\sim$11°. The morphology of the CO emission is broadly consistent with the SED model, but with a larger CO J=3–2/J=2–1 line ratio than predicted for the SED model. This is a likely indication of additional gas heating relative to dust in the upper disk atmosphere.

Given the observed properties of the GM Aur system, photoevaporation, grain growth, and binarity are unlikely physical mechanisms for inducing a sharp decrease in opacity or surface density at the disk center. The inner hole plausibly results from the dynamical influence of a planet on the disk material, with the inner disk possibly cleared by spiral density waves or the MRI. While a recent flyby is statistically unlikely, warping induced by a planet could also explain the difference in position angle between the continuum and CO data sets.

Chapter 4

A Resolved Molecular Gas Disk around the Nearby A Star 49 Ceti

A. M. Hughes, D. J. Wilner, I. Kamp, & M. R. Hogerheijde 2008, *The Astrophysical Journal*, Vol. 681, pp. 626-635

Abstract

The A star 49 Ceti, at a distance of 61 pc, is unusual in retaining a substantial quantity of molecular gas while exhibiting dust properties similar to those of a debris disk. We present resolved observations of the disk around 49 Ceti from the Submillimeter Array in the J=2-1 rotational transition of CO with a resolution of 1.0×1.2 arcsec. The observed emission reveals an extended rotating structure viewed approximately edge-on and clear of detectable CO emission out to a distance of $\sim$ 90 AU from the star. No 1.3 millimeter continuum emission is detected at a 3σ sensitivity of 2.1 mJy/beam. Models of disk structure and chemistry indicate that the inner disk is devoid of molecular gas, while the outer gas disk between 40 and 200 AU from the star is dominated by photochemistry from stellar and interstellar radiation. We determine parameters for a model that reproduces the basic features of the spatially resolved CO J=2-1 emission, the spectral energy distribution, and the unresolved CO J=3-2 spectrum. We investigate variations in disk chemistry and observable properties for a range of structural parameters. 49 Ceti appears to be a rare example of a system in a late stage of transition between a gas-rich protoplanetary disk and a tenuous, virtually gas-free debris disk.

4.1 Introduction

A key to understanding the formation of planetary systems lies in characterizing the transitional phase between the gas-rich primordial disks found around young T Tauri stars and the tenuous, virtually gas-free debris disks around their main-sequence counterparts. Unfortunately, disks in this transitional phase are rare and difficult to identify. Dust disks around young stars are commonly identified through the "Vega-excess" phenomenon (first observed using the Infrared Astronomical Satellite by Aumann et al. 1984; see review by Zuckerman 2001), in which an infared excess over the stellar photosphere is attributed to reprocessing of optical and ultraviolet starlight by thermally emitting circumstellar dust grains. 49 Ceti was first identified in this way by Sadakane & Nishida (1986). The quantity $\tau = L_{IR}/L_{bol}$ is often used as an indicator of the "optical depth" of the dust disk, as it provides a rough estimate of the quantity of optical/ultraviolet light intercepted and reemitted by the dust. Jura et al. (1993) correlated the IRAS Point Source Catalog with the Yale Bright Star Catalog (Hoffleit & Jaschek 1991) and identified three A stars with $\tau > 10^{-3}$, indicative of tenuous, optically thin circumstellar dust. Two were the stars β Pic and HR4796, which are now known to host debris disks. The third was 49 Ceti, which unlike the other two defies classification as a debris disk because it retains a substantial quantity of molecular gas, first observed in the CO J=2-1 line (Zuckerman et al. 1995) and later confirmed in J=3-2 (Dent et al. 2005). At a distance of only 61 pc (Hipparcos), it is one of the closest known gas-rich circumstellar disks, farther only than TW Hydrae (51pc; Mamajek 2005). Its outward similarity to a debris disk, combined with the substantial quantity of molecular gas still present in the system, suggest that the disk may be in an unusual transitional evolutionary phase.

All three high-τ A stars are young: HR 4796A has an age of 8 ± 2 Myr (Stauffer et al. 1995) and β Pic has been placed at $\sim$ 20 Myr by Thi et al. (2001b), consistent with the age determination of 20 ± 10 Myr by Barrado y Navascués et al. (1999). The age of 49 Ceti is uncertain due to its isolation; unlike β Pic or HR 4796A there are no known associated low-mass stars to provide a corroborating age estimate. Jura et al. (1998) demonstrate that on an HR diagram, all three stars exhibit a low luminosity for their color, which is likely attributable to their young ages ($\sim$ 10 Myr). Using the evolutionary tracks of Siess et al. (2000), Thi et al. (2001b) assign an age of 7.8 Myr to 49 Ceti based on its position on the HR diagram.

Few conclusive measurements have been made of the dust properties in the

49 Ceti system. HST/NICMOS coronographic observations of 49 Ceti failed to detect any scattered light in the near infrared at $r > 1\farcs6$ (Weinberger et al. 1999). Recent subarcsecond-scale imaging at mid-infrared wavelengths with Keck (Wahhaj et al. 2007) revealed dust emission at 12.5 and 17.9 μm, extended along a NW-SE axis and apparently inclined at an angle of 60°. Simple models of the dust emission suggest a radial size segregation of dust grains, with a population of very small grains ($a \sim 0.1\mu$m) confined between 30 and 60 AU from the star, and a population of larger grains ($a \sim 15\mu$m) from 60 to 900 AU from the star. However, the outer radius of this latter component is uncertain due to its dependence on the millimeter flux, which is not well determined. There are two contradictory single dish measurements of the millimeter dust emission, both with modest signal-to-noise. Bockelée-Morvan et al. (1994) report a IRAM 1.2 mm flux of 12.7 ± 2.3 mJy, while Song et al. (2004) report a JCMT/SCUBA 850 μm flux of 8.2 ± 1.9 mJy. These measurements are mutually inconsistent for either a thermal spectrum ($F_\lambda \propto \lambda^{-2}$) or a typical optically thin circumstellar disk spectrum ($F_\lambda \propto \lambda^{-3}$) in this wavelength regime.

If we accept the lower value of the 850 μm flux and make standard assumptions about the dust opacity (e.g. Beckwith & Sargent 1991), then the total mass of the 49 Ceti dust disk is 0.1 $M_\oplus$. If we compare this to other nearby dusty disks at potentially similar stages of evolution, we find that 49 Ceti, with an 850 μm flux of 8.2 mJy at a distance of 61 pc, has a dust mass ($\propto F_{850\mu m} d^2$) approximately 80% that of β Pic (104.3 mJy, 19.3 pc; Holland et al. 1998) but only 0.3% that of the typical Herbig Ae star HD 169142 (554 mJy, 145 pc; Sylvester et al. 1996). Thus the 49 Ceti disk appears to have a tenuous dust disk more akin to that of the debris disk around β Pic than a gas-rich protoplanetary disk.

Studies of the distribution of gas in the 49 Ceti system have been similarly inconclusive, particularly since it is not obvious that a substantial reservoir of molecular gas should persist in the strong UV field of an A star at this apparently advanced stage. Attempts to detect pure rotational transitions of the H_2 molecule have resulted in contradictory reports, with Thi et al. (2001a) reporting a marginal detection using SWS/ISO, which Chen et al. (2006) did not confirm with Spitzer/IRS observations; nor did Carmona et al. (2007) detect H_2 emission with VLT/CRIRES observations. Models of the double-peaked JCMT CO J=3-2 line profile observed by Dent et al. (2005) indicated that the gas is likely distributed in either a very compact disk with $\sim 16°$ inclination or a more inclined ring of radius ~ 50 AU and inclination $\sim 35°$. The latter was deemed more consistent with the dust distribution seen in the mid-infrared, although it fails to reproduce

the high-velocity wings that may be present in the CO J=3-2 line profile.

In order to obtain spatially resolved information on the distribution of material in the system, we observed 49 Ceti with the Submillimeter Array in the J=2-1 transition of CO and associated continuum. We detect a rotating structure of much greater extent than predicted from the single-dish measurements, with a large central region devoid of molecular gas emission. We also model the disk emission using COSTAR (Kamp & Bertoldi 2000; Kamp & van Zadelhoff 2001), a code that combines thin hydrostatic equilibrium models of disks with a rich chemistry network and a detailed heating and cooling balance to determine gas properties. The models provide some insight into basic properties of the disk, including the region of photodissociation of CO in the inner disk and the spatial extent of the emission.

The observations are described in §4.2, and results presented in §4.3. In §4.4 we discuss the process undertaken to model the data, including the basic model structure, the initial conditions for the chemistry, and the initial model adopted from the dust emission analysis of Wahhaj et al. (2007), as well as adjustments to that fiducial model necessitated by the new observations. The parameter space is explored in §4.4.1, including an investigation of the varying influence of chemistry across the model grid, and §4.4.2 discusses the dust properties in the context of the spectral energy distribution predicted from the gas model. The best-fit model is discussed in §4.4.3, including an a posteriori comparison of the model prediction with the observed CO J=3-2 spectrum; inadequacies of the model are also noted. The results are discussed in the broader context of disk evolution in §4.5, and a summary is presented in §4.6.

4.2 Observations

We observed 49 Ceti with the SMA at 230 GHz during an 11-hour track on the night of October 13, 2006. Atmospheric phase was extremely stable, with typical phase changes of $< 15^\circ$ between calibrator scans (every 25 minutes). Seven antennas were used in the "extended" configuration, with projected baselines between 15 and 130 meters. The primary flux calibrator was Uranus, and the passband calibrators were the quasars 3C454.3 and J0530+135. Gain calibration was carried out using the quasar J0132-169, located just 1.3° from 49 Ceti; the flux derived for this quasar was 0.93 Jy. The nearby quasar J0006-063 was also included to test the quality of the phase transfer from J0132-169.

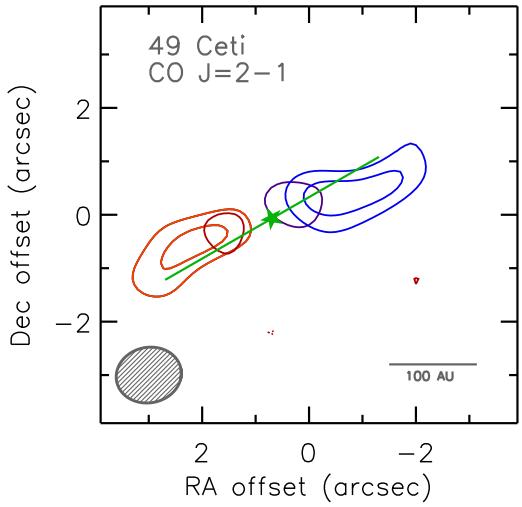

Figure 4.1.— A renzogram of SMA observations of 49 Ceti in the CO J=2-1 line. The beam size is 1.″0×1.″2, and the position angle is −79°. Contours are -3, 3, and 5 × 37 mJy/beam (the rms noise). The position of 49 Ceti is marked with a star symbol, while the green line indicates the position angle derived by Wahhaj et al. (2007) from mid-IR imaging. The contour colors indicate heliocentric line-of-sight velocity; the four distinct velocities shown are 9.0, 11.1, 13.2, and 15.3 km/s, in the order of bluest to reddest channel. No emission was detected outside this velocity range.

Two 2-GHz sidebands separated by 10 GHz were used, yielding a continuum sensitivity of 0.7 mJy (1σ). Spectral resolution in the line was 0.26 km/s, subsequently binned to 2.1 km/s, with rms sensitivity 0.030 Jy in a single 2.1 km/s channel. The LSR velocities were converted to heliocentric using an offset of -9.14 km/s. The synthesized naturally weighted beam in the CO J=2-1 line was 1.″0×1.″2, at a position angle of -78.6°. Imaging was carried out using the MIRIAD software package.

4.3 Results and Analysis

Figure 4.1 shows the observed line emission from the region around 49 Ceti. Four velocity channels are shown, with the velocity indicated by the color of the contour lines. The observations are centered on the J2000 coordinates of 49 Ceti; the star symbol indicates the position corrected for the proper motion measured by *Hipparcos*. The maximum signal-to-noise ratio in the line is 8. The CO

J=2-1 emission appears to be in an extended rotating structure of > 2" radius, apparently viewed close to edge-on. The symmetric distribution of the emission in the four velocity channels implies a heliocentric velocity near 12.2 km/s, consistent with previous determinations of the systemic velocity (10.5 and 9.9 km/s for the disk and the star, respectively; see Dent et al. 2005, and references therein). No emission is detected outside the range of velocities shown. The wide separation of the emission peaks, combined with a lack of compact, high-velocity emission, suggests that the central regions are clear of CO J=2-1 emission out to ∼90 AU radius (∼1.″5), twice that of the larger ring predicted from the CO J=3-2 single dish data. Table 4.1 lists the observed parameters of the system.

Assuming optically thin lines and LTE, the total mass in CO probed by the J=2-1 transition is given by

$$M = \frac{4\pi}{h\nu_{21}} \frac{F_{21} m d^2}{A_{21} x_2} \tag{4.1}$$

where the subscript 21 refers to the CO(2-1) transition, F is the integrated flux in the line, d is the distance to the source (61 pc; Hipparcos), m is the mass of the CO molecule, ν is the rest frequency of the transition, h is Planck's constant, and $x_2 \equiv \frac{N_2}{N_{tot}}$ where N_2 is the population in the J=2 rotational level while N_{tot} is the total CO population. The CO mass calculated using this method is 2.2×10^{-4} $M_\oplus$. Using the canonical CO/H_2 ratio of 10^{-4} this yields a molecular hydrogen mass of 2.2 $M_\oplus$, consistent with the value of 6.3×10^{-3} $M_{Jup} = 2.0$ $M_\oplus$ calculated by Zuckerman et al. (1995).

No continuum emission was detected at this combination of resolution and sensitivity. This indicates one of two things: either the continuum flux is concentrated at the center of the disk but the total flux is too low to be detected, or the total flux may be larger but spread over many beams, so that the brightness within each beam is below our detection threshold. These observations were sensitive enough to detect the higher continuum flux reported by Bockelée-Morvan et al. (1994) if it were concentrated within a few synthesized beams. However, an extrapolation of the Song et al. (2004) value for a typical circumstellar dust spectrum predicts a lower flux by a factor of 6, which is just below the detection threshold. The lack of an SMA continuum detection at 230 GHz is therefore inconclusive: if the Song et al. (2004) value is correct, we would not expect to detect even centrally concentrated emission, and so we cannot constrain the spatial extent of dust emission through the nondetection at 230 GHz.

4.4 Disk Modeling

In order to gain insight into the physical processes at work in the 49 Ceti system, we carried out modeling of the disk with COSTAR (Kamp & Bertoldi 2000; Kamp & van Zadelhoff 2001), a code which solves the chemical equilibrium simultaneously with a detailed heating and cooling balance to determine gas properties of circumstellar disks. In the following, the salient features of these models are summarized. The chemistry is modeled using a network of 48 different species covering the elements H, He, C, O, S, Mg, Si, and Fe. The elemental abundances and key parameters of these models, including the stellar mass, radius, effective temperature, surface gravity, and ultraviolet flux, are summarized in Table 4.2. The 48 species are connected through 281 reactions, including cosmic ray chemistry, photochemistry and the chemistry of excited H_2. We compute equilibrium chemistry using a modified Newton-Raphson algorithm. The solution then only depends on the element abundances and not on initial conditions.

We use the results of dust modeling by Wahhaj et al. (2007) and assume large 30 μm black body grains with radiative efficiencies of $Q_\lambda = 2\pi a/\lambda$ for $\lambda > 2\pi a$ and $Q_\lambda = 1$ otherwise. These grains are efficient absorbers and inefficient emitters, thus achieving dust radiative equilibrium temperatures of

$$T_{\rm dust} = 324 \left(\frac{L_*}{L_\odot}\right)^{0.2} (a_{\mu\rm m})^{-0.2} (r_{\rm AU})^{-0.4} \quad \text{K} \ . \tag{4.2}$$

Here, L_* and $L_\odot$ are the stellar and solar luminosity respectively, $a_{\mu\rm m}$ is the grain size in micron and $r_{\rm AU}$ the distance from the star in astronomical units. The gas temperature is derived from a detailed energy balance including the most relevant heating and cooling processes (Kamp & van Zadelhoff 2001).

The radiation field consists of both stellar and interstellar components. The stellar properties are determined by a Kurucz model fit to photometric points collected from the literature (Wahhaj et al. 2007; Sylvester et al. 1996; Bockelée-Morvan et al. 1994; Song et al. 2004); using $T_{\rm eff}$=10000 K and $\log g$ = 4.5, consistent with the values quoted by Chen et al. (2006), the derived stellar luminosity is $L_* = 26.1 L_\odot$ and the radius is 1.7 $R_\odot$. The spectral energy distribution and Kurucz model are plotted in Figure 4.2, including dereddening according to extinction derived by Sylvester et al. (1996) and using a Cardelli et al. (1989) extinction law. The solid line in the figure denotes the fit to the photometry of a Kurucz stellar atmosphere model at the Hipparcos distance of 61 pc. The dashed line shows the spectral energy distribution of the best-fit model of the outer disk as described in §4.4.3. The interstellar radiation field in the ultraviolet is assumed to be 1.2×10^7 cm^{-2} s^{-1} (Habing 1968).

Table 4.1: Observational parameters for 49 Ceti

Parameter	^{12}CO(3-2)[a]	^{12}CO(2-1)	^{13}CO(2-1)	continuum
Rest frequency (GHz)	345.796	230.538	220.399	230.5 (USB[b])
Channel width	0.27 km s^{-1}	2.1 km s^{-1}	8.4 km s^{-1}	2×2 GHz
Beam size (FWHM)	14"	1.″0×1.″2	1.″0×1.″2	1.″0×1.″2
PA	–	-78.6°	-78.6°	-78.6°
rms noise (Jy beam^{-1})	0.22	0.030	0.017	7.0×10^{-4}
Dust flux (mJy)	–	–	–	< 2.1
Peak brightness temperature (K)	0.076±0.008	3.5±0.5	< 0.8	–
Integrated intensity (Jy km s^{-1})	9.5±1.9	2.0±0.3	< 0.5	–

[a] Dent et al. (2005)

[b] Upper sideband frequency; lower sideband is centered at 220.5 GHz. Both sidebands have 2 GHz width.

Table 4.2: Element abundances and parameters used in the disk models

Parameter[a]	Value
$A_{\rm He}$	7.5×10^{-2}
$A_{\rm C}$	1.3×10^{-4}
$A_{\rm O}$	2.9×10^{-4}
$A_{\rm Mg}$	4.2×10^{-6}
$A_{\rm Si}$	8.0×10^{-6}
$A_{\rm S}$	1.9×10^{-6}
$A_{\rm Fe}$	4.3×10^{-6}
$T_{\rm eff}$	10 000 K
$\log g$	4.5
R_*	1.7 $R_\odot$
M_*	2.3 $M_\odot$
$\sigma_{\rm UV}$	$4.68\,10^{-24}$ cm^{-2} H − atom^{-1}

[a] Gas-phase abundances (A) are relative to hydrogen.

A basic model of the dust disk was constructed according to the Bayesian analysis of mid-infrared emission carried out by Wahhaj et al. (2007). Their model consists of an inner disk extending from 30 to 60 AU, composed primarily of small grains ($a \sim 0.1$ μm) with a surface density of 5×10^{-8} g/cm^2, and an outer disk extending from 60 to 900 AU composed of larger grains ($a \sim 15$ μm) with a surface density of 3×10^{-6} g/cm^2. They derive a surface density distribution for the outer disk that is constant with radius, yielding a total disk mass of 0.35 $M_\oplus$. From the mid-IR images, they also determine a position angle of $125^\circ \pm 10^\circ$ (indicated in Figure 4.1) and an inclination of $60^\circ \pm 15^\circ$. We use this model as a starting point for the disk structure, since it reflects the best available information on the dust density distribution. However, since the molecular gas emission provides better constraints on some aspects of disk structure, including the vertical density distribution and the surface density structure of the outer disk, we introduce refinements to this initial model where justified, as described in §4.4 and §4.4.1 below. For the large grain population, our model uses 30 μm grains instead of 15 μm grains, although the grain size used in this simple model is highly degenerate with other disk properties, as discussed in §4.4.2.

To predict gas properties from this dust model, we make two primary assumptions: (1) gas and dust are well-mixed, (2) the gas:dust mass ratio is constant. We initially assume a constant scale height H=2 AU, since there is no information on disk scale height from the dust model of Wahhaj et al. (2007); we also begin by retaining the inner and outer radii and radially constant surface density structure from the Wahhaj et al. (2007) model, although these assumptions are modified in §4.4 below. Throughout the modeling process, we use the canonical gas:dust mass ratio of 100 and assume that the disk is embedded in interstellar material of density 10 cm^{-3} to avoid model densities dropping to unrealistically low values near the boundaries of the numerical grid.

To compare our models with the SMA data, we use the radiative transfer code RATRAN (Hogerheijde & van der Tak 2000) to generate a sky-projected image of the CO J=2-1 emission predicted for the physical model. We then use the MIRIAD task *uvmodel* to sample the image with the combination of spatial frequencies and visibility weights appropriate for our SMA data. We allow the inclination and position angle of the system to vary in order to best match the data.

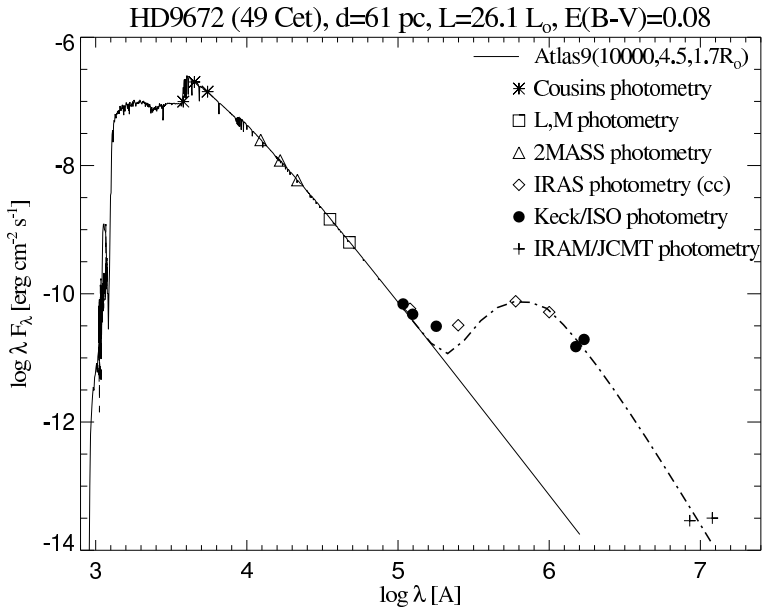

Figure 4.2.— Spectral energy distribution (de-reddened according to extinction derived by Sylvester et al. 1996 and Cardelli et al. 1989 extinction law) for 49 Ceti using available optical, infrared, and submillimeter photometry. The solid line denotes a Kurucz stellar atmosphere model fitted to the photometry using the Hipparcos distance of 61 pc. The dot-dashed line shows the SED for the best-fit model of the outer disk see text of §4.4.2 for details.

Inner Disk

In the inner disk, inside 60 AU, composed primarily of small grains, the stellar radiation field raises the dust temperature to 1000-2000 K and dissociates most of the molecular gas. In this region, the dominant form of carbon is C^+, and even hydrogen is predominantly atomic. We therefore ignore the inner disk component in subsequent modeling and focus on reproducing the observed CO emission with only the outer disk component.

This lack of molecular gas in the inner disk is consistent with the non-detection of warm H_2 by Chen et al. (2006) and Carmona et al. (2007), and with the lack of high-velocity CO emission in Figure 4.1. The lack of CO emission more than 4.3 km/s from the stellar velocity is consistent with an absence of CO within a radius of ~ 90 AU, for gas in Keplerian rotation around a star of 2.3 $M_\odot$.

Outer Disk

There are three primary features of the observed CO emission from the outer disk that we attempted to reproduce with this modeling effort: (1) the separation of the emission peaks in the outer channels (~ 3"), (2) the spatial extent of the CO emission in all channels, and (3) the strength of the emission. Reproducing these features of the observed CO emission requires several modifications to the best-fit Wahhaj et al. (2007) model of the outer dust disk, including adjustments to the inner and outer radii and a departure from the constant surface density prescription.

At first glance, the inner radius of 60 AU derived by Wahhaj et al. (2007) might seem consistent with the lack of emission within 90 AU derived from the missing high-velocity wings in our data; however, there is a large region at the inner edge of the outer disk subject to photodissociation by stellar radiation which therefore contributes little to the CO emission. In order to reproduce the separation of the emission peaks, material is required interior to this 60 AU radius. We therefore take the uncertainties in the Wahhaj et al. (2007) dust distribution into account and allow the inner disk radius to vary. However, moving the inner radius closer than ~ 40 AU to the star results in high-velocity emission that we do not observe in the data, while still producing emission peaks wider than observed. We therefore set the disk inner radius at 40 AU, and then adjust the gas densities to further reduce the separation of the emission peaks.

Increasing the total gas mass leads to an elongated morphology with an aspect ratio larger than the observations, as the optical depth rises throughout the disk. To meet the three criteria of (1) enough gas-phase CO near the inner disk edge to reproduce the observed peak separation, (2) low enough optical depth in the outer parts of the disk to keep the emission from becoming more elongated than the data (through photodissociation by interstellar UV photons), and (3) maintaining an inner radius large enough to avoid generating high-velocity emission that is not present in the data, we must "pile up" material at the inner disk edge to enhance shielding and concentrate emission. We therefore modify the initial assumption of constant surface density as derived from the infrared analysis, instead adopting an $r^{-\epsilon}$ density profile. We simultaneously relax the constant scale height assumption, introducing a scale height H that increases linearly with radius r, with proportionality constant $h = H/r$. The full 2-D density structure then becomes $n(r, z) = r^{-\epsilon} \exp\left(-z^2/2H^2\right)$, where the exponent ϵ and scale height constant h are varied to obtain the best fit to the CO data.

The power-law surface density profile results in a much better match between

the model and the observed emission peak separation. It also curbs the elongation of the emission to some extent, as the vertical column density of the outer disk drops and the material far from the star becomes subject to dissociation by interstellar radiation. However, even steep power law indices for the surface density profile do not result in a completely photoevaporated outer disk and consequently produce emission that is much more elongated than observed. In a next step, we therefore reduce the outer radius from 900 to 200 AU. While this is at the lower end of the range allowed by Wahhaj et al. (2007), their derived outer radius was based largely on the uncertain millimeter flux measurement, and the gas geometry is likely a better probe of the disk extent.

4.4.1 Grid of Disk Models

After these initial studies of the outer disk, it became clear that several model parameters were ill-constrained by previously existing data. Specifically, the disk mass is constrained only by the weakly-detected and contradictory millimeter flux measurements; similarly, the density power law index ϵ is ill-determined by the infrared observations, which are primarily sensitive to inner disk emission. The scale height h is also completely unconstrained by the continuum or single-dish measurements, neither of which is sensitive to disk structure in the vertical direction. The disk geometry (PA and inclination) quoted by Wahhaj et al. (2007) is also subject to large uncertainties, due to the irregular shape of the emission observed in the infrared. We therefore attempt to better constrain these disk parameters by using our resolved CO gas line observations. Gas lines are generally more sensitive than dust emission to temperature and density gradients, and can thus provide means to break model degeneracies. We ran grids of models for the three structural parameters (disk mass, density index, scale height) and two geometrical parameters (PA, inclination), finding the best-fit values by calculating and minimizing a χ^2 value comparing the model to the observed emission from the disk. Due to the computational intensity of the calculations necessary to determine the chemistry and radiative transfer solutions for each model, we ran only a sparsely sampled grid of models. In order to ensure that the final model reflects all available observational constraints, we centered the grid on the fiducial model of §4.4 and adjusted the parameters only as necessary to better reproduce the new CO(2-1) observations, moving from coarse to fine grids to ensure adequate exploration of the parameter space. We use the modeling primarily as a demonstration that the basic features of the observed CO emission can be reproduced by a simple azimuthally symmetric model of disk

structure; the "best-fit" model should therefore be viewed as representative of an initial understanding of the features of the system rather than as a conclusive determination of the disk structural parameters.

CO Chemistry Across the Model Grid

The CO chemistry is dominated by photodissociation in a number of UV bands and thus the abundance of CO in each model is mostly dependent on the radial and vertical column densities being able to shield the stellar and interstellar UV radiation respectively. In the following we briefly discuss some basic characteristics of the model grid.

The surface density in the models is independent of the scale height and hence the radial mass distribution in each model can be written as $M(R) \propto R^{-\epsilon+3}$, where $M(R)$ denotes the mass inside a radius R. So, as we increase the density power law exponent ϵ, the inner region of the outer disk harbors a larger fraction of the total mass. The densities in this region of the disk become higher and hence it is easier to obtain the critical column densities necessary for UV shielding in the radial direction. On the other hand, a shallower gradient for the density distribution translates into higher densities in the outer parts of the disk, thus enhancing the vertical shielding in the outer disk compared to models with high ϵ. None of our models is optically thick in the dust continuum, so the UV shielding is mainly H_2 shielding of the CO bands due to their overlap in wavelengths; CO self-shielding also plays a role.

With this basic picture, we can understand the CO chemistry displayed in Fig. 4.3 as a function of disk mass (right column) and density gradient ϵ (center column). As the total disk mass is increased, CO first starts to build up in the radial direction. It can still be dissociated by the vertically impinging interstellar UV radiation field in the outer regions of the disk (150-200 AU) until the disk reaches a mass of ~ 17 $M_\oplus$, at which point it becomes opaque in the CO bands even in the vertical direction. A shallow density gradient always leads to smaller radial column densities at the same reference radius, thus pushing the C^+/C/CO transition further out in radial distance. In our best-fit model of 13 $M_\oplus$, a change in ϵ from 2.5 to 1.1 changes the radius for the C^+/C/CO front from close to 40 AU to 190 AU.

The scale height h of the models affects only the vertical density structure in the models. However, since density and chemistry are closely intertwined, it can strongly impact the overall radial and vertical structure of the CO chemistry.

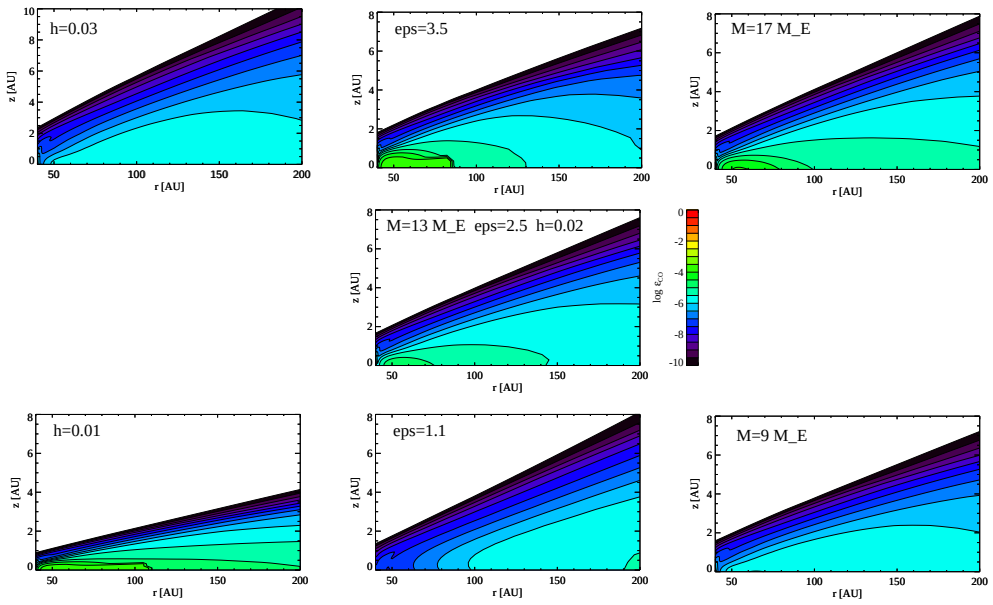

Figure 4.3.— Two-dimensional CO abundances in a subset of disk models. The center panel shows the best-fit model ($M = 13\mathrm{M}_{\oplus}$, $\epsilon = 2.5$, $h = 0.02$), while the rows of models above and below show the effects of incrementing and decrementing, respectively, each of the three structural parameters that were allowed to vary during the fitting process: *h (left column)*, ϵ *(center column)*, and M_{disk} *(right column)*. The values of the parameters shown are $h = 0.01$, 0.03; $\epsilon = 1.1$, 3.5; and $M = 9$, 17 $\mathrm{M}_{\oplus}$.

From a comparison of the center panel with the bottom left panel in Figure 4.3, we see that a factor 2 lower scale height with respect to the best fit model ($h = 0.02$), enhances the CO abundance in the disk significantly, leading to radial and vertical column densities that are more than a factor 10 higher with respect to the best fit model. The total CO mass increases by a factor of 10 as well, with the integrated emission undergoing a corresponding dramatic increase.

Table 4.3 displays some key results from a subset of grid models such as characteristic radial and vertical CO column densities, CO masses and total CO J=2-1 line emission. For all models in the table, the inner radius is fixed at 40 AU and the outer radius at 200 AU.

From Chemistry to Observables

The predicted CO J=2-1 emission for the models in Figure 4.3 is displayed in Figure 4.4; a comparison of these figures illustrates the ways in which differences

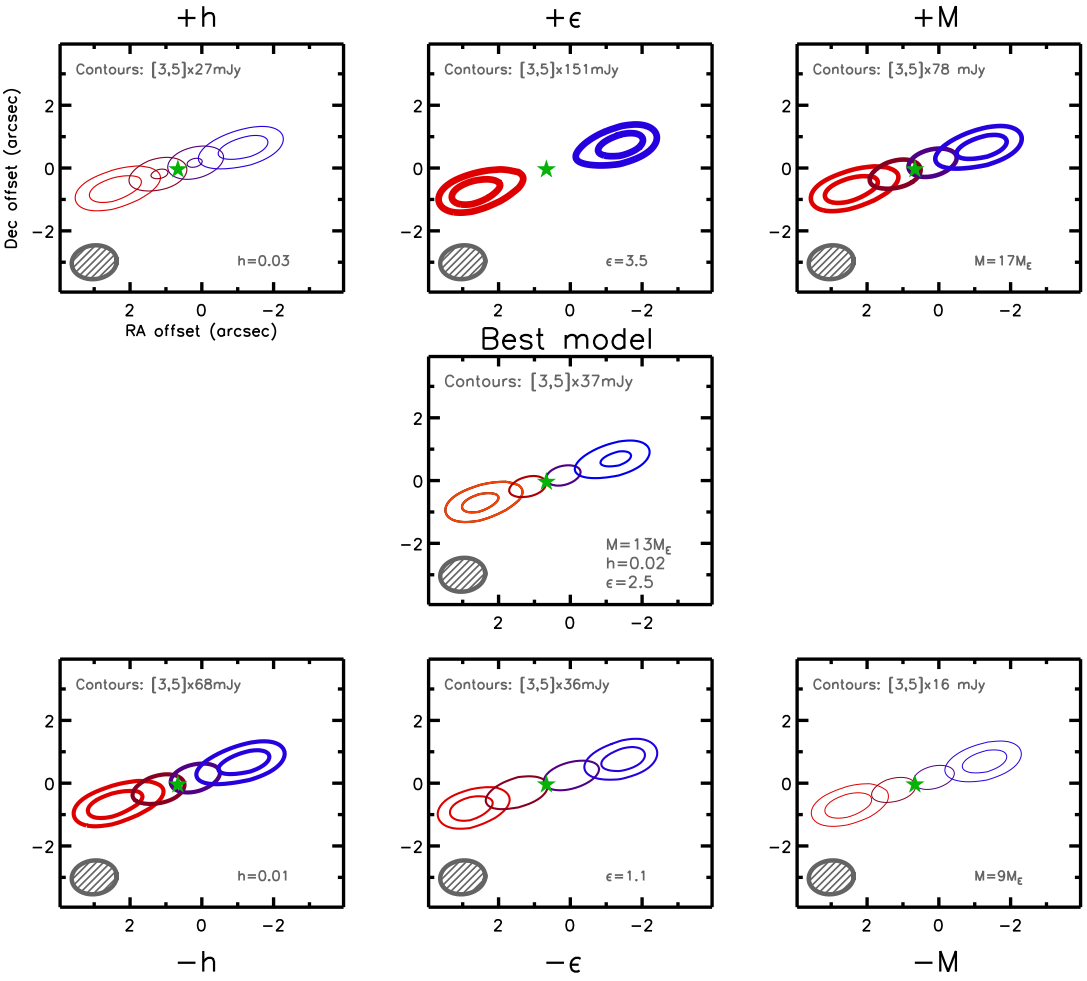

Figure 4.4.— CO J=2-1 emission predicted for the subset of models shown in Figure 4.3, sampled with the same spatial frequencies and visibility weights as the SMA data in Figure 4.1. The center panel shows the best-fit model, while the rows of models above and below show the effects of incrementing and decrementing, respectively, each of the three structural parameters that we allowed to vary during the fitting process: *h (left column)*, ϵ *(center column)*, and M_{disk} *(right column)*. The contour levels are displayed in the upper left corner of each panel; they are set at 3 and 5 $\times$ 15% of the peak flux for each model. The thickness of the contours is proportional to the absolute flux: thicker contours indicate that the source is brighter than the data, while thinner contours indicate that it is fainter than the data. The contour levels in the center panel are identical to those in Figure 4.1. Table 4.4 gives the full list of parameters for the best-fit model.

Table 4.3: Derived quantities from a subset of the 49 Ceti disk models

$M^a_{\rm disk}$ ($M_\oplus$)	ϵ	h	$N({\rm CO})^b_{\rm radial}$ ($10^{18}\,{\rm cm}^{-2}$)	$N({\rm CO})^{\rm 100AU,c}_{\rm vertical}$ ($10^{15}\,{\rm cm}^{-2}$)	$M^d_{\rm CO}$ ($10^{-4}\,M_\oplus$)	$I_{\rm CO}$(J=2-1)^e (Jy km s^{-1})
13	2.5	0.020	2.76	4.23	9.66	2.6
9	2.5	0.020	0.32	1.82	2.46	1.2
17	2.5	0.020	13.5	9.06	37.2	6.9
13	3.5	0.020	15.1	4.47	98.0	11.7
13	1.1	0.020	0.13	0.91	3.74	2.3
13	2.5	0.010	42.8	78.4	96.6	14.5
13	2.5	0.030	0.12	2.20	2.97	1.5

[a] Total disk gas mass

[b] Total radial CO column density through the midplane

[c] CO vertical column density at 100 AU

[d] Total CO mass in the disk

[e] Integrated CO(J=2-1) line emission

in chemical structure are manifested in the observable properties of the CO emission. The CO emission is sampled with the same spatial frequencies and visibility weights as the SMA data and displayed in renzogram form with the same velocity structure as in Figure 4.1. In order to emphasize the relative structural differences between models, the contour levels are 15% of the peak flux for each model, with the absolute flux indicated by the thickness of the contours, and also printed explicitly at the top of each panel.

The decreased shielding in the inner disk caused by reducing the density gradient ϵ is visible as a lengthening of the emission in the central channels and a widening of the emission peaks in the outer channels in the low-epsilon model (bottom center panel). Increasing ϵ (top center panel) leads to enhanced shielding at the disk inner edge, causing much higher CO fluxes in the outer part of the disk and extremely high contrast between the inner and outer velocity channels.

The primary observable consequence of adjusting the mass (right panels, top and bottom) is that the increased or decreased shielding from extra gas leads to a corresponding increase or decrease in the total CO flux; changes to the shape of the emission are minimal, and the primary difference between models of different

mass over the mass range under consideration is simply in the relative brightness of the emission.

Differences in the scale height of the disk similarly manifest as differences in the flux scale; however, decreasing the scale height (bottom left panel) also causes greater shielding at the inner disk edge, leading to greater elongation of the outer velocity channels and causing the inner velocity channels to draw together and overlap as the CO flux rises throughout the inner areas of the disk. An increase in scale height (top left panel) leads to a greater area in the front and back of the disk, projected along our line of sight, which increases the flux in the central channels and leads to a lower contrast between the inner and outer channels of the disk.

Table 4.4: Parameters for Best-Fit Disk Model

h	$0.020^{+0.015}_{-0.005}$
ϵ	$2.5^{+0.5}_{-1.0}$
M_{gas}	13 ± 3 M$_\oplus$
M_{dust}	0.02 ± 0.01 M$_\oplus$
i	$90° \pm 5°$
PA	$-70° \pm 10°$
R_{in}	40 AU[a]
R_{out}	200 AU[a]

[a]For a description of the constraints on the inner and outer radii, see §4.4

4.4.2 Spectral Energy Distribution

After converging initially on a model that was able to reproduce the observed CO J=2-1 emission, we used that model to predict the spectral energy distribution. This serves as an *a posteriori* test of the consistency between the gas and dust properties in the models and the available observables.

We integrate over the disk volume to obtain the flux as a function of wavelength

$$F_\lambda = (\pi a^2/d^2) \int\int 2\pi r \, B_\lambda(T_{dust}(r,z)) n_{dust}(r,z) \, Q(\lambda) \, dz \, dr \quad , \tag{4.3}$$

where d is the distance to the source and n_{dust} is the number density of dust grains in cm^{-3}. We assume throughout a grain density of 2.5 g/cm^3.

While the predicted shape of the spectral energy distribution matches the observations well, the absolute fluxes are too high by a factor of ~ 5. Adjusting the temperature of the dust grains alters the shape of the SED curve, causing it to deviate from the observed shape; we were therefore required to increase the gas:dust ratio from 100 to 500 in order to reproduce the observed photometry. This unusually high ratio is likely an artifact of the simple assumptions of the model, since little information is available about the dust distribution in this system (and none at all from our data). For example, the mass of the system is likely not all in 30 μm grains, and a significant fraction of the mass may be in larger grains that contribute little to the infrared emission. Another possibility is that the overall gas:dust ratio is consistent with the standard value, but that gas and dust are not well-mixed: for example, much of the excess emission may arise from the inner edge of the disk, which will be directly illuminated and heated by the stellar radiation. Resolved observations of the dust continuum emission would test this hypothesis by placing constraints on the spatial distribution of the emitting region. Including effects such as this would significantly complicate the model presented here, as the H_2 formation rate would be affected by varying the abundance of the dust on which it forms. In general, the dust size and gas:dust mass ratio are strongly related by the total dust surface required to maintain the observed quantity of molecular gas; these are in turn dependent on the stellar properties determining dust grain temperatures. None of these dust-dependent quantities are well constrained by available data. Given the observations available and the extremely simplified dust model, which not only neglects the size distribution but also the possibility of a mixture of compositions and opacities, we use the simplest assumption of an altered gas:dust ratio in order to conduct a consistency check of the temperature and density structure of the gas model.

Decreasing the total dust mass in the model to match the SED reduces the grain surface area for H_2 formation. Thus molecular hydrogen begins to form at larger radii and greater depth, compared to the initial model with the canonical gas:dust ratio of 100. As a consequence of less effective UV shielding, the total CO mass decreases. Hence the total mass of the best-fit model has to be increased slightly to compensate for the lower molecular gas fraction. As a secondary effect, the overall gas temperature of the dust-depleted model also decreases due to the diminished photoelectric heating in the disk. The corresponding SED predicted for these parameters is indicated by the dashed line in Figure 4.2. The

mid-infrared flux points are underestimated by this model because we do not include the inner disk component of Wahhaj et al. (2007); as our data provide no constraints on the properties of the inner disk, we ignore this component and concentrate on the fit to the outer disk. The flux predicted by the model SED is consistent with our own continuum upper limit reported in Table 4.1.

4.4.3 Best-Fit Disk Model

The center panel of Figure 4.4 shows the best-fit model from the grid, with the minor modifications introduced by reproducing simultaneously the spectral energy distribution. The structural and geometric parameters for this model are listed in Table 4.4. The errors given in the table are the approximate 1-σ uncertainty range interpolated from the χ^2 grid.

This model reproduces the basic features of the CO J=2-1 emission well, including the strength of the emission, the separation of the emission peaks, and the spatial extent of the emission. There are still several important differences between the model and the data, however, including (1) an inability to reproduce the changes in position angle with radius evident in the data (the "wings" of emission extending to the southeast and northwest of the position angle axis), and (2) the separation of the innermost, low-velocity channels. Both of these may be indicative of departures from azimuthal symmetry in the disk structure, the former possibly indicating a warp in the disk and the latter apparently pointing to a deficit of emission along the minor axis of the disk. In none of our models were we able to reproduce the wide separation between the inner channels; while the signal-to-noise ratio in these channels is low, the observed CO morphology is difficult to reproduce in detail with a simple, azimuthally symmetric disk model. The CO emission for this best-fit model is optically thin in both the J=2-1 and J=3-2 transitions, even for the edge-on disk orientation, and therefore traces the full column density of disk material.

The densities in the disk are too low for efficient gas-dust coupling and thus the gas finds its own equilibrium temperature determined mainly by photoelectric heating and line cooling. The most important cooling lines from surface to midplane are [C II], [O I], and H_2. CO abundances are only high in a region between 45 and 70 AU (Fig. 4.3). Outside that region, CO cooling is less important for the energy balance. Fig. 4.5 summarizes the most important heating and cooling processes and also shows the resulting gas temperature structure. The disk surface stays well below 100 K due to efficient fine structure line cooling. The molecular cooling is however less efficient in competing with the

photoelectric heating from the large silicate grains (Kamp & van Zadelhoff 2001), leading to temperatures of a few 100 K in the disk interior.

In order to test the robustness of the best-fit model to the gas properties, we used this model to predict the CO J=3-2 spectrum. It compares favorably with the spectrum observed by Dent et al. (2005), reproduced in Figure 4.6. The heavy solid line shows the J=3-2 spectrum predicted from the best-fit disk model, while the light solid line shows the observed JCMT spectrum. Although the observed spectrum is noisy and likely subject to an absolute calibration uncertainty, the overall agreement is within $\sim 30\%$, which is very good given that the CO J=3-2 spectrum was not used *a priori* to determine these model parameters.

4.5 Discussion

The processes determining the amount and distribution of gas and dust in transition disks like that around 49 Ceti are the same processes that shape the features of emergent planetary systems around these young stars. Resolved observations of individual disks in this phase are desirable to address such basic questions as when in the lifetime of a star its disk disperses, whether the gas clears before the dust, and whether the disk clears from the center or in a radially invariant manner.

In the 49 Ceti system, the infrared dust properties appear similar to those of a debris disk (Wahhaj et al. 2007). Yet observations presented here indicate that a substantial quantity of molecular gas persists in the outer disk, between radii of 40 and 200 AU, where photochemistry from stellar and interstellar radiation dominates. The lack of molecular gas emission interior to this radius as indicated by our observations, combined with the lack of dust emission within a radius of 30 AU inferred by Wahhaj et al. (2007), implies that the 49 Ceti system appears to be clearing its gas and dust from the center out. The mechanism responsible for this central clearing is not indicated; in general, the best-developed theories to explain this transitional morphology are (1) central clearing through the influence of a massive planet and (2) photoevaporation by radiation from the central star.

The clearing of gaps and inner holes has long been predicted as a consequence of the formation of massive planets in circumstellar disks (e.g. Lin & Papaloizou 1986; Bryden et al. 1999). In the case of 49 Ceti, the formation of a Jupiter-mass planet would be required at a distance of ~ 40 AU from the star, roughly the inner radius of the observed hole in the gas distribution. Such a scenario could

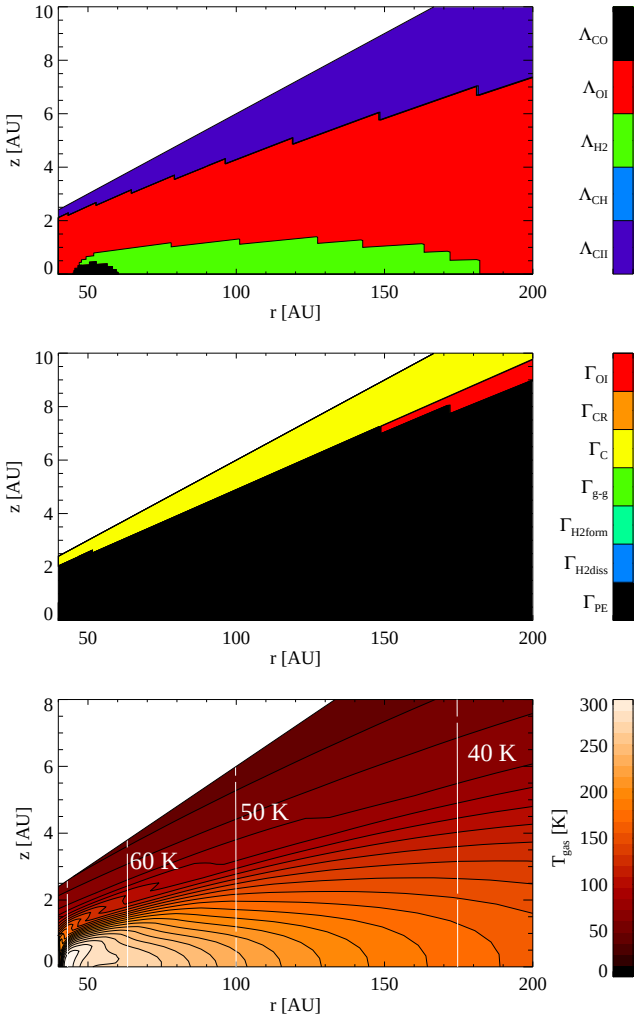

Figure 4.5.— Two-dimensional gas temperatures in the best fit disk model ($M_{\rm disk}$ = 13 $M_\oplus$, $\epsilon = 2.5$, $h = 0.02$. Shown are the most important heating (top panel) and cooling (middle panel) processes as well as the gas temperature (bottom panel). The dust temperature, which depends only on radius, is overlaid in white contour lines (steps of 10 K).

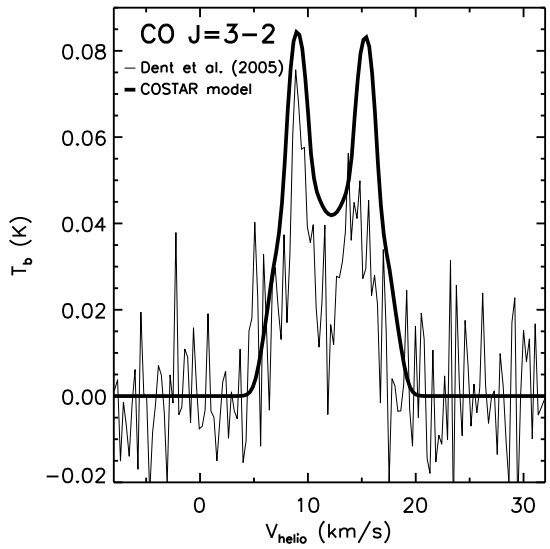

Figure 4.6.— CO J=3-2 spectrum predicted for the model that provides the best fit to the resolved J=2-1 emission (heavy solid line), compared with the Dent et al. (2005) JCMT CO J=3-2 spectrum (light solid line). The x-axis shows heliocentric velocity while the y-axis gives the JCMT main beam brightness temperature.

also help to explain the size segregation of dust grains observed by Wahhaj et al. (2007); a predicted consequence of inner disk clearing by gravitational influence of a massive planet is a filtration of dust grains by size, with only those below a certain threshold (typically 1-10 μm) accreted across the gap along with a reduced amount of gas (Rice et al. 2006). However, this scenario ultimately requires the accretion of substantial amounts of gas into the inner disk, and searches for molecular gas in the inner disk of 49 Ceti (Chen et al. 2006; Carmona et al. 2007) have not detected such a population. Another indication that an inner hole is likely caused by a massive planet in formation would be non-axisymmetric features resulting from its gravitational influence, such as spiral waves. While the CO emission from 49 Ceti does not appear asymmetric within the limits of the SMA observations, more sensitive spatially resolved observations could address this hypothesis.

The absence of gas in the inner disk is, however, consistent with a photoevaporation scenario: as the photoevaporative wind produced by stellar radiation becomes comparable to the accretion rate in the disk, material within the gravitational radius $R_g = GM_\star/c_s^2$ will quickly drain onto the star, leaving an evacuated inner hole free of gas and dust (e.g. Hollenbach et al. 1994; Alexander et al. 2006). The gravitational radius for 49 Ceti is roughly 20 AU, which is comparable to the inferred inner radius of 40 AU for the outer disk. The larger

outer radius may in fact be consistent with the later stages of photoevaporation, after the inner disk has become optically thin to ultraviolet radiation and the inner disk radius slowly increases under the influence of the photoevaporative wind (Alexander et al. 2006). Alexander & Armitage (2007) propose a method of discriminating between inner holes caused by photoevaporation and those caused by the formation of a giant planet, involving a simple comparison between two observables: the disk mass and the accretion rate. As there is no measured accretion rate for 49 Ceti, we cannot apply the criteria presented by these authors; however, we note that the low disk mass does indeed fall within the parameter space consistent with a photoevaporative scenario. Further observations are necessary to determine the origin of the inner hole; in particular, stringent limits on the accretion rate could suggest a photoevaporative mechanism.

There are few disks which appear to be in a similar evolutionary stage to that of 49 Ceti; a rare example is the disk around the A star HD 141569. Like 49 Ceti, it hosts a disk composed primarily of subμm-size grains with infrared properties approaching those of a debris disk (Wahhaj et al. 2007; Marsh et al. 2002), while still retaining a substantial quantity of molecular gas with central region clear of gas emission, in this case out to a radius of ~ 11 AU (Goto et al. 2006; Brittain et al. 2007). It exhibits a transitional SED (Merín et al. 2004), and observations of the rovibrational CO spectrum reveal gas with disparate rotational and vibrational temperatures (200 K and 5000 K respectively; Brittain et al. 2007), indicative of UV fluorescence on the outer edges of an inner disk region cleared of gas and dust. An analysis of the chemistry and gas properties of the system similar to the one presented here for 49 Ceti was conducted by Jonkheid et al. (2006). While the presence and extent of the inner hole are clearly indicated, the physical origin of this clearing is less obvious. The Brγ profile is indicative of substantial accretion, and Brittain et al. (2007) deem a photoevaporative clearing mechanism unlikely due to the large column density outside the cleared region and the lack of evidence for a photoevaporative wind in the FUV (Martin-Zaïdi et al. 2005). However, Merín et al. (2004) place a much lower limit of 10^{-11} $M_{\odot}$/yr on the accretion rate, based on the assumed gas:dust ratio of 100 and the low optical depth of the inner disk, which would be much more consistent with a photoevaporation scenario. Goto et al. (2006) note that the rough coincidence of the inner rim of the disk with the gravitational radius suggests that photoevaporation in concert with viscous accretion is a likely cause for the inner disk clearing.

Whatever the origin of their morphology, the observed gas and dust properties indicate that the disks surrounding both 49 Ceti and HD 141569 appear to be in

a transitional state of evolution during which the dust properties are beginning to appear more like those of a debris disk, while the gas is in the process of being cleared from the disk from the center out.

4.6 Conclusions

The SMA CO J=2-1 observations presented here provide the first spatially resolved observations of molecular gas in the 49 Ceti system. The data reveal a surprisingly extended and complex molecular gas distribution in rotation about the central star, viewed approximately edge on and clear of molecular gas emission in the central region of the disk. Modeling the disk structure and chemistry in this system indicates that the inner disk is entirely devoid of molecular gas due to irradiation by the central star, while a ring of molecular gas persists between 40 and 200 AU, subject to photodissociation at the inner edge by stellar radiation. The disk model presented here reproduces well the observed properties of the system, including the resolved CO J=2-1 emission, the CO J=3-2 spectrum, and the spectral energy distribution. With dust properties similar to those of a debris disk and a substantial reservoir of gas maintained in the outer disk, 49 Ceti appears to be a rare example of a system in a late stage of transition between a gas-rich protoplanetary disk and a tenuous, gas-free debris disk.

Chapter 5

Structure and Composition of Two Transitional Circumstellar Disks in Corona Australis

A. M. Hughes, S. M. Andrews, D. J. Wilner, M. R. Meyer, J. M. Carpenter, C. Qi, A. S. Hales, S. Casassus, M. R. Hogerheijde, E. E. Mamajek, S. Wolf, T. Henning, & M. D. Silverstone *The Astronomical Journal*, submitted

Abstract

We consider basic structural models for the transition disks around two ∼10 Myr-old members of the nearby RCrA association, RX J1842.9-3532 and RX J1852.3-3700. We present new arcsecond-resolution maps of their 230 GHz continuum emission from the Submillimeter Array and unresolved CO(3-2) spectra from the Atacama Submillimeter Telescope Experiment. By combining these data with broadband fluxes from the literature and infrared fluxes and spectra from the catalog of the Formation and Evolution of Planetary Systems (FEPS) Legacy program on the *Spitzer* Space Telescope, we assemble a multiwavelength data set probing the gas and dust disks. Using the Monte Carlo radiative transfer code `RADMC` to model simultaneously the SED and resolved millimeter continuum visibilities, we derive basic dust disk properties and identify an inner cavity of radius 16 AU in the disk around RX J1852.3-3700. We also identify an optically thin 5 AU cavity in the disk around RX J1842.9-3532, with a small amount of optically thick material close to the star. The molecular line observations confirm

the intermediate disk inclination in RX J1842.9-3532. In combination with the dust models, the molecular data allow us to derive a lower CO content than expected for standard assumptions, suggesting that the process of gas clearing is likely underway in both systems. With their advanced age, reduced CO content, and substantial outer dust disks, these transitional systems present interesting opportunities for follow-up with next-generation instruments like the Atacama Large Millimeter Array.

5.1 Introduction

One of the key problems in planet formation is understanding how the reservoir of planet-forming material – the disk of gas and dust around a young star – evolves with time. Perhaps the most compelling stage in the evolution of protoplanetary disks is the "transitional" stage during which gas and dust are cleared from the system (e.g. Strom et al. 1989; Skrutskie et al. 1990). This stage appears to be either rapid or rare, since fewer than 10% of low- to intermediate-mass stars in young star-forming regions are typically observed to be transitional systems (e.g. Cieza et al. 2007; Uzpen et al. 2008). Transition disks are traditionally identified empirically by a deficit of mid-infrared dust excess over the stellar photosphere relative to other systems at comparable ages. This deficit is associated with a lack of hot dust close to the star. The advent of the *Spitzer* Space Telescope has revolutionized the quality and quantity of available data on the dust content of young stellar systems, particularly transitional objects (see e.g. Najita et al. 2007). One of its many contributions has been to reveal a new class of gapped or "pre-transitional" disks, in which an anomalously faint mid-infrared spectrum is bracketed by substantial near- and far-infrared excesses (Espaillat et al. 2007, 2008). Follow-up of *Spitzer*-identified transitional systems with high spatial resolution observations of continuum emission at millimeter wavelengths has led to the confirmation that mid-IR spectral deficits are associated with a lack of long-wavelength emission from the disk center (Calvet et al. 2002, 2005; Hughes et al. 2007, 2009a; Brown et al. 2007, 2008, 2009; Piétu et al. 2007; Espaillat et al. 2008). The properties of systems with gaps and holes are beginning to provide valuable insight into the physical mechanisms responsible for the dispersal of the circumstellar disk, many of which may come into play over the lifetime of the star. Gas dynamics, the presence of unknown binary companions, grain growth, dynamical interactions with giant planets in formation, and photoevaporation have all been suggested as clearing mechanisms; there is some indication that different processes may dominate at different ages (see, e.g., Sicilia-Aguilar et al.

2010).

The Formation and Evolution of Planetary Systems (FEPS) Legacy program on the *Spitzer* Space Telescope (Meyer et al. 2006; Carpenter et al. 2008) is a spectrophotometric survey of nearby young Solar analogues, with masses from 0.7 to 1.3 $M_{\odot}$ and ages between 3 Myr and 3 Gyr. These ages bracket the period of time when gas and dust were cleared from the primordial Solar nebula, and the epoch when the Solar system achieved its present configuration. For 328 objects in the FEPS sample, the survey includes IRAC 3.6-8.0 μm photometry to probe for hot, dusty analogues to the asteroid belt in the Solar system, MIPS 24 and 70 μm photometry to probe dust in the Kuiper Belt regions, and IRS 5-40 μm spectra to search for mineralogical features. The excellent coverage of the infrared spectral energy distribution (SED) permits modeling of the temperature, size, composition, and an initial estimate of the spatial distribution of dust grains (see, e.g., Kim et al. 2005; Bouwman et al. 2008; Cortes et al. 2009). The IRS spectra are particularly useful for identifying systems with inner cavities or gaps in their dust distribution. However, there are many degeneracies inherent in the derivation of spatial information from unresolved spectra, and the SED provides little information about the large grains that comprise most of the dust mass in the system. It is therefore desirable to combine the information from the SED with spatially resolved observations at millimeter wavelengths. Since the emission is dominated by dust grains comparable in size to the wavelength of observation, resolved millimeter observations primarily trace the spatial mass distribution of large (millimeter-size) particles in the disk. Spectral line observations of low-level rotational emission from the CO molecule can provide a complementary probe of the total mass, which is dominated by molecular gas, and can yield important clues to the gas evolution of transitional objects.

In this paper, we analyze the SEDs and resolved millimeter continuum emission of two sources from the FEPS sample, RX J1842.9-3532 and RX J1852.3-3700. These sources were detected in the *ROSAT* All-Sky Survey and identified as young stars by Neuhäuser et al. (2000). They have spectral type K2 and K3, respectively (Carpenter et al. 2008), and have been classified as classical T Tauri stars (cTTSs) based on the presence of strong Hα emission lines. Neither was identified as a multiple-star system in the speckle-interferometric observations of Köhler et al. (2008). They are located within a few degrees of the CrA molecular cloud (distance 130 pc; Neuhäuser et al. 2000), and have kinematics and secular parallaxes consistent with the RCrA association (E. Mamajek, private communication). The estimated stellar ages are $\sim$10 Myr, among the oldest in the 1-10 Myr range for T Tauri objects in CrA measured by Neuhäuser et al.

(2000). These sources were selected for study on the basis of their age, their brightness in the 1.2 mm continuum (Carpenter et al. 2005), and their accessibility to the Submillimeter Array (SMA), so that the spectral information from the FEPS survey could be combined with resolved submillimeter observations. They were also chosen for their proximity on the sky, which increases the efficiency of submillimeter observations by allowing them to share calibrators. The high-quality *Spitzer* IRS spectra provide constraints on the dust composition and temperature structure on the two systems, and both exhibit a flux deficit in the mid-IR photospheric excess that points to the presence of an inner hole or gap.

Sections 5.2 and 5.3 describe the collection of new data from the SMA and the Atacama Submillimeter Telescope Experiment (ASTE) that complement the spectra and broadband fluxes from the FEPS survey and the literature. In Section 5.4.1 we present the tools and techniques that we use to model the SED and resolved millimeter-wavelength data, and we present the models of the dust disk structures in Section 5.4.2. In Section 5.4.3, we explore the dust disk model in the context of the constraints on the gas content of the two systems. We summarize our results and discuss their implications in Section 5.5.

5.2 Observations and Data Reduction

5.2.1 SMA Observations

The SMA observations of the two sources took place on 2005 May 14 during a full six-hour track with six of the 6-meter diameter antennas operating in the compact-north configuration, yielding baseline lengths between 10 and 180 meters (8 and 140 kλ). The phase stability was adequate for most of the track, with phase differences of 20-30 degrees between calibrator scans, but the phases lost coherence during the last hour of the night. The weather was fair, with the 225 GHz atmospheric opacity increasing from 0.10 to 0.14 throughout the night. Observations of the two FEPS sources were alternated with observations of the quasar J1924-292 at 15-minute intervals to calibrate the atmospheric and instrumental variations of phase and amplitude gain. Callisto was used as the flux calibrator, with a calculated brightness of 6.59 Jy; the derived flux of J1924-292 was 5.4 Jy, with an estimated uncertainty of $\lesssim 20\%$. The correlator was configured to provide a spectral resolution of 512 channels over the 104 MHz bandwidth in the chunk containing the CO(2-1) line, corresponding to a velocity resolution of 0.26 km s^{-1}. Two other 104 MHz chunks were observed

at high resolution at frequencies corresponding to the ^{13}CO(2-1) and C^{18}O(2-1) lines. The remainder of bandwidth in each 2 GHz-wide sideband was devoted to measuring the 230 GHz continuum, observed at a spectral resolution of 4.2 km s^{-1}. The data were calibrated using the MIR software package and imaging was carried out with the MIRIAD software package.

5.2.2 ASTE Observations

Observations of both FEPS sources took place on 2008 June 28 and 29 using the CATS345 receiver on the 10.4-meter ASTE dish. RX J1842.9-3532 was observed on both nights, while RX J1852.3-3700 was observed only on the second night. The receiver was tuned to place the CO(3-2) rotational transition in the lower sideband with the HCO$^+$(4-3) transition in the upper sideband. The high resolution spectrometer mode was used to partition the 128 MHz bandwidth into 1024 channels, yielding a spectral resolution of 0.11 km/s. Position switching was used to subtract the instrumental and sky background. In order to ensure that the detected CO emission originated at the position of the star, we used an offset position 1.5 arcmin to the east on the night of June 28 and 1.5 arcmin to the west on June 29 and averaged the baseline-subtracted spectra to create the final spectrum. The double-peaked CO(3-2) line from RX J1842.9-3532 is detected independently on both nights using the different offset positions, which allows us to localize the emission to within 1.5 arcmin of the star (∼4 beam widths).

The CO(3-2) and HCO$^+$(4-3) tuning of the receiver resulted in a spurious 1.11 MHz sinusoidal ripple of variable amplitude and phase across the bandpass, which was subtracted individually from each 10-second integration in the following manner. The amplitude and frequency of the ripple were estimated by finding the peak in a fast fourier transform of the spectrum, and then a least squares fit was performed to determine the precise amplitude, phase, and frequency of the sinusoidal ripple, plus the slope and intercept of a linear component to remove the worst of the baseline features. During this process, the region of the spectrum containing the line was not included in the fit so as to avoid inadvertently subtracting it. Integrations with an abnormally large ripple amplitude or highly irregular baseline shape across the bandpass were discarded (roughly 10% of each data set). After subtracting the sinusoid and linear fit, a third-order polynomial was subtracted from each integration using the CLASS software package[1], fitting the 20 km s^{-1} to each side of the region that appeared to contain the line. The

[1] http://www.iram.fr/IRAMFR/GILDAS

10-second integrations were then averaged together to produce a spectrum for each night; the spectra for each night were averaged and weighted according to their total integration time to produce the final spectrum. Due to differing exposure times and poorer weather on the night of June 29, the rms noise in the spectrum of RX J1842.9-3532 is 24 mK, while the rms noise in the spectrum of RX J1852.3-3700 is 39 mK. To derive the absolute flux scale, we calculated the main beam efficiency using observations of the calibrator M17SW taken throughout the night. Assuming a peak main beam temperature in the CO(3-2) line of 85.3K, derived on the CSO 10.4 m telescope by Wang et al. (1994), we derive main beam efficiencies that varied between 0.55 and 0.63 over the course of the two nights.

5.3 Results

5.3.1 Millimeter Continuum

With the SMA observations, we detect 230 GHz continuum emission from the disks around both target stars. The contour maps in Figure 5.1 show the strong detection of emission centered on the star position at the middle of the field. In order to estimate the integrated flux and approximate disk geometry, a Gaussian fit to the visibilities was performed using the MIRIAD task `uvfit`. For RX J1842.9-3532, the fit yields an integrated flux of 49±8 mJy and indicates that the disk is only marginally resolved: the major and minor axes lengths of $0\farcs74\pm0\farcs32$ and $0\farcs44\pm0\farcs32$ suggest that the disk is probably not viewed face-on, but do not place strong constraints on the inclination. We estimate an inclination angle of 54° based on these measurements, which is consistent with the morphology of the ASTE CO(3-2) spectrum described in Section 5.3.2 below. The fit to the RX J1852.3-3700 visibilities yields a flux of 60±8 mJy and major and minor axes of length $0\farcs76\pm0\farcs21$ and $0\farcs73\pm0\farcs21$, consistent with a nearly face-on geometry; we estimate an inclination of 16°. The inclination estimates are highly uncertain, but the intermediate geometry of RX J1842.9-3532 is supported by the line profile in Section 5.3.2 and the more face-on geometry of RX J1852.3-3700 is supported by the Hα line profile modeling of Pascucci et al. (2007). While observations at higher resolution would be advantageous for constraining the detailed mass distribution, even the rudimentary estimates of disk geometry provided by these observations are useful for constraining the disk properties when combined with constraints from the broadband SED. Simultaneous modeling of the SED and millimeter-wavelength visibilities is described in Section 5.4.1 below.

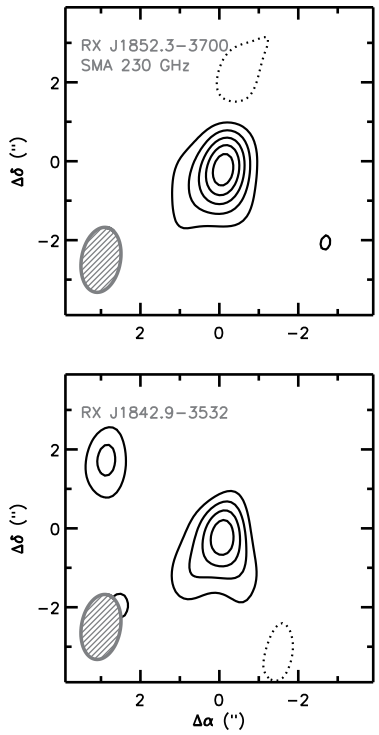

Figure 5.1.— SMA 230 GHz maps of the continuum emission from RX J1852.3-3700 (*top*) and RX J1842.9-3532 (*bottom*). The contour levels are [2,4,6,...]×3.5 mJy beam^{-1} (the rms noise), with solid lines indicating positive contours and dotted line indicating negative contours. The 1.″0×1.″7 synthesized beam is indicated by the ellipse in the lower left corner.

The 4σ peak to the northeast of RX J1842.9-3532 does not correspond to the position of any known star, as there are no other stars within 6" of RX J1842.9-3532 (Köhler et al. 2008). It is likely a spurious detection.

5.3.2 CO(2-1) and CO(3-2) Line Observations

We do not detect molecular gas emission from either system in the interferometric SMA observations of the CO(2-1), ^{13}CO(2-1), or C^{18}O(2-1) lines. The data provide a 3σ upper limit of 0.4 Jy beam^{-1} in each 0.26 km s^{-1} channel, with a synthesized beam size of 1.″5×0.″8. Although the disks are only marginally resolved in the continuum emission, there is reason to expect that the extent of CO(2-1) emission may be several times larger than that of the continuum (see, e.g., Hughes et al. 2008b). As a result, spatial filtering may be a factor in the non-detection (see further discussion in Section 5.4.3).

We do not detect any CO(3-2) emission in the ASTE observations of the disk around RX J1852.3-3700, with an rms of 39 mK in each 0.1 km s^{-1} channel. Observations of the disk around RX J1842.9-3532 reveal a double-peaked line profile, shown as a solid black line in Figure 5.2. The integrated strength of the CO(3-2) line is 0.24 K km s^{-1} with a peak main-beam brightness temperature of 130 mK and FWHM of 2.6 km s^{-1}. The double-peaked profile is consistent with material in Keplerian rotation about the star, viewed at an intermediate inclination angle of $\sim$54°. We detect no emission from the CrA molecular cloud near the line in velocity space, although it is possible that absorption from the cloud in the vicinity of the disk might influence the line shape. In Section 5.4.3 below, we investigate the relationship of the CO(3-2) emission to the dust properties, including implications for the disk geometry and gas-to-dust mass ratio.

5.4 Analysis

In order to characterize the basic properties of the disks, we seek to generate a model that can reproduce the observational features of each system. We assemble a data set that combines the millimeter-wavelength properties of the gas and dust described above with constraints from the broadband SED and IRS spectrum. We include the IRS spectrum and SED from the FEPS database (described in Carpenter et al. 2008) with the addition of optical, near-IR, and millimeter fluxes collected from the literature (Neuhäuser et al. 2000; Skrutskie et al. 2006; Carpenter et al. 2005). Figures 5.3 and 5.4 plot the SED (black points) and the IRS spectrum (red line) in the left panel for each disk, alongside the SMA 230 GHz visibilities (black points) in the right panel. In order to improve the signal-to-noise ratio of the plotted data, the visibilities have been deprojected (see, e.g., Lay et al. 1997) according to the disk geometry inferred in Section 5.3.1 and averaged in bins of 15 kλ. For a mathematical description of the abscissae of the visibility plots, refer to Hughes et al. (2008b).

5.4.1 Modeling the SED and Millimeter Visibilities

In an effort to reproduce these observations, we generated synthetic broadband SEDs, *Spitzer* IRS spectra, and millimeter continuum visibilities using the radiative transfer method and disk structure models described by Andrews et al. (2009). In these flared, axisymmetric disk structure models, the radial surface

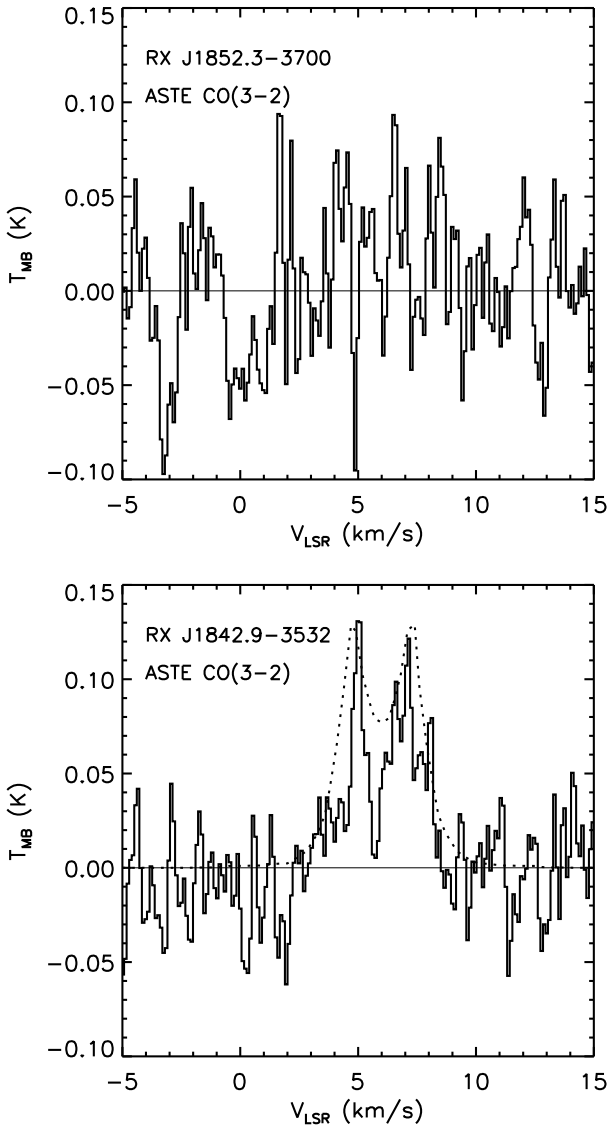

Figure 5.2.— ASTE CO(3-2) spectra of the disks around RX J1852.3-3700 (*upper*) and RX J1842.9-3532 (*lower*). No emission is detected from the RX J1852.3-3700 system. The RX J1842.9-3532 emission (solid line) displays the double-peaked profile characteristic of an inclined structure in Keplerian rotation about the central star. The line profile predicted by the SED- and visibility-based model of the dust disk structure (dotted line) compares favorably with the observations.

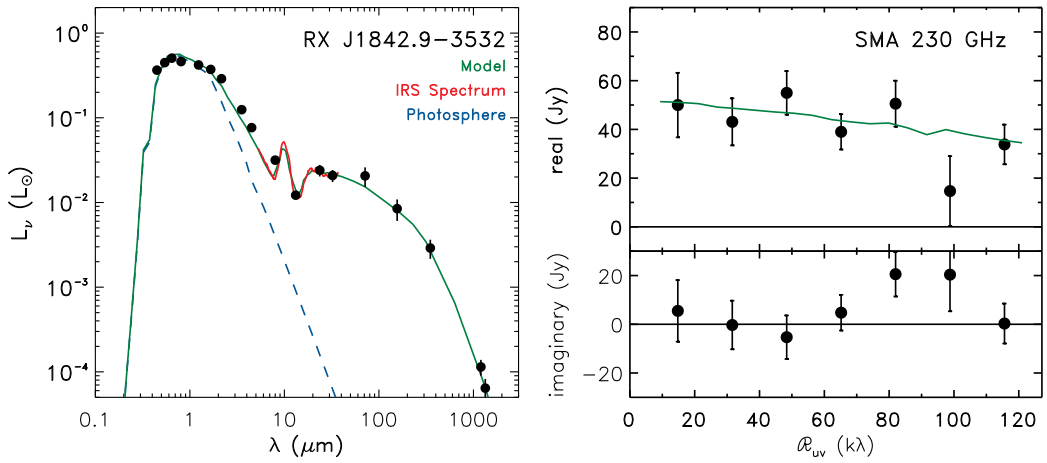

Figure 5.3.— Spectral energy distribution (*left*) and the real and imaginary components of the deprojected SMA 230 GHz visibilities (*right*) for RX J1842.9-3532. The broad-band SED (black points) and IRS spectrum (red line) are well reproduced by the best-fit `RADMC` disk structure model (green line). The model stellar photosphere (dashed blue line) is plotted for comparison. The units of the ordinate are defined so that $L_\nu = 4\pi d^2 \nu F_\nu$ in units of $L_\odot$. For a mathematical definition of the abscissa, refer to Hughes et al. (2008b); the deprojection is carried out as in Lay et al. (1997).

density profile is characterized by a similarity solution for viscous accretion disks, $\Sigma \propto (R_c/R)^\gamma \exp -(R/R_c)^{2-\gamma}$, where R_c is a characteristic radius and the normalization is proportional to the disk mass (for simplicity, the radial index has been fixed to $\gamma = 1$; Lynden-Bell & Pringle 1974; Hartmann et al. 1998). Vertically, the densities are distributed as a Gaussian with a scale height that varies as a power-law with radius, $H \propto R^{1+\psi}$. This parametric definition of the vertical dust distribution is maintained to mimic the sedimentation of dust grains below the disk atmosphere (e.g., Dullemond & Dominik 2004b); no attempt is made to iterate on the density structure to force the dust into vertical hydrostatic equilibrium. To model the cleared inner disks for these transitional sources, we scale down the surface densities by a factor δ_Σ inside a radius $R_{\rm cav}$ ($\Sigma_{\rm cav} = \delta_\Sigma \Sigma$; Andrews et al. 2009). Moreover, in an effort to better reproduce the detailed shape and solid state features in the IRS spectra, we permit a small (multiplicative) increase in the scale-height at the cavity edge (δ_H) and adjust the dust grain properties in the inner disk (for details, see Andrews et al. 2010).

For a given parametric disk structure, fixed input stellar information (Carpenter et al. 2008), and opacities (see Andrews et al. 2009), we use the

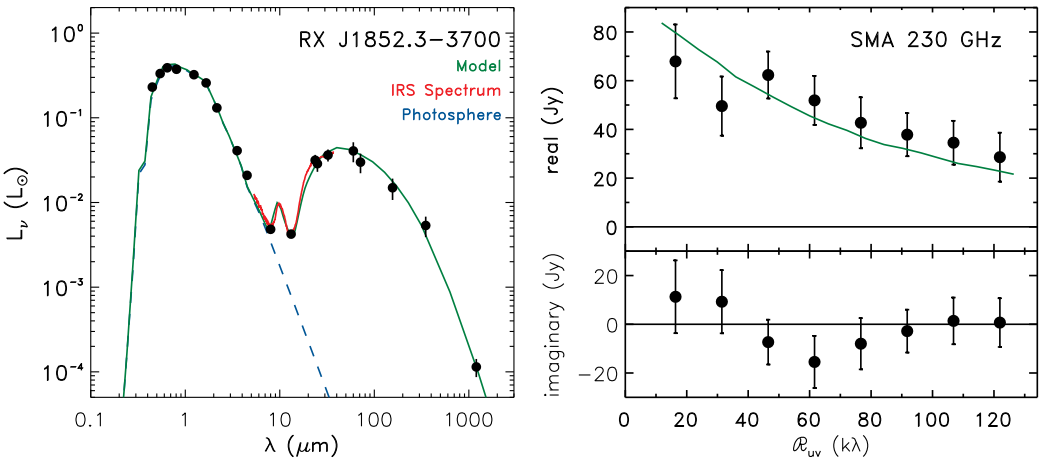

Figure 5.4.— Same as Fig. 5.3 above, but for RX J1852.3-3700.

two-dimensional Monte Carlo radiative transfer code `RADMC` (Dullemond & Dominik 2004a) to calculate an internally-consistent temperature structure and generate synthetic data products that can be compared to the observations. However, the parameter degeneracies introduced by the additional inner disk parameters and the high quality of the IRS spectra make the minimization method described by Andrews et al. (2009) prohibitive. Instead, we aimed to produce a representative model that can reproduce all of the basic features of the data set by focusing on varying parameters like the cavity size ($R_{\rm cav}$) and surface density reduction (δ_Σ). These models serve as initial estimates of the disk structures that can be substantially improved when future observations are available (e.g., high angular resolution millimeter data).

5.4.2 Representative Models

Table 5.1 presents the parameters of representative disk structure models capable of reproducing the observational data for both systems, and indicates those parameters that were fixed by particular observational constraints. The 130 pc distance to the RCrA association is from Neuhäuser et al. (2000) and the visual extinction is drawn from the FEPS database (Carpenter et al. 2008), while the inclination and position angle are estimated from the data as described in Sections 5.3.1 and 5.3.2 above. The other parameters are defined in Section 5.4.1; Andrews et al. (2009, 2010) include extensive discussion of the degeneracies between parameters and the ways in which the observational features are linked to the components of the disk structure model. Here we include comments on several

parameters that are particularly relevant for reproducing the data described in this paper.

Inner disk structure (R_{cav} and δ_{cav}) — These parameters are tied primarily to the wavelength and magnitude of the rise in the far-IR flux longward of the 10 μm silicate feature. It should be noted that while the density reduction $\delta_{\rm cav}$ is greater for RX J1842.9-3532 than for RX J1852.3-3700, the initial difference in surface density must be taken into account: because RX J1842.9-3532 is almost a factor of four more compact than RX J1852.3-3700, the surface density throughout most of the disk, including within the cavity, is larger. As a result, the inner disk of RX J1852.3-3700 is entirely optically thin, while that of RX J1842.9-3532 includes both optically thick and optically thin regimes. The surface density profile of the two models is plotted in Figure 5.5. As indicated in Section 5.5 below, the details of the inner disk structure are not well constrained by these models, although the presence of an inner cavity of greatly reduced surface density is firmly indicated.

Puffing at inner edge of outer disk (δH) — The parameter δH describes the extent to which the scale height at the edge of the cavity is puffed up, which is tied primarily to the shape of the far-IR SED. While a small δH can help to account for the very steep mid- to far-IR jump in flux observed in the RX J1852.3-3700 IRS spectrum, no shadowing is required to reproduce the spectrum of RX J1842.9-3532. This parameter is somewhat degenerate with the other vertical structure parameters (ψ and $\rm H_{100}$).

Inner disk dust properties — The 10 μm silicate feature and steep rise in flux near 20 μm from the disk around RX J1852.3-3700 are reproduced well by an inner disk and cavity edge populated entirely by small ($\sim$0.1 μm) amorphous silicate grains. For the disk around RX J1842.9-3532, the strength and position in wavelength of the silicate feature are well reproduced by a mixture of small and large ISM-composition grains ($\sim$80%) and crystalline and amorphous silicates ($\sim$20%). This combination of grain compositions is by no means a unique solution to the problem of fitting the mid-IR spectrum, but merely demonstrates that a mixture of different grain properties is helpful in accounting for the observed spectral features. A more detailed mineralogical analysis of these systems can be found in Bouwman et al. (2008).

The model SED and millimeter visibilities for the structural parameters in Table 5.1 are shown by the green lines in Figures 5.3 and 5.4. They reproduce the basic features of all of the available dust disk diagnostics, including the broadband SED, the IRS spectrum, and the millimeter-wavelength visibilities. In the discussion below, we focus on the most robustly-constrained model parameters,

including the extent and surface density reduction of the inner cavity and the size and dust mass of the outer disk.

Table 5.1: Estimated Disk Parameters

Parameter	RX J1842.9-3532	RX J1852.3-3700
Distance (pc)[a]	130	130
A_V (magnitudes)[a]	1.06	0.97
i (°)[a]	54	16
P.A. (°)[a]	32	-56
γ[a]	1.0	1.0
R_C (AU)	50	180
M_D ($M_\odot$)[b]	0.010	0.016
ψ	0.2	0.2
H_{100} (AU)	4.8	6.3
R_{cav} (AU)	5	15
δ_{cav}	9×10^{-6}	3×10^{-6}
δH	1	1.4

[a]Fixed

[b]Total mass in gas and dust, assuming a gas-to-dust mass ratio of 100

5.4.3 Constraints on Molecular Gas Content

Here we compare the predictions of the dust disk model with the constraints on the CO emission described in Section 5.3.2. For simplicity, we assume that gas and dust are well-mixed, and "paint" CO on top of the dust disk structure using the standard assumptions of a gas-to-dust mass ratio of 100:1 and a CO abundance of 10^{-4} relative to H_2. As in Andrews et al. (2009), we then use the Monte Carlo molecular line radiative transfer code `RATRAN` (Hogerheijde & van der Tak 2000) to calculate the level populations and predict the sky-projected intensity of CO arising from each system, given the underlying structure of the representative models derived in Section 5.4.2. We use the `MIRIAD` task `convol` to convolve the resulting intensity distributions with the 21.″1 beam of the 10.4 m ASTE telescope, since the ASTE spectra provide the most stringent limits on the CO emission from the systems.

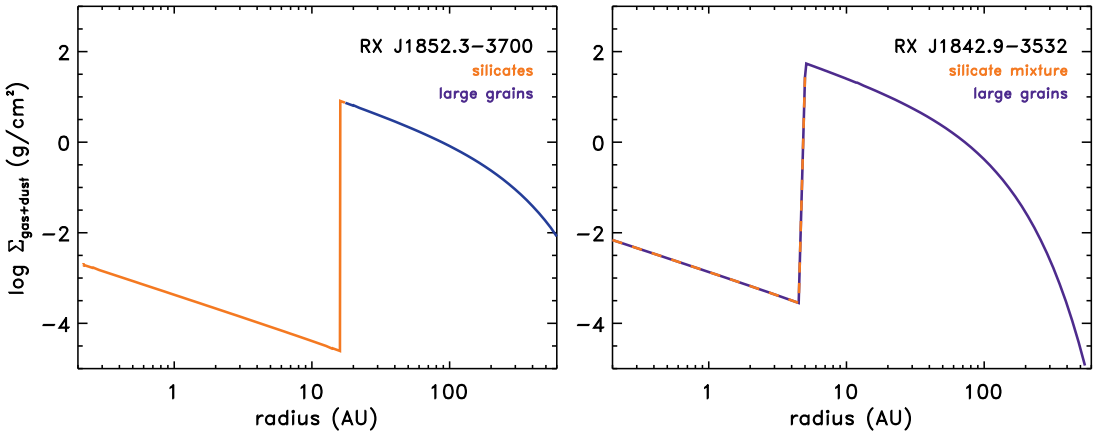

Figure 5.5.— Surface density profiles for the representative model parameters in Table 5.1. The line colors indicate the dust grain composition at each position within the disk; the dust grain composition is described in Section 5.4.2. The surface density incorporates the total mass in gas and dust, assuming a gas-to-dust mass ratio of 100.

Because the scale height of the dust in our models is affected by settling, the thickness of the dust disk would generally be expected to be lower than that of the gas disk if it is in vertical hydrostatic equilibrium. As a result the gas in our model, which is not required to obey the conditions for hydrostatic equilibrium, would be expected to be at somewhat lower temperatures than it might be in a thicker disk. We therefore expect to somewhat underpredict the CO emission from these systems; any constraints on the CO abundance or gas-to-dust ratio may therefore be taken as upper limits since they may be artificially inflated by this effect.

However, with the standard assumptions of gas-to-dust and CO-to-H_2 ratios, the model projection of CO(3-2) line flux strongly *overpredicts* both the upper limit for the disk around RX J1852.3-3700 and the detection of CO(3-2) emission from the disk around RX J1842.9-3532. In order for the model to successfully reproduce the weak emission from RX J1842.9-3532, the number density of CO must be decreased to 8±3% of its initial value. A model spectrum for this case is given by the dotted line in Figure 5.2, and compares well with the strength and width of the observed CO spectrum. While the line peaks appear narrower than the model, the noise in the line is too large to merit modeling the profile in detail; it is also possible that contamination from remnant molecular cloud material could contribute to the narrowing of the peaks.

In the absence of measurements of the H_2 content of the outer disk, it is not possible to determine whether the lower CO content results from a reduction in gas-to-dust mass ratio or abundance of CO relative to H_2, but in either case it marks a significant departure from standard assumptions. Because the rms in the ASTE spectrum of RX J1852.3-3700 is larger than that of RX J1842.9-3532, the upper limit on the CO content of the disk is similarly $\sim$8% of the initial value, assuming a standard gas-to-dust ratio and CO abundance. The model with reduced CO content relative to standard assumptions is also consistent with the limits on CO(2-1) emission from the SMA. We use RATRAN to generate a sky-projected CO(2-1) emission map, which is then sampled with the fourier components of the SMA data using the MIRIAD task `uvmodel` to account for spatial filtering effects. The model with standard CO abundance should be detected by the SMA observations, whereas the model with 8% CO content is consistent with the upper limits on the CO(2-1) emission from both systems.

If the gas disk were truncated relative to the dust disk, this could contribute to the low CO content; however, it is unlikely that both systems would undergo truncation, especially given the dearth of companions within 6" (Köhler et al. 2008), and the truncation would have to be severe in order to account for an order of magnitude reduction in CO content. It should also be noted that the conclusion of reduced CO content is largely independent of the model parameters describing the inner disk and the transitional region between inner and outer disk. The CO(3-2) emission arises only from the cold outer disk, and the gas-to-dust ratio is derived only for this region. The extent of the outer disk and its total dust mass are derived from two observational parameters: the millimeter flux and size scale indicated by the resolved visibilities. While the vertical structure and inner disk properties can affect the temperature of the outer disk and therefore the magnitude of the CO(3-2) emission, these effects are secondary to the basic midplane temperature structure determined by the radial scale of the dust disk. The reduced CO content is therefore robust to variations in the details of the inner disk structure, since variations in inner disk properties will have only second-order effects on the gross outer disk properties from which this conclusion is derived.

Both systems therefore appear to have undergone a reduction in molecular gas content relative to the standard assumptions for primordial disks. Given their age and transitional SEDs, this may indicate that gas dispersal is underway simultaneously with dust clearing from the inner disk.

5.5 Discussion and Conclusions

We have generated models that can reproduce simultaneously the basic observational diagnostics of the gas and dust disks around RX J1842.9-3532 and RX J1852.3-3700, including their broadband SEDs, IRS spectra, resolved millimeter-wavelength visibilities, and CO(3-2) spectra. As indicated by the mid-IR flux deficit, both systems are transitional, with an inner cavity of significantly decreased dust optical depth.

The disk around RX J1842.9-3532 also exhibits a substantial near-IR excess over the stellar photosphere. It shares this feature with the sample of objects labeled gapped, or "pre-transitional" by Espaillat et al. (2007). They model such systems with an optically thin inner disk bracketed by an optically thick ring close to the star and the optically thick outer disk at large radii. Similar models for the LkCa 15 system, refined with the addition of radiative transfer through the inner disk, are described in Mulders et al. (2010). Isella et al. (2009) modeled the near-IR excess and mid-IR deficit in the LkCa 15 system using a density distribution that increases with distance from the star, but includes a puffed-up inner rim at the dust disk edge. In our study, the inner disk model retains the continuous surface density profile of the outer disk (decreasing with distance from the star), suppressed by the factor $\delta_{\rm cav}$ (see Figure 5.5), with no change in scale height at the inner edge of the inner disk. Due to the relatively small scale heights in the inner disk, we can approximate the optical depth to starlight as the product of surface density and 1 μm opacity, $\Sigma_{\rm R}\kappa_{1\mu{\rm m}}$. In this approximation, the cavity is optically thick between 0.01 and $\sim$0.2 AU but optically thin between $\sim$0.2 and 5 AU, comparable to the models described in Espaillat et al. (2007). These results suggest that transition disks with near-IR excess are not necessarily "gapped" in terms of their surface density or discontinuous in terms of their scale height, since we demonstrate that the inner disk can be modeled using a single, continuous surface density function for the disk cavity that contains just enough mass to have both optically thick and optically thin regimes. Effectively, this indicates that we can place no constraint on the contrast in surface density or scale height between the "gap" and the optically thick ring near the star based on the morphology of the IRS spectrum. This is reflected by the success of several very different models of inner disk structure (Espaillat et al. 2007; Isella et al. 2009; Mulders et al. 2010, this work) in reproducing the characteristic mid-IR deficit surrounded by near- and far-IR excesses.

The global properties of the two disks modeled in this paper are similar to those of the the nine disks in Ophiuchus that were modeled using this method

by Andrews et al. (2009). This is perhaps unsurprising, since these targets were similarly selected on the basis of their large submillimeter fluxes. RX J1842.9-3532 and RX J1852.3-3700 have slightly lower masses due to missing material in the otherwise dense disk center, as for the transitional systems in the high-resolution Ophiuchus sample; yet as with the other transition disks in Andrews et al. (2009) they are still on the more massive end of the distribution of masses of Taurus and Ophiuchus disks in the sample of Andrews & Williams (2007).

While relatively little is known about the gas evolution of circumstellar disks, it is somewhat surprising that such massive dusty disks should have such low CO content. While relatively little information is available about the gas and dust conditions within the inner disk, the indications of low CO abundance in the outer disk from the ASTE spectra provide some clues. One popularly invoked mechanism for clearing central cavities in transition disks is gravitational interaction with a giant planet in formation (e.g., Lin & Papaloizou 1986; Bryden et al. 1999); this should not affect the CO content of the outer disk. Photoevaporation, on the other hand, is predicted to take hold at disk masses very close to those inferred for these systems (see, e.g., Clarke et al. 2001; Alexander et al. 2006; Alexander & Armitage 2007). It should be noted that the masses in Table 5.1 may be misleading, since they represent the total mass in gas and dust of the `RADMC` model assuming a standard gas-to-dust mass ratio of 100, without taking into account the evidence for low CO content described in Section 5.4.3; if the low CO content is a result of reduced gas-to-dust mass ratio, the disk masses may be reduced by an order of magnitude or more, placing them squarely within the region of parameter space preferred by photoevaporative clearing models. This may be true of other systems as well; to date no studies have been done of the consistency between models of millimeter dust emission and their predicted flux in cold molecular gas lines. However, if standard assumptions are true for non-transitional systems at similar ages, this would provide support for photoevaporation as the dominant clearing mechanism in the systems studied here.

One complicating factor, however, is the measured accretion rate of material onto the stars based on modeling of the Hα profiles by Pascucci et al. (2007). They calculate an accretion rate of $1 \times 10^{-9}\,M_\odot\,yr^{-1}$ for RX J1842.9-3532 and $5 \times 10^{-10}\,M_\odot\,yr^{-1}$ for RX J1852.3-3700. These are roughly an order of magnitude below the average for 1 Myr-old stars in Taurus (Gullbring et al. 1998; Calvet et al. 2004), which is consistent with the trend for transitional systems in Taurus noted by Najita et al. (2007). While this relatively low but measurable accretion rate is inconsistent with the original predictions of some

photoevaporation models (see, e.g., Alexander & Armitage 2007), recent work by Owen et al. (2010) indicates that accretion rates of this magnitude are in fact consistent with more recent predictions of radiation-hydrodynamic models that incorporate both x-ray and EUV photoevaporation. The pre-transitional source RX J1842.9-3532 in particular shares many characteristics with their predictions for an intermediate phase with a gapped disk and a low but still detectable accretion rate. Furthermore, Pascucci et al. (2007) report a blueshifted absorption feature in the Hα line profile indicative of significant mass loss, which may be associated with photoevaporative processes. The larger, emptier cavity and still-substantial accretion rate in the RX J1852.3-3700 system are somewhat more compatible with clearing by a giant planet than photoevaporation, although this does not explain the reduced CO content of the outer disk.

At least two other well-studied systems at ages of $\sim$10 Myr have been identified as candidate transition disks undergoing photoevaporation: HD 100453 (Collins et al. 2009) and 49 Ceti (Hughes et al. 2008a). The former exhibits a strong IR excess indicative of an optically thick outer disk, but with no evidence of accretion and a maximum gas-to-dust ratio of 4:1 in the outer disk. The latter exhibits dust properties similar to a debris disk, yet retains an extended optically thin molecular gas disk with an inner hole. The differences between these systems and the CrA transition disks in this paper are striking, and are perhaps indicative of the range of evolutionary paths over which the transition from protoplanetary to debris disk may occur.

The transitional systems in CrA observed in this paper therefore mark interesting test cases for distinguishing between proposed mechanisms for gas and dust clearing at late ages. Follow-up of these objects with instruments at various wavelengths can help to fill in our picture of the properties of the inner and outer disks. For example, the far superior spatial resolution of the Atacama Large Millimeter Array (ALMA) will permit vastly improved modeling of the structure of the extended gas and dust disk, as well as providing direct access to the conditions within the cavity, removing ambiguity about surface densities and scale heights in the inner disk. The sensitivity to spectral line emission provided by ALMA and *Herschel* will yield insight into the gas mass and chemistry and therefore the origin of the reduced CO content of the outer disk. In the meantime, observations of rovibrational lines can aid in determining the gas content of the warm inner disk, which will aid in distinguishing between proposed clearing mechanisms. Scattered light images would also be useful for constraining the vertical structure of the disks and reducing degeneracies in these initial models. The suite of instruments currently coming online is poised to revolutionize our

ability to characterize the physics of individual disks in the compelling transitional stage of evolution.

Chapter 6

Gas and Dust Emission at the Outer Edges of Protoplanetary Disks

A. M. Hughes, D. J. Wilner, C. Qi, & M. R. Hogerheijde 2008, *The Astrophysical Journal*, Vol. 678, pp. 1119-1126

Abstract

We investigate the apparent discrepancy between gas and dust outer radii derived from millimeter observations of protoplanetary disks. Using 230 and 345 GHz continuum and CO J=3-2 data from the Submillimeter Array for four nearby disk systems (HD 163296, TW Hydrae, GM Aurigae, and MWC 480), we examine models of circumstellar disk structure and the effects of their treatment of the outer disk edge. We show that for these disks, models described by power laws in surface density and temperature that are truncated at an outer radius are incapable of reproducing both the gas and dust emission simultaneously: the outer radius derived from the dust continuum emission is always significantly smaller than the extent of the molecular gas disk traced by CO emission. However, a simple model motivated by similarity solutions of the time evolution of accretion disks that includes a tapered exponential edge in the surface density distribution (and the same number of free parameters) does much better at reproducing both the gas and dust emission. While this analysis does not rule out the disparate radii implied by the truncated power-law models, a realistic alternative disk

model, grounded in the physics of accretion, provides a consistent picture for the extent of both the gas and dust.

6.1 Introduction

Characterizing the gas and dust distribution in the disks around young stars is important for understanding the planet formation process, as these disks provide the reservoirs of raw material for nascent planetary systems. A common method of modeling circumstellar disk structure is to use models described by power laws in surface density and temperature that are truncated at a particular outer radius. This prescription has its historical roots in calculations of the minimum mass solar nebula, which indicated a surface density profile of $\Sigma \propto r^{-3/2}$ (e.g. Weidenschilling 1977), as well as theoretical predictions of a radial power-law dependence of temperature for accreting disks around young stars (Adams & Shu 1986; Adams et al. 1987). Observationally, the parameterization of temperature and surface density as power-law functions of radius began with early spatially unresolved studies of continuum emission from disks (Beckwith et al. 1990; Beckwith & Sargent 1991). These models have since been refined and applied to spatially resolved observations of many disks with success (e.g. Mundy et al. 1993; Dutrey et al. 1994; Lay et al. 1994; Dutrey et al. 1998), and they have proven useful for understanding the basic global properties of disk structure. Recently, however, with the advent of high signal-to-noise, multi-frequency observations of gas and dust in protoplanetary disks, these models have begun to encounter difficulties, particularly in the treatment of the outer disk edge.

The extent of the gas and dust distribution in circumstellar disks has implications for our understanding of the planet formation process in our own solar system. There is some evidence for a sharp decrease in the surface density of Kuiper Belt objects beyond a distance of 50 AU from the Sun (Jewitt et al. 1998; Trujillo & Brown 2001; Petit et al. 2006). However, the origin of this edge is unclear. Adams et al. (2004) note that the observed distance is far interior to the radius at which truncation by photoevaporation would be expected to occur, while Youdin & Shu (2002) find that the presence of such an edge in planetesimal density could be explained by drift-induced enhancement. A compelling possibility is that the Sun formed in a cluster environment, and the early solar disk was truncated by a close encounter with a passing star (see Reipurth 2005, and references therein). A more complete understanding of the outer regions of protoplanetary disks may provide insight into the processes that

shape the outer solar system.

Piétu et al. (2005) present multiwavelength millimeter continuum and CO isotopologue observations of the disk around the Herbig Ae star AB Aurigae and found from fitting models of disk structure described by truncated power laws that the outer radius of the dust derived from continuum emission (350 ± 30 AU) was much smaller than that of the gas derived from ^{12}CO J=2-1 emission (1050 ± 10 AU). They suggest that a change in dust grain properties resulting in a drop in opacity could be responsible for the difference, and note the possible association with a ring feature in the disk at 200 AU. A similar result was obtained by Isella et al. (2007) from observations of the disk around the Herbig Ae star HD 163296: they found a significant discrepancy between the outer radius derived for the dust continuum emission (200 ± 15 AU) and that derived from CO emission (540 ± 40 AU). These data appeared to require a sharp drop in surface density, opacity, or dust-to-gas ratio beyond 200 AU; however, as they discuss, there is no obvious physical basis for such a discontinuity. As Isella et al. (2007) demonstrate, the discrepancy in outer radii derived from the dust and gas is not simply an issue of sensitivity; the observations were sufficiently sensitive to detect emission from the power-law dust disk if it did extend to the radius indicated by the CO emission. The underlying issue is that the truncated power law model does not simultaneously reproduce the extent of both the continuum and CO emission for these disks.

Using data from the Submillimeter Array we show that the same apparent discrepancy in gas and dust outer radius applies to the circumstellar disks around several more young stars. In an attempt to understand the origin of this discrepancy, we investigate an alternative surface density profile based on work by Hartmann et al. (1998), which is similar to a power law profile in the inner disk but includes a tapered outer edge. We show that this model, which has a physical basis in similarity solutions of disk evolution with time, is capable of simultaneously reproducing both continuum and CO emission from these disks. The primary difference between this model and the truncated power-law disk is that instead of a sharp outer edge the surface density falls off gradually, with sufficient column density at large radii that CO emission extends beyond the point at which dust continuum emission becomes negligible.

6.2 Dust Continuum and CO J=3-2 Data

The analysis was conducted on extant SMA data of the disks around of HD 163296, TW Hydrae, GM Aurigae, and MWC 480. The dates, frequencies, antenna configurations, number of antennas, and original publications associated with the data sets are listed in Table 6.1. The four disk systems chosen for this analysis are all nearby, bright, isolated, and have been well studied at a wide range of wavelengths. The velocity fields of these disks all appear to be well described by Keplerian rotation (Isella et al. 2007; Qi et al. 2004; Dutrey et al. 1998; Piétu et al. 2007). The relevant properties of these systems (spectral type, distance, stellar mass, age, and disk inclination and position angle) are listed in Table 6.2.

6.3 Disk Models

Using the SMA data available for the four disk systems, we compared two classes of disk models: the first model is described by power laws in surface density and temperature and is truncated at an outer radius R_{out} (details in §6.3.1), and the second model is described by a power law in temperature and a surface density profile similar to a power law in the inner disk but tapered with an exponential edge in the outer disk (details in §6.3.2). This latter model is not intended to be a definitive description of these disks, but rather illustrative of the broader category of models without a sharp outer edge. The model fitting process involved deriving a minimum χ^2 solution for those parameters of each class of model that best fit the continuum emission, and then using standard assumptions to predict CO emission (described in §6.3.4). The CO emission was not used to determine the model fits, due to the computational intensity of solving the excitation and radiative transfer for the molecular line for a large grid of models.

6.3.1 Truncated Power Law

For the truncated power law models, we used the prescription of Dutrey et al. (1994). In this framework, the disk structure is described by power laws in temperature and surface density, with the scale height specified through the

Table 6.1: Sources of SMA 230/345 GHz continuum and CO J=3-2 data.

Freq./ Transition	Object	Dates	Array Config.	No. of Antennas	Reference
230 GHz	HD 163296	23/24 Aug 2003	Compact N	7	1
	TW Hydrae	10 Apr 2005	Extended	8	2
		27 Feb 2005	Compact	8	2
	GM Aurigae	10 Dec 2006	Extended	8	3
	MWC 480	18/20 Nov 2003	Compact N	8	1
345 GHz/	HD 163296	23 Aug 2005	Compact	8	4
CO J=3-2	TW Hydrae	28 Dec 2006	Compact N	8	5
	GM Aurigae	26 Nov 2005	Compact	7	6
	MWC 480	21 Oct 2005	Compact	8	1

References. — (1) SMA archive; (2) Qi et al. (2006); (3) Qi et al. (in prep); (4) Isella et al. (2007) ; (5) Qi et al. (2007, submitted); (6) Andrews & Williams (2007).

Table 6.2: Stellar and disk properties

System	Spectral Type	Dist. (pc)	Stellar Mass ($M_\odot$)	Age (Myr)	Disk PA (°)	Disk i (°)
HD 163296	A1V	122[a]	2.3[a]	5[b]	145[c]	46[c]
TW Hydrae	K8V	51[d,e]	0.6	5-20[f,g]	-45[h]	7[h]
GM Aurigae	K5V	140	0.8[i]	2-10[j,k]	51[i]	56[i]
MWC 480	A3	140[m]	1.8[n]	7-8[n,o]	143[p]	37[p]

References. — (a) van den Ancker et al. (1998a); (b) Natta et al. (2004); (c) Isella et al. (2007); (d) Mamajek (2005); (e) Hoff et al. (1998); (f) Kastner et al. (1997); (g) Webb et al. (1999); (h) Qi et al. (2004); (i) Dutrey et al. (1998); (j) Beckwith et al. (1990); (k) Simon & Prato (1995); (m) The et al. (1994); (n) Piétu et al. (2007); (o) Simon et al. (2000); (p) Hamidouche et al. (2006).

assumption that the disk is in hydrostatic equilibrium:

$$T(R) = T_{100}\left(\frac{R}{100AU}\right)^{-q} \tag{6.1}$$

$$\Sigma(R) = \Sigma_{100}\left(\frac{R}{100AU}\right)^{-p} \tag{6.2}$$

$$H(R) = \sqrt{\frac{2R^3 k_B T_k(R)}{GM_\star m_0}} \tag{6.3}$$

where the subscript '100' refers to the value at 100 AU, k_B is Boltzmann's constant, G is the gravitational constant, $M_\star$ is the stellar mass, and m_0 is the mass per particle (we assume 2.37 times the mass of the hydrogen atom). Combining these expressions and the assumption of hydrostatic equilibrium, the volume density $n(R, z)$ is given by:

$$n(R, z) = \frac{\Sigma(R)}{\sqrt{\pi}H(R)} \exp -(z/H(R))^2 \tag{6.4}$$

where z is the vertical height above the midplane. As noted by Dutrey et al. (2007), this definition implies a scale height of $H(r) = \sqrt{2}c_s/\Omega$, where c_s is the sound speed and Ω the angular velocity, while other groups use $H(r) = c_s/\Omega$; this difference should be taken into account when comparing our results with other disk structure models. During the modeling process, we recast the surface density normalization in terms of the midplane density at 100 AU, so that the parameter Σ_{100} is replaced by n_{100}. This power-law model of disk structure has five free parameters: T_{100}, q, n_{100}, p, and R_{out}.

6.3.2 Similarity Solution from Accretion Disk Evolution

While versatile and ubiquitous, the truncated power law models of disk structure have one obviously unphysical feature: a sharp outer edge. In the absence of dynamical effects (e.g. from a binary companion) or large pressure gradients to confine the material, disk structure at the outer edge is expected to taper off gradually. A description of the structure of an isolated, steadily accreting disk as it evolves with time is provided by Hartmann et al. (1998), who expand on the work of Lynden-Bell & Pringle (1974) to show that if the viscosity in a disk can be written as a time-independent power law of the form $\nu \propto R^\gamma$, then the similarity solution for the disk surface density is given by

$$\Sigma(r) = \frac{C}{r^\gamma} T^{-(5/2-\gamma)/(2-\gamma)} \exp\left[-\frac{r^{2-\gamma}}{T}\right] \tag{6.5}$$

where C is a constant, r is the disk radius in units of the radial scale factor R_1 such that $r = R/R_1$, and T is the nondimensional time $T = t/t_s + 1$ where t_s is the viscous scaling time (eq. 20 in Hartmann et al. 1998). For simplicity, when applying these models to our data we used physical units and absorbed several of the parameters into two constants so that the surface density is of the form

$$\Sigma(R) = \frac{c_1}{R^\gamma} \exp\left[-\left(\frac{R}{c_2}\right)^{2-\gamma}\right], \tag{6.6}$$

where R is the disk radius in AU and c_1, c_2, and γ are constants that we allowed to vary during the fitting process.

The temperature profile for the similarity solution disk model is identical to that of the truncated power-law disk, except that its spatial extent is infinite. We do not allow it to drop below 10 K, but this low temperature limit is not problematic for any of the disks considered here. This model therefore includes five free parameters: T_{100}, q, c_1, γ, and c_2. The constant c_1 describes the normalization of the surface density, similar to n_{100} in the power-law model, while the constant c_2 is analogous to the outer radius, since it describes the radial scale length over which the exponential taper acts to cause the surface density to drop towards zero.

6.3.3 Model Comparison

The surface density description for the similarity solution is similar to the truncated power law except at the outer edge of the disk. In the inner regions of the disk for which $R \ll c_2$, we may expand the exponential so that $\exp\left[-(R/c_2)^{2-\gamma}\right] \rightarrow 1 - (\frac{R}{c_2})^{2-\gamma} + \cdots$, and the surface density becomes

$$\Sigma(R) = \frac{c_1}{R^\gamma}(1 - \left(\frac{R}{c_2}\right)^{2-\gamma}) = \frac{c_1}{R^\gamma} - \frac{c_1}{c_2^{2-\gamma}} R^{2(1-\gamma)} \tag{6.7}$$

In the α-viscosity context (Shakura & Syunyaev 1973), for a vertically isothermal disk with the typical temperature index $q = 0.5$, we would expect that $\gamma = 1$. This implies that for standard assumptions, the inner disk surface density will be described by a power law in R with index γ, modified by a constant $(\frac{c_1}{c_2})$ due to the influence of the exponential. If γ deviates from 1, an additional shallow dependence on R would be expected.

It is illuminating to consider the behavior of these models in the Fourier domain, the natural space for interferometer observations. To do so we define the

coordinate $\mathcal{R}_{uv}$, the distance from the phase center of the disk in the (u, v) plane, as it would be observed if the disk were viewed directly face-on. To perform the deprojection from the inclined and rotated sky coordinates, we calculate the position of each point in the (u, v) plane as a projected distance from the major and minor axes of the disk, respectively: $d_a = \mathcal{R} \sin\phi$ and $d_b = \mathcal{R} \cos\phi \cos i$, where i is the disk inclination, $\mathcal{R} = (u^2 + v^2)^{1/2}$, ϕ is the polar angle from the major axis of the disk, $\phi = \arctan(v/u - PA)$, and PA is the position angle measured east of north; then $\mathcal{R}_{uv} = (d_a^2 + d_b^2)^{1/2}$ (Lay et al. 1997; Hughes et al. 2007).

In the Fourier domain, the truncated disk models show "ringing" and the visibilities will drop rapidly to zero in the vicinity of $\mathcal{R}_{uv} = 1/R_{out}$. Under the simplifying assumption of $\gamma = 1$, the Fourier transform of the similarity solution becomes a convolution of two functions: (1) $1/\mathcal{R}$, which is just the Fourier transform of the $1/R$ dependence of a power law extending from zero to infinity, and (2) $c^2/(1 + \mathcal{R}^2 c^2)^{3/2}$, where c is a scaling constant for the term that describes the exponential taper. Since these two functions both decrease monotonically and are always positive, the visibilities drop smoothly to zero without any ringing.

6.3.4 Model Fitting

For both disk models, we fit for the five parameters describing the disk temperature and surface density structure using the continuum data for each disk with the widest range of available baseline lengths. The position angle and inclination were fixed and adopted from previous studies (see Table 6.2). For opacity, we assume the standard millimeter value adopted by Beckwith & Sargent (1991) ($\kappa_\nu = \kappa_0(\nu/\nu_0)^\beta$, where $\kappa_0 = 10.0$ cm^2/g$_{dust}$, ν_0=1 THz, and $\beta = 1$), although we allow β to vary in order to obtain the proper normalization when extrapolating from one frequency to another. Due to the $\sim$ 100 AU spatial resolution, these data are not sensitive to the inner radius of the disk. For both sets of models, therefore, we simply fix the inner radius at a value of 4 AU for TW Hya (Calvet et al. 2002; Hughes et al. 2007), 24 AU for GM Aur (Calvet et al. 2005), and 3 AU for the other two systems, for which reliable inner radius information is not available; this is sufficiently small that changes in the inner radius do not affect the derived model parameters. To compare the models to the data, we use the Monte-Carlo radiative transfer code RATRAN (Hogerheijde & van der Tak 2000) to calculate sky-projected images of the dust continuum and CO emission, with frequency and bandwidth appropriate for the observations, and assuming Keplerian rotation. We then use the MIRIAD task *uvmodel* to simulate

the SMA observations, with the same antenna positions and visibility weights.

For each set of parameters, we directly compare the model visibilities to the continuum data and calculate a χ^2 value, using the minimum χ^2 value to determine the best-fit parameters. The resulting best-fit models are shown along with continuum data for both frequencies in the left panels of Figure 6.1. The abscissa gives the deprojected radial distance in the (u, v) plane, and the ordinate shows the real and imaginary components of the visibility. For a disk with circular symmetry, the imaginary components should average to zero. The 230 GHz continuum data are depicted as open circles, while the 345 GHz data are filled circles. The best-fit power-law model is shown in blue and the similarity solution in orange. Dotted and dashed lines distinguish between the 230 and 345 GHz model predictions; the fit was determined at that frequency with the largest baseline coverage and extrapolated to the other frequency, by varying β. The uncertainties quoted for β reflect an assumed 10% calibration uncertainty. Note that varying β has no effect on the modeled CO emission.

We measure values of β that are consistent with 1, which is in agreement with the typical values measured for disks in the Taurus-Auriga association (e.g. Dutrey et al. 1996; Rodmann et al. 2006). These shallow millimeter spectral slopes indicate that some grain growth has occurred from ISM grain sizes, which typically exhibit a steeper spectral slope ($\beta \sim 2$). In particular, the value of 1.2 measured for GM Aur matches well the value of 1.2 reported by Andrews & Williams (2007), and the value of 0.7 measured for TW Hydrae matches well the value of 0.7 reported by Calvet et al. (2002) and Natta et al. (2004).

After fitting the continuum, we then assumed a gas/dust mass ratio of 100 and a standard interstellar CO/H_2 mass ratio of 10^{-4} to predict the expected strength and spatial extent of CO emission from the disks, based on the best-fit continuum model. We assume throughout that the gas and dust are well-mixed, and that CO traces molecular hydrogen. We do not take into account the complexities of disk chemistry, such as the depletion of CO molecules in the cold, dense midplane (Aikawa 2007; Semenov et al. 2006). However, deviations from these simple assumptions should have no appreciable effect on our conclusions concerning the radial extent of CO emission.

Since we neglect the vertical temperature gradient in the disk, we might expect to underpredict the strength of optically thick CO line emission, which likely originates in the upper layers of the disk that are subject to heating by stellar irradiation. The continuum emission, by contrast, is likely weighted toward the cold midplane of the disk. For this reason, after obtaining an initial fit from

the continuum, we allowed the temperature scale (T_{100}) to vary to best reproduce the flux levels of the observed CO emission, and then iteratively fit for the other structural parameters (q, n_{100}, c_2/R_{out}, and γ/p).

Deriving the temperature from the CO emission in this way may underestimate the midplane density in some cases, due to the degeneracy between T_{100} and n_{100}: the temperature derived from CO emission is typically greater than or equal to that of the shielded midplane, depending in detail on the dust opacity and molecular dissociation due to ultraviolet radiation in the upper disk layers (for a discussion of the processes involved, see Jonkheid et al. 2007; Isella et al. 2007). For the disks considered, the temperature derived for the dust continuum emission was within $\sim 40\%$ of that derived to match the CO line strength.

6.4 Results and Discussion

The parameters for the best-fit model solutions to the continuum data for each source and for each of the two model types are listed in Table 6.3. This table lists only the set of parameters with the minimum χ^2 value; formal errors are not quoted as these are not intended to be definitive structural models but simply illustrative of the differences between the model classes in their treatment of the outer edge. The midplane surface density profiles for these models are plotted in Figure 6.2. The solid lines depict the profile for the power-law solution, while the dashed lines are for the similarity solution. The parameters of the two model solutions are very similar, particularly for HD 163296 and MWC 480. For all four disks, the two model solutions are particularly similar just within the outer edge of the disk, around the range of radii well-matched to the resolution of the data (~ 200 AU for HD 163296, ~ 90 AU for TW Hydrae, ~ 200 AU for GM Aurigae, and ~ 300 AU for MWC 480). The outer radius for the power-law solution typically falls at roughly twice the scale length (c_2) of the similarity solution. The analogous parameters γ and p, which describe how quickly the midplane density drops with radius, are also very similar between the two models.

Figure 6.1.— Comparison between the data and the two types of models (similarity solution and power law) for the four disks in our sample: *(a)* HD 163296, *(b)* TW Hydrae, *(c)* GM Aurigae, and *(d)* MWC 480. For each source, the left panel shows the real and imaginary visibilities as a function of deprojected (u, v) distance from the phase center. Symbols are SMA data; open circles are 230 GHz and filled circles are 345 GHz continuum. The lines represent the best fit to the 345 GHz continuum for the power law (orange) and similarity (blue) models. Dashed lines show the model at 345 GHz while solid lines are 230 GHz. The right panel shows position-velocity diagrams of the J=3-2 rotational transition of CO along the major axis of the disk. The left plot (black contours) shows the SMA data. The middle plot (blue contours) displays the emission predicted by the similarity solution parameters that provide the best fit to the continuum emission, and the right plot (orange contours) displays the emission predicted for the best-fit power-law model. The horizontal dashed line across the right panel represents the extent of the outer radius (R_{out}) derived for each source through fitting of the continuum emission in the context of the power-law model. The contour levels, beam, and velocity resolution for each source are as follows: *(a)* [2,4,6,8,10,12]×1.1 Jy/beam, 3.0×2.1 arcsec at a position angle of 14.3°, and 0.35 km/s; *(b)* [2,4,6,8]×2.0 Jy/beam, 4.0×1.8 arcsec at a position angle of 3.2°, and 0.18 km/s; *(c)* [2,4,8,12,16]×0.5 Jy/beam, 2.3×2.1 arcsec at a position angle of 12.9°, and 0.35 km/s; *(d)* [2,4,6,8,10]×0.5 Jy/beam, 2.5×2.3 arcsec at a position angle of 45.3°, and 0.35 km/s.

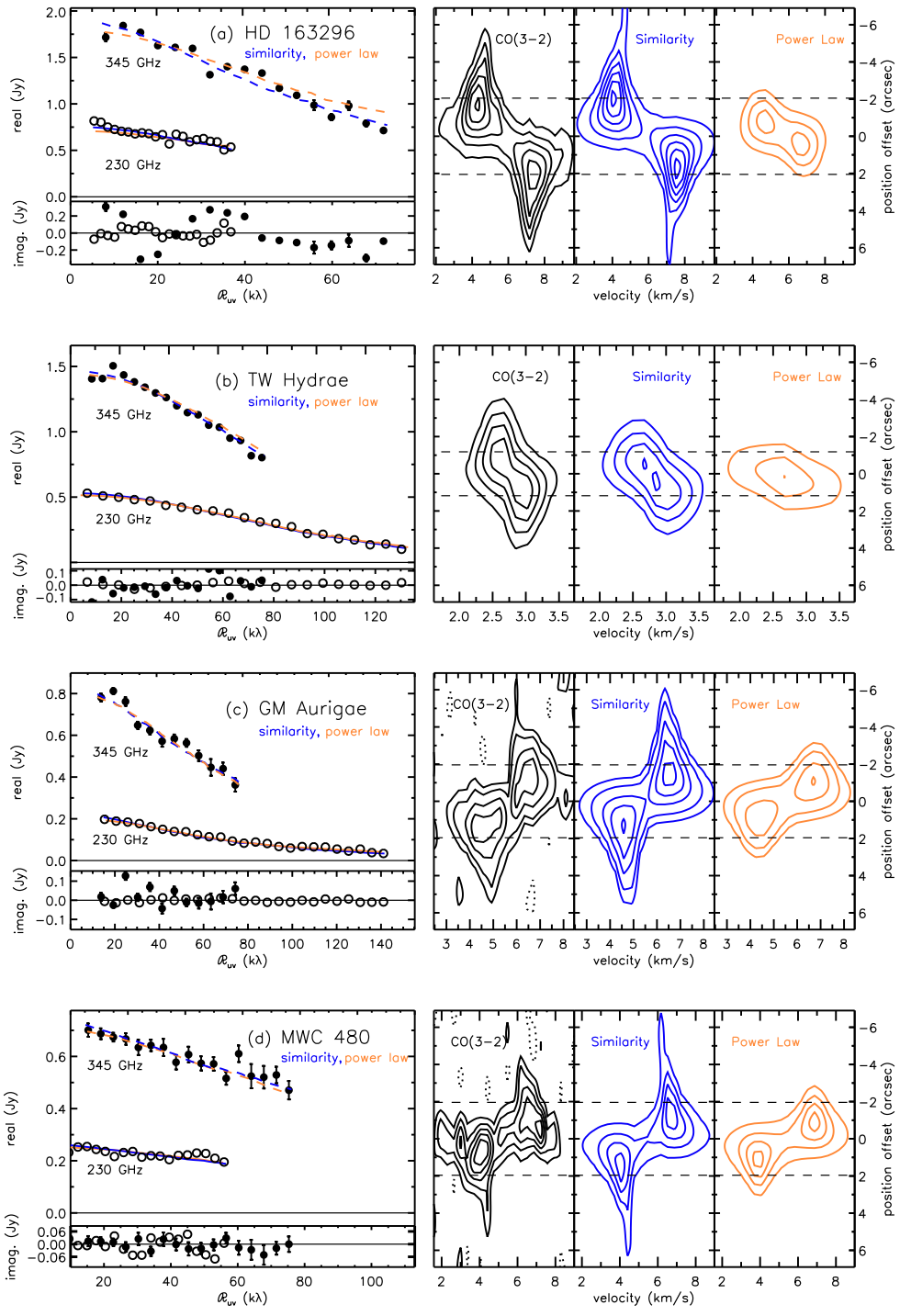

Figure 6.1 (Continued)

Table 6.3: Parameters for best-fit continuum models

Source	Model	χ^2	T_{100} (K)	q	$n_{10}{}^a$ (cm^{-3})	c_2 (AU) / R_{out} (AU)	γ / p	β
HD 163296	Similarity	2.29	65	0.4	5.3×10^{11}	125	0.9	$0.4^{+0.5}_{-0.3}$
	Power Law	2.26	60	0.5	6.7×10^{11}	250	1.0	$0.5^{+0.5}_{-0.3}$
TW Hydrae	Similarity	2.42	40	0.2	2.3×10^{11}	30	0.7	$0.7^{+0.5}_{-0.1}$
	Power Law	2.41	30	0.5	7.1×10^{10}	60	1.0	$0.7^{+0.5}_{-0.1}$
GM Aurigae	Similarity	2.19	50	0.5	1.1×10^{11}	140	0.9	$1.2^{+0.5}_{-0.1}$
	Power Law	2.17	40	0.4	5.0×10^{11}	275	1.3	$1.3^{+0.5}_{-0.1}$
MWC 480	Similarity	1.86	50	0.8	1.0×10^{11}	200	1.1	$0.7^{+0.5}_{-0.4}$
	Power Law	1.86	45	0.7	1.3×10^{11}	275	1.3	$0.7^{+0.5}_{-0.4}$

[a] Midplane density at 10 AU. We use the value at 10 AU rather than 100 AU to compare better the power law and similarity models in the region where their behavior is similar.

CO J=3-2 emission predicted from these best-fit models is shown in the right panel of Figure 6.1. The similarity solution is shown in the blue-contoured central plot, and the power-law model in the orange-contoured plot on the right. Recessional velocity is plotted on the abscissa while the position offset along a slice through the disk major axis is plotted on the ordinate. The horizontal dashed line in each figure represents the extent of the outer radius (R_{out}) derived for that source in the context of the truncated power-law model. For all four sources, the extent of molecular gas emission from the similarity solution is much more closely matched to the data than that of the power-law model, even though both reproduce the continuum dust emission equally well.

From Figure 6.1, it is clear by eye that for all four sources, the extent of the CO emission is severely underpredicted by the power law model but matches well the predicted emission from the similarity solution model. A calculation of the χ^2 value comparing the predicted CO emission for the two models to the observed emission shows that the similarity solution matches the data better than the truncated power-law model for all of the disks in our study. The difference is at the 2σ level for MWC 480, for which there is only short-baseline data with relatively low signal-to-noise, and at the 4σ level for GM Aur; for TW Hydrae and HD 163296, the χ^2 analysis shows that, formally, the similarity solution provides a better fit to the CO emission than the power-law model at the $> 10\sigma$ level.

The tapered edge of the similarity solution density distribution evidently permits a large enough column density to produce detectable CO 3-2 line emission, even though it has dropped off enough that the continuum emission

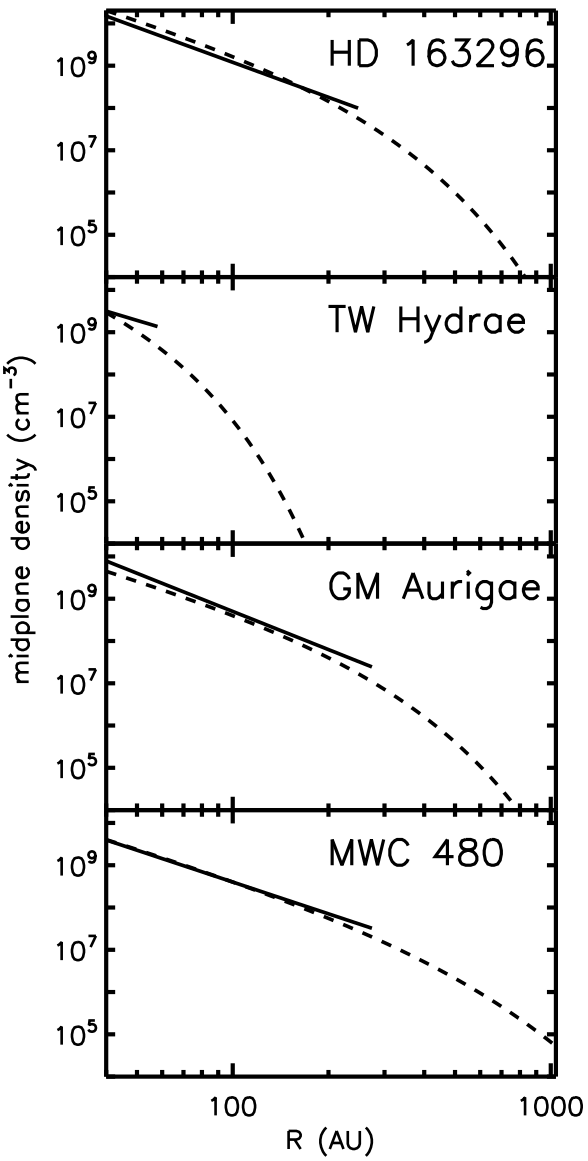

Figure 6.2.— Midplane density structure of the models that provide the best fit to the continuum data. Solid lines show truncated power-law models while dashed lines show similarity solution models.

is negligible. The power-law model, by contrast, is strictly limited in the extent of its CO emission by the sharp outer radius. In particular, for the case of HD 163296, the CO emission predicted by the power law model (orange contours in the right panel of Figure 6.1a) falls to 4.4 Jy/beam at a distance of 1.8 arcsec (220 AU) from the source center, while the similarity solution (blue contours) maintains this brightness out to a distance of 4.7 arcsec (570 AU). This latter size is well matched to the data (black contours) which extends at this brightness to a distance of 5.0 arcsec (600 AU). These distances likely overestimate the true physical extent of the disk due to convolution with the 2.1×3.0 arcsec beam, though they are very comparable to the values observed by Isella et al. (2007). While the similarity solution does not provide a perfect fit to the data, nor do we intend it to do so, it illustrates that the outer radius discrepancy is peculiar to the truncated power-law model; other disk structure models with a tapered outer edge may be able to reproduce the gas and dust emission as well as, or better than, the similarity solution adopted here.

Analysis of the CO excitation in the similarity solution model shows that the extent of the CO J=3-2 emission in these disks coincides roughly with the radius at which the line excitation becomes subthermal, determined primarily by where the mid-plane density drops below the critical density ($\sim 4.4 \times 10^4$ cm^{-3} at 20 K, though effectively lowered when photon trapping plays a role). In the similarity solution model, the surface density distribution steepens dramatically at large radii, but without the sharp truncation of the power-law model. This suggests that caution should be exercised not only when comparing outer radius measurements based on dust continuum and molecular gas emission, but also when comparing measurements based on emission from different transitions of CO or from isotopologues of the CO molecule that have differing abundances and optical depths. Piétu et al. (2007) fit truncated power law models to the disks around DM Tau, LkCa 15, and MWC 480 in several different isotopologues and rotational transitions of CO. For the two cases in which multiple transitions of the ^{13}CO molecule were observed, the derived outer radius is marginally smaller for the J=2-1 transition than the J=1-0 transition. This result is consistent with the expected trend that lower-J transitions will exhibit larger outer radii due to their lower critical density: a lower critical density will be reached at a greater distance as the surface density tapers off near the outer edge of the disk. In all cases the Piétu et al. (2007) analysis also yielded a smaller outer radius in ^{13}CO than in ^{12}CO, as well as a flatter surface density power law index for ^{13}CO than for ^{12}CO. These differences may be related to selective photodissociation, or other chemical processes. However, the trends of smaller outer radius and shallower surface density index in ^{13}CO are also consistent with surface density falling off rapidly

at large radii, as expected for a disk with a tapered outer edge. In the similarity solution model, the less abundant ^{13}CO isotopologue will become undetectable at smaller radii than ^{12}CO, which is more sensitive to the exponential drop in surface density in the outer disk.

It is noteworthy that studies of six largest "proplyds" with the most distinct silhouettes in the Orion Nebula Cluster reveal radial profiles in extinction that are well-described by an exponential taper at the outer edge (McCaughrean & O'Dell 1996). These isolated disks may be analogous to the systems considered here with a tapered outer edge.

Models with tapered outer edges also aid in addressing discrepancies between the size of the dust disk observed in the millimeter and the extent of scattered light observed in the optical and near-infrared. For example, coronographic observations of TW Hydrae detect scattered light to a distance of ~ 200 AU from the star (Krist et al. 2000; Trilling et al. 2001; Weinberger et al. 2002), while the truncated power-law model places the outer edge of the dust disk closer to 60 AU. Similarly, observations of HD 163296 by Grady et al. (2000) detect scattered light out to ~ 400 AU from the star, much larger than the 250 AU radius of the dust disk implied by the truncated power-law model. While the exponential taper causes the density of the similarity solution to drop rapidly with radius, these models retain a substantial vertical column density for several exponential scale lengths. It is therefore plausible that scattered light can remain visible at this distance, in contrast to the case of the smaller truncated power-law disk.

Although we intend for the similarity solution applied here to be an illustrative rather than definitive description of the disk structure, it is important to note that the particular form applied here has potential implications for the study of the evolutionary status of these disks. The form of the similarity solution developed by Lynden-Bell & Pringle (1974) and Hartmann et al. (1998) relates the observed structure to the disk age, viscosity, and initial radius. Although all three of these variables are poorly constrained by current observations, a large and homogeneous sample of objects studied in this way might reveal evolutionary trends in the disk structure.

6.5 Summary and Conclusions

With the advent of high signal-to-noise interferometer observations that resolve the outer regions of nearby protoplanetary disks, an apparent discrepancy has

emerged between the extent of the dust continuum and molecular gas emission (Piétu et al. 2005; Isella et al. 2007). Using multi-frequency interferometric data from the Submillimeter Array, we have investigated this disparity for four disk systems (HD 163296, TW Hydrae, GM Aurigae, and MWC 480) in the context of two distinct classes of disk structure models: (1) a truncated power law, and (2) a similarity solution for the time evolution of an accretion disk. The primary difference between these models is in their treatment of the disk outer edge: the abruptly truncated outer edge of the power-law disk causes the visibilities to drop rapidly to zero, leading to an inferred outer radius that is small in comparison with the observed molecular gas emission. The similarity solution, by contrast, tapers off smoothly, creating a broader visibility function and allowing molecular gas emission to persist at radii well beyond the region in the disk where continuum falls below the detection threshold. The outer radius discrepancy appears to exist only in the context of the power-law models.

In light of this result, it appears that an abrupt change in dust properties for these disks is unlikely, as there is no physical mechanism to explain such a discontinuity. This may imply that a sharp change in dust properties in the early solar nebula is similarly an unlikely explanation for the Kuiper belt edge observed by Jewitt et al. (1998), and that a dynamical mechanism such as truncation by a close encounter with a cluster member (Reipurth 2005, and references therein) may provide a more plausible origin. In this case, we would expect to observe disks with sharp outer edges only in clustered environments, and a model with a tapered edge would be a more realistic prescription for investigating the structure of a typical isolated disk. The tapered disk models provide a natural explanation for the disparate outer radii observed using different probes of the disk extent, including comparison of continuum and molecular gas observations (Piétu et al. 2005; Isella et al. 2007), and also comparison of different isotopologues and rotational transitions of a particular molecule (Piétu et al. 2007). When predicting CO emission, this simple model does neglect potential variance in the CO abundance due to depletion in the midplane and photodissociation at the disk surface; however, the results presented are intended simply to illustrate the global differences between gas and dust emission from the two model classes, independent of detailed CO chemistry.

While we cannot rule out disparate gas and dust radii in these disks, we show that an alternative disk structure model, grounded in the physics of accretion, resolves the apparent size discrepancy without the need to invoke dramatic changes in dust opacity, dust density, or dust-to-gas ratio in the outer disk.

Chapter 7

Stringent Limits on the Polarized Submillimeter Emission from Protoplanetary Disks

A. M. Hughes, D. J. Wilner, J. Cho, D. P. Marrone, A. Lazarian, S. M. Andrews, & R. Rao 2009, *The Astrophysical Journal*, Vol. 704, pp. 1204-1217

Abstract

We present arcsecond-resolution Submillimeter Array (SMA) polarimetric observations of the 880 μm continuum emission from the protoplanetary disks around two nearby stars, HD 163296 and TW Hydrae. Although previous observations and theoretical work have suggested that a 2-3% polarization fraction should be common for the millimeter continuum emission from such disks, we detect no polarized continuum emission above a 3σ upper limit of 7 mJy in each arcsecond-scale beam, or $< 1\%$ in integrated continuum emission. We compare the SMA upper limits with the predictions from the exploratory Cho & Lazarian (2007) model of polarized emission from T Tauri disks threaded by toroidal magnetic fields, and rule out their fiducial model at the $\sim 10\sigma$ level. We explore some potential causes for this discrepancy, focusing on model parameters that describe the shape, magnetic field alignment, and size distribution of grains in the disk. We also investigate related effects like the magnetic field strength and geometry, scattering off of large grains, and the efficiency of grain alignment, including recent advances in grain alignment theory, which are not considered

in the fiducial model. We discuss the impact each parameter would have on the data and determine that the suppression of polarized emission plausibly arises from rounding of large grains, reduced efficiency of grain alignment with the magnetic field, and/or some degree of magnetic field tangling (perhaps due to turbulence). A poloidal magnetic field geometry could also reduce the polarization signal, particularly for a face-on viewing geometry like the TW Hya disk. The data provided here offer the most stringent limits to date on the polarized millimeter-wavelength emission from disks around young stars.

7.1 Introduction

The magnetic properties of circumstellar disks are central to a wide range of physical processes relevant for planet formation. Dust and gas transport and mixing (e.g. Ciesla 2007), meteoritic composition (e.g. Boss 2004), disk chemistry (e.g. Semenov et al. 2006), and the migration of planetary embryos through the disk (e.g. Chambers 2006) are all thought to be influenced by magnetohydrodynamic (MHD) turbulence. But perhaps the greatest impact of a magnetized disk is that MHD turbulence can provide the source of viscosity that drives disk evolution. Since the seminal work by Lynden-Bell & Pringle (1974), the photospheric excess and variability exhibited by pre-main sequence stars have been attributed to an accretion disk. The viscous transport mechanism that supports the accretion process can also explain many aspects of the time evolution of circumstellar disks (Hartmann et al. 1998), and by extension can help to constrain the physical conditions and timescales relevant for planet formation. However, there are remarkably few observational constraints on the magnitude and physical origin of viscosity in circumstellar disks.

As conjectured by Shakura & Syunyaev (1973), turbulence can provide large enough viscosities to account for accretion and disk evolution on the appropriate timescales. The mechanism most commonly invoked as the source of this turbulence is the magnetorotational instability (MRI), in which magnetic interactions between fluid elements in the disk combine with an outwardly decreasing velocity field to produce torques that transfer angular momentum from the inner disk outwards (Balbus & Hawley 1991, 1998; see also Velikhov 1959 and Chandrasekhar 1960). Indeed, it is unlikely that turbulence in an unmagnetized, azimuthally symmetric Keplerian disk can sufficiently redistribute angular momentum: magnetic fields must be invoked to enable Shakura-Sunyaev viscosity (e.g. Balbus et al. 1996). The ionization fraction is likely high enough

for magnetic coupling of material over much of the outer disk (see e.g. Sano et al. 2000; Turner et al. 2007), and the observed Keplerian rotation of protoplanetary disks provides the requisite velocity shear. However, the magnetic field properties (strength and geometry) far from the central star remain unconstrained.

Resolved observations of polarized submillimeter continuum emission are uniquely suited to constrain the magnetic field geometry – independent of disk structure – via the orientation of polarization vectors produced by dust grains aligned with the magnetic field (Aitken et al. 2002). In the presence of an anisotropic radiation field, irregularly shaped grains with different cross sections to left and right circular polarizations of light can be spun up to high speeds by radiative torques (e.g. Dolginov 1972; Dolginov & Mitrofanov 1976; Draine & Weingartner 1996)[1]. These spinning grains precess around magnetic field lines, and ultimately align with their long axes perpendicular to the local magnetic field direction. Polarized emission or absorption by these aligned grains can thus trace magnetic field structure in dusty interstellar media (see Lazarian 2007, and references therein).

The first models of polarized emission from disks incorporating the radiative torque alignment mechanism have recently been calculated by Cho & Lazarian (2007). Using a two-layer Chiang et al. (2001) disk structure model threaded by a toroidal magnetic field (with circular field lines in the plane of the disk, centered on the star), they calculated the polarization emitted as a function of wavelength and position in the disk, incorporating emission and selective absorption mechanisms, but not scattering. They predict a 2-3% polarization fraction at 850 μm, and note that grain alignment is particularly efficient in the low-density outer disk regions. At millimeter wavelengths, dust grain opacities are low and optically thin thermal continuum emission primarily originates in the midplane where most of the mass is located. Polarimetric observations of millimeter-wavelength dust continuum emission therefore trace magnetic field geometry near the midplane in the outer disk, in regions where the magnetic field is strong enough for grains to become aligned and the density is low enough that grain spin-up is not impeded by gas drag.

The first attempt to observe polarized millimeter-wavelength emission from

[1]More recent research in Lazarian & Hoang (2007) shows that in many cases rather than being spun up paramagnetic grains get slowed down by radiative torques, which means that the grains aligned by radiative torques do not necessarily rotate suprathermally. Nevertheless, the maximal rotational rate provides a useful parameterization of the effect of the radiative torques as discussed in detail in Hoang & Lazarian (2008).

protoplanetary disks was made by Tamura et al. (1995, 1999). They used the James Clerk Maxwell Telescope (JCMT) to observe several young systems in the Taurus-Auriga molecular cloud complex – HL Tau, GG Tau, DG Tau and GM Aur – and reported tentative ($\sim 3\sigma$) detections of polarized millimeter-wavelength continuum emission from three of the four systems. The exception was GG Tau, for which they report a 2σ upper limit of 3%. While the disks are unresolved in the 14" JCMT beam, the approximate alignment of the GM Aur and DG Tau polarization vectors with the known orientation of the disk minor axis is suggestive of a globally toroidal magnetic field structure. However, finer resolution is required to confirm the magnetic field structure in the disks, and differentiate it from any potential contamination from an envelope or cloud material. DG Tau was followed up at a wavelength of $350\,\mu$m using the Caltech Submillimeter Observatory by Krejny et al. (2009), and no polarization was detected with an upper limit of $\sim 1\%$. They suggest that the decrease of polarization percentage relative to the tentative $850\,\mu$m detection and the corresponding Cho & Lazarian (2007) prediction at $350\,\mu$m may be due to some combination of polarization self-suppression – effectively an absorption optical depth effect (see e.g. Hildebrand et al. 2000) – or increased scattering at shorter wavelengths, which would produce a signal orthogonal to that expected for a toroidal magnetic field. In summary, while the Cho & Lazarian (2007) predictions are consistent with the magnitude of the tentative JCMT detections, as discussed by Krejny et al. (2009), the predicted polarization spectrum is inconsistent with the 350 and $850\,\mu$m observations of DG Tau.

In the absence of spatially resolved observations, the origin of the polarized emission in these systems remains unclear. While the position angle of the polarized emission observed in the three systems in the Taurus-Auriga complex suggests association with the circumstellar disk, at least two of these sources (DG Tau and HL Tau) are flat-spectrum sources host to jets and likely retain envelope material that could aid in generating a polarization signal (Kitamura et al. 1996; D'Alessio et al. 1997, e.g.). Tamura et al. (1995) suggest that the emission from HL Tau may arise from an interface region between the disk and a small envelope, and that the upper limit for GG Tau may be due to the lack of an envelope combined with weak, compact emission from the circumbinary ring. Observations of the GM Aur system using the NICMOS instrument on the Hubble Space Telescope indicate that it too may host a tenuous remnant outflow and envelope (Schneider et al. 2003). Nevertheless, with both theoretical predictions and observational evidence pointing to a 2-3% polarization fraction at $850\,\mu$m in several T Tauri disks, resolved observations revealing the magnetic field geometry should be possible with current millimeter interferometers for bright

disks. At $\sim$ 1" resolution, such data would be well matched to the size scales at which the polarization fraction is expected to be the largest in the context of the Cho & Lazarian (2007) models.

In order to test the Cho & Lazarian (2007) model predictions and constrain magnetic field strengths and geometries, we observed two nearby systems, HD 163296 and TW Hya, with the Submillimeter Array (SMA) polarimeter. These targets were selected primarily for their large millimeter-wave fluxes to maximize the expected polarization signal. Unlike the previously-observed Taurus targets, they are isolated from molecular cloud material. HD 163296 has a total flux of 1.92 Jy at 850 μm (Mannings 1994), while TW Hya has a flux of 1.45 Jy at 800 μm (Weintraub et al. 1989), predicting a total polarized flux of $\sim$40 mJy in each system. Polarization of this magnitude should be observable with the SMA even if resolved across a few beams. HD 163296 is a Herbig Ae star with a mass of 2.3 $M_\odot$ located at a distance of 122 pc (van den Ancker et al. 1998b). It is surrounded by a flared disk viewed at an intermediate inclination of $\sim 45°$, observed to extend to at least 500 AU in molecular gas and scattered light (Isella et al. 2007; Grady et al. 2000), which has been extensively observed and modeled at millimeter wavelengths (Mannings & Sargent 1997; Natta et al. 2004; Isella et al. 2007). TW Hya is a K star located at a distance of only 51 pc (Mamajek 2005; Hoff et al. 1998). It hosts a massive circumstellar disk viewed nearly face-on at an inclination of 7° and extending to a radius of $\sim$200 AU in molecular gas and scattered light (Qi et al. 2004; Roberge et al. 2005). It is also a prototypical example of the class of disks with infrared deficits in their spectral energy distribution, known as "transition" disks. It has been shown to have a central deficit of dust emission extending out to 4 AU (Calvet et al. 2002; Hughes et al. 2007), with a low mass accretion rate (Muzerolle et al. 2000) that may indicate clearing by a giant planet in formation (Alexander & Armitage 2007).

We describe our observations of these systems in Section 7.2 and present the upper limits in Section 7.3. In Section 7.4.1 we describe the initial predictions generated by the Cho & Lazarian (2007) models and compare these predictions to the SMA observations. We then use these initial models as a starting point for an exploration of parameter space that seeks to describe how the different factors affect the predicted polarization properties (Section 7.4.2). We expand on these results by discussing the potential effects of physical mechanisms not included in the models (Section 7.4.3). In Section 7.5, we evaluate which physical conditions are most likely to contribute to the suppression of polarization relative to the fiducial model and summarize our results. Appendix B presents supplementary polarimetric observations of two more circumstellar disks, GM Aur and MWC 480.

7.2 Observations and Data Reduction

Observations were conducted using the SMA polarimeter, described in detail in Marrone & Rao (2008). The polarimeter uses a set of quarter-wave plates to convert the normally linear SMA feeds to circular polarization. By rotating the wave plate between two orientations separated by 90°, a single linear feed can be converted into either of the circular bases (left and right, or L and R). Since only one polarization (L or R) can be sampled on any antenna at any given time, full sampling of all four polarization states (LL, RR, RL, and LR) for all baselines (numbering $N(N-1)/2$, where N is the number of antennas) must be accomplished by rotating the waveplates through a series of orientation patterns conveniently described by the two-state Walsh functions (see Marrone 2006). A full set of polarization states can be obtained for all baselines in ∼5 minutes using a series of short (10-second) integrations with the waveplates rotated through patterns described by Walsh functions for the appropriate number of antennas. These 5-minute intervals of data are combined into quasi-simultaneous Stokes parameters for each baseline ($I = (RR + LL)/2$, $Q = (RL + LR)/2$, $U = i(LR - RL)/2$, $V = (RR - LL)/2$), where I measures the total intensity, V measures the intensity of circular polarization, and $\sqrt{Q^2 + U^2}$ gives the total linearly polarized intensity, which can also be used to calculate the local fractional (or percent) linear polarization $\sqrt{Q^2 + U^2}/I$. Note that the aligned states (RR and LL) separate the total intensity from the circularly polarized intensity, while the crossed states (LR and RL) provide information about the linearly polarized intensity. Of course, this represents an idealization. Two relevant non-ideal effects are (1) if the R and L gains are not perfectly matched, then some of the bright Stokes I flux can leak into Stokes V when the difference is taken between LL and RR, and (2) instrumental "leakage" of left circularly polarized light through a nominally right circularly polarized waveplate (and vice versa) can transfer Stokes I to the linear states Q and U.

Polarimetric SMA observations of the HD 163296 disk at 880 μm wavelength were carried out in the compact configuration on 29 May 2008, and in the extended configuration on 12 July 2008. The weather was excellent, with the 225 GHz opacity below 0.05 both nights, reaching as low as 0.03 on the night of 12 July. The phases were also extremely stable on both nights. The projected baseline lengths spanned a range of 9 to 260 kλ, providing a synthesized beam size of $1\farcs1 \times 0\farcs89$ for the combined data set, using natural weighting (see Table 7.1 for details). The quasar 3c454.3 was observed for 2.5 hours through more than 90° of parallactic angle during its transit, in order to calibrate the complex leakages

of the quarter-wave plates. The quasar J1733-130 was used to calibrate the atmospheric and instrumental gain, and the quasar J1924-292 was observed at 45-minute intervals throughout the night to test the quality of the phase transfer from J1733-130 as well as the calibration of the quarter-wave plate leakage. Uranus was used as the flux calibrator, yielding a flux for J1733-130 of 1.62 Jy on the night of May 29 and 2.01 Jy on the night of July 12. Uranus, Callisto, 3c273, and 3c279 were included as passband calibrators.

Observations of the disk around TW Hya were conducted in the subcompact and extended configurations of the SMA during the nights of 25 January and 15 February 2009, respectively. Due to the far southern declination of TW Hya in combination with the stringent elevation limits imposed to avoid antenna collisions in the subcompact configuration, the source was only observable for three hours on the night of 25 January, while a full six hours of observations were obtained on 15 February. The weather was again excellent, particularly for the extended configuration, during which the 225 GHz opacity remained stable between 0.03 and 0.04 for most of the night. The projected baseline lengths in the final data set varied from 6 to 250 kλ, providing a synthesized beam size of $1\farcs2\times0\farcs9$ in the final data set (see Table 7.1). The instrumental polarization was calibrated by observing 3c273 over 90 degrees of parallactic angle for three hours across its transit. The quasar J1037-295 was used as the gain calibrator, and 3c279 was observed once per hour to test both the quality of the phase transfer and the instrumental polarization calibration. The primary flux calibrator was Titan, yielding a flux for J1037-295 of 0.64 Jy on the night of 25 Jan and 0.53 Jy on the night of 15 Feb. 3c279, 3c273, and J1037-295 were included as passband calibrators.

The double sideband receivers were tuned to a central frequency of 340.75 GHz (880 μm) for the HD 163296 observations and 341.44 GHz (877 μm) for the TW Hya observations, with each 2 GHz-wide sideband centered ±5 GHz from that value. The correlator was configured to observe the CO(3-2) transition (rest frequency 345.796 GHz) with a velocity resolution of 0.70 km s^{-1}. The data were edited and calibrated using the MIR software package, while the standard tasks of Fourier transforming the visibilities, deconvolution with the CLEAN algorithm, and restoration were carried out using the MIRIAD software package. For a summary of the observational parameters, including the 3σ upper limits in Stokes Q and U for the individual tracks and the combined data sets, refer to Table 7.1. The test quasars for all tracks were point-like and unresolved. We detect polarized emission from the test quasars independently in each data set with a polarization fraction of between 8 and 12% and a direction consistent

Table 7.1: Observational Parameters

	HD 163296			TW Hya		
	Compact	Extended	C+E	Compact	Extended	C+E
Parameter	29 May 2008	12 July 2008		25 Jan 2009	15 Feb 2009	
340 GHz Continuum						
Beam Size (FWHM)	2.″2×1.″3	0.″9×0.″7	1.″0×0.″9	4.″7×2.″0	1.″1×0.″8	1.″2×0.″8
P.A.	50°	-8°	7°	-1°	6°	6°
RMS Noise (mJy beam^{-1})						
Stokes I	11	7.8	5.7	35	6.8	5.5
Stokes Q & U	3.8	2.7	2.4	6.3	2.4	2.3
Peak Flux Density (mJy beam^{-1})						
Stokes I	996	639	739	990	450	474
Stokes Q & U (3σ upper limit)	<11	<8.1	<7.2	<19	<7.2	<6.9
Integrated Flux (Stokes I; Jy)	1.65	1.79	1.64	1.24	1.33	1.26
CO(3-2) Line						
Beam Size (FWHM)	2.″2×1.″4	0.″9×0.″7	1.″1×1.″0	5.″0×1.″2	1.″1×0.″7	1.″2×0.″7
P.A.	50°	-8°	17°	-1°	9°	9°
RMS Noise (mJy beam^{-1})	25	19	15	55	14	13
Peak Flux Density (mJy beam^{-1})						
Stokes I	6500	2650	3730	1520	1800	3090
Stokes Q & U (3σ upper limit)	<75	<57	<45	<170	<42	<39
Integrated Flux (Stokes I; Jy km s^{-1})	110	56	95	47	13	27

[a] All quoted values assume natural weighting.

[b] The rms in Stokes I is limited by dynamic range rather than sensitivity.

[c] The integrated continuum flux is calculated using the MIRIAD task `uvfit`, assuming an elliptical Gaussian brightness profile.

[d] The rms for the line is calculated using a channel width of 0.7 km s^{-1}.

[e] The integrated line flux is calculated by integrating the zeroth moment map inside the 3σ brightness contours.

between lower and upper sidebands, as expected for linearly polarized emission from quasars at these wavelengths (see Marrone 2006).

7.3 Results

Figure 7.1 shows the Stokes I (unpolarized) visibilities as a function of distance from the phase center in the (u,v) plane, corrected for the projection effects due to the disk inclination as in Lay et al. (1997) (for the mathematical definition of the abscissa, see Section 3.3 of Hughes et al. 2008b). This is effectively the Fourier transform of the radial brightness distribution of the disk. Both the HD 163296 and TW Hya disks are well resolved with high signal-to-noise ratios.

We detect no polarized emission, in the CO(3-2) line or 880 μm continuum, from the HD 163296 or TW Hya disks. The rms values achieved in Stokes Q and

U for the combined (compact+extended) continuum data are 2.4 mJy beam^{-1} and 2.3 mJy beam^{-1}, respectively, yielding a 3σ upper limit in both data sets of 7 mJy beam^{-1}. Given the integrated Stokes I fluxes of 1.65 Jy and 1.25 Jy for HD 163296 and TW Hya (see Table 7.1), the Cho & Lazarian (2007) result predictions of 2-3% polarization at these wavelengths imply ∼30-50 mJy of polarized flux. Even if the spatial distribution of polarized flux in the source differs from that of the unpolarized emission, we should be able to detect it given that we recover most of the Stokes I flux. Figures 7.2 and 7.3 compare the data with the fiducial model predictions (described in Section 7.4.1 below). The upper right panel of each figure displays the amount and direction of observed polarized flux for each source, while the bottom row presents contour maps for each of the individual Stokes parameters. The emission in Stokes Q and U (linear polarization), as well as in Stokes V (circular polarization), is consistent with noise. As noted in Section 7.2, since Stokes V is calculated as the difference between the measured right and left (RR and LL) circular polarization, the difficulty of calibrating the gains precisely enough to remove the influence of the bright Stokes I emission raises the rms value in this Stokes parameter relative to Stokes Q and U, which are calculated instead from the crossed (RL and LR) polarization states.

We can rule out calibration errors as the reason for the lack of polarized emission for three reasons: (1) The point-like test quasars and the similarity of the visibility profiles in Figure 7.1 with previous observations of these sources (see e.g. Isella et al. 2007; Hughes et al. 2008b) illustrate both the success of the atmospheric and instrumental gain calibration and the high sensitivity of the data set. (2) The detection of polarized emission from the test quasars in each of the data sets, with direction consistent between sidebands, demonstrates the success of the instrumental leakage calibration. Furthermore, (3) several of the nights were shared with other SMA polarization projects and our solutions for the instrumental leakage between Stokes parameters for the eight quarter-wave plates were effectively identical to those derived by other observers, who successfully detect polarization in their targets.

It is worthwhile to compare the rms noise achieved here with the limiting precision of the current SMA polarimeter. Errors in alignment of the quarter-wave plates introduce instrumental "leakage" between Stokes parameters, allowing some of the flux from Stokes I to bleed into the linear Stokes parameters. The instrumental leakage correction is quite small ($\lesssim 3\%$) and can to a large extent be calibrated by observing a bright point source as it rotates through 90° of parallactic angle. Nevertheless, the uncertainty of this correction under typical

observing conditions is ∼0.2%, although this can be reduced to $\lesssim 0.1\%$ with parallactic angle rotation, provided the source polarization does not vary with time (Marrone 2006). Given the $2\,\mathrm{mJy\,beam^{-1}}$ rms noise from our observations compared with the peak Stokes I fluxes of 740 and $470\,\mathrm{mJy\,beam^{-1}}$ (∼0.3%), our constraints on the polarized flux are approaching the limit of what is achievable with the SMA polarimeter.

It is difficult to directly compare the observations presented here with the Cho & Lazarian (2007) model predictions and the Tamura et al. (1999) JCMT result. The 2-3% polarization factor reported by both sources refers to the integrated emission over the entire spatial extent of the disk. Since the SMA spatially resolves the emission from the disk, the limit on the percent polarization varies with position across the disk. The emission structure is predicted to be quite complicated (Cho & Lazarian 2007), with the percent polarization increasing as a function of distance from the star, so there is no straightforward way to quote a single value for the percent polarization that can be easily compared with the data. By tapering the SMA visibilities with a Gaussian whose FWHM is equal to the diameter of the disk as measured by a truncated power law model (Hughes et al. 2008b), we can simulate an unresolved observation, similar to the JCMT result from Tamura et al. (1999). Using this method, we place a 3σ upper limit of 1% on the total polarized flux from both disks. However, such an extreme taper severely down-weights the visibilities on the longest baselines, which still have very high signal-to-noise ratios (see Figure 7.1). This effectively neglects the majority of the data: when all of the spatially resolved data are taken into account, the limits are much more stringent, but they must be compared with the more complicated predictions from the spatially resolved model. Furthermore, decreasing the resolution may be additionally detrimental in the case of more face-on disks like TW Hya: if the magnetic field is perfectly toroidal, then the resulting radial polarization signal will cancel to zero in a large beam, no matter how strong the emission. To give a rough estimate, the $\sim 40\,\mathrm{mJy}$ of integrated polarized flux predicted for a 2-3% polarization fraction resolved into a few beams might predict a peak flux density of $\sim 20\,\mathrm{mJy\,beam^{-1}}$, which is about 10σ above the $\sim 2\,\mathrm{mJy\,beam^{-1}}$ noise in the data. However, a detailed comparison with the spatially resolved model predictions for each disk can give a more robust result.

The highest signal-to-noise ratio in an image is achieved using natural weighting, which assigns each visibility a weight inversely proportional to its variance. In the case of observations with the SMA polarimeter, the bandwidth and integration time are the same for each integration, so the visibilities are primarily weighted by system temperature. For this reason, we use natural

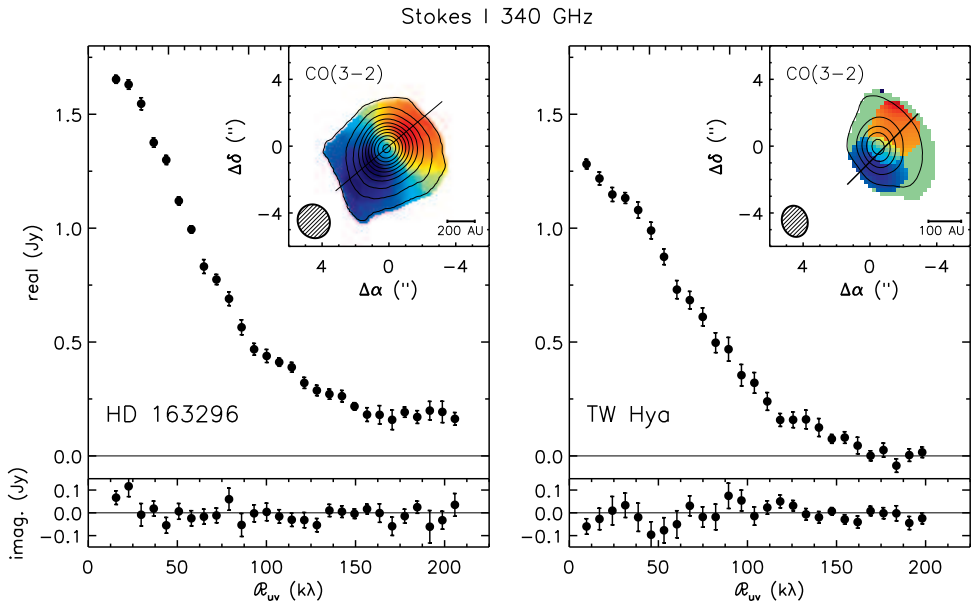

Figure 7.1.— Real (top) and imaginary (bottom) Stokes I continuum visibilities for HD 163296 (left) and TW Hya (right) as a function of distance from the disk center in the (u,v) plane, corrected for projection effects due to the inclination of the disk to our line of sight. Error bars show the standard error of the mean in each 7 kλ bin. See Lay et al. (1997) for details of the deprojection process. The inset in the upper right of each plot shows the CO(3-2) moment maps in Stokes I for the two disks. The colors indicate the first moment (intensity-weighted velocity), and the contours show the zeroth moment (velocity-integrated intensity) in intervals of 3 Jy km s^{-1}. The solid line marks the position angle of the disk as determined by Isella et al. (2007) and Qi et al. (2004). The size and orientation of the synthesized beam is indicated at the lower left of each moment map.

weighting to generate all images presented here. Using the upper limits from the naturally weighted images, it is possible to make comparisons with predictions of the spatially resolved emission generated from the models of Cho & Lazarian (2007). We pursue this avenue of investigation in the following section.

7.4 Analysis and Discussion

The constraints on polarized millimeter wavelength emission from the disks around TW Hya and HD 163296 are inconsistent with previous observational (Tamura et al. 1999) and theoretical (Cho & Lazarian 2007) work that suggested that a

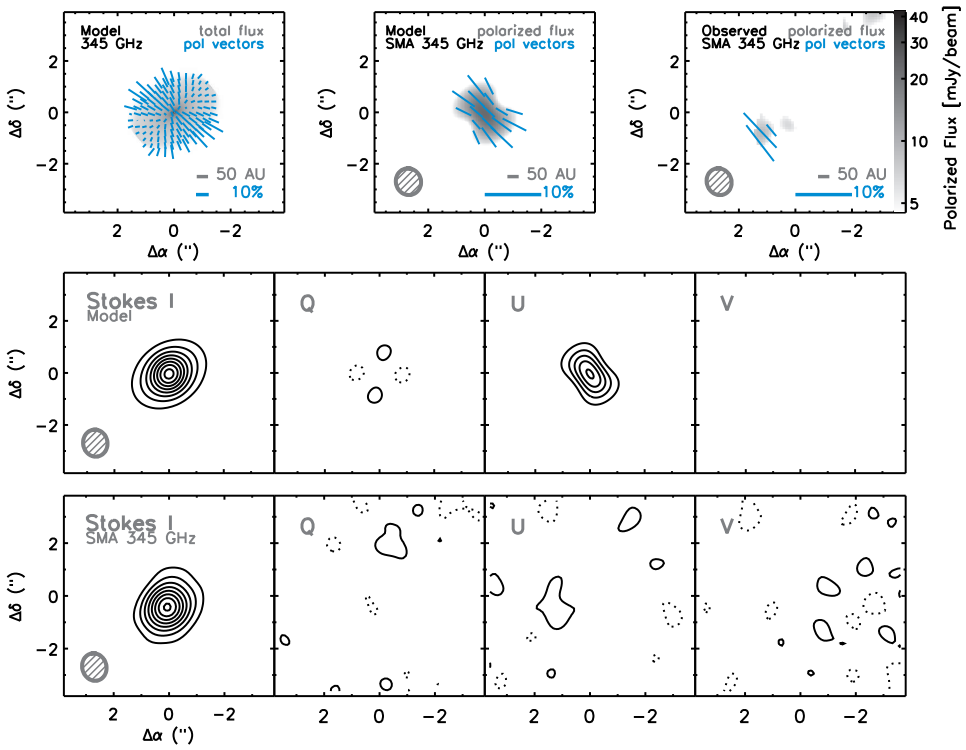

Figure 7.2.— Comparison between the Cho & Lazarian (2007) model and the SMA 340 GHz observations of HD 163296. The top row shows the prediction for the model at full resolution (left), a simulated observation of the model with the SMA (center), and the 2008 SMA observations (right). The grayscale shows either the total flux (left) or the polarized flux (center, right), and the blue vectors indicate the percentage and direction of polarized flux at half-beam intervals. The center and bottom rows compare the model prediction (center) with the observed SMA data (bottom) in each of the four Stokes parameters (I, Q, U, V, from left to right). Contour levels are the same in both rows, either multiples of 10% of the peak flux (0.9 Jy/beam) in Stokes I or in increments of 2σ for Q, U, and V, where σ is the rms noise of 2.4 mJy/beam. The size and orientation of the synthesized beam is indicated in the lower left of each panel.

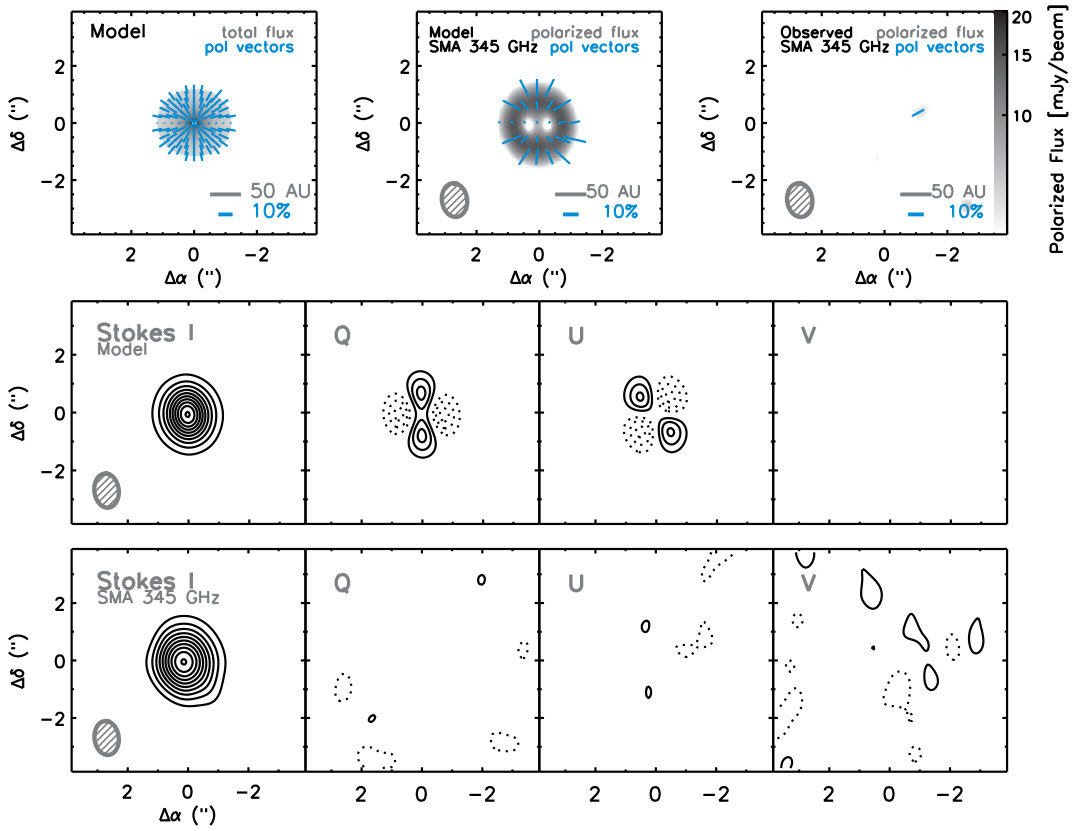

Figure 7.3.— Comparison between the Cho & Lazarian (2007) model and the SMA 340 GHz observations of TW Hya. The top row shows the prediction for the model at full resolution (left), a simulated observation of the model with the SMA (center), and the SMA observations (right). The center and bottom rows compare the model prediction (center) with the observed SMA data (bottom) in each of the four Stokes parameters (I, Q, U, V, from left to right). Contour levels are the same in both rows, either multiples of 10% of the peak flux (47 mJy/beam) in Stokes I or at 2σ intervals for Q, U, and V, where σ is the rms noise of 2.3 mJy/beam. Symbols as in Figure 7.2.

polarization fraction of 2-3% should be common among protoplanetary disks. The stringent limit on the polarization fraction, when investigated within the context of the Cho & Lazarian (2007) model, can provide clues to the physical conditions within the disk that may be responsible for the suppression of polarized emission relative to the fiducial model prediction. We therefore use the code described in Cho & Lazarian (2007) to generate models of the emission predicted for the TW Hya and HD 163296 disks, using available observational constraints on the disk properties as inputs, and compare these predictions to the upper limits from the SMA observations (Section 7.4.1). We then identify parameters that are not well constrained by existing observations, and which have the greatest effect on the polarized emission rather than unpolarized Stokes I emission. We vary these parameters and investigate their effects on the predicted polarized submillimeter emission. We infer the range of values over which the predictions are consistent with the observations as well as the interactions between parameters in the context of the models (Section 7.4.2). Finally, we investigate other effects *not* implemented in these models that may contribute to the suppression of polarized disk emission, and estimate the magnitude of their contribution (Section 7.4.3).

7.4.1 Initial Models

The Cho & Lazarian (2007) predictions employ a two-layered Chiang et al. (2001) model of the density and temperature structure of a protoplanetary disk, including a surface layer with hot, small dust grains and an interior with cooler, larger grains. Within this model, the elongated dust grains are allowed to align via the radiative torque mechanism with a perfectly toroidal magnetic field threading the disk. The dust grains are assigned a size distribution described by a power law $dN \propto r^{-q_{\rm grain}} dr$ where N is the number of grains of size r, and $q_{\rm grain}$ is initially taken to be 3.5 (Mathis et al. 1977). The grains are also assigned a degree of elongation given by the ratio of long-to-short axis cross sections, $C_\perp/C_\parallel$, where $C_\perp$ and $C_\parallel$ are the polarization cross sections for the electric field perpendicular and parallel to the grain symmetry axis, respectively. The grain size is defined as r, such that $C_\perp = (1+\alpha)\pi r^2$ and $C_\parallel = (1-\alpha)\pi r^2$, where α parameterizes the degree of elongation. The ratio of the major and minor axes of the grain are then given by $a/b = \sqrt{(1+\alpha)/(1-\alpha)}$. The grain shape is assumed to be oblate as in Cho & Lazarian (2007), consistent with observational evidence described in Hildebrand & Dragovan (1995). The initial 2-3% polarization estimates are based on the parameters for the "typical" T Tauri disk investigated in Chiang et al. (2001).

In order to generate a model prediction that can be compared with the upper limits from the SMA observations, we adjust these parameters to reflect the best available information about the grain properties and density structures in the disks around HD 163296 and TW Hya. The initial model inputs, with references, are summarized in Table 7.2. We use temperature and surface density power law indices and outer radii derived from previous SMA 345 GHz continuum observations (Hughes et al. 2008b). The temperatures are calculated from the stellar temperature and gas and dust densities and opacities as in Chiang et al. (2001), while the surface density is adjusted to best reproduce the observed 880 μm continuum flux. The temperatures and surface densities calculated here are consistent with previously determined values (e.g. Isella et al. 2007; Hughes et al. 2008b) to within a factor of two. Variations can be attributed to differences in the vertical temperature structure and dust grain opacities assumed in the models. While these disk structure models do not precisely reproduce the observed brightness profile, they represent a reasonable approximation within which the parameters determining the polarization properties of interest can be investigated.

We use the model routines to generate 400×600 pixel sky-projected images (i.e. with 6- and 8-milliarcsecond pixels for TW Hya and HD 163296, respectively, significantly more finely spatially sampled than the data) giving the total continuum flux, percent polarization, and orientation of polarized emission at each position across the disk. The full-resolution model is shown in the upper left panel of Figures 7.2 and 7.3, although the lines indicating orientation have been vector-averaged in bins of several pixels for clarity of display. We then use the MIRIAD task `uvmodel` to sample the image with the same spatial frequencies as the SMA data. We invert the visibilities and image with natural weighting to create a simulated SMA observation of the disk model, shown in the top center panel of Figures 7.2 and 7.3. We also create simulated images in each of the four Stokes parameters (center row), since the Stokes parameter images are most directly comparable to the upper limits set by the observations. The model images show the distinctive quadrupolar pattern in Stokes Q and U predicted by the model for a toroidal magnetic field geometry, due to the radial orientation of the polarization vectors. The intermediate inclination of HD 163296 creates an hourglass-shaped bright region along the disk minor axis, where the synthesized beam picks up emission from the highly polarized regions along the front and back of the outer disk, concentrated towards the disk center by the viewing geometry. This predicted morphology echoes the alignment of polarization vectors with the minor axes of the disk observed by Tamura et al. (1999). With predicted peak Stokes Q and U fluxes of 23 and 16 mJy beam^{-1}, these initial models of polarized

Table 7.2: Initial Model Parameters

	HD 163296		TW Hya	
Parameter[a]	Value	Ref.	Value	Ref.
T_* (K)	9330	1	4000	2
R_* ($R_\odot$)	2.1	1	1.0	2
M_* ($M_\odot$)	2.3	1	0.6	2
p	0.8	3	1.0	3
$a_{\rm inner}$ (AU)	0.45	4	4.0	5,6
a_0 (AU)	200	3	60	3
$r_{\rm max,i}$ (μm)	10^3	4	10^4	7
i	46°	4	7°	8
d (pc)	122	1	51	9,10
Σ_0 (g cm^{-2})	130	–	170	–

[a]Symbols as in Chiang et al. (2001): T_*, R_*, and M_* are stellar temperature, radius, and mass, respectively; p and Σ_0 describe the surface density profile $\Sigma(R) = \Sigma_0(R/1{\rm AU})^{-p}$; a_0 is the outer disk radius; and $r_{\rm max,i}$ is the maximum dust grain size in the disk interior. Additionally, we define $a_{\rm inner}$ (disk inner radius), i (inclination), and d (distance). All parameters not listed here are equal to the fiducial input parameters from Chiang et al. (2001).

References. — (1) van den Ancker et al. (1998b); (2) Webb et al. (1999); (3) Hughes et al. (2008b); (4) Isella et al. (2007); (5) Calvet et al. (2002); (6) Hughes et al. (2007); (7) Wilner et al. (2005); (8) Qi et al. (2004); (9) Mamajek (2005); (10) Hoff et al. (1998)

emission are ruled out at the 10σ and 7σ level for HD 163296 and TW Hya, respectively, by the SMA upper limits.

7.4.2 Parameter Exploration

With the fiducial model prediction ruled out at high confidence, we turn to an exploration of the input parameter space to provide information about the conditions in the disk that might be responsible for the suppression of polarized emission. We first identify several parameters that most strongly affect the polarization properties of the disk, without significant impact on the Stokes I emission. In the Cho & Lazarian (2007) model, the radiative torque mechanism that spins up elongated dust grains along magnetic field lines is impeded primarily by gas drag in regions of high density. Since we normalize the surface density to

reproduce the 880 μm flux (for the assumed opacities and derived temperatures), we cannot vary this quantity. However, the degree of elongation of the dust grains, the threshold set within the model for grain alignment, and the dust grain size distribution are all important factors that affect the polarization properties of the disk rather than the Stokes I emission. These parameters are discussed in greater detail in the following sections.

Grain Elongation

The elongation of the dust grains is important both for the radiative torque and because the differing cross-sections parallel and perpendicular to the magnetic field allow the grain to emit polarized continuum emission at millimeter wavelengths. The fiducial model assumes a long-to-short axis cross-section ratio $C_\perp/C_\parallel = 2.1$, corresponding to an axial ratio of 1.5:1 for oblate dust grains (for the relationship between cross section and axial ratios for different grain geometries, see e.g. Padoan et al. 2001). Varying this ratio determines the radial extent of the disk over which the dust grains are aligned with the magnetic field, as well as how much polarized light is emitted from the disk: it effectively changes the efficiency of grain alignment and the emission cross-section of the grains.

In order to obtain a quantitative description of the effect of grain elongation on the predicted intensity of polarized emission from the disk, we generate a series of models with different cross section ratios as described in Cho & Lazarian (2007) with initial parameters listed in Table 7.2. We then sample the model images with the SMA spatial frequencies, as described in Section 7.4.1 above, and compare the peak flux in Stokes Q and U with the 3σ upper limit from the SMA observations. Figure 7.4 plots the peak flux in the Stokes Q and U model images as a function of the dust grain cross section ratio. For comparison, the shaded area marks the region of parameter space consistent with the 3σ upper limits from the SMA observations. The series of panels across the top of the plot show the model images in Stokes Q and U, sampled with the SMA spatial frequencies, for three representative values of the dust grain cross section ratio. From these maps, it is clear that the dust grain elongation acts primarily as a scaling factor for observations at this resolution: the emission morphology does not change, but simply becomes stronger or weaker as the dust grains become more or less elongated. From the HD 163296 plot on the left and the TW Hya plot on the right, we can see that if the dust grain elongation were the only factor suppressing polarized emission from the disk, the grains would have to be quite round, with $C_\perp/C_\parallel \lesssim 1.2 - 1.3$.

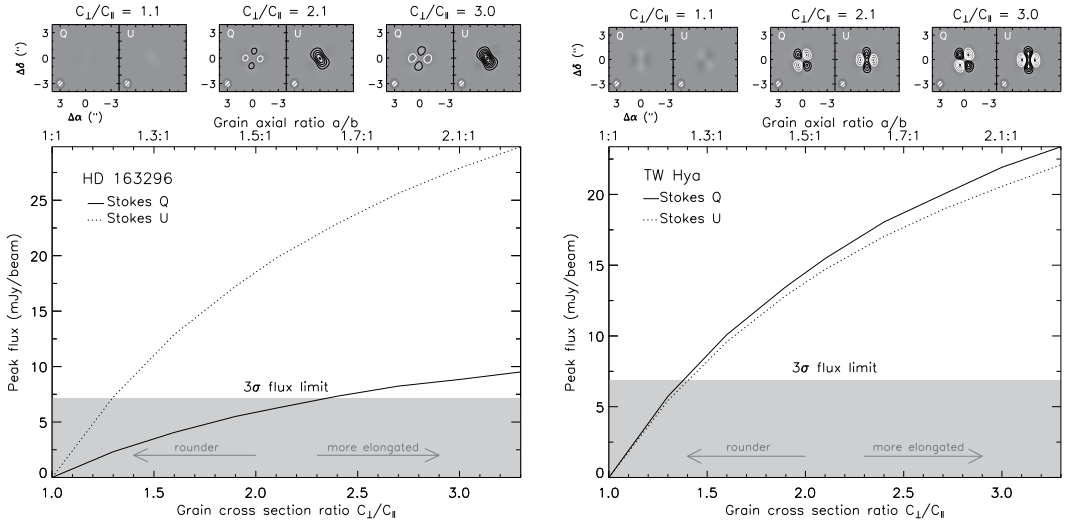

Figure 7.4.— Peak continuum flux in Stokes Q and U as a function of dust grain cross section ratio for HD 163296 (left) and TW Hya (right). The top row shows the resolved emission in Stokes Q and U predicted for three values of the dust grain cross section ratio, sampled at the same spatial frequencies as the data. The grayscale indicates the intensity of emission relative to the peak flux of the data when the grain cross section ratio equals three, with white indicating positive emission and black indicating negative emission. Contours are [2,4,6,...] times the rms noise (2.4 mJy for HD 163296 and 2.3 mJy for TW Hya) with positive contours in black and negative contours in white. The plots below give the peak flux in the synthesized beam predicted by the models as a function of the grain cross section ratio. Stokes Q is plotted as a solid line while Stokes U is a dotted line. The three-sigma upper limit on the peak flux from the SMA observations is indicated by the gray region of the plot. The y-axis along the upper edge of the plot gives the dust grain axial ratio. Images and peak flux values assume natural weighting to minimize noise.

Grain Alignment Criterion

Another model input that is important for the polarization properties of the disk is the value at which the threshold for grain alignment via the radiative torque is set. In order to determine whether or not the dust grains are aligned with the magnetic field in a particular region of the disk, a comparison is made between the rotational kinetic energy imparted by the radiative torque and that imparted by random collisions with gas particles in the disk. A useful parameterization is $(\omega_{\rm rad}/\omega_{\rm th})^2$, where $\omega_{\rm rad}$ and $\omega_{\rm th}$ are the angular velocities of the grains due to radiative torques and thermal collisions, respectively. The radiative torques act to align grains with the magnetic field, while gas drag inhibits alignment and causes grains to point in random directions: the ratio $(\omega_{\rm rad}/\omega_{\rm th})^2$ therefore serves as a measurement of the effectiveness of the radiative torque in aligning the grains with the magnetic field. This ratio will generally be highest, and the grains most aligned, in the outer disk where the gas density is low. We therefore expect grains to be aligned in the outer disk, and oriented randomly in the inner disk. Since the value of $(\omega_{\rm rad}/\omega_{\rm th})^2$ varies with radial distance from the star, the chosen threshold value for alignment effectively varies the radius at which grains become aligned with the disk magnetic field. The threshold is initially set so that grains are assumed to be aligned in regions of the disk where the kinetic energy imparted by the radiative torque is 10^3 times greater than that imparted by thermal collisions. We vary this threshold in order to study its effects on the polarization properties of the disk.

Figure 7.5 shows the peak flux predicted for Stokes Q and U as a function of the grain alignment threshold $(\omega_{\rm rad}/\omega_{\rm th})^2$, compared with the 3σ upper limit from the SMA observations for HD 163296 (left) and TW Hya (right). It is clear that for both disks, the threshold would have to be set many orders of magnitude higher than the conservative initial value in order for the alignment to be weak enough to account for the lack of a polarization signal. Indeed, in order for this to be the primary mechanism suppressing the disk polarization, the threshold would need to be raised until alignment is permitted to occur only when the rotational kinetic energy imparted by the radiative torque is at least 5-7 orders of magnitude greater than that of gas grain collisions. This is most likely an unrealistically stringent constraint.

It should be noted here that the approach to alignment in Cho & Lazarian (2007) requires revisions to account for recent advances in the quantitative theory of grain alignment. First of all, in the calculations of the ratio $(\omega_{rad}/\omega_{th})$, the simplifying assumption is made that the radiation seen by each grain is

coming from a point source. In fact, the bulk of the radiation field originates as reprocessed starlight from neighboring regions of the disk, so although there should be an overall radial gradient, it is better approximated by multipoles rather than a purely unidirectional signal. When the effects of this radiation structure are accounted for, the ratio (ω_{rad}/ω_{th}) can decrease by up to a factor of 10 (Hoang & Lazarian 2009, Figure 17). An additional decrease by another factor of $\sim$10 may come from the fact that the overall direction of anisotropy is perpendicular to the assumed toroidal magnetic field in the disk (Hoang & Lazarian 2009, Figure 17). This effect may be mitigated somewhat in a clumpy disk, where local anisotropies will not necessarily be radially oriented and may even be aligned with the magnetic field. Taking both effects into account and squaring the ratio demonstrates that the kinetic energy of the grains in their maximal state of rotation may be up to 4 orders of magnitude less than is assumed using ad hoc assumptions in the spirit of the old understanding of radiative torque alignment. An additional decrease comes from the fact that an appreciable portion of grains may be aligned in the so-called "zero-J" alignment point (Lazarian & Hoang 2007). Grains in this point are not perfectly aligned as assumed in Cho & Lazarian (2007), but instead will wobble, reducing the degree of alignment to only $\sim$20% (see Hoang & Lazarian 2008). In addition, while interstellar grains are always aligned with long axes perpendicular to magnetic field, larger grains in circumstellar disks may not have efficient internal relaxation and can be occasionally aligned with long axes parallel to magnetic field (Hoang & Lazarian 2009). These factors can significantly decrease the observed degree of polarization expected from the circumstellar disks compared to the Cho & Lazarian (2007) estimate, making the predictions roughly comparable (to within an order of magnitude or so) to the SMA upper limits.

Grain Size Distribution

Cho & Lazarian (2007) emphasize the importance of the grain size distribution in determining the observed polarization properties of circumstellar disks. We fix the minimum grain size at $r_{\rm min} = 0.01\,\mu$m as in Cho & Lazarian (2007) and Chiang et al. (2001). Although growth to larger sizes may have occurred, the minimum grain size affects the millimeter-wavelength polarization properties in the context of the model only through the normalization of the total mass: increasing the minimum grain size to $1\,\mu$m (required to reproduce the $10\,\mu$m silicate feature from the inner disk; see e.g. Calvet et al. 2002) changes the predicted polarization by less than 0.1%, since it does not bring the density above the threshold value necessary to suppress grain alignment in the outer disk. Two aspects of the grain

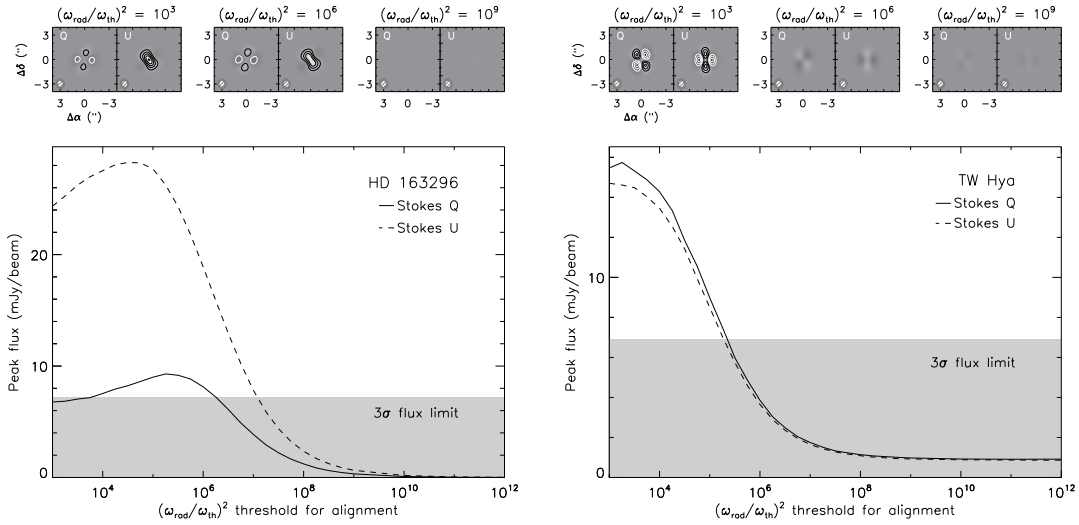

Figure 7.5.— Peak continuum flux in Stokes Q and U as a function of the threshold for grain alignment (see Section 7.4.2 in the text) for HD 163296 (left) and TW Hya (right). The top row shows the resolved emission in Stokes Q and U predicted for three values of the alignment threshold, sampled at the same spatial frequencies as the data. The grayscale indicates the intensity of emission relative to the peak flux of the data when the alignment threshold equals 10^3, with white indicating positive emission and black indicating negative emission. Contours are [2,4,6,...] times the rms noise (2.4 mJy for HD 163296 and 2.3 mJy for TW Hya) with positive contours in black and negative contours in white. The plots below give the peak flux in the synthesized beam predicted by the models as a function of the alignment threshold. Stokes Q is plotted as a solid line while Stokes U is a dotted line. The three-sigma upper limit on the peak flux from the SMA observations is indicated by the gray region of the plot. The y-axis along the upper edge of the plot gives the dust grain axial ratio. Images and peak flux values assume natural weighting to minimize noise.

size distribution that can be varied in the context of the model are the maximum grain size $r_{\rm max}$ and the power law index $q_{\rm grain}$, where the grain size number density goes as $dN \propto r^{-q_{\rm grain}} da$.

Observational evidence points to grain growth up to at least 1 mm in the HD 163296 disk (Isella et al. 2007) and 1 cm in the TW Hya disk (Wilner et al. 2005), without ruling out the possibility that grains have grown to even larger sizes (perhaps even planetary dimensions in the case of TW Hya; see Calvet et al. 2002; Hughes et al. 2007). Since the surface density is chosen to maintain consistency with the observed 880 μm flux in Stokes I, the number density of particles with sizes near 880 μm, which dominate the 880 μm flux, remains roughly constant regardless of the maximum grain size in the distribution. Thus the effect of raising the maximum grain size in the distribution is primarily to introduce "invisible" grains at sizes larger than 1 mm or 1 cm, which has no effect on the observable polarization properties (cf. Figure 7 in Cho & Lazarian 2007). However, adding mass at the large-grain end of the size distribution while keeping constant the mass in small grains has the effect of raising the total surface density of the disk. This is unrealistic for all but a small increase in maximum grain size, as the disk quickly becomes Toomre unstable and gravitational collapse or deviations from Keplerian rotation should rapidly become observable. While this is most likely an artifact of the assumed grain size distribution, it suggests that within the context of the model, grain growth is unlikely to be the mechanism suppressing the emission of polarized radiation.

The power law index $q_{\rm grain}$ controlling the relative population of large and small grains in the disk is somewhat more promising. In general, the polarized emission observed at a particular wavelength will tend to originate primarily from dust grains smaller than the wavelength, while the unpolarized emission will be dominated by grains of roughly the same size as the wavelength. Because dust grains of size $\sim$880 μm are within the geometric optics regime ($2\pi r/\lambda > 1$, where λ is the wavelength of observation, 880 μm), they do not contribute to the polarized emission predicted by the models. Most of the Stokes Q and U emission at these wavelengths originates from dust grains with sizes less than $\lambda/2\pi \approx 100\,\mu$m (Cho & Lazarian 2007), while most of the Stokes I emission originates from grains with sizes similar to the wavelength of observation. The relative number of 100 and 880 μm grains in the disk, determined by $q_{\rm grain}$, therefore plays a role in determining the amount of polarized emission observed. However, since the differences in grain sizes is not large, the power law index must change substantially before the effect on the polarization properties becomes appreciable. Varying $q_{\rm grain}$ from 3.5 to 2 changes the peak linearly polarized flux

in the model by only 20%. Therefore, when comparing the SMA limits with the model predictions, the dust grain size distribution has relatively little impact on the predicted polarization properties of the disks.

Interactions Between the Parameters

The analysis so far has explored individual model parameters as though they were fully independent, determining the range of values permitted by the SMA upper limit for each parameter separately. However, it is useful to understand how the parameters relate to one another in determining the polarization properties of the disk. Here we investigate relationships between pairs of the parameters considered above.

We first study the relationship between dust grain elongation and the grain alignment threshold. As discussed in §2.3 of Cho & Lazarian (2007), the rotation rate of dust grains due to the radiative torque is a function of the peak wavelength of the radiation field and the dust grain size, with no explicit dependence on grain axial ratio. As described in Dolginov & Mitrofanov (1976), spin-up by the radiative torque mechanism is caused by the irregular shape of the grain, which gives it differing cross sections to left and right circular polarization; elongation does not necessarily favor either polarization basis. This is reflected in the table of timescales relevant for grain alignment in Lazarian (2007): neither the radiative precession time nor the gas damping time depends on the grain axial ratio. The primary effect of the grain elongation in alignment is to decrease the Larmor precession time, which causes the spinning grains to align their major axes more quickly with the magnetic field lines (or, alternatively, decreases the critical magnetic field strength in a given region of the disk; see Section 7.4.3 below). We therefore do not expect much, if any, dependence between these variables. In order to test this expectation, we vary the dust grain cross section ratio and the grain alignment threshold for the HD 163296 disk. The model prediction of peak flux in Stokes U (which provides the most stringent limits when compared to the SMA data) are shown in Figure 7.6. The shaded gray region of the plot represents the parameter space within which the model prediction is less than the 3σ upper limit given by the SMA data, i.e., combinations of parameters consistent with the observational results. The contours show the predicted peak flux of the model in Stokes U for each combination of parameters: model predictions with greater polarized intensity are more strongly inconsistent with the observational limits. Because of the assumption in the models that grains meeting the alignment criterion will become aligned with 100% efficiency, grain alignment and elongation

are evidently only weakly coupled.

Another potentially important relationship is that between the grain size distribution and grain elongation. Little is known about the relationship between these variables, since both are notoriously difficult to constrain observationally. Nevertheless, if grains grow simply by accumulating material evenly over their surface then they may naturally become more spherical as they become larger. Spherical grains emit less strongly polarized radiation than more elongated grains, so it might be expected that grain growth can suppress the emission of polarized light, even in cases where the alignment mechanisms are quite efficient (as expected for large grains, e.g. Cho & Lazarian 2005). Indeed, a corresponding inverse relationship between grain size and polarization fraction has been observed in molecular clouds (e.g. Vrba et al. 1993). Given the observed growth to millimeter and even centimeter sizes within the disks around HD 163296 and TW Hya (Isella et al. 2007; Wilner et al. 2005), and the large ($\sim$100 μm) sizes of the grains responsible for emitting most of the polarized radiation (see Section 7.4.2), it is perhaps plausible that the grains in these disks should have cross section ratios consistent with the values of 1.2-1.3 constrained in Section 7.4.2 above. We know that this cannot be true everywhere in the interstellar medium (ISM): polarization at 850μm is observed in star-forming regions at much earlier stages (e.g. Girart et al. 2006), and far-infrared polarimetry indicates that grains with axial ratios a/b between 1.1-3 are common at sizes of tens of microns in molecular clouds (Hildebrand & Dragovan 1995). However, a tendency towards spherical grains in T Tauri disks, even just at the low end of the distribution inferred by Hildebrand & Dragovan (1995), should be able to suppress the emission of polarized radiation from the disk enough to bring the models within range of the observational constraints.

We can test the plausibility of this degree of elongation by modifying the discussion of grain growth based on turbulent coagulation in Vrba et al. (1993). If we assume that the grains in T Tauri disks originate exclusively from small, highly elongated grains in the ISM, e.g. with initial major axis $a_i = 0.1\,\mu$m and axial ratio $a_i/b_i = 2$ (Aannestad & Purcell 1973; Hildebrand & Dragovan 1995), then we can estimate how the axial ratio changes with grain size. Neglecting asymmetric effects like collisional destruction, grain size might be expected to grow roughly evenly in all directions with the number of grain-grain collisions, N, in such a way that the final grain size is simply $a_f = a_i N^{1/3}$. The change in any dimension of the grain, δ, is then given by $\delta = a_i N^{1/3} - a_i$, yielding a final minor axis size of $b_f = b_i + \delta$, or $a_f/b_f = a_f/(a_f - a_i + b_i)$. If $a_i = 0.1\,\mu$m and a_f = 100 μm, then $a_f/b_f = 1.001$, significantly more round than the upper limit set

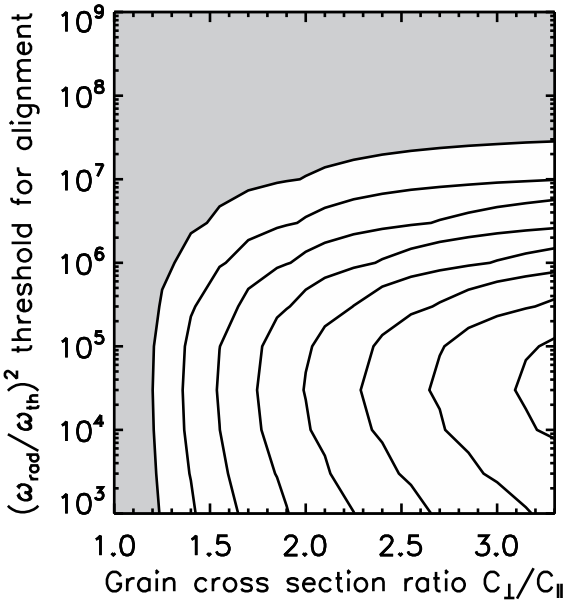

Figure 7.6.— Detectability of Stokes U continuum emission from the HD 163296 disk as a function of the dust grain cross section ratio (Section 7.4.2) and the threshold for dust grain alignment (Section 7.4.2). The gray regions of the plot represent portions of the parameter space that would be undetectable given the 3σ upper limit from the SMA observations, while contours show the peak flux of the model for each set of parameters, beginning at the 3σ level (7.2 mJy) and increasing by intervals of 2σ (4.8 mJy). The two parameters are only weakly degenerate.

by the SMA data. The timescale needed for grain growth to these (up to meter) sizes is of order 10^5 years at a distance of 50 AU from the central star (see e.g. Weidenschilling 1988; Dullemond & Dominik 2005). This calculation is highly simplified and neglects complications like the evolution of conditions within the disk, shaping by grain-grain collisions (e.g. Dullemond & Dominik 2005), and the complexity of the grain size distribution. Yet the extremely spherical grains produced on relatively short timescales in this oversimplified scenario represent a lower limit to the grain elongation that perhaps suggests a scenario by which grains might have grown into shapes that are nearly spherical enough (with axial ratios of 1.2 rather than 1.001) to plausibly account for the suppression of polarized emission.

7.4.3 Other Effects

In the previous section, we investigated the effects of those parameters considered in the Cho & Lazarian (2007) model. However, there are additional effects that may also play a role in suppressing polarized emission from the disk relative to the fiducial 2-3% prediction. Among these are the magnetic field strength, the geometric regularity of the magnetic field, and polarization due to scattering.

Magnetic Field Strength

The magnetic field strength plays a role in determining whether or not grains can become aligned via the radiative torque. If the magnetic field is above some critical strength, grains will become aligned provided that the radiative torque can generate more rotational kinetic energy than thermal collisions. At low magnetic field strengths, grains are not expected to align with the magnetic field at all. The critical magnetic field strength for alignment may be estimated by comparing the Larmor precession time t_L with the gas damping time t_{gas}. Following Lazarian (2007) and using fiducial values for the magnetic susceptibility and dust grain density, alignment is possible when $t_L < t_{gas}$, or:

$$B > 4.1 \times 10^{-5} \frac{rnT_d T_g^{1/2}}{s^2} \tag{7.1}$$

where B is the magnetic field strength in units of μG, r is the grain size in cm, n is the gas density in units of cm^{-3}, T_d is the dust temperature in K, T_g is the gas temperature in units of K, and s is the ratio of minor to major dust grain axes. Using the power law models of density and temperature derived in Hughes et al. (2008b), it is possible to estimate these quantities for the regions of the outer disk probed by the SMA data. Taking the values at disk radii equivalent to the spatial resolution of the data ($\sim$1.″0, or 50 and 120 AU for TW Hya and HD 163296, respectively), and assuming equivalent gas and dust temperatures, we derive densities of several times 10^8 cm^{-3} and temperatures of $\sim 40 - 50$ K. For the 10-100 μm grains contributing most of the polarized emission in the models, the critical magnetic field strength is of order 10-100 mG.

This strength matches reasonably well with theoretical expectations. Shu et al. (2007) developed a model of steady-state magnetized accretion disks that predict magnetic field strengths of order 10-100 mG on the spatial scales probed by the data. Wardle (2007) pointed out that Zeeman splitting of OH in molecular cloud cores and masers in star forming regions place a lower limit of $\sim$10 mG on the magnetic field strength, which will likely be amplified by compression and

shear during the process of collapse that forms the central star and disk. It should also be noted that the value quoted above should be taken as a lower limit, since superparamagnetic inclusions would significantly decrease the required magnetic field strength for alignment (Lazarian & Hoang 2008). The critical magnetic field strength required to align grains within the conditions of the model is therefore reasonable compared to theoretical expectations. We do not expect that the lack of polarized emission is due to extremely low magnetic field strengths.

Geometric Regularity of the Magnetic Field

The assumption that the field is toroidal arises from the supposition that the rotational motion of the disk has affected the magnetic field geometry. Yet for this to occur, the ionization fraction must be large enough that disk material and magnetic fields can interact. However, this also implies that turbulent motions within the disk (perhaps even of magnetic origin) may tangle the magnetic fields locally, adding a random component to the ordered toroidal magnetic field. It is extremely difficult to estimate the magnitude of such an effect without knowing both the ionization fraction and the magnitude of turbulence as a function of position in the disk. Lee & Draine (1985) discuss the effect of a random magnetic field component on the strength of the observed polarization signature, and note that the strength of polarized emission will be reduced by a factor $F = 3/2(\langle \cos^2 \theta \rangle - 1/3)$, where θ is the angle between the local magnetic field and the direction of the ordered global magnetic field. This quantity varies from one (perfectly ordered field; $\langle \cos^2 \theta \rangle = 1$) to zero (perfectly random field; $\langle \cos^2 \theta \rangle = 1/3$), but the exact value depends on the details of the local magnetic field geometry. If magnetic field tangling were the sole factor responsible for the difference between the fiducial modeling prediction and the SMA upper limits, we would constrain F to be less than ~ 0.1 for the case of HD 163296, implying $\langle \cos^2 \theta \rangle < 0.4$, which indicates an almost completely random magnetic field structure.

It should also be noted that grain alignment efficiency would play a similar role, quantified in exactly the same way as F above, with θ indicating the angle between the long axis of the grain rather than the angle between the local and global magnetic fields (Greenberg 1968; Lee & Draine 1985). The Cho & Lazarian (2007) code assumes 100% efficient alignment in regions that meet the grain alignment criterion (Section 7.4.2). In order to account fully for the suppression of polarized emission relative to the fiducial model, the alignment efficiency would have to be quite low, less than 10% in the case of HD 163296.

The tentative single-dish detections appear to indicate a toroidal magnetic field geometry for the disks around DG Tau and GM Aur, consistent with observations indicating a dominant toroidal component to the magnetic field in the flattened structures around YSOs at earlier evolutionary stages (see Wright 2007, and references therein). However, it is also possible that the field could be poloidal: as discussed e.g. in Shu et al. (2007), a magnetic field gathered from the interstellar medium that threads vertically through the disk might be expected to remain poloidal in geometry as it interacts with disk material. While the SMA limits are unable to constrain the magnetic field geometry, a poloidal geometry might be expected to reduce the expected polarization signature particularly for the case of a face-on viewing geometry as in the case of the TW Hya disk. The effects of a poloidal geometry for a disk viewed at intermediate inclination, like HD 163296, are less clear and are not investigated in the context of the Cho & Lazarian (2007) models, although it is plausible that the strength of polarized emission from a toroidal or poloidal field would be comparable.

Scattering

Cho & Lazarian (2007) argue that scattering contributes significantly less than thermal emission to the polarized flux at millimeter wavelengths in the disk. In order to estimate the relative contribution of scattering and emission at a range of radii throughout the disk, they compare the product $J_\lambda \kappa_{\rm scatt}$, where J_λ is the mean radiation field and $\kappa_{\rm scatt}$ is the mass scattering coefficient, to the product $B_\lambda \kappa_{\rm abs}$, where B_λ is the intensity of blackbody radiation in the region of interest and $\kappa_{\rm abs}$ is the mass absorption coefficient. They show that in the outer disk, where $R \gtrsim 10\,{\rm AU}$, the ratio of these products falls below one (and ultimately below 0.5), indicating that emission is dominant over scattering in the outer disk.

It is of interest, however, that pure scattering of light from a central source off of large grains in the outer disk should produce a polarization signal precisely orthogonal to that expected for elongated grains aligned with a toroidal magnetic field. While the radiation field at $850\,\mu$m is dominated by the local conditions rather than a central source, as discussed in Section 7.4.2 there will be an overall radially anisotropic component of the radiation field that might be expected to produce a weaker, but still orthogonal on average, scattering signal. The contribution from scattering would therefore generally act to cancel the expected polarization signal from emission. An estimate of the magnitude of the scattered light signal compared with the predicted strength of polarized emission is beyond the scope of this paper, but we note that for scattering to be the

dominant mechanism suppressing the expected polarization signal, the intensity of polarized emission arising from scattering and emission would have to be precisely equivalent, to within 10-15%, in both disks. Furthermore, since the scattering and emission have different wavelength dependences, the coincidental canceling of the emission signal would only occur at the wavelength of observation. In the absence of any expectation that these quantities should be related, this seems an unlikely coincidence.

7.5 Summary and Conclusions

Despite the expectation of a 2-3% polarization fraction in circumstellar disks based on previous observational and theoretical work (Tamura et al. 1999; Cho & Lazarian 2007), the SMA polarimeter observations presented here show no polarization from the disks around two nearby stars. With these observations we place a 3σ upper limit on the integrated polarization fraction of less than 1% and rule out the fiducial Cho & Lazarian (2007) models at the $\sim 10\sigma$ level. These represent the most stringent limits to date on the magnitude of submillimeter polarized emission from circumstellar disks. We are therefore left with the question of which model assumptions are unrealistic enough to account for an approximately order-of-magnitude (at minimum) overprediction of the polarization signal from these disks.

Among the model parameters and additional effects considered in Section 7.4, several seem unlikely as the source of the suppression of polarized emission. The critical magnetic field strength expected for alignment seems reasonable relative to theoretical expectations and observations. An almost completely random magnetic field with no dominant toroidal (or poloidal) component would also be surprising, although a poloidal field geometry would be expected to significantly weaken the polarized emission arising from a face-on disk like TW Hya. Scattering is expected to be weak, but it should produce a polarization signature perpendicular to that expected for emission from aligned grains. However, scattering and emission signals would have to cancel nearly perfectly in order to account entirely for the low observed polarization fraction. Nevertheless, there are promising candidates to describe how the suppression of polarized emission might have occurred. Cho & Lazarian (2007) assume 100% efficient alignment of grains with the magnetic field in regions of the disk where the alignment criterion is met, which is overly optimistic and now known to be unrealistic (see discussion in Section 7.4.2). In light of the recent work on

the quantitative theory of grain alignment (Lazarian & Hoang 2007; Hoang & Lazarian 2008, 2009), the Cho & Lazarian (2007) result may be considered an upper limit to the theoretical expectation for the polarization properties of disks. A reduction to 10% efficiency, which is within the expectations based on recent developments in grain alignment theory, could alone explain the low polarization fraction observed. Another possibility is that the grains contributing most of the polarized emission in the model are well (or not so well) aligned, but rounder than the cross section ratio assumed in the initial model and therefore inefficient emitters of polarized radiation. This is also reasonable based on a rough estimate of the timescales and shapes expected for collisional growth of elongated ISM grains.

While each of these factors would have to be substantially different from what is expected in the initial model to alone account for the low polarization fraction, it is of course entirely possible that several effects are playing a combined role. For example, grains with a cross section ratio of 1.5 instead of 2.1 could combine with a 50% alignment efficiency to account entirely for the difference between observations and models. A small degree of field tangling (expected because of turbulence in the disk) could further reduce the expected polarization signature. While we cannot constrain precisely which factors are contributing in which proportions to the suppression of polarization in the disks observed with the SMA, we identify these three factors (grain elongation, alignment efficiency, and field tangling) as the most plausible sources of the suppression of polarized emission. They produce the greatest change in polarization properties within a reasonable range of parameter values, and there exists a theoretical justification for why they should exist, even if the magnitude of the effect is not well constrained.

Future observations with higher sensitivity may be able to disentangle these effects to some extent, particularly the degree of field tangling. It would also be useful to obtain high spatial resolution observations of the disks with tentative detections of a 2-3% polarization fractions to confirm the strength and origin of the emission on small spatial scales, and to expand the sample size in order to determine whether the low polarization fraction constrained by the SMA is universal for disks around young stars. These latter points are addressed in Appendix B, in which we present observations of the disks around GM Aur, which has a previously reported 2.5σ detection of polarized emission, and MWC 480. The non-detection of polarized millimeter-wavelength emission from additional systems strengthens the conclusions of this study.

Chapter 8

Empirical Constraints on Turbulence in Protoplanetary Accretion Disks

A. M. Hughes, D. J. Wilner, S. M. Andrews, C. Qi, & M. R. Hogerheijde 2010

Abstract

We present arcsecond-scale Submillimeter Array observations of the CO(3-2) line emission from the disks around the young stars HD 163296 and TW Hya at a spectral resolution of $44\,\mathrm{m\,s^{-1}}$. These observations probe below the $\sim$$100\,\mathrm{m\,s^{-1}}$ turbulent linewidth inferred from lower-resolution observations, and allow us to place constraints on the turbulent linewidth in the disk atmospheres. We reproduce the observed CO(3-2) emission using two physical models of disk structure: (1) a power-law temperature distribution with a tapered density distribution following a simple functional form for an evolving accretion disk, and (2) the radiative transfer models developed by D'Alessio et al. (1998) that can reproduce the dust emission probed by the spectral energy distribution. Both types of models yield a low upper limit on the turbulent linewidth in the TW Hya system ($\lesssim$$40\,\mathrm{m\,s^{-1}}$), and a tentative ($3\sigma$) detection of a $\sim$$300\,\mathrm{m\,s^{-1}}$ turbulent linewidth in the upper layers of the HD 163296 disk. These correspond to roughly $\leq$10% and 40% of the sound speed at size scales commensurate with the resolution of the data. The derived linewidths imply a turbulent viscosity coefficient, α, of order 10^{-2} and provide observational support for theoretical

predictions of subsonic turbulence in protoplanetary accretion disks.

8.1 Introduction

The circumstellar accretion disks around young stars provide the raw material and physical conditions for the planet formation process. The viscous transport of angular momentum drives the evolution of the protoplanetary disks around young stars (Lynden-Bell & Pringle 1974; Hartmann et al. 1998), determining when, where, and how much material is available for planet formation. Understanding the physical mechanisms behind the viscous transport process is therefore central to constraining planet formation theory. The source of viscosity is uncertain, since molecular viscosity implies a disk evolution timescale far longer than the observed 1-10 Myr. The classic result from Shakura & Syunyaev (1973) demonstrates that turbulence can provide viscosities large enough to account for disk evolution on the appropriate timescales. However, while turbulence is commonly invoked as the source of viscosity in disks, its physical origin, magnitude, and spatial distribution are not well constrained.

The mechanism most commonly invoked as the source of this turbulence in disks around young stars is the magnetorotational instability (MRI), in which magnetic interactions between fluid elements in the disk couple with an outwardly decreasing velocity field to produce torques that transfer angular momentum from the inner disk outward (Balbus & Hawley 1991, 1998). Models of disk structure indicate that the conditions for the MRI are likely satisfied over much of the extent of a typical circumstellar disk, with the possible exception of an annular dead zone (Gammie & Johnson 2005, and references therein). MRI turbulence has also been invoked to address a wide array of problems in planet formation theory. For example, it has been proposed to regulate the settling of dust particles (e.g., Ciesla 2007), to explain mixing in meteoritic composition (e.g., Boss 2004), to form planetesimals (e.g., Johansen et al. 2007), and to slow planet migration (e.g., Nelson & Papaloizou 2003). Measurements that constrain the magnitude and physical origin of disk turbulence therefore promise to provide important insight into the physics of planet formation on a variety of physical and temporal scales.

The only directly observable manifestation of turbulence is the non-thermal broadening of spectral lines. To date, no lines have been detected in disks that would allow an independent determination of temperature and non-thermal broadening, similar to NH_3 in molecular cloud cores. Previous interferometric observations of molecular line emission from several disks show gas in Keplerian

rotation around the star with inferred subsonic turbulent velocity widths, close to the scale of the spectral resolution of $\sim$200 m s^{-1} (e.g. Piétu et al. 2007). Spectroscopic observations of infrared CO overtone bandhead emission originating from smaller disk radii indicate larger, approximately transonic, local line broadening that may be associated with turbulence (Carr et al. 2004), although as for CO(3-2) these observations of optically thick lines can only probe far above the midplane. In combination with the millimeter data, this may indicate variations of turbulent velocity with radius. However, this interpretation is uncertain: it is important to exercise caution when deriving information about velocity fluctuations on scales smaller than the spectral resolution of the data (as noted by, e.g., Piétu et al. 2007). The advent of a high spectral resolution mode of the Submillimeter Array (SMA) correlator, capable of resolving well below the $\sim$200 m s^{-1} linewidths in the low-J transitions of CO derived from lower-resolution observations, permits access to turbulent linewidth measurements in the cold, outer regions of molecular gas disks around young stars.

In this paper, we conduct high spectral resolution (44 m s^{-1}) observations of the CO(3-2) emission from the disks around two nearby young stars, HD 163296 and TW Hya. These systems were selected on the basis of their bright CO(3-2) line emission (e.g. Dent et al. 2005), to ensure adequate sensitivity for high-resolution spectroscopy. They are also particularly well-studied using spatially-resolved observations at millimeter wavelengths, so that excellent models of the temperature and density structure of the gas and dust disks are already available (Calvet et al. 2002; Isella et al. 2007, 2009; Hughes et al. 2008b; Qi et al. 2004, 2006, 2008, 2010 in prep). Both exhibit CO(3-2) emission that is consistent with Keplerian rotation about the central star, and neither suffers from significant cloud contamination. TW Hya is a K7 star with an age of $\sim$10 Myr (Webb et al. 1999), located at a distance of only 51 ± 4 pc (Mamajek 2005). It hosts a nearly face-on "transition" disk, with an optically thin inner cavity of radius $\sim$4 AU indicated by the SED (Calvet et al. 2002) and interferometrically resolved at wavelengths of 7 mm (Hughes et al. 2007) and 10 μm (Ratzka et al. 2007). The low spectral resolution CO(3-2) line emission from the disk around TW Hya was modeled with a 50 m s^{-1} turbulent linewidth by (Qi et al. 2004). HD 163296 is a Herbig Ae star with a mass of 2.3 $M_\odot$, located at a distance of 122 pc (van den Ancker et al. 1998b). Its massive, gas-rich disk extends to at least 500 AU (Grady et al. 2000) and is viewed at an intermediate inclination angle of 45° (Isella et al. 2007).

We describe the high spectral resolution SMA observations of the CO(3-2) line emission from TW Hya and HD 163296 in Section 8.2 and present the results

in Section 8.3 (with full channel maps provided in Appendix C). In Section 8.4 we outline the widely-used procedures that we use to model the temperature, density, and velocity structure of the disk, including the fixed parameters and assumptions about how the turbulent linewidth is spatially distributed. Section 8.4.3 presents the best-fit models, and a discussion of the degeneracies between parameters is provided in Section 8.4.4. We compare our results to theoretical predictions of the magnitude and spatial distribution of turbulence in Section 8.5, and describe the implications for planet formation. A summary is provided in Section 8.6.

8.2 Observations

The SMA observations of TW Hya took place on 2008 March 2 in the compact configuration, with baseline lengths of 16-77 m, and on 2008 February 20 during the move from compact to extended configuration, with baseline lengths of 16-182 m. The weather was good both nights, with stable atmospheric phases. Precipitable water vapor levels were extremely low on February 20, with 225 GHz atmospheric opacities less than 0.05 throughout the night, while the March 2 levels were somewhat higher, rising smoothly from 0.08 to 0.11. In order to calibrate the atmospheric and instrumental gain variations, observations of TW Hya were interleaved with the nearby quasar J1037-295. To test the efficacy of phase transfer, observations of 3c279 were also included in the observing loop. Flux calibration was carried out using observations of Callisto; the derived fluxes of 3c111 were 0.76 and 0.78 Jy on February 20 and March 2, respectively.

The observations of HD 163296 were carried out in the compact-north configuration on 2009 May 6, with baseline lengths of 16 to 139 m, and in the extended configuration on 2009 August 23, with baseline lengths of 44 to 226 m. Atmospheric phases were stable on both nights, and the 225 GHz opacities were 0.05 on May 6 and 0.10 on August 23. The observing loop included 1733-130 for gain calibration and 1924-292 for testing the phase transfer. Callisto again served as the flux calibrator, yielding derived fluxes of 1.17 and 1.30 Jy for 1733-130 on May 6 and August 23, respectively.

For all observations, the correlator was configured to divide a single 104 MHz-wide chunk of the correlator into 2048 channels. This high-resolution chunk was centered on the 345.796 GHz frequency of the CO(3-2) line, yielding a spectral resolution of 44.1 $\mathrm{m\,s^{-1}}$ across the line. Because this used up a large portion of the available correlator capacity, only 1.3 GHz of the 2 GHz bandwidth in each sideband was available for continuum observations. The bandpass response was

calibrated using extended observations of 3c273, 3c279, and Saturn for the TW Hya tracks and 3c454.3, Callisto, and 1924-292 for the HD 163296 tracks. Since the sidebands are separated by 10 GHz and the CO(3-2) line was located in the upper sideband for the HD 163296 observations and in the lower sideband for the TW Hya observations, the continuum observations are at frequencies of 340 GHz for HD 163296 and 350 GHz for TW Hya.

Routine calibration tasks were carried out using the MIR software package[1], and imaging and deconvolution were accomplished with MIRIAD. The observational parameters, including the rms noise for both the line and continuum data, are given in Table 8.1. Note that due to weather the compact observations of HD 163296 were substantially more sensitive than the extended data and so the combined data set is dominated by the compact data; the reverse is true for TW Hya.

8.3 Results

We detect CO(3-2) emission at 44 $\mathrm{m\,s^{-1}}$ resolution from both TW Hya and HD 163296 in the compact and extended configurations. Figures 8.1 and 8.2 present the line emission from HD 163296 and TW Hya, respectively. The upper left panel shows the full line profile summed within a 6" square box (neglecting emission within the range $\pm 2\sigma$), with emission detected across $\sim$50 channels for TW Hya and $\sim$200 for HD 163296. Beneath the line profiles are the spatially resolved channel maps for a subset of the data, indicated by the gray box around the line peak. In the upper right are the zeroth (contours) and first (colors) moment maps: these are the velocity-integrated intensity and intensity-weighted velocity of the emission, respectively. The line emission is regular, symmetric, and consistent with material in Keplerian rotation around the central star viewed at an inclination to our line of sight.

The peak and integrated fluxes for each of the four tracks and the combined data sets are listed in Table 8.1. Appendix C presents the full channel maps of the combined (compact and extended configuration) data set for each source.

Along with the high spectral resolution molecular line data, we obtained 340 and 350 GHz continuum observations of HD 163296 and TW Hya, respectively. The continuum data are of excellent quality, and the visibility profiles and images

[1]See http://cfa-www.harvard.edu/$\sim$cqi/mircook.html.

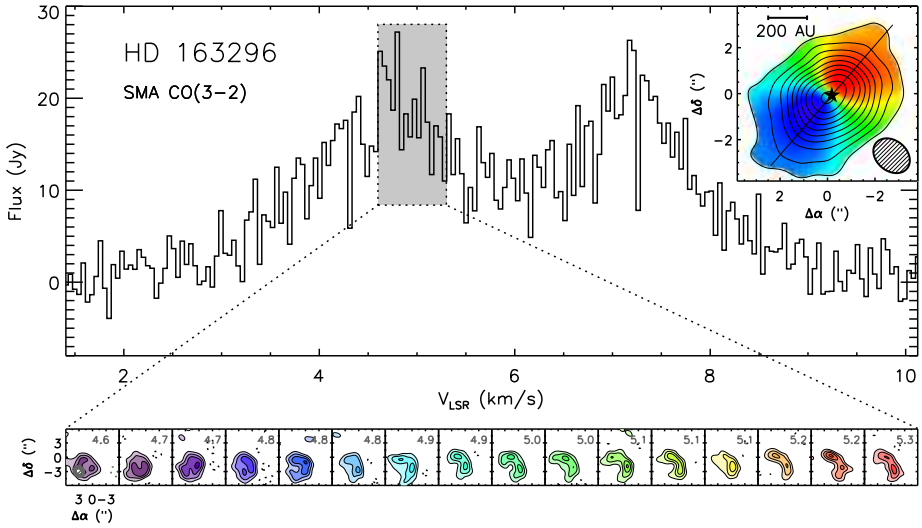

Figure 8.1.— CO(3-2) emission from the disk around HD 163296 observed with the SMA at a spectral resolution of $44\,\mathrm{m\,s^{-1}}$. Top plot shows the line profile, summed within a 6" box using the MIRIAD task `imspec` (neglecting emission with absolute values between $\pm 2\sigma$). Channel maps across the bottom show the segment of the line indicated by the shaded gray box at its full spatial and spectral resolution, imaged with a 1.″0 taper to bring out the large-scale emission (complete channel maps are provided in Appendix C). LSR velocity is indicated by the gray numbers in the upper right of each channel. Contours are $[3,6,9,...]\times 0.55\,\mathrm{Jy\,beam^{-1}}$ (the rms noise). Inset in the upper right corner shows a zeroth (contours) and first (colors) moment map of the CO(3-2) line emission, which represents the velocity-integrated intensity and intensity-weighted velocity, respectively. The $2.''0\times 1.''7$ beam is indicated in the lower right of the inset. Note that while the colors in the channel and moment maps both represent LSR velocity (blue is low; red is high), the scales are different for the two representations: the moment map contains the full line data, while the channel maps span only a subset of the line.

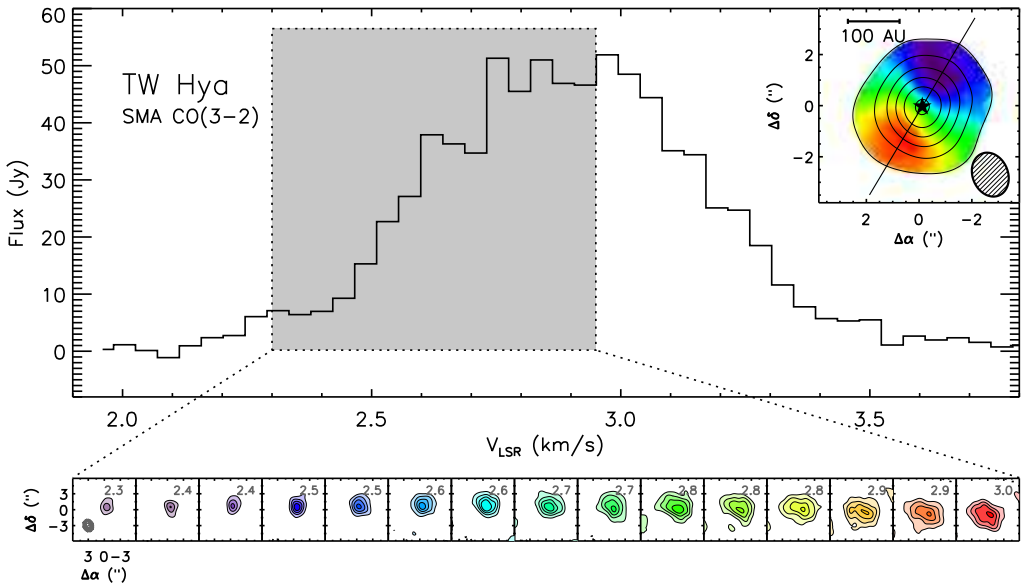

Figure 8.2.— Same as Figure 8.1 but for TW Hya. The channel maps were imaged with a 1.″2 Gaussian taper to emphasize the emission on larger scales, and the contours are [4,8,12,...]×0.55 Jy beam^{-1} (the rms noise). For the full set of channel maps, see Appendix C.

of the two sources are presented in Figure 8.3. While we do not include the continuum observations as a constraint on the models of disk structure described in Section 8.4 below (in order to avoid potential complications from differences between the gas and dust distribution), the data presented here are consistent with previous continuum observations of the sources (see, e.g., Hughes et al. 2009b).

8.4 Analysis

In order to constrain the turbulent linewidth in the disks around TW Hya and HD 163296, we fit models of the temperature, density, and velocity structure to the high spectral resolution CO(3-2) line data. For the initial modeling effort presented here, we use two well-tested physical models of disk structure: (1) power-law models of the disk temperature structure combined with tapered surface density profiles corresponding to the functional form predicted for a simple viscous accretion disk (Lynden-Bell & Pringle 1974; Hartmann et al. 1998), and (2) the 1+1D radiative transfer models first developed by D'Alessio et al. (1998)

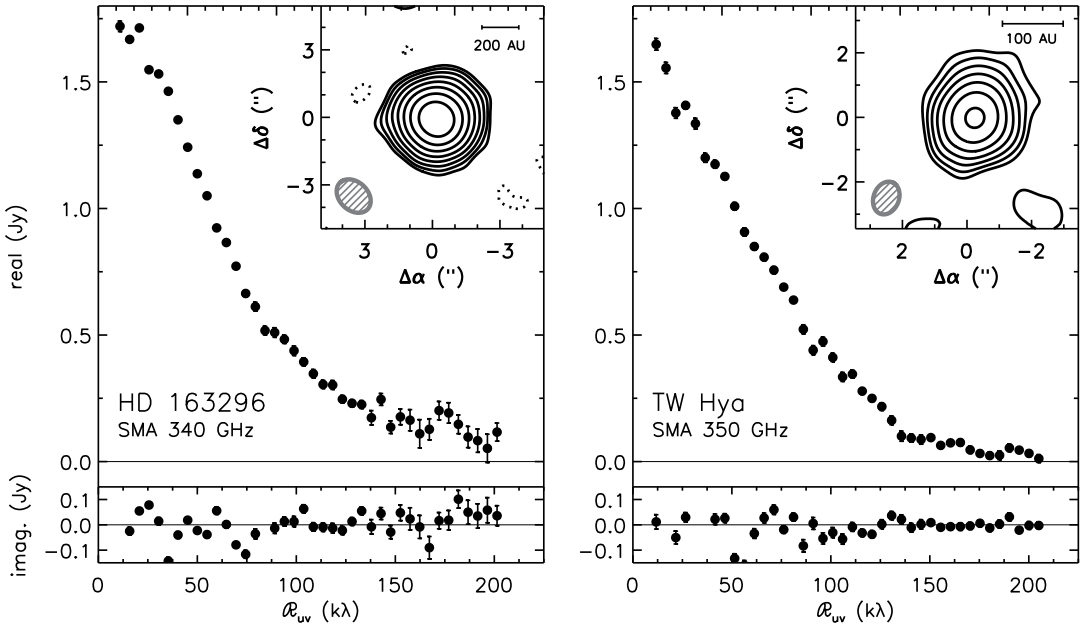

Figure 8.3.— Continuum observations of the disks around HD 163296 (*left*) and TW Hya (*right*). For each source, the real and imaginary components of the complex visibilities are plotted as a function of the deprojected distance from the disk center (for a mathematical definition of the abscissa, see Hughes et al. (2008b)). The inset shows the naturally-weighted images generated from the visibilities. Contours start at 2σ and increase by factors of $\sqrt{3}$, where σ is the rms noise for each data set (7 mJy for HD 163296 and 8.5 mJy for TW Hya). The size and orientation of the synthesized beam is indicated in the lower left of each inset and listed in Table 8.1.

to reproduce the dust emission represented in the SEDs of young systems. These models are described in more detail in Section 8.4.1.

We use these two classes of models because they are well established and have been successful in describing the observed structure of circumstellar disks across a wide range of wavelengths, particularly in the submillimeter (see, e.g., Calvet et al. 2002, 2005; Andrews et al. 2009). However, each class of models has limitations. The similarity solution models have a large number of free parameters, some with significant and severe degeneracies (see discussion in Andrews et al. 2009) . By fitting only the CO(3-2) emission, these models also neglect potential information provided by dust emission, including stronger constraints on the disk density. However, the neglect of dust emission avoids

complications due to heating processes and chemistry that affect gas differently than dust. The D'Alessio et al. (1998) models of dust emission include only stellar irradiation and viscous dissipation as heating sources, and do not take into account the additional heating processes that may affect molecular line strengths in the upper layers of circumstellar disks (Qi et al. 2006). While the constraints from the dust continuum reduce the number of free parameters in this class of models, they also have the disadvantage of an unrealistic treatment of the density structure at the disk outer edge: since they are simply truncated at a particular outer radius, they are not capable of simultaneously reproducing the extent of gas and dust emission in these systems (Hughes et al. 2008b).

The primary reason for using the two types of models, however, is that they differ substantially in their treatment of the disk temperature structures. For the D'Alessio et al. (1998) models, the temperature structure is fixed by the dust continuum. The similarity solution models, by contrast, allow the temperature to vary to best match the data. There are a few independent constraints on temperature: it should increase with height above the midplane, due to surface heating by the star and low viscous heating in the midplane, and the dust will generally not be colder than the gas, since the gas is subject to additional heating processes beyond the stellar irradiation that determines dust temperature. Both classes of models adhere to these constraints. The temperature structure in the disk is the single factor most closely tied to the derived value of the turbulent linewidth (see discussion in Section 8.4.4), which will be model-dependent. We therefore fit both classes of models to the data, in order to compare the model-dependent conclusions about turbulent linewidth for two distinct classes of models with very different treatments of gas temperature. The spatial dynamic range of the data is insufficient to investigate radial variations in turbulent linewidth. We therefore assume a global value, ξ, that will apply to size scales commensurate with the spatial resolution of the data.

8.4.1 Description of Models

D'Alessio et al. (1998) Model

While we refer to these as D'Alessio et al. (1998) models for convenience, it should be noted that they have been developed and improved upon since the original paper in a series of related work; see also D'Alessio et al. (1999, 2001, 2006). Here we provide a general outline of the model properties and discuss the particular models used in this paper.

The D'Alessio et al. (1998) models were developed to reproduce the unresolved SEDs arising from warm dust orbiting young stars, although they have also been demonstrated to be successful at reproducing spatially resolved dust continuum emission at millimeter wavelengths (see, e.g., Calvet et al. 2002; Hughes et al. 2007, 2009a) as well as spatially-resolved molecular line emission (see, e.g., Qi et al. 2004, 2006). The models include heating from the central star and viscous dissipation within the disk, although they tend to be dominated by stellar irradiation. The structure is solved iteratively to provide consistency between the irradiation heating and the vertical structure. The mass accretion rate is assumed to be constant throughout the disk. The assumed dust properties are described by Calvet et al. (2002), and the model includes provisions for changing dust properties, dust growth, and settling. We allow the outer radius of the model to vary to best reproduce the extent of the molecular line observations.

We use the structure model for TW Hya that was developed by Calvet et al. (2002) and successfully compared to molecular line emission by Qi et al. (2004, 2006). For HD 163296, we use a comparable model that reproduces the spatially unresolved SED and is designed to reproduce the integrated line strengths of several CO transitions as well as other molecules (Qi et al., in prep).

Since the D'Alessio et al. (1998) models were developed primarily to reproduce the dust emission from the SED, we are required to fit several parameters to match the observed CO(3-2) emission using the SED-based models. We fit the structural parameters $\{R_D,\ X_{\rm CO}\}$ (the disk outer radius and CO abundance, respectively), the geometrical parameters $\{i,\ {\rm PA}\}$ (the disk inclination and position angle), and the turbulent linewidth, $\{\xi\}$.

Viscous Disk Similarity Solution Models

We also fit the observations using a power-law temperature distribution and surface density profile that follows the class of similarity solutions for evolving viscous accretion disks described by Lynden-Bell & Pringle (1974) and Hartmann et al. (1998). This particular method of parameterizing circumstellar disk structure has a long history of success in reproducing observational diagnostics, although with limitations. Theoretical predictions of the power-law dependence of temperature for accretion disks around young stars were first made by Adams & Shu (1986), and power-law parameterizations of temperature and surface density have been used by many studies since then (e.g. Beckwith et al. 1990; Beckwith & Sargent 1991; Mundy et al. 1993; Dutrey et al. 1994; Lay et al. 1994; Andrews & Williams 2007). The similarity solutions are equivalent to a power-law surface

density description in the inner disk, but with an exponentially tapered outer edge, which was shown by Hughes et al. (2008b) to better reproduce the extent of gas and dust emission than traditional power-law descriptions with abruptly truncated outer edges. Recent high spatial resolution studies have used this class of models to reproduce successfully the extent of gas and dust emission in circumstellar disks from several nearby star-forming regions (e.g. Andrews et al. 2009; Isella et al. 2009).

The temperatures and surface densities of these models are parameterized as follows:

$$T(R) = T_{100} \left(\frac{R}{100\mathrm{AU}} \right)^{-q} \tag{8.1}$$

$$\Sigma(R) = \frac{c_1}{R^{\gamma}} \exp \left[- \left(\frac{R}{c_2} \right)^{2-\gamma} \right] \tag{8.2}$$

where R is the radial distance from the star in AU, T_{100} is the temperature indicated by the CO(3-2) line at 100 AU from the star, q describes how the temperature decreases with distance from the star, c_1 is a constant describing the surface density normalization, c_2 is a constant related to the radial scale on which the exponential taper decreases the disk density, and γ describes how surface density falls with radius in the inner disk regions (comparable to the parameter p in typical power-law descriptions of surface density; see e.g. Dutrey et al. 1994, for a description of the power-law model parameters). Because the high optical depth of the CO(3-2) line is a poor tracer of the radial dependence of Σ, we fix γ at a value of 1 for both systems, which is consistent with theoretical predictions for a constant-α accretion disk (Hartmann et al. 1998), as well as observations of young disks in Ophiuchus (Andrews et al. 2009) and previous studies of the continuum emission from these systems (Hughes et al. 2008b). We therefore fit the high spectral resolution CO(3-2) observations using four structural parameters, $\{T_{100}$, q, c_1, $c_2\}$, two geometric parameters, $\{i$, PA$\}$, and the turbulent linewidth, $\{\xi\}$.

8.4.2 Modeling Procedure

We assume that the disks have a Keplerian velocity field, using stellar masses and distances from the literature to model the rotation pattern ($0.6\,\mathrm{M}_{\odot}$ at 51 pc for TW Hya and $2.3\,\mathrm{M}_{\odot}$ at 122 pc for HD 163296; see Calvet et al. 2002; Webb et al. 1999; Mamajek 2005; van den Ancker et al. 1998b). Gas and dust are assumed to be well-mixed in both models; the gas-to-dust mass ratio is fixed at 100 while the CO abundance is allowed to vary in the D'Alessio et al. (1998)

models in order to reproduce the CO emission while maintaining consistency with the dust continuum emission from which the model was derived. Since we don't include continuum emission in the fits, we fix the CO abundance at 10^{-4} for the similarity solution models because there is no constraint on the relative content of gas and dust. In regions of the disk where the temperature drops below 20 K, the CO abundance is reduced by a factor of 10^{-4} to simulate the effects of freeze-out onto dust grains. We assume a global, spatially uniform value of the turbulent linewidth, which is implemented as an addition to the thermal linewidth.

In order to compare the models with the data, the systemic velocity, or central velocity of the line, must be determined. We calculated the visibility phases for the spatially integrated CO(3-2) emission and fit a line to the central few channels (45 for HD 163296; 12 for TW Hya) to determine the systemic velocity. The visibility phases encode information about the spatial symmetry of the line emission in each channel: for a Keplerian disk, it is most symmetric, and therefore the phase is zero, at line center. The channel maps are most asymmetric about disk center near the line peaks, with opposite spatial offsets at the two line peaks. The phase therefore reverses sign between one peak and the other, with an approximately linear relationship near the line center. The linear fit therefore uses the integrated emission from the central few channels to pinpoint the precise location where the phase is zero and the line is most symmetric, i.e., at the systemic velocity (it should be noted that if there were large-scale asymmetries in the CO data this method would not produce a reliable systemic velocity, but we see no evidence of such asymmetries in the data). We derive a systemic velocity of $5.79\,\mathrm{km\,s^{-1}}$ for HD 163296 and $2.86\,\mathrm{km\,s^{-1}}$ for TW Hya. In order to generate model emission with the appropriate velocity offset, we generate a model image at higher spectral resolution than the data, and then re-bin it at the appropriate velocity sampling using the MIRIAD task `regrid`.

Each disk model specifies a particular density, temperature, and velocity structure. We use the Monte-Carlo radiative transfer code RATRAN (Hogerheijde & van der Tak 2000) to calculate equilibrium populations for each rotational level of the CO molecule and generate a sky-projected image of the CO(3-2) line emission at a given viewing geometry $\{i$,PA$\}$ for each model. We compare these simulated models directly to the data in the Fourier domain. In order to sample the model images at the appropriate spatial frequencies for comparison with the SMA data, we use the MIRIAD task `uvmodel`. We then compute the χ^2 statistic for each model compared with the data using the real and imaginary simulated visibilities. Due to the high computational intensity of the molecular line radiative transfer, it is prohibitively time-intensive to generate very large and well-sampled

grids of models for the χ^2 comparison. Instead, we move from coarsely-sampled grids that cover large regions of parameter space to progressively more refined (but still small) grids to avoid landing at a local minimum. However, this has the result that the degeneracies of the parameter space are poorly characterized. A discussion of these degeneracies is included in Section 8.4.4 below.

8.4.3 Best-fit Models

The best-fit parameters for both types of models are presented in Table 8.2. Their temperature and density structures are plotted in Figure 8.6. Note that the midplane temperatures for the similarity solution models are likely much lower than indicated; the power-law temperature representation parameterizes only the radial dependence of temperature in the upper disk layers from which the optically thick CO(3-2) emission arises.

The χ^2 values for the similarity solutions are lower than for the D'Alessio et al. (1998) models; this may be due to gradients between gas and dust properties that influence the D'Alessio et al. (1998) model fit but not the similarity solution models. A sample of channel maps comparing the data with the two classes of models are presented in Figures 8.4 and 8.5. From the residuals in the D'Alessio et al. (1998) model of TW Hya, there is evidence of a mismatch in the temperature gradient between the model and the data: the residuals are systematically more positive near the disk center and negative farther from the star. For HD 163296, the difference is more subtle: the residuals are small and apparently spatially random (with the exception of some positive emission seen near a velocity of $4.7\,\mathrm{m\,s^{-1}}$ but not near the corresponding position in the mirror half of the line). It should be noted that the CO abundance derived for this source is extremely low, nearly three orders of magnitude below the standard value of 10^{-4}. The reason for this is most likely an overestimate of the temperature in the upper disk layers. In the absence of better information, this SED model was created with a very low turbulent linewidth ($\sim$$50\,\mathrm{m\,s^{-1}}$) and correspondingly little stirring of large dust grains above the midplane. The addition of a turbulent linewidth comparable to the best-fit value for the CO lines would substantially reduce settling and lower the temperature of the upper disk layers as more of the mass is placed in large dust grains. Such a model is under development by Qi et al. (in prep), and can also aid in explaining the spatial distribution of the DCO^+ emission from this disk.

One important outcome of the modeling process is the consistency in the measurement of turbulent linewidth in each source for the two types of models,

despite the differences in their treatment of temperature. In both types of models for HD 163296, the best-fit model with turbulence fits the data better than a comparable model without turbulence at the $\sim 3\sigma$ level. If the turbulent linewidth is fixed at $0\,\mathrm{m\,s^{-1}}$ in the similarity solution and the temperature allowed to vary to compensate, the parameter T_{100} must increase to 77 K; even then, the χ^2 for a model with higher temperature and no turbulence is a poorer fit than the best-fit model with turbulence at the $\sim 3\sigma$ level. The TW Hya data are consistent with no turbulent linewidth whatsoever.

8.4.4 Parameter Degeneracies

In order to better characterize our ability to measure turbulent linewidth, it is important to understand its relationship to the other parameters. The interdependence between parameters *other* than the turbulent linewidth has been explored at length in previous papers (see, e.g., discussion of similarity solution parameters in Andrews et al. 2009), so here we focus on the relationships and degeneracies specific to the turbulent linewidth. There are four main categories of line broadening in circumstellar disks that are relevant to our investigation: rotational, thermal, turbulent, and optical depth. These types of line broadening are all incorporated in detail into the ray-tracing portion of the RATRAN radiative transfer code, and will be handled appropriately for a given disk structure. The goal is to understand how to distinguish the distinct contributions of each of these different sources of line broadening and their relationships to the parameters of our disk structure models.

As discussed above, a detailed characterization of the multi-dimensional parameter space is prohibitively computationally expensive. We therefore investigate parameter relationships in two complementary ways: (1) by generating two-dimensional χ^2 plots for pairs of variables with the other parameters fixed at their best-fit values in order to identify strongly dependent parameters, and (2) using a toy model of an optically thick spectral line profile to highlight the distinct contribution of each related parameter to the observable properties.

The χ^2 plots show that for the similarity solution models, the parameters that are most strongly degenerate with the turbulent linewidth are the temperature (T_{100} and q) and inclination (i). This is unsurprising, given the obvious relationship between temperature and thermal broadening and between inclination and rotational broadening. The optically thick CO(3-2) line responds only weakly to variations in density, and the outer radius and position angle of emission should intuitively be unrelated to line broadening, hence the

Table 8.1: Observational Parameters[a]

	HD 163296			TW Hya		
	Compact-N	Extended	C+E	Compact	Extended	C+E
Parameter	2009 May 6	2009 August 23		2008 March 2	2008 February 20	
			CO(3-2) Line			
Beam Size (FWHM)	2.″1×1.″4	0.″9×0.″7	1.″7×1.″3	1.″0×0.″8	1.″0×0.″7	1.″0×0.″8
P.A.	50°	8°	47°	5°	-17°	-16°
RMS Noise (Jy beam^{-1})	0.51	0.97	0.49	0.35	0.52	0.40
Peak Flux Density (Jy beam^{-1})	8.9	3.1	8.1	4.8	4.0	4.8
Integrated Flux[b] (Jy km s^{-1})	76	14	76	19	4.8	24
	340 GHz Continuum			350 GHz Continuum		
Beam Size (FWHM)	2.″1×1.″4	0.″9×0.″7	1.″7×1.″3	3.″7×1.″9	1.″0×0.″7	1.″0×0.″8
P.A.	52°	9°	47°	-8°	-21°	-21°
RMS Noise (mJy beam^{-1})	7.0	10	7.0	16	10	8.5
Peak Flux Density (Jy beam^{-1})	1.14	0.6	1.05	1.21	0.47	0.51
Integrated Flux[c] (Jy)	1.78	1.72	1.75	1.67	1.49	1.57

[a] All quoted values assume natural weighting.

[b] The integrated line flux is calculated by integrating the zeroth moment map inside the 3σ brightness contours using the MIRIAD task `cgcurs`.

[c] The integrated continuum flux is calculated using the MIRIAD task `uvfit`, assuming an elliptical Gaussian brightness profile.

Table 8.2: Best-Fit Model Parameters

Parameter	HD 163296	TW Hya
Similarity Solution		
T_{100} (K)	60	40
q	0.5	0.4
c_1 (cm^{-2})	1.0×10^{12}	1.0×10^{11}
c_2 (AU)	150	50
ξ (m s^{-1})	300	$\lesssim 40$
i (°)	40	6.0
PA (°)	131	155
Reduced χ^2	2.642	2.106
D'Alessio et al. (1998) Model		
R_D (AU)	525	155
$X_{\rm CO}$	5×10^{-7}	1.5×10^{-5}
ξ (m s^{-1})	300	$\lesssim 40$
i (°)	40	5
PA (°)	138	155
Reduced χ^2	2.885	2.108

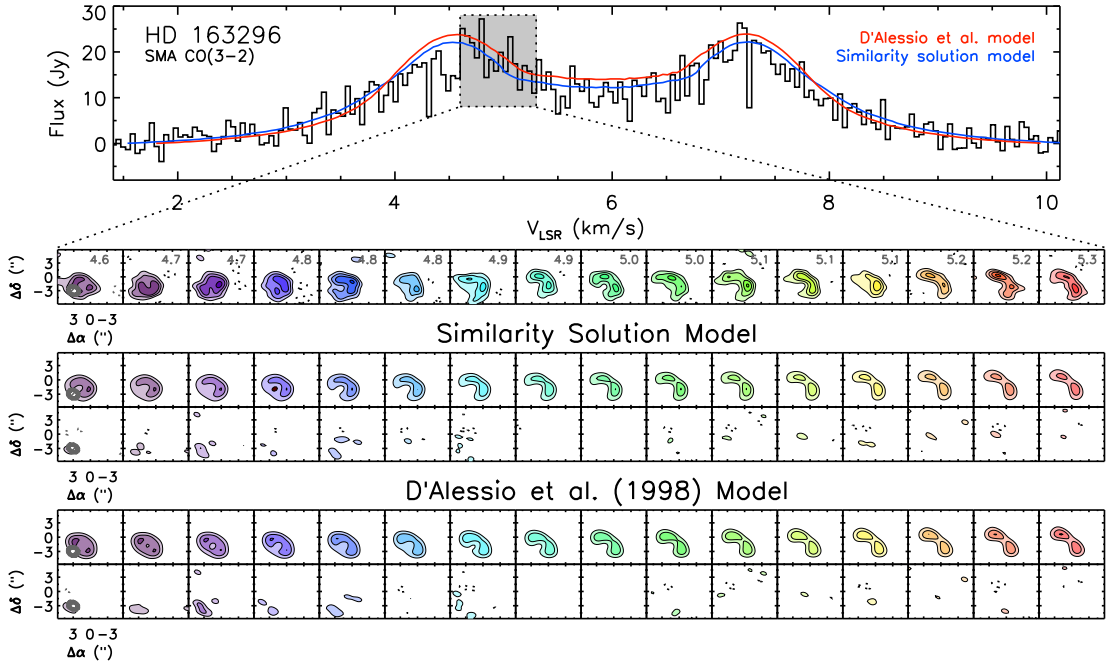

Figure 8.4.— Comparison of CO(3-2) emission from HD 163296 between the data and best-fit models for a subset of the data. The top row shows the same subset of channels as in Figure 8.1. The central set of channel maps shows the corresponding channels of the best-fit similarity solution model and the residuals (subtracted in the visibility domain). The bottom set of channel maps shows the best-fit D'Alessio et al. (1998) model and residuals. Contour levels, beam sizes, and imaging parameters are identical to those in Figure 8.1.

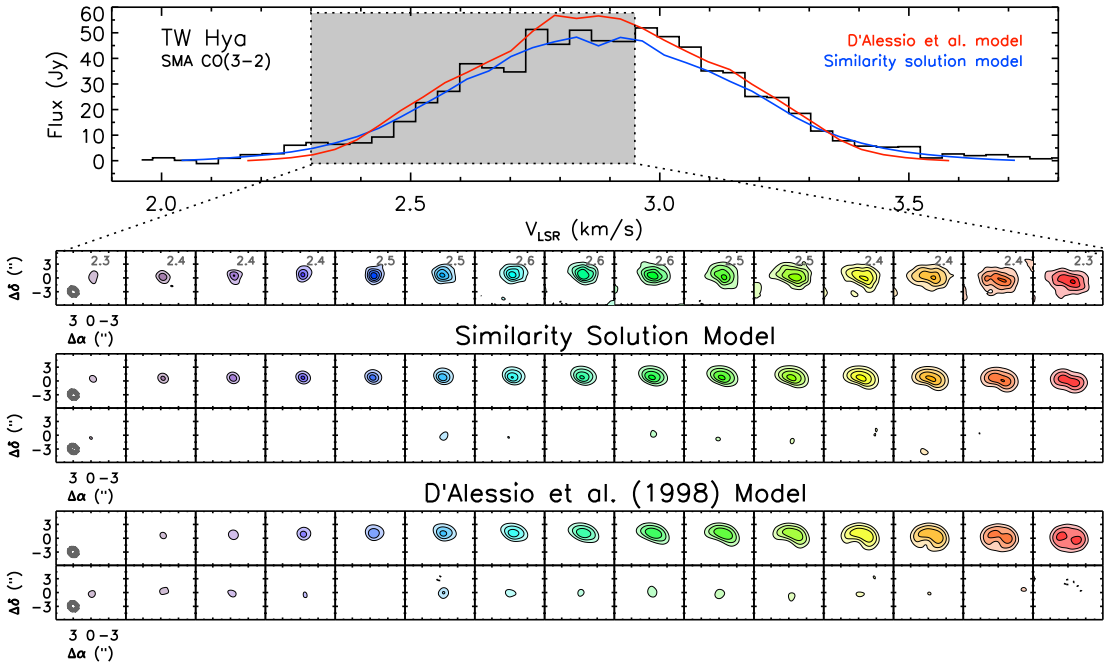

Figure 8.5.— Same as Figure 8.4 but for TW Hya. The channels, contour levels, and imaging parameters are identical to those in Figure 8.2.

independence of turbulent linewidth from c_1, c_2, and PA. For the D'Alessio et al. (1998) models, inclination and CO abundance (i and X_{CO}) have the strongest relationships with turbulent linewidth. The contribution of the CO abundance in this case can be understood as a thermal broadening effect: because of the vertical temperature gradient (see Figure 8.6), the CO abundance controls the location of the τ=1 surface and therefore the apparent temperature of the CO(3-2) line emission.

To characterize the effects of these variables on the observable properties of the CO(3-2) emission, we investigate their influence on a toy model of optically thick line emission. We assume a power-law temperature distribution for a geometrically flat, optically thick, azimuthally symmetric circumstellar disk. In the Rayleigh-Jeans approximation, the brightness of the line at a given frequency will be directly proportional to the temperature. We include two sources of line broadening, thermal and turbulent, implemented by the relationship $\Delta v(r) = \sqrt{2k_BT(r)/m + \xi^2}$, where δv is the total linewidth, ξ is the turbulent linewidth, and the thermal linewidth is $\sqrt{2k_BT/m}$ where k_B is Boltzmann's constant, T is the local temperature in the disk, and m is the average mass per particle. Rotational broadening is implicitly included in the assumed Keplerian

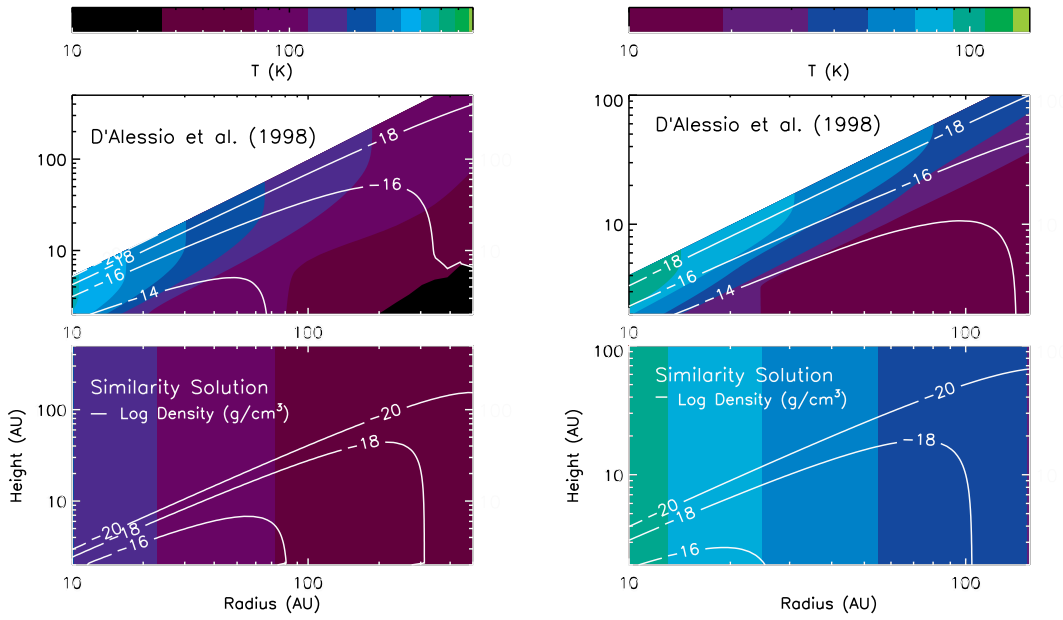

Figure 8.6.— Comparison between the temperature and density structures of the similarity solution and D'Alessio et al. (1998) models for HD 163296 (*left*) and TW Hya (*right*). The bar across the top shows the temperature scale represented by the colors, while the white contours represent density, marked with the base 10 logarithm of the total (gas+dust) mass density in units of $\mathrm{g\,cm^{-3}}$. Note that while the D'Alessio et al. (1998) model of HD 163296 appears to be two orders of magnitude more dense than the similarity solution model, the CO abundance is more than two orders of magnitude lower, making the CO mass densities comparable. The CO abundance of the TW Hya model is one order of magnitude lower than for the similarity solution. The abscissae of the plots are scaled to match the radial extent of the power-law disk model (excising the central 10 AU, which are not accessible with the data), although the similarity solution models will extend farther.

rotation pattern of the material, so that in polar coordinates, the central frequency of the line as a function of position is given by $\nu(r,\theta) = \nu_0/c\sqrt{GM_*/r}\sin i\cos\theta$, where ν_0 is the line frequency and M_* is the stellar mass. The line profile at any point in the disk is then given by

$$\phi(\nu, r) \propto \frac{T(r)}{\Delta v(r)\nu_0/c} \exp\left[\frac{-(\nu-\nu_0)^2}{(\Delta v(r)\nu_0/c)^2}\right] \tag{8.3}$$

where ν_0 is the frequency of the line center and c is the speed of light. To project the disk onto the sky, we define a radial coordinate $r_{eff} = \sqrt{(r\cos\theta)^2 + (r\sin\theta/\cos i)^2}$, with θ used as a polar coordinate so that the isophotes are elliptical, and substitute this expression for r in the line profile. We then integrate over the r and θ coordinates across the extent of the elliptical disk to calculate the line profile as a function of frequency. We investigate the contribution of the different sources of broadening by varying ξ, $T(r)$, and i to correspond to the turbulent, thermal, and rotational broadening effects. Here we discuss the ways in which turbulent broadening can be distinguished from the other two effects in the context of our toy model.

Temperature — The left panel of Figure 8.7 shows model line profiles that illustrate the relationship between broadening due to temperature and broadening due to a global turbulent linewidth. The solid line is the model line profile calculated using values from the best-fit similarity solution: T_{100}=60 K, q=0.5, and ξ=300 m s^{-1}. The dotted line represents the profile for a model with the same parameters but no turbulent linewidth. To create the dashed line profile, the temperature was varied until the peak line flux of the model without turbulence matched the peak flux of the original model with turbulence. This sequence of line profiles illustrates how thermal and turbulent broadening produce distinct effects on the observable properties of the data, rather than being fully interchangeable. Since increases in temperature increase the line flux throughout the disk while turbulence simply redistributes the flux in frequency space, turbulence tends to shift flux from the line peaks to the center, changing the shape of the line. As a result, the peak-to-center line flux ratios will be different for line profiles with comparable widths and peak fluxes, depending on the relative contributions of turbulence and temperature to line broadening. The difference between the best-fit 300 m s^{-1} turbulent linewidth in HD 163296 and a comparable model without turbulence corresponds to a 30% change in peak-to-center line flux in the context of this toy model, which should be easily distinguishable given the uncertainty of our data.

Inclination — The right panel of Figure 8.7 shows model line profiles that illustrate the relationship between turbulent broadening and rotational

broadening due to inclination. As in the left panel, we first generate a model with no turbulent broadening (dotted line), and then adjust the inclination until the peak flux matches the original line model (dashed line). In this case, the absence of turbulence once again alters the peak-to-center line ratio. But another obvious difference between the turbulent model and the more inclined model without turbulence is that rotational broadening through inclination alters the separation between the line peaks in velocity space. The sequence of toy models shows that the contribution of the $300\,\mathrm{m\,s^{-1}}$ turbulent linewidth in the HD 163296 model corresponds to a 6° change in inclination, in addition to the large depression of flux at the line center. Since spatially resolved spectra of the Keplerian rotation patterns in molecular lines allow for very precise determination of circumstellar disk inclination (to within a degree or less; see discussion in Qi et al. 2004), turbulent line broadening at the level detected in HD 163296 should be distinguishable from rotational broadening.

8.5 Discussion

8.5.1 Comparison with Theory

The problem of accurately modeling and predicting the magnitude of velocity fluctuations arising from magnetohydrodynamic (MHD) turbulence is historically fraught, but a few general features seem to be agreed upon. The difficulty hinges largely on derived values of α and how they relate to the expected magnitude of the turbulent linewidth. The dimensionless parameter α was defined by Shakura & Syunyaev (1973) to describe the effective viscosity in terms of a proportionality constant multiplied by the largest velocity and length scales on which turbulence may act: the scale height and the sound speed. In mathematical terms, $\nu_{\mathrm{eff}} = \alpha c_s H$, where ν_{eff} is the effective viscosity, c_s is the sound speed, H is the local scale height, and α is then an efficiency factor with a value $\leq$1. The magnitude of turbulent velocity fluctuations depends both on the value of α and on how this efficiency factor is apportioned between the sound speed and the scale height. If, for example, the majority of the power in turbulent fluctuations occurs at the length of the scale height, the velocity fluctuations can be as small as αc_s (perhaps augmented by a geometric factor of a few). On the other hand, if the proportionality factor α applies evenly to the length and velocity scales in the problem, the turbulent fluctuations could be as large as $\sqrt{\alpha} c_s$ (again possibly modified by a geometric factor). Since there is no evidence of shocks that would point to sonic or supersonic turbulence in circumstellar disks, it is unlikely that

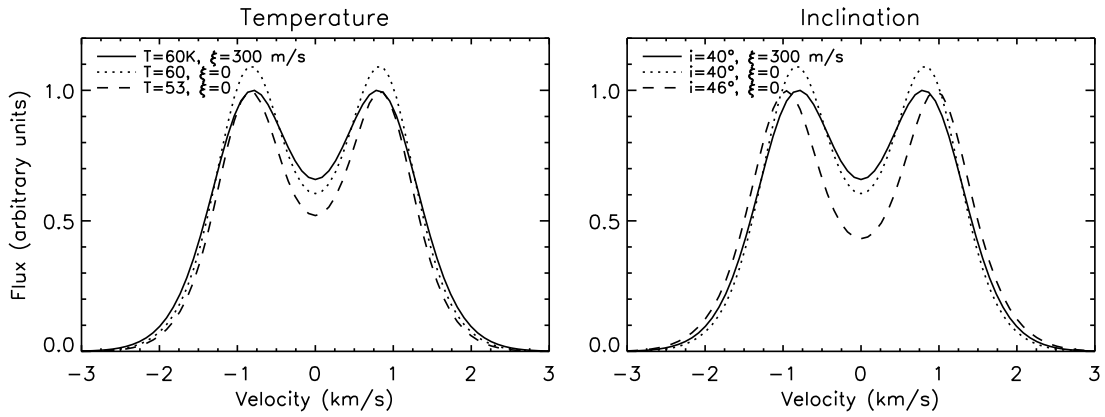

Figure 8.7.— Model spectral line profiles for a geometrically flat, optically thick, azimuthally symmetric circumstellar disk (for details, see toy model description in Section 8.4.4). The left panel explores the relationship between thermal and turbulent line broadening, while the right panel explores the relationship between turbulent broadening and rotational broadening through changes in inclination. The solid line in each panel is generated using values from the best-fit similarity solution model (T_{100}=60 K, q=0.5, and ξ=300 m s^{-1}), while the dotted lines are the same model without turbulence, and the dashed lines seek to compensate for the lack of turbulence through the alternative line broadening mechanisms, scaled so that the peak flux is the same as the original model. The parameters for each line are given in the legend. The obvious differences between the solid and dashed lines in each panel (e.g., peak-to-center flux ratios and velocity separation between peaks) illustrate how the effects of rotational and thermal broadening differ from those of turbulent broadening in the context of this toy model.

the turbulent velocity fluctuations would be much larger than $\sqrt{\alpha}c_s$.

It seems clear that shearing box simulations of MHD turbulence with zero net magnetic field flux do not give reliable values of the viscosity parameter α due to numerical dissipation, which results in values of α that depend entirely on resolution (Pessah et al. 2007; Fromang & Papaloizou 2007). This may be mitigated somewhat by the use of more realistic stratified shearing boxes (e.g., Stone et al. 1996; Fleming & Stone 2003), but the resulting dependence of α and therefore turbulent velocity fluctuations on the magnitude of the magnetic field is troublesome, since magnetic field strengths and geometries in circumstellar disks are unconstrained by observations (e.g., Hughes et al. 2009b).

Observational attempts at constraining the value of α in circumstellar disks, while generally quite uncertain, seem to cluster near values of 10^{-2}, with

large scatter (e.g., Hartmann et al. 1998; Andrews et al. 2009). If the velocity fluctuations are estimated as $\sqrt{\alpha}c_s$, this result would imply velocity fluctuations up to 10% of the sound speed near the midplane, although this global value is likely to vary widely depending on local conditions that affect the ionization fraction and the coupling of ions and neutrals. A theoretical comparison between circumstellar disks and the Taylor-Couette flow by Hersant et al. (2005) finds that the $100\,\mathrm{m\,s^{-1}}$ turbulent linewidth (of order $\lesssim$30% of the sound speed) derived from low spectral resolution observations of DM Tau by Guilloteau & Dutrey (1998) are on par with expectations from laboratory measurements by Dubrulle et al. (2005). There is some evidence, both from the study of FU Ori objects (Hartmann et al. 2004) and global MHD simulations of stratified disks (e.g. Fromang & Nelson 2006), that the turbulent linewidth may be larger at several scale heights above the midplane of the disk, perhaps up to 40% of the sound speed.

In this context, HD 163296 seems to fit in fairly seamlessly, with a turbulent linewidth of $300\,\mathrm{m\,s^{-1}}$ corresponding to about 40% of the sound speed at the size scales probed by our data (if $1\farcs5$ corresponds to $\sim$180 AU at a distance of 122 pc). The lower turbulent linewidth in TW Hya, $\lesssim$10% of the turbulent linewidth at the scale of our observations (80 AU at 51 pc), could be associated with a lower global value of α, although the reason for such a difference is unclear. Following Andrews et al. (2009), the best-fit similarity solution model parameters imply $\alpha = 0.03$ for TW Hya and 0.009 for HD 163296, although these numbers are quite uncertain given the reliance on the optically thick CO(3-2) tracer for the determination of density. The D'Alessio et al. (1998) models use $\alpha = 0.0018$ for TW Hya and 0.003 for HD 163296. Perhaps the only conclusion that should be drawn from this estimate is that our observations are consistent with estimates that place α in the range of 10^{-2}-10^{-3}. With a sample of only two sources and with a wide range of theoretical results and approaches to the study of turbulence, it can be difficult to compare our results to theoretical predictions in a detailed way. Nevertheless, the detection of a turbulent linewidth in the HD 163296 system and the upper limit on turbulence in the TW Hya system are suggestive. There are several potential explanations for this difference rooted in theoretical studies of protoplanetary disk turbulence.

Inclination and Vertical Structure — In general, the CO(3-2) line emission from these systems is expected to be optically thick, and therefore will arise from the tenuous upper disk layers several scale heights above the midplane. However, this simple picture can be complicated by geometry and velocity: the combination of inclination and rotational line broadening in HD 163296 will permit the escape

of radiation from deeper layers of the disk. As a result, a different vertical height may be probed in the HD 163296 system than in TW Hya. Naively, it would be expected that the turbulent linewidth in TW Hya should be *larger* as a result, since turbulence is predicted to become stronger farther from the midplane. But it is also possible that poor coupling of ions to neutrals in the low-density uppermost disk layers could inhibit the detection of turbulence even if it is present. This may also depend on the relative amounts of small dust grains in the upper layers of the two disks, since small grains are more adept at absorbing free electrons.

Stellar Mass and Ionizing Flux — One of the factors determining the extent of turbulent regions in circumstellar disks is the magnitude of ionizing X-ray flux from the star (e.g., Gammie 1996; Igea & Glassgold 1999). With stellar masses differing by a factor of 4, the radiation (and therefore ionization) properties of TW Hya and HD 163296 are likely to be quite different. Despite the tendency for X-ray flux to be lower for intermediate-mass than low-mass stars of comparable ages, HD 163296 has the largest X-ray flux of the sample of 13 Herbig Ae stars studied by Hubrig et al. (2009), comparable to that of lower-mass T Tauri stars. Nevertheless, its measured X-ray luminosity of $4.0 \times 10^{29}\,\mathrm{erg\,s^{-1}}$ is still lower than that of TW Hya, which is estimated as $2.0 \times 10^{30}\,\mathrm{erg\,s^{-1}}$ by Kastner et al. (1999). Given the comparable disk densities, by X-ray luminosity alone, TW Hya should be the more active disk. However, since we are observing these disks on relatively large spatial scales (∼80 AU for TW Hya and ∼180 AU for HD 163296, with 1.″5 resolution viewed from their respective 51 and 122 pc distances), the ionization at these distances may instead be dominated by cosmic rays. It is extremely difficult to determine how the cosmic ray environment of these two sources might compare; if HD 163296 were located in a region of greater cosmic ray activity, that could account for the greater turbulent linewidth observed for this system.

Evolutionary State — One of the most obvious differences between TW Hya and HD 163296 is their respective evolutionary states. TW Hya is a 10 Myr-old transition disk with an inner cavity of ∼4 AU radius, while HD 163296 is a primordial disk with an inner radius consistent with the expected ∼0.4 AU extent of the dust destruction zone (see, e.g., Isella et al. 2007). It is possible that X-ray ionization and the MRI might operate differently at different stages of evolution; one example is the inside-out MRI clearing proposed by Chiang & Murray-Clay (2007) to explain the cavities in transition disks. In their scenario, the mass accretion rate onto the star can be explained entirely by the MRI operating on the disk inner rim, and requires no resupply from the outer disk; they therefore require little to no turbulent viscosity in the outer disk to explain the observed accretion rates in transitional systems. However, they note that their theory

cannot be readily applied to primordial systems, leaving the viscous transport mechanism responsible for large accretion rates at earlier stages unexplained. There is no reason to expect MRI turbulence in the outer disk to "shut off" when a gap is opened, so while our observation of a small turbulent linewidth in the TW Hya system is consistent with the Chiang & Murray-Clay (2007) hypothesis, it is still surprising that the turbulent linewidth in HD 163296 should be so much larger.

8.5.2 Implications for Planet Formation

The presence of subsonic turbulence in protoplanetary accretion disks – likely strongly subsonic in the midplane – is consistent with the observations presented in this study. Subsonic turbulence has important implications for the formation and evolution of young planetary systems. One series of papers (Papaloizou & Nelson 2003; Papaloizou et al. 2004; Nelson & Papaloizou 2003, 2004) explores in detail the effects of turbulence on planet-forming disks. Their cylindrical models of turbulent disks have an average α in the range of 10^{-2}-10^{-3}, but they demonstrate that the realistic implementation of turbulence results in different effects than are seen in laminar disk simulations with comparable values of α incorporated as an anomalous Navier-Stokes viscosity. They show that for massive planets, turbulence can widen and deepen the gap opened by massive protoplanets, and may reduce the accretion rate onto the protoplanet. For the case of migrating low-mass planet cores, the presence of turbulence in the disk can slow or even reverse the migration rate, converting the monotonic inward motion of the planet into a random walk. The presence of dead zones in the radial direction may also act to halt migration and encourage the survival and growth of protoplanets (e.g. Matsumura et al. 2009). Another important proposed effect of subsonic turbulence is to aid in concentrating planetesimals to allow them to collapse gravitationally (Johansen et al. 2007). MHD turbulence on these scales can also reduce the strength of the gravitational instability and reduce disk fragmentation (Fromang 2005). There is also substantial literature on the effects of turbulence on dust settling and grain growth (e.g. Johansen & Klahr 2005; Carballido et al. 2006; Ciesla 2007; Balsara et al. 2009; Fromang & Nelson 2009).

Although it is difficult to compare the properties of the simulations directly with our observations, the generic features of these models (α=10^{-2}-10^{-3}, subsonic turbulence even in the upper disk layers) are globally consistent with the derived properties of turbulence in the disks around HD 163296 and TW Hya, indicating that these effects are likely to play a role in planet formation.

8.5.3 Future Directions

The most obvious improvement to our method would be to include additional spectral lines from different transitions or isotopologues of the CO molecule in order to provide independent constraints on the gas temperature. While this would necessarily introduce additional parameters into the model (i.e., to describe the vertical distribution of temperature and turbulence, as well as a consistent density distribution to properly account for the line opacity), the addition of several lines that are resolved in the spectral and spatial domains would more firmly constrain the models. It might also provide direct measurements of the vertical profile of the turbulent velocity structure. Dartois et al. (2003) and Panić et al. (2008) provide examples of studies that use multiple molecular lines to study the vertical structure of density and temperature in circumstellar disks; these techniques could be extended to constrain the turbulent linewidths in similar systems.

Another possibility is to observe ions rather than neutral species. This would eliminate complications introduced by the interaction between ions and neutrals, and would more directly probe the turbulent motions of the charged gas.

Even with the current set of observations, greater sensitivity would be extremely valuable in constraining the turbulent linewidth, since the distinctions between turbulent and thermal broadening are subtle (see Section 8.4.4). The vast improvements in sensitivity provided by the Atacama Large Millimeter Array will permit significantly better modeling of the velocity structure of young disks. In addition, higher sensitivity combined with a greater spatial dynamic range will allow for the investigation of radial variations in the turbulent linewidth.

8.6 Summary and Conclusions

We have obtained the first spatially resolved observations of molecular line emission from two nearby circumstellar disks with spectral resolution finer than the expected turbulent linewidth. We fit these high spectral resolution observations of the CO(3-2) line emission using two well-tested models of circumstellar disk structure, and derive a turbulent linewidth of $\sim$300 m s^{-1} for the disk around HD 163296 and $\lesssim$40 m s^{-1} for the disk around TW Hya. The results are consistent for the two model classes despite their different treatments of the temperature structure of the disk, which is significant since thermal broadening is closely related to turbulent broadening. The magnitude of turbulent

velocity fluctuations implied by these results – up to tens of percent of the sound speed – is broadly consistent with theoretical predictions for MRI turbulence in the upper layers of circumstellar disks, although it is unclear why the linewidth should be lower for TW Hya than for HD 163296.

These results demonstrate the potential of this method for constraining theories of the magnitude and spatial distribution of turbulence. Future observations with greater sensitivity, perhaps incorporating different molecular line species and isotopologues of the same molecule, have the potential to vastly improve our ability to characterize turbulence in these systems.

Chapter 9

Conclusions and Future Directions

We have used spatially resolved observations at millimeter wavelengths to characterize the structure and evolution of circumstellar disks during their critical planet-forming stages. Sections 9.1 and 9.2 summarize the results of the work presented in this thesis, organized according to the themes laid out in Chapter 1. In Section 9.3 we discuss likely future directions that the work will take.

9.1 Disk Dissipation

Chapters 2-5 study the structure and composition of individual disks apparently in the process of clearing their natal gas and dust. Most of the sources – with the exception of 49 Ceti – fall under the original definition of a transition disk, with a pronounced mid-IR deficit in the SED.

Chapters 2 and 3 test the paradigm that mid-IR deficits are associated with inner cavities in the dust distribution. We use millimeter-wavelength interferometry to spatially resolve the distribution of large dust grains in the system, and find that the SED-based models predict well the resolved observations. The inherent degeneracy between surface density and opacity at long wavelengths does not allow us to uniquely identify the absence of millimeter-wavelength emission with missing mass at the disk center. However, combining these observations with constraints on the inner hole properties from other wavelengths strongly suggests that the dust surface density is lower within the cavity, and that dynamical interactions with giant planets in formation are

the dominant dust clearing mechanism in these systems. The measured inner hole sizes are comparable to but slightly different from those predicted from SED modeling. Because inferred cavity sizes depend on poorly-constrained dust grain properties, which affect the inferred temperature structure of the inner disk, spatially resolved observations at long wavelengths are the more accurate diagnostic of inner hole size.

We also generate basic models of the structure and composition of two newly-identified transition disks in Corona Australis. Chapter 5 presents these models, including constraints from marginally-resolved SMA observations of the outer disks, and examines the implications of the models for the molecular gas content of the outer disk. In both cases, we find evidence for CO content significantly below that predicted using standard assumptions. This echoes the low CO abundance derived for GM Aur in Chapter 3 and for TW Hya in Qi et al. (2004). While it is unclear whether the low CO content results from a reduced gas-to-dust mass ratio or CO abundance relative to H_2, this result is suggestive of significant chemical or dynamical evolution of the gas disk in parallel with the dust disk clearing. It is unclear whether protoplanetary disks share this property; very few protoplanetary disks in the literature exhibit bright, uncontaminated CO emission with which to compare the results for these transition disks. Further study is required to understand the implications of the low CO content of the transitional systems. One of the systems studied, RX J1842.9-3532, now adds to the growing number of recently-identified "pre-transitional" objects that exhibit evidence for a band of optically thick material within their inner cavities (Espaillat et al. 2007). Given the $\sim$10 Myr ages, the inferred disk properties, and the far southern declination of Corona Australis, the systems studied in Chapter 5 will be interesting targets for follow-up with next-generation interferometers like ALMA.

49 Ceti, discussed in Chapter 4, differs markedly from the other transitional objects studied in this thesis. In fact, according to some definitions (including the original) it should not be classified as a transition disk at all. It nevertheless appears to represent a unique stage of disk evolution, with characteristics intermediate between the protoplanetary and debris disk phases. Despite dust properties consistent with those of a debris disk, it retains a substantial reservoir of molecular gas, apparently in rotation about the star. The gas-to-dust mass ratio in this system is also much lower than predicted for typical assumptions, approximately of order unity; even the CO(2-1) line is apparently optically thin throughout the disk. There is evidence for a deficit of CO emission within a distance of 40 AU from the star. The low gas mass and inner cavity in the

gas disk are strongly consistent with a photoevaporative clearing scenario. 49 Ceti therefore represents an interesting case study that argues caution in the identification and interpretation of transition disks: it is likely that several different clearing mechanisms play a role in disk dissipation, whether different mechanisms are relevant for different systems or different mechanisms come into play at different times in the life of a star. While systems like 49 Ceti appear even more rare and difficult to identify than systems with inner dust cavities in otherwise massive gas-rich disks, they evidently represent an important missing piece in the puzzle of disk dissipation.

Overall, our results are consistent with the following: (1) SED-based models of mid-IR deficits accurately predict a deficit of long-wavelength flux from the disk center, at roughly the correct size scales. (2) Molecular gas disks can persist to ages as late as $\sim$10 Myr, and several transitional systems show evidence of lower CO content than expected based on typical assumptions of gas-to-dust mass ratio and CO abundance for primordial disks. (3) Several distinct physical mechanisms likely contribute to the dissipation of gas and dust disks, and there is good evidence based on the observable properties of individual systems for photoevaporation by energetic stellar radiation and dynamical interactions with giant planets.

9.2 Protoplanetary Disks as Accretion Disks

Chapters 6-8 look for observational signatures of the viscous transport processes that drive accretion in protoplanetary disks. In particular, a sample of the brightest, largest, and best-studied nearby disks is examined for evidence of turbulence, magnetic fields, and large-scale structure reflective of ongoing viscous evolution. We focus on observable features of the most popular theoretical mechanism proposed for generating turbulent viscosity in accretion disks, the magnetorotational instability.

In Chapter 6 we use archival continuum and molecular line observations from the SMA to study the large-scale structure of four nearby objects: TW Hya, GM Aur, MWC 480, and HD 163296. We model the systems with two distinct parameterizations of surface density structure, including the widely used power-law descriptions with truncated outer edges and the theoretically motivated similarity solutions for viscous accretion disks with exponentially tapered outer edges. We show that the tapered edge of the similarity solution model resolves an apparent discrepancy between the spatial extent of gas and dust disks arising

as a result of the truncated outer edge in the ubiquitous power-law models. While we are not able to constrain independently the shape of the outer edge, the similarity solution models have the dual advantages of being grounded in the physics of accretion and providing a consistent description of both the gas and dust distribution, despite having the same number of free parameters as the power-law models. This result provides indirect evidence for the viscous evolution of circumstellar disks, and suggests that the present-day properties of disks may reflect their accretion history.

The more directly observable features of the MRI are the presence of large-scale magnetic fields and turbulence. Chapter 7 uses the SMA polarimeter to search for evidence of large-scale magnetic fields through polarized thermal emission from aligned dust grains in TW Hya and HD 163296. We place upper limits on the polarization fraction approximately an order of magnitude below the 2-3% level expected based on previous observational and theoretical studies. Appendix B adds the other objects from the Chapter 6 sample, including GM Aur, which had a tentative detection of polarization at the 2% level from Tamura et al. (1999). However, it is difficult to relate polarization fraction directly to magnetic field strength. Instead of weak magnetic fields, the low polarization fraction likely reflects the inefficient alignment of large dust grains with the magnetic field, perhaps in combination with other sources of inefficiency like magnetic field tangling or rounding of large grains.

We use the high spectral resolution capabilities of the SMA correlator to search directly for turbulence in the CO(3-2) line emission from the disks around HD 163296 and TW Hya. Chapter 8 describes the observations and the modeling procedure used to tease the turbulent linewidth from other sources of broadening. We place an upper limit on the turbulent linewidth in the disk around TW Hya and report a 3σ detection of turbulence at the $300\,\mathrm{m\,s^{-1}}$ level in the disk around HD 163296, corresponding to $\lesssim$10% and $\sim$30% of the turbulent linewidth at the spatial scales probed, respectively. While it is not clear why the linewidths should be so different for these two systems (which themselves differ in age, mass, evolutionary state, and environment), both results appear consistent with the broad range of values predicted from simulations of MRI turbulence in protoplanetary disks. This first step in characterizing observationally the properties of protoplanetary disk turbulence has many obvious extensions, including broadening the sample to search for trends by system property, using molecular line tracers of differing optical depths to trace the properties in the vertical directions, studying lines of ions that may be more sensitive to magnetic turbulence, and improving the resolution to characterize radial variations in

turbulent linewidth, including seeking observational evidence for the presence of the dead zones that are expected to extend throughout the inner disk.

On the whole, the observations described in these chapters are generally in agreement with the predicted properties of circumstellar disks undergoing viscous evolution as a result of the operation of the MRI.

9.3 Future Directions

It is impossible to contemplate the future of the types of observations presented in this thesis without considering the transformative role that ALMA and the EVLA will play, beginning only months from now. With improvements in both sensitivity and spatial resolution of an order of magnitude or more over current instruments, ALMA in particular is poised to initiate a revolution in millimeter-wavelength studies of circumstellar disks (and everything else). While it is impossible to predict the new research directions that will inevitably unfold with such extreme advances in instrumentation, we discuss here some of the ways in which the new capabilities will contribute to our understanding of circumstellar disk structure and evolution, particularly for the types of objects and questions that have been central to this thesis work.

Inside Transition Disk Cavities — ALMA's combination of sensitivity and spatial resolution will for the first time provide direct access to the gas and dust content of the inner disk. In addition to providing the first look at the amount and location of planet-forming material on the spatial scale of the inner Solar system, this will have profound implications in particular for the study of the disk clearing processes operating in transition disks. As in the Dutrey et al. (2008) result that provided spectroscopic evidence for a deficit of cold CO within the central cavity in the GM Aur disk, knowledge of the cold molecular gas content in inner disk cavities will provide a strong discriminator between theoretical clearing mechanisms for a large sample of transitional objects. This will aid in distinguishing between clearing mechanisms in transition disks, similar to the work described in Chapters 2-5. The forest of molecular lines observable with the sensitive ALMA receivers, including low optical depth tracers, will allow for chemical modeling of the gas within the cavity, and has the potential to constrain the total gas mass throughout the disk. Multiwavelength continuum observations of the inner disk with ALMA and the EVLA will constrain the dust grain size distribution within the cavity, another important discriminator between clearing mechanisms.

Planet-Disk Interactions — High-resolution continuum observations with next-generation instruments should provide direct evidence for planet formation through dynamical interactions, as well as constraints on the masses of young planets. SED modeling is insensitive to small radial gaps (rather than large inner holes) as well as azimuthal asymmetries in the dust distribution, both of which should be accessible to the combination of sensitivity and resolution available with ALMA. If giant planets are indeed responsible for clearing the inner cavities in transition disks, their dynamical signatures may be imprinted in particular on the wall at the inner edge of the outer disk. One particularly exciting prediction is that the accretion luminosity of the planet itself may be observable for the closest and most favorably oriented systems, by pushing ALMA to its limits in sensitivity and resolution (Wolf & D'Angelo 2005).

Molecular Lines — Some of the unexpected questions raised by this thesis are: what is the molecular gas content of protoplanetary and transition disks, and why does it appear to differ from standard expectations? Are protoplanetary disks different from transition disks in this way? Why is it that (nearly) all of the bright molecular gas disks seem to be transition disks? Next-generation instruments will provide the capability to carry out detailed studies of the chemistry and kinematics of disks using molecular line observations, including rare tracers that will be less sensitive to cloud contamination and will permit the study of the gas properties of embedded disks. In general, a more sophisticated understanding of disk chemistry will permit improved characterization of the gas content of circumstellar disks. One exciting possibility in the study of disk dynamics is that the type of high spectral resolution observations described in Chapter 8 can be extended to few-AU-scale linear resolution, potentially revealing the signature of a dead zone. This could provide some of the best evidence yet for the dominant role of the MRI in protoplanetary disks. Combining sensitive spectral line surveys with high spatial resolution can also yield detailed information about the temperature, density, and kinematics as a function of height above the disk midplane (extending the work of Dartois et al. 2003; Panić et al. 2008, as well as that described in Chapter 8).

Polarimetry — While it is unclear how much more sensitive the new instruments will be to polarized emission at millimeter wavelengths, it will be valuable to survey large samples spanning evolutionary stages, stellar and disk masses, and environments, to determine whether and how the polarization fraction differs between objects. The increase in resolution will also be important, as turbulent motions are expected to take place on scales no larger than the scale height; resolving below this linear scale is therefore desirable and should help

to answer the question of how much of the low polarization fraction is due to field tangling. The sensitivity to molecular line polarization provided by ALMA will also provide access to tracers of various optical depth through the disks, which could have profound effects on the diagnostic value of line observations for unraveling magnetic field structure (e.g., Goldreich & Kylafis 1981, 1982).

The capabilities of next-generation instruments promise to open exciting new research directions in all of the lines of study discussed in this thesis. The observations and analysis described here are beginning to pave the way towards answering some of the fundamental questions in planet formation: the physics driving the evolution and dissipation of gas and dust disks, the role that planet-disk interactions play in shaping systems, and the bridge between the properties of natal disks and the architectures of planetary systems.

Appendix A

Protoplanetary Disk Visibility Functions

We analyze a simplified disk model parameterized by power law distributions in surface density and temperature and including a central hole, to illustrate how the model parameters affect the shape of the visibility function. We also discuss the visibility function of a model consisting of a thin ring. For both cases, we provide analytical expressions for calculating the position of the null in the (deprojected) visibility function, which is an easily observed feature.

A.1 Power-Law Disk with a Central Hole

For a flat, optically thin disk described by power-law distributions in temperature and surface density, assumed to be radiating in the Rayleigh-Jeans limit and viewed face-on, the intensity of radiation as a function of radial angular scale θ from the center of the disk is

$$I_\nu(\theta) = \frac{2\nu^2 k_B \kappa_\nu}{c^2} T_0 \left(\frac{\theta}{\theta_0}\right)^{-q} \Sigma_0 \left(\frac{\theta}{\theta_0}\right)^{-p} \tag{A.1}$$

The visibility as a function of (u,v) distance, $\mathcal{R}$, is given by the Fourier transform of the intensity:

$$V(\mathcal{R}) = \frac{4\pi\nu^2 k_B \kappa_\nu T_0 \Sigma_0 \theta_0^{p+q}}{c^2} \int_{\theta_a}^{\theta_b} \theta^{1-(p+q)} J_0(2\pi\theta\mathcal{R}) d\theta \tag{A.2}$$

where J_0 is a zeroeth order Bessel function. The integral term in the above expression can be evaluated as

$$\int_{\theta_a}^{\theta_b} \theta^{1-(p+q)} J_0(2\pi\theta\mathcal{R})d\theta = \frac{\theta_b^{2-(p+q)}\Gamma\left(1-\frac{p+q}{2}\right)}{2\left(\theta_b-\theta_a\right)}\left[f(\theta_b)-f(\theta_a)\right] \equiv \mathcal{F}(\theta_b)-\mathcal{F}(\theta_a) \quad \text{(A.3)}$$

where

$$f(\theta) = \frac{1}{\Gamma\left(2-\frac{p+q}{2}\right)}\ {}_1F_2\left[\{1-\frac{p+q}{2}\},\{1,2-\frac{p+q}{2}\},-\pi^2\mathcal{R}^2\theta^2\right] \quad \text{(A.4)}$$

and ${}_xF_y(\mathbf{a},\mathbf{b},z)$ is a generalized hypergeometric function of one variable. For a disk with an inner hole, the limits of integration θ_a and θ_b are the inner and outer angular radii of the disk, respectively.

For characterizing the visibility function on angular scales $\frac{1}{\mathcal{R}}$ between θ_a and θ_b, we can make the approximation $\mathcal{R}^2\theta_a^2 \ll 1$ and $\mathcal{R}^2\theta_b^2 \gg 1$. In these limits, the hypergeometric function attains manageable analytic forms.

For $z \ll 1$, appropriate for the inner disk of radius θ_a, the function ${}_xF_y(\mathbf{a},\mathbf{b},z)$ has the following series expansion:

$$\lim_{z\to 0}\ {}_xF_y(\mathbf{a},\mathbf{b},z) = \sum_{k=0}^{\infty}\frac{\prod_{i=1}^{x}PH(a_i,k)}{\prod_{j=1}^{y}PH(b_j,k)}\frac{z^k}{k!}$$
$$PH(c,k) = (c+k)!/c! \quad \text{(A.5)}$$

and in this limit the quantity $\mathcal{F}$ goes to

$$\mathcal{F}(\theta_a) = \frac{\theta_a^{2-(p+q)}}{2-(p+q)}\lim_{\mathcal{R}\theta_a\to 0}\ {}_1F_2\left[\{1-\frac{p+q}{2}\},\{1,2-\frac{p+q}{2}\},-\pi^2\mathcal{R}^2\theta_a^2\right] \quad \text{(A.6)}$$

with the limit approximated by the sum in A.5 above.

In the limit of $z \gg 1$, appropriate for the outer radius $\mathcal{R}^2\theta_b^2$, the quantity $\mathcal{F}$ approaches the analytical form

$$\lim_{\mathcal{R}\theta_b\to\infty}\ \mathcal{F}(\theta_b) = \frac{|\pi\mathcal{R}\theta_b|^{p+q-2}\Gamma(2-\frac{p+q}{2})}{\Gamma(\frac{p+q}{2})} \quad \text{(A.7)}$$

The total visibility function (A.2, with integral A.3) is then the difference between a smooth power-law disk without a hole ($\mathcal{F}(\theta_b)$, equation A.7) and the contribution of the evacuated inner region ($\mathcal{F}(\theta_a)$, equation A.6 with limit A.5).

A.1.1 Position of the Null

For a disk with an inner hole, the position of a null in the visibility function is an easily observed quantity. Here we show how the angular scale of the first null depends on the disk model parameters. Substituting expansion A.5 and equation A.7 into A.3 and setting the result equal to zero, we obtain the following expression which can be solved for the position of the first null:

$$\frac{\Gamma\left(1-\frac{p+q}{2}\right)\left(1-\frac{p+q}{2}\right)}{\Gamma\left(\frac{p+q}{2}\right)} = (\pi\mathcal{R}_{null}\theta_a)^{2-(p+q)}\left(1-\frac{2-(p+q)}{4-(p+q)}\pi^2\mathcal{R}_{null}^2\theta_a^2+\cdots\right) \quad \text{(A.8)}$$

Since $\mathcal{R}$ and θ_a always appear in tandem in this expression, $\mathcal{R}_{null} \propto \frac{1}{\theta_a}$.

The dependence of the null position on the power law indices p and q is illustrated in Figure A.1, which shows the null position as a function of $p+q$ for a fixed inner disk radius. Several orders of the power series expansion (A.5) are shown. For typical values of the power law indices, the null position shifts monotonically to longer baselines as $p+q$ increases, exhibiting an essentially linear relationship in the vicinity of $p+q$=2. As $p+q$ increases, the temperature and surface density distributions (and therefore the intensity) become more sharply centrally peaked, and so the position of the null, which is effectively the angular scale on which the inner disk contribution to the visibility equals that of the outer disk, moves to smaller and smaller angular scales (i.e., larger $\mathcal{R}$).

These approximations begin to lose validity longwards of the vicinity of the first null, which occurs at $\mathcal{R}\theta_a < 0.3$ for all $p+q < 3$. The series expansion quickly diverges past $\mathcal{R}\theta_a = 1$. However, it should be also noted that this constraint places no limit on the size of the hole that can be investigated by this method, i.e., for any disk with a central hole there will always be at least one null shortward of $\mathcal{R}\theta_a$=1, and so this method is robust for any case in which θ_b is large compared to θ_a. It is also valid for an inclined (symmetric) disk, as long as the deprojection is handled appropriately, as in §2.3.2.

For ease of use, it is possible to approximate the $(p+q)$ dependence by a linear fit of the curve in the region $1 \le p+q \le 3$, which results in the following formula for the position of the null, good to within 4%:

$$\mathcal{R}_{null}(k\lambda) = \left(\frac{1\ AU}{R_{hole}}\right)\left(\frac{D_{source}}{100\ pc}\right)[2618 + 1059 \times (p+q)] \quad \text{(A.9)}$$

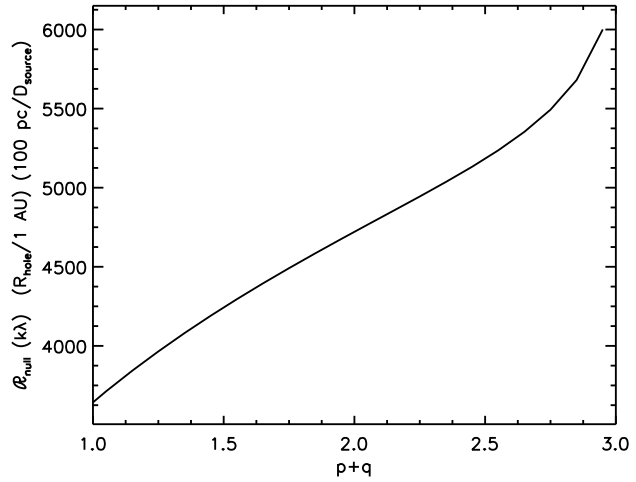

Figure A.1.— The dependence of $\mathcal{R}$ on disk temperature and surface density power law indices $(p+q)$, source distance (D_{source}), and inner hole size (R_{hole}).

A.2 Thin Wall

A thin wall ($\Delta R \ll$ R) can be described by a ring of constant brightness at a distance R_{hole} from the star, with a visibility function which is a zeroeth order Bessel function:

$$\begin{aligned} V(\mathcal{R}) &= 2\pi \int_0^\infty I_\nu(\theta) J_0(2\pi\theta\mathcal{R})\theta d\theta \\ &= 2\pi\theta_{hole} I_{wall} J_0(2\pi\theta_{hole}\mathcal{R}) \end{aligned} \tag{A.10}$$

where θ_{hole} is the angular radius of the hole and I_{wall} is the intensity of emission from the wall. The position of the null in the visibility function of a thin wall will then be

$$\mathcal{R}_{null}(k\lambda) = \frac{77916}{\pi^2} \left(\frac{D_{source}}{100\ pc}\right) \left(\frac{1\ AU}{R_{hole}}\right) \tag{A.11}$$

A.3 Application to TW Hya

The TW Hya disk has an outer radius of 196 AU (CO emission, Qi et al. (2004)) and an inner hole with radius 4 AU (SED models, Calvet et al. (2002); imaging, this paper). These size scales correspond to (u,v) distances of 54 k$\lambda \leq \mathcal{R} \leq$ 2600 kλ, a range well matched to the coverage of the Very Large Array 7 millimeter observations, and we may apply the method of §A.1 to generate the visibility

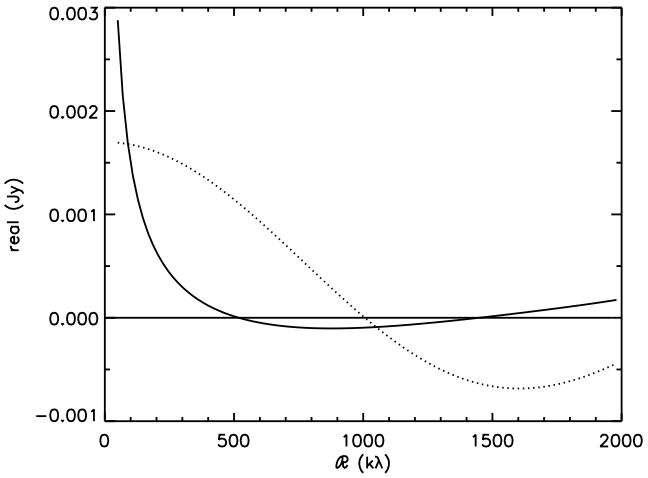

Figure A.2.— The visibility function for the TW Hya disk, based on the power-law model with an inner hole in which expansion A.5 is carried to third order (solid line). The visibility function for a thin ring interior to the inner disk edge is also shown (dotted line; see equation A.10).

function based on the simple power-law disk model. Approximating the Calvet et al. (2002) model with power laws in surface density and temperature yields the profile $T(R) = T_{100}\,(R/100\ AU)^{-q}$ and $\Sigma(R) = \Sigma_{100}\,(R/100\ AU)^{-p}$ where T_{100}= 28 K, q=0.44, Σ_{100}=3.7$g\ cm^{-2}$, and p=0.90 For the dust opacity, we adopt a power-law distribution with $\kappa_\nu = \kappa_0\,(\nu/\nu_0)^\beta$, where $\kappa_0 = 1.8 cm^2\ g^{-1}$, $\nu_0 = 1.0 \times 10^{12}$Hz, and $\beta = 0.8$ (D'Alessio et al. 2001). Figure A.2 shows the visibility function calculated according to equation A.2 with the limits as in equations A.5 and A.7, expanding to third order in $(\mathcal{R}\theta_a)^2$. The resulting curve agrees well with the visibility function derived for the power law disk model obtained with the full radiative transfer calculation, shown in Figure 7.1 (light solid line). Figure A.2 also shows the visibility function of a thin ring interior to the disk (dotted line), as in §A.2, with radius 4 AU and flux 1.7 mJy.

Appendix B

Supplementary Disk Polarimetry

We present polarimetric observations of two additional systems not discussed in Chapter 7: GM Aurigae and MWC 480. These systems were selected on the basis of their 880 μm brightness and also, in the case of GM Aur, because of the tentative detection of polarized 850 μm emission reported by Tamura et al. (1999). Here we report on the arcsecond-scale SMA observations of these systems, which yield upper limits on the polarization fraction comparable to those reported for HD 163296 and TW Hya in Chapter 7. By doubling the sample size of circumstellar disks observed with the SMA polarimeter, we strengthen our conclusion that the polarization fraction of disks is substantially lower than the 2-3% expected based on the results of Tamura et al. (1999) and Cho & Lazarian (2007).

B.1 Observations

We conducted observations of GM Aur with the SMA polarimeter on the night of 2009 November 6. The array was in the compact-north configuration, with baseline lengths between 16 and 123 m and the longest baselines along the north-south direction. The weather was good, with the 225 GHz opacity at around 0.07 and the atmospheric phase remaining steady over the course of the night. MWC 480 was observed on the night of 2009 December 11 in similarly good weather with stable phase and 225 GHz opacity of 0.06. The array was in the compact configuration for the MWC 480 observations, with baseline lengths between 16 and 77 m.

The data were collected with the receivers tuned to a frequency of 341 GHz.

These observations differ from those described in Chapter 7 in that a new double-bandwidth observing mode was introduced on the SMA in the intervening period. Effectively, this doubles the bandwidth of each sideband from 2 GHz to 4 GHz, increasing the sensitivity of the continuum observations by a factor of slightly less than $\sqrt{2}$ (due to lower sensitivity in the upper 2 GHz of each sideband). We use a uniform correlator configuration that divides each 104 MHz-wide correlator chunk into 128 channels to achieve maximum continuum sensitivity at the highest possible uniform spectral resolution ($0.7\,\mathrm{km\,s^{-1}}$).

For both sources, the quasar 3c111 served as the atmospheric and instrumental gain calibrator, while J0510+180 was included in the observing loop to test the quality of the phase transfer. Callisto was observed near the beginning of each track to determine the absolute flux scale, and Titan was also included at the end of the MWC 480 track; we derive fluxes of 1.09 and 1.52 Jy for 3c111 on the nights of November 6 and December 11, respectively. The instrumental polarization calibration was carried out as described in Chapter 7, by observing 3c273 and 3c279 in the hours before and after transit. We derive consistent instrumental leakage solutions for both sources, and adopt the solutions from the brighter 3c273. 3c111, J0510+180, Callisto, 3c273, and 3c279 were used as passband calibrators. The passband, gain, and instrumental polarization calibrations were carried out independently for each 2 GHz segment of each sideband.

The data were edited and calibrated with the MIR software package, and the standard tasks of inversion and beam deconvolution were carried out using the `MIRIAD` software package.

B.2 Results and Analysis

We detect no polarized CO(3-2) line or continuum emission from the disks around GM Aur and MWC 480. The measured Stokes I fluxes and Stokes Q & U upper limits are listed in Table B.1. The same table notes apply as in Table 7.1.

As in Chapter 7, we generate initial models of the disk temperature and surface density structure that allow us to reproduce the Stokes I continuum data. We then use these models as inputs to the Cho & Lazarian (2007) code to predict the magnitude of polarized flux that should be observed in Stokes Q and U. Table B.2 gives the model parameters with references. Figures B.1 and B.2 show a comparison between the data and the polarization properties predicted by the Cho & Lazarian (2007) code for GM Aur and MWC 480, respectively. The

Table B.1: Observational Parameters

	GM Aur Com-N	MWC 480 Compact
341 GHz Continuum		
Beam Size (FWHM)	$2\farcs0\times1\farcs3$	$2\farcs6\times2\farcs1$
P.A.	56°	12°
RMS Noise ($\mathrm{mJy\,beam^{-1}}$)		
Stokes I	12	13
Stokes Q & U	2.8	3.1
Peak Flux Density ($\mathrm{mJy\,beam^{-1}}$)		
Stokes I	360	880
Stokes Q & U (3σ upper limit)	$\leq$8	$\leq$9
Integrated Flux (Stokes I; Jy)	0.53	0.95
CO(3-2) Line		
Beam Size (FWHM)	$2\farcs1\times1\farcs3$	$2\farcs5\times2\farcs2$
P.A.	75°	35°
RMS Noise ($\mathrm{Jy\,beam^{-1}}$)		
Stokes I	0.17	0.28
Stokes Q & U	0.17	0.23
Peak Flux Density ($\mathrm{Jy\,beam^{-1}}$)		
Stokes I	4.6	5.4
Stokes Q & U (3σ upper limit)	$\leq$0.5	$\leq$0.7
Integrated Flux (Stokes I; $\mathrm{Jy\,km\,s^{-1}}$)	49	23

Table B.2: Model Parameters

	GM Aur		MWC 480	
Parameter	Value	Ref.	Value	Ref.
T_* (K)	4000	1	8460	2
R_* ($R_\odot$)	1.7	1	1.6	2
M_* ($M_\odot$)	0.84	3	1.65	4
p	1.1	5	1.0	6
$a_{\rm inner}$ (AU)	20	5	0.1[a]	–
a_0 (AU)	300	5	275	6
$r_{\rm max,i}$ (μm)	10^3	5	10^3	6
i	56°	3	37°	7
d (pc)	140	8	140	8
Σ_0 (g cm^{-2})	175	–	275	–

[a]Estimated dust destruction radius

References. — (1) Beckwith et al. (1990); (2) Kenyon & Hartmann (1995); (3) Dutrey et al. (1998); (4) Simon et al. (2000); (5) Hughes et al. (2009a); (6) Hughes et al. (2008b); (7) Hamidouche et al. (2006); (8) Elias (1978)

symbols are as in Figure 7.2. Just as for the HD 163296 and TW Hya systems, the theory substantially overpredicts the upper limit on the polarized flux. While we would expect to detect polarized emission at the 7 and 5σ levels for GM Aur and MWC 480, respectively, we detect no polarized 880 μm emission from either system.

B.3 Discussion and Conclusions

The non-detection of polarized continuum emission from the disks around GM Aurigae and MWC 480 supports the conclusions reached in Chapter 7. The upper limits for these systems are less significant than those for HD 163296 and TW Hya, largely due to the fainter Stokes I continuum emission from GM Aur and MWC 480, which means that observations comparably sensitive in flux are less sensitive in percentage of unpolarized light. Nevertheless, the 2-3% polarization fraction indicated by the work of Cho & Lazarian (2007) and Tamura et al. (1999) is ruled out at the 5 and 7σ level by these observations, strengthening

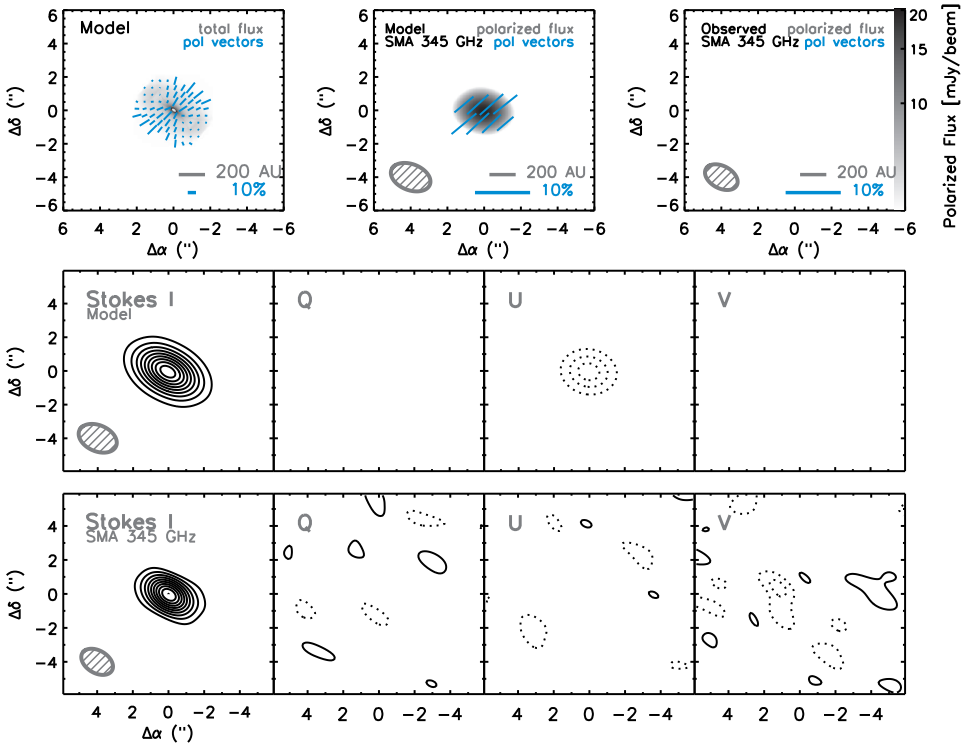

Figure B.1.— Comparison between the Cho & Lazarian (2007) model and the SMA 341 GHz observations of GM Aur. The top row shows the prediction for the model at full resolution (left), a simulated observation of the model with the SMA (center), and the SMA observations (right). The grayscale shows either the total flux (left) or the polarized flux (center, right), and the blue vectors indicate the percentage and direction of polarized flux at half-beam intervals. The center and bottom rows compare the model prediction (center) with the observed SMA data (bottom) in each of the four Stokes parameters (I, Q, U, V, from left to right). Contour levels are the same in both rows, either multiples of 20% of the peak flux (0.34 Jy/beam) in Stokes I or in increments of 2σ for Q, U, and V, where σ is the rms noise of 2.8 mJy/beam. The size and orientation of the synthesized beam is indicated in the lower left of each panel.

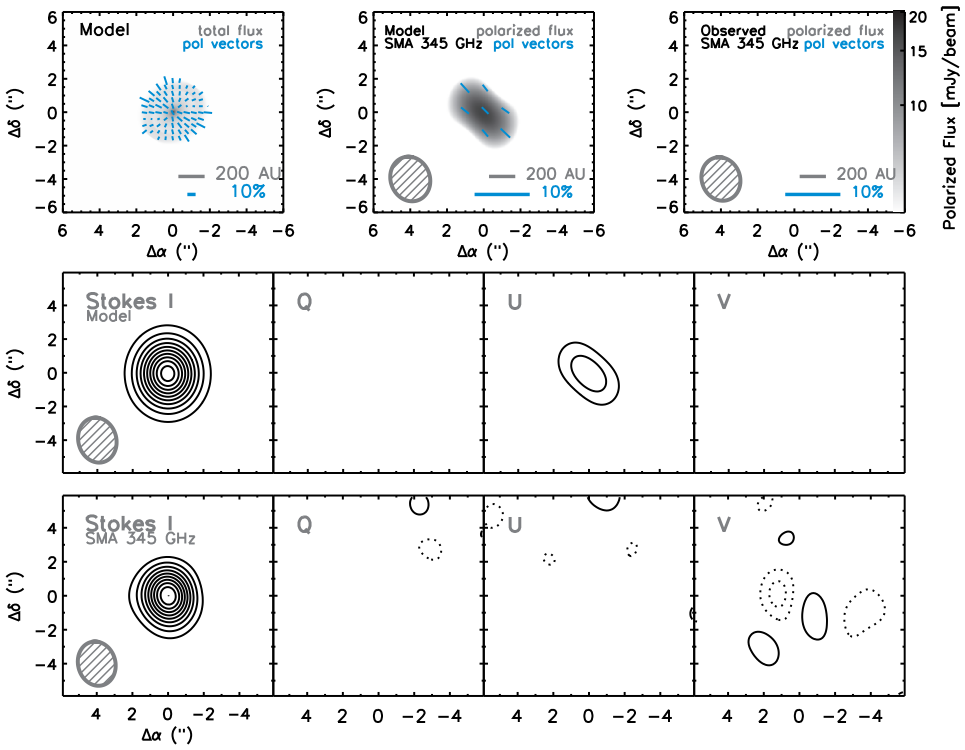

Figure B.2.— Same as Figure B.1, but for MWC 480. The Stokes I contours are multiples of 10% of the peak flux (0.87 Jy/beam), while the Stokes Q, U, and V contours are in increments of 2σ, where σ is the rms noise of 3.1 mJy/beam.

the implication that a lower polarization fraction is common to circumstellar disks.

The observations of GM Aur are particularly interesting in light of the Tamura et al. (1999) results. They report a $(3.3 \pm 1.3)\%$ polarization fraction based on observations of GM Aur with the single-dish James Clerk Maxwell Telescope (JCMT) at a wavelength of $850\,\mu$m, oriented at a position angle consistent with that of the disk minor axis. Although the formal significance of this detection is low (2.5σ), they note that the alignment of the polarization vector with the disk geometry is suggestive. Given the stringent upper limit reported here, there are two possibilities to explain the discrepancy between the SMA and JCMT results: (1) the emission arises from an extended remnant envelope that is picked up by the 14" JCMT beam but spatially filtered by the SMA so as to be undetectable, or (2) the 2.5σ result is a spurious detection. Either way, it is unlikely that significant polarized emission is generated by the disk. This effectively removes the observational justification for expecting a 2-3% polarization fraction in circumstellar disks; the follow-up work to the Cho &

Lazarian (2007) result (Lazarian & Hoang 2007; Hoang & Lazarian 2009) weakens the theoretical justification by predicting a smaller alignment efficiency for large grains than that assumed in the original analysis (see Section 7.4.2).

Based on the increased sample size of disks exhibiting low 880 μm polarization fractions, as well as the non-detection of polarized emission at predicted levels from GM Aur, we conclude that a low polarization fraction ($\lesssim$0.5%) is likely common to circumstellar disks.

Appendix C

High Spectral Resolution Channel Maps

Figures C.1 and C.2 show the full channel maps for the high spectral resolution observations of the CO(3-2) emission from the disks around TW Hya and HD 163296. The line overlaid on the emission indicates the disk major axis. The TW Hya and HD 163296 maps have been imaged with Gaussian tapers of 1.″2 and 1.″0, respectively, to bring out the large-scale emission.

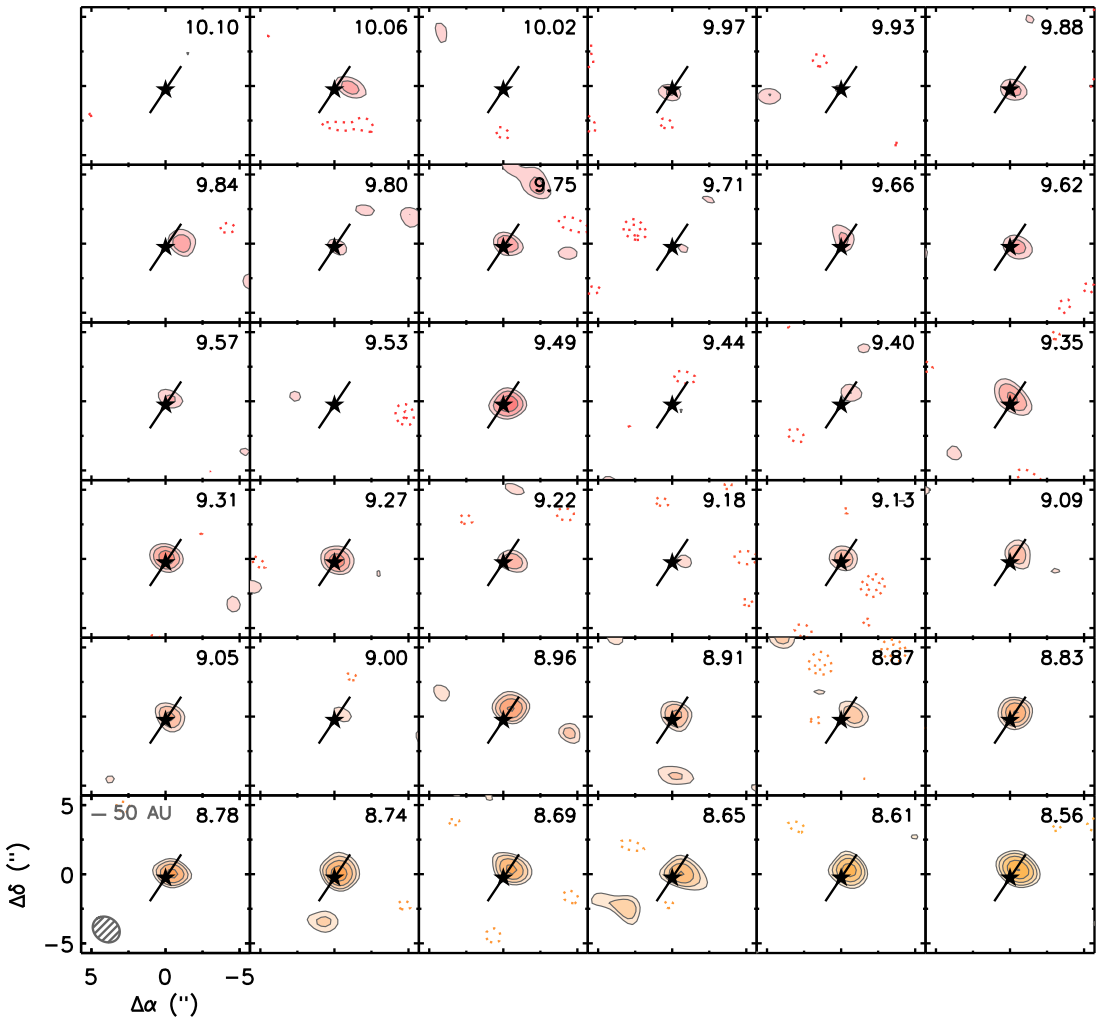

Figure C.1.— Channel maps of the CO(3-2) line emission from the disk around HD 163296. The LSR velocity is indicated in the upper right of each channel, while the synthesized beam size and orientation ($2\farcs0 \times 1\farcs7$ at a position angle of 41°) is indicated in the lower left panel. The contour levels start at 2σ and increase by factors of $\sqrt{2}$, where σ is the rms noise of 0.6 Jy beam^{-1}. The star symbol indicates the disk center while the dark solid line indicates the disk position angle as determined by CO fitting in Section 8.4.

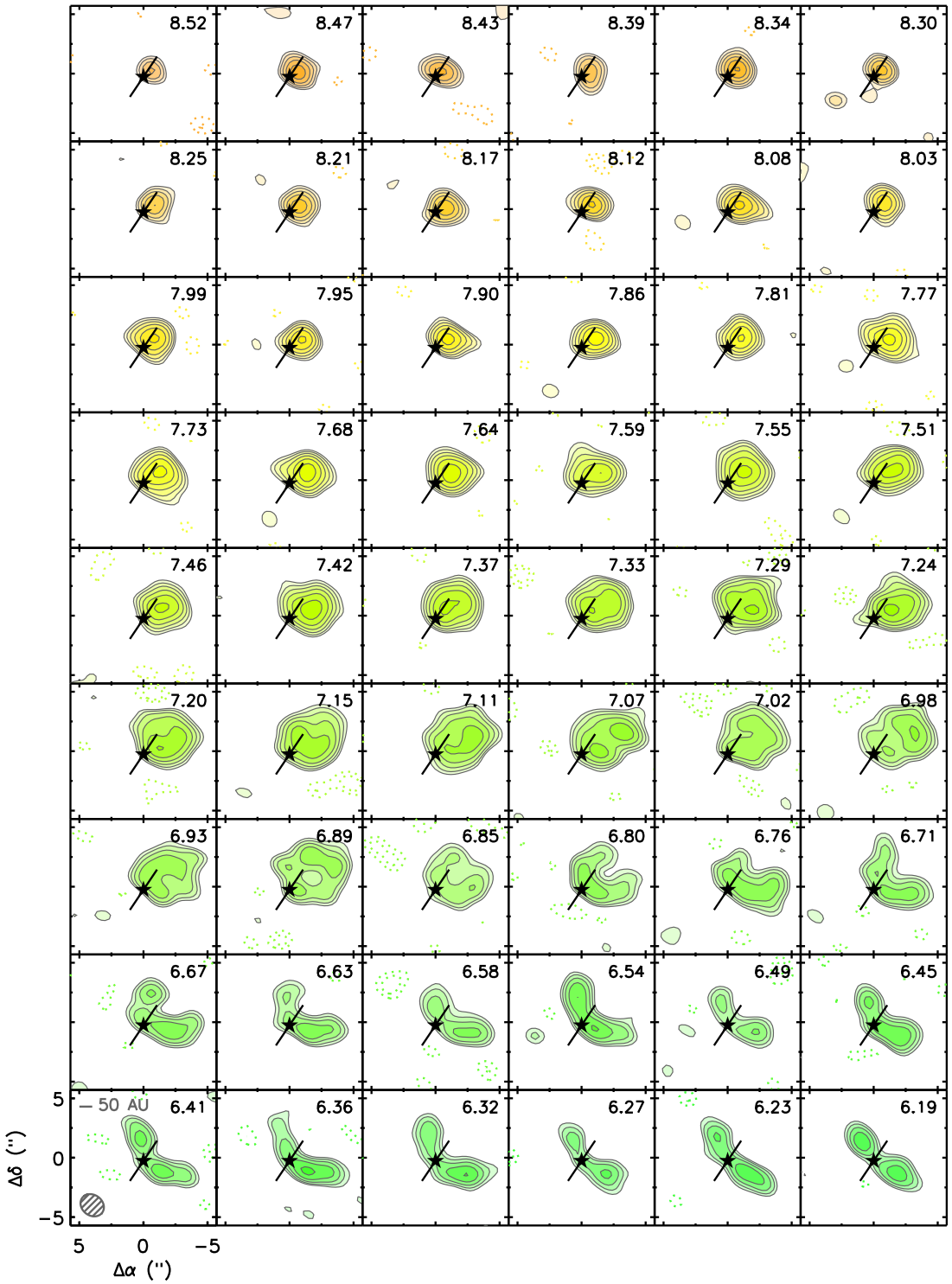

Figure C.1 (Continued)

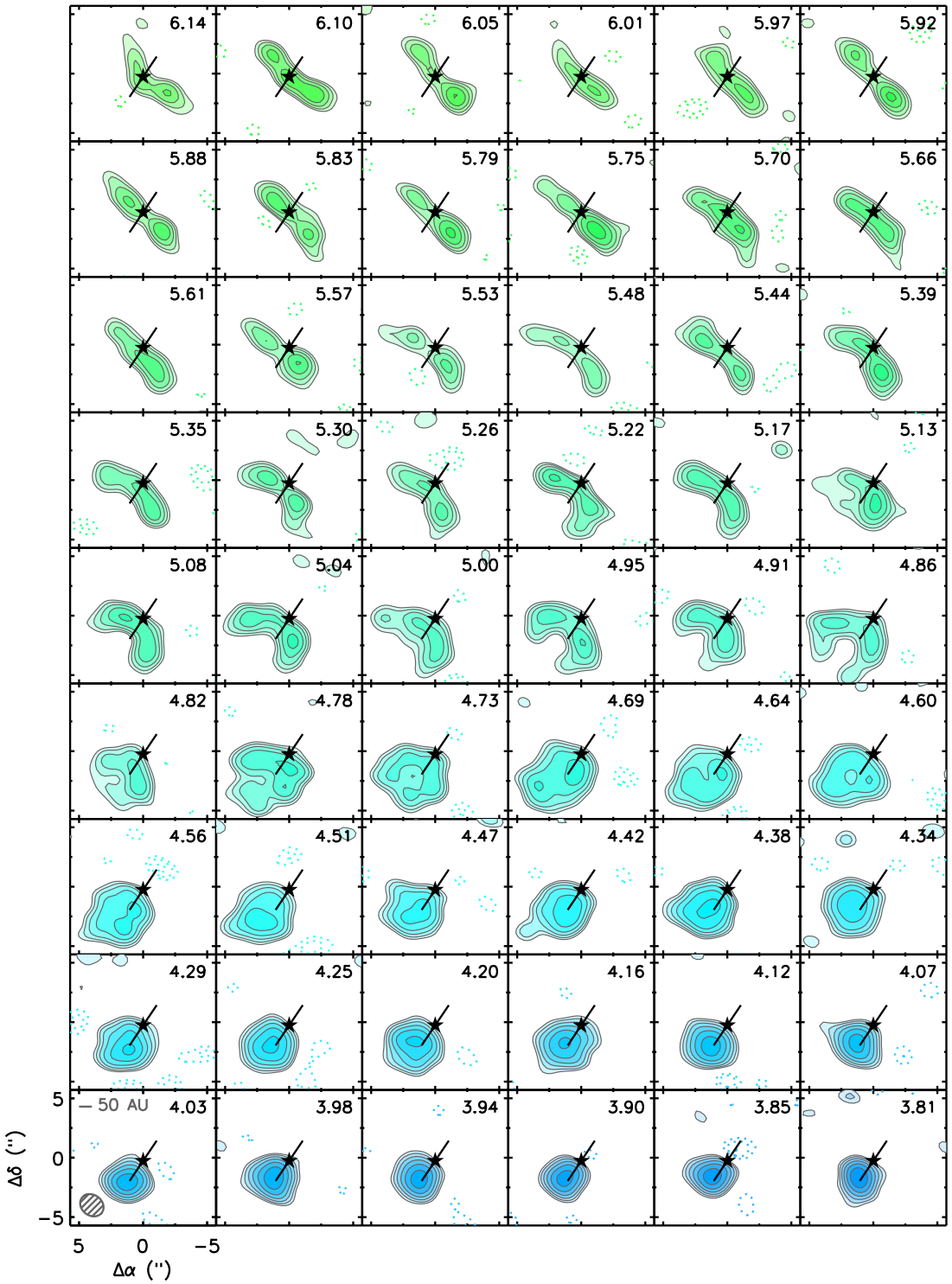

Figure C.1 (Continued)

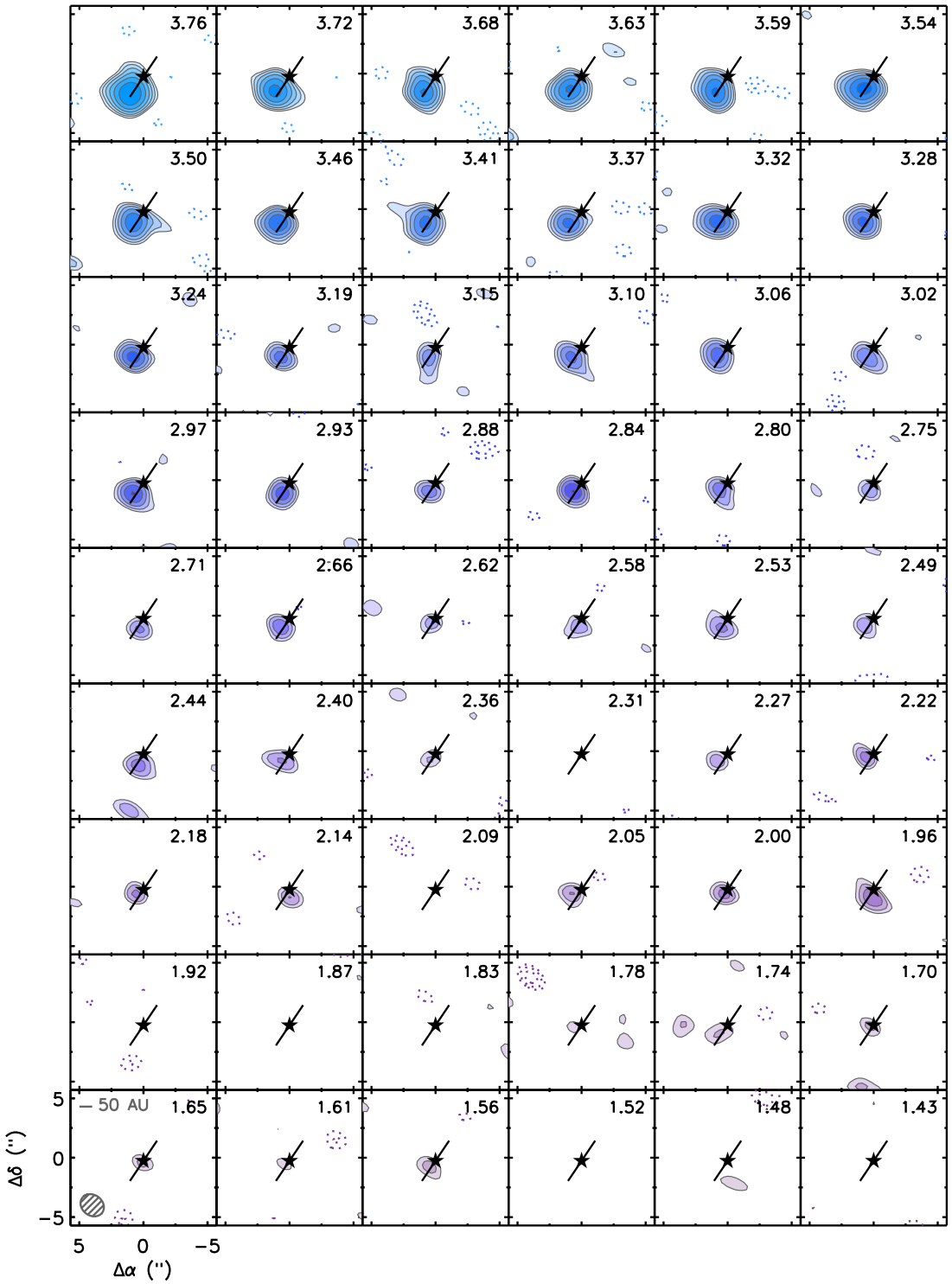

Figure C.1 (Continued)

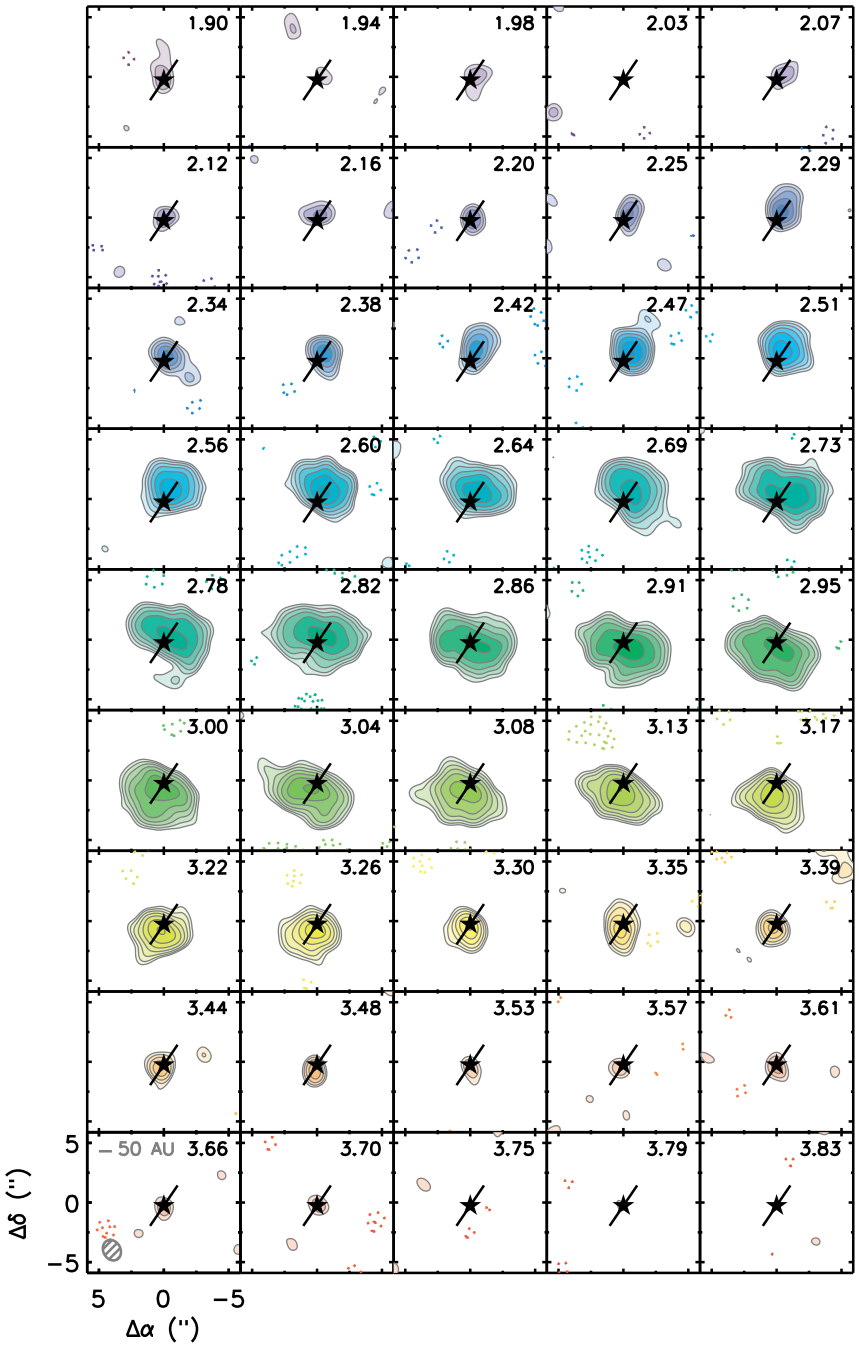

Figure C.2.— Same as Figure C.1 above, but for TW Hya. The beam size is 1.″9×1.″4 at a position angle of 21° and the contour levels are the same as in Figure C.1.

References

Aannestad, P. A. & Purcell, E. M. 1973, ARA&A, 11, 309

Adams, F. C., Hollenbach, D., Laughlin, G., & Gorti, U. 2004, ApJ, 611, 360

Adams, F. C., Lada, C. J., & Shu, F. H. 1987, ApJ, 312, 788

Adams, F. C. & Shu, F. H. 1986, ApJ, 308, 836

Aikawa, Y. 2007, ApJ, 656, L93

Aitken, D. K., Efstathiou, A., McCall, A., & Hough, J. H. 2002, MNRAS, 329, 647

Alexander, R. D. & Armitage, P. J. 2007, MNRAS, 375, 500

Alexander, R. D., Clarke, C. J., & Pringle, J. E. 2006, MNRAS, 369, 229

Andrews, S. M., Czekala, I., Wilner, D. J., Espaillat, C., Dullemond, C. P., & Hughes, A. M. 2010, ApJ, 710, 462

Andrews, S. M. & Williams, J. P. 2005, ApJ, 631, 1134

—. 2007, ApJ, 659, 705

Andrews, S. M., Wilner, D. J., Hughes, A. M., Qi, C., & Dullemond, C. P. 2009, ApJ, 700, 1502

Artymowicz, P. 1987, Icarus, 70, 303

Aumann, H. H., Beichman, C. A., Gillett, F. C., de Jong, T., Houck, J. R., Low, F. J., Neugebauer, G., Walker, R. G., & Wesselius, P. R. 1984, ApJ, 278, L23

Balbus, S. A. & Hawley, J. F. 1991, ApJ, 376, 214

—. 1998, Reviews of Modern Physics, 70, 1

Balbus, S. A., Hawley, J. F., & Stone, J. M. 1996, ApJ, 467, 76

Balsara, D. S., Tilley, D. A., Rettig, T., & Brittain, S. D. 2009, MNRAS, 397, 24

Barrado y Navascués, D., Stauffer, J. R., Song, I., & Caillault, J.-P. 1999, ApJ, 520, L123

Beckwith, S., Gatley, I., Matthews, K., & Neugebauer, G. 1978, ApJ, 223, L41

Beckwith, S. V. W. & Sargent, A. I. 1991, ApJ, 381, 250

Beckwith, S. V. W., Sargent, A. I., Chini, R. S., & Guesten, R. 1990, AJ, 99, 924

Bergin, E., Calvet, N., Sitko, M. L., Abgrall, H., D'Alessio, P., Herczeg, G. J., Roueff, E., Qi, C., Lynch, D. K., Russell, R. W., Brafford, S. M., & Perry, R. B. 2004, ApJ, 614, L133

Bertout, C. & Genova, F. 2006, A&A, 460, 499

Bockelée-Morvan, D., André, P., Colom, P., Colas, F., Crovisier, J., Despois, D., & Jorda, L. 1994, in Circumstellar Dust Disks and Planet Formation, ed. R. Ferlet & A. Vidal-Madjar, 341–+

Boss, A. P. 2004, ApJ, 616, 1265

Boss, A. P. & Yorke, H. W. 1993, ApJ, 411, L99

—. 1996, ApJ, 469, 366

Bouvier, J., Bertout, C., Benz, W., & Mayor, M. 1986, A&A, 165, 110

Bouwman, J., Henning, T., Hillenbrand, L. A., Meyer, M. R., Pascucci, I., Carpenter, J., Hines, D., Kim, J. S., Silverstone, M. D., Hollenbach, D., & Wolf, S. 2008, ApJ, 683, 479

Brittain, S. D., Simon, T., Najita, J. R., & Rettig, T. W. 2007, ApJ, 659, 685

Brown, A., Jordan, C., Millar, T. J., Gondhalekar, P., & Wilson, R. 1981, Nature, 290, 34

Brown, J. M., Blake, G. A., Dullemond, C. P., Merín, B., Augereau, J. C., Boogert, A. C. A., Evans, II, N. J., Geers, V. C., Lahuis, F., Kessler-Silacci, J. E., Pontoppidan, K. M., & van Dishoeck, E. F. 2007, ApJ, 664, L107

Brown, J. M., Blake, G. A., Qi, C., Dullemond, C. P., & Wilner, D. J. 2008, ApJ, 675, L109

Brown, J. M., Blake, G. A., Qi, C., Dullemond, C. P., Wilner, D. J., & Williams, J. P. 2009, ApJ, 704, 496

Bryden, G., Chen, X., Lin, D. N. C., Nelson, R. P., & Papaloizou, J. C. B. 1999, ApJ, 514, 344

Butler, R. P., Wright, J. T., Marcy, G. W., Fischer, D. A., Vogt, S. S., Tinney, C. G., Jones, H. R. A., Carter, B. D., Johnson, J. A., McCarthy, C., & Penny, A. J. 2006, ApJ, 646, 505

Calvet, N., D'Alessio, P., Hartmann, L., Wilner, D., Walsh, A., & Sitko, M. 2002, ApJ, 568, 1008

Calvet, N., D'Alessio, P., Watson, D. M., Franco-Hernández, R., Furlan, E., Green, J., Sutter, P. M., Forrest, W. J., Hartmann, L., Uchida, K. I., Keller, L. D., Sargent, B., Najita, J., Herter, T. L., Barry, D. J., & Hall, P. 2005, ApJ, 630, L185

Calvet, N., Muzerolle, J., Briceño, C., Hernández, J., Hartmann, L., Saucedo, J. L., & Gordon, K. D. 2004, AJ, 128, 1294

Carballido, A., Fromang, S., & Papaloizou, J. 2006, MNRAS, 373, 1633

Cardelli, J. A., Clayton, G. C., & Mathis, J. S. 1989, ApJ, 345, 245

Carmona, A., van den Ancker, M. E., Henning, T., Goto, M., Fedele, D., & Stecklum, B. 2007, ArXiv e-prints, 710

Carpenter, J. M., Bouwman, J., Silverstone, M. D., Kim, J. S., Stauffer, J., Cohen, M., Hines, D. C., Meyer, M. R., & Crockett, N. 2008, ApJS, 179, 423

Carpenter, J. M., Wolf, S., Schreyer, K., Launhardt, R., & Henning, T. 2005, AJ, 129, 1049

Carr, J. S. 1990, AJ, 100, 1244

Carr, J. S., Tokunaga, A. T., & Najita, J. 2004, ApJ, 603, 213

Chambers, J. E. 2006, ApJ, 652, L133

Chandrasekhar, S. 1960, Proceedings of the National Academy of Science, 46, 253

Chen, C. H., Sargent, B. A., Bohac, C., Kim, K. H., Leibensperger, E., Jura, M., Najita, J., Forrest, W. J., Watson, D. M., Sloan, G. C., & Keller, L. D. 2006, ApJS, 166, 351

Chiang, E. & Murray-Clay, R. 2007, Nature Physics, 3, 604

Chiang, E. I. & Goldreich, P. 1997, ApJ, 490, 368

—. 1999, ApJ, 519, 279

Chiang, E. I., Joung, M. K., Creech-Eakman, M. J., Qi, C., Kessler, J. E., Blake, G. A., & van Dishoeck, E. F. 2001, ApJ, 547, 1077

Cho, J. & Lazarian, A. 2005, ApJ, 631, 361

—. 2007, ApJ, 669, 1085

Ciesla, F. J. 2007, Science, 318, 613

Cieza, L., Padgett, D. L., Stapelfeldt, K. R., Augereau, J., Harvey, P., Evans, II, N. J., Merín, B., Koerner, D., Sargent, A., van Dishoeck, E. F., Allen, L., Blake, G., Brooke, T., Chapman, N., Huard, T., Lai, S., Mundy, L., Myers, P. C., Spiesman, W., & Wahhaj, Z. 2007, ApJ, 667, 308

Clarke, C. J., Gendrin, A., & Sotomayor, M. 2001, MNRAS, 328, 485

Collins, K. A., Grady, C. A., Hamaguchi, K., Wisniewski, J. P., Brittain, S., Sitko, M., Carpenter, W. J., Williams, J. P., Mathews, G. S., Williger, G. M., van Boekel, R., Carmona, A., Henning, T., van den Ancker, M. E., Meeus, G., Chen, X. P., Petre, R., & Woodgate, B. E. 2009, ApJ, 697, 557

Cortes, S. R., Meyer, M. R., Carpenter, J. M., Pascucci, I., Schneider, G., Wong, T., & Hines, D. C. 2009, ApJ, 697, 1305

D'Alessio, P. 2009, in Revista Mexicana de Astronomia y Astrofisica Conference Series, Vol. 35, Revista Mexicana de Astronomia y Astrofisica Conference Series, 33–38

D'Alessio, P., Calvet, N., & Hartmann, L. 1997, ApJ, 474, 397

—. 2001, ApJ, 553, 321

D'Alessio, P., Calvet, N., Hartmann, L., Franco-Hernández, R., & Servín, H. 2006, ApJ, 638, 314

D'Alessio, P., Calvet, N., Hartmann, L., Lizano, S., & Cantó, J. 1999, ApJ, 527, 893

D'Alessio, P., Canto, J., Calvet, N., & Lizano, S. 1998, ApJ, 500, 411

D'Alessio, P., Hartmann, L., Calvet, N., Franco-Hernández, R., Forrest, W. J., Sargent, B., Furlan, E., Uchida, K., Green, J. D., Watson, D. M., Chen, C. H., Kemper, F., Sloan, G. C., & Najita, J. 2005, ApJ, 621, 461

Dartois, E., Dutrey, A., & Guilloteau, S. 2003, A&A, 399, 773

de Val-Borro, M., Edgar, R. G., Artymowicz, P., Ciecielag, P., Cresswell, P., D'Angelo, G., Delgado-Donate, E. J., Dirksen, G., Fromang, S., Gawryszczak, A., Klahr, H., Kley, W., Lyra, W., Masset, F., Mellema, G., Nelson, R. P., Paardekooper, S., Peplinski, A., Pierens, A., Plewa, T., Rice, K., Schäfer, C., & Speith, R. 2006, MNRAS, 370, 529

Dent, W. R. F., Greaves, J. S., & Coulson, I. M. 2005, MNRAS, 359, 663

Dolginov, A. Z. 1972, Ap&SS, 18, 337

Dolginov, A. Z. & Mitrofanov, I. G. 1976, Ap&SS, 43, 291

Draine, B. T. & Lee, H. M. 1984, ApJ, 285, 89

Draine, B. T. & Weingartner, J. C. 1996, ApJ, 470, 551

Dubrulle, B., Dauchot, O., Daviaud, F., Longaretti, P., Richard, D., & Zahn, J. 2005, Physics of Fluids, 17, 095103

Dullemond, C. P. & Dominik, C. 2004a, A&A, 417, 159

—. 2004b, A&A, 421, 1075

—. 2005, A&A, 434, 971

Dullemond, C. P., Dominik, C., & Natta, A. 2001, ApJ, 560, 957

Dullemond, C. P., van Zadelhoff, G. J., & Natta, A. 2002, A&A, 389, 464

Dutrey, A., Guilloteau, S., Duvert, G., Prato, L., Simon, M., Schuster, K., & Menard, F. 1996, A&A, 309, 493

Dutrey, A., Guilloteau, S., & Ho, P. 2007, in Protostars and Planets V, ed. B. Reipurth, D. Jewitt, & K. Keil, 495–506

Dutrey, A., Guilloteau, S., Piétu, V., Chapillon, E., Gueth, F., Henning, T., Launhardt, R., Pavlyuchenkov, Y., Schreyer, K., & Semenov, D. 2008, A&A, 490, L15

Dutrey, A., Guilloteau, S., Prato, L., Simon, M., Duvert, G., Schuster, K., & Menard, F. 1998, A&A, 338, L63

Dutrey, A., Guilloteau, S., & Simon, M. 1994, A&A, 286, 149

Edgar, R. G., Quillen, A. C., & Park, J. 2007, MNRAS, 381, 1280

Eisner, J. A., Chiang, E. I., & Hillenbrand, L. A. 2006, ApJ, 637, L133

Elias, J. H. 1978, ApJ, 224, 857

Espaillat, C., Calvet, N., D'Alessio, P., Hernández, J., Qi, C., Hartmann, L., Furlan, E., & Watson, D. M. 2007, ApJ, 670, L135

Espaillat, C., Calvet, N., Luhman, K. L., Muzerolle, J., & D'Alessio, P. 2008, ApJ, 682, L125

Fleming, T. & Stone, J. M. 2003, ApJ, 585, 908

Fromang, S. 2005, A&A, 441, 1

Fromang, S. & Nelson, R. P. 2006, A&A, 457, 343

—. 2009, A&A, 496, 597

Fromang, S. & Papaloizou, J. 2007, A&A, 476, 1113

Gammie, C. F. 1996, ApJ, 457, 355

Gammie, C. F. & Johnson, B. M. 2005, in Astronomical Society of the Pacific Conference Series, Vol. 341, Chondrites and the Protoplanetary Disk, ed. A. N. Krot, E. R. D. Scott, & B. Reipurth, 145–+

Girart, J. M., Rao, R., & Marrone, D. P. 2006, Science, 313, 812

Glassgold, A. E., Najita, J., & Igea, J. 2004, ApJ, 615, 972

Goldreich, P. & Kylafis, N. D. 1981, ApJ, 243, L75

—. 1982, ApJ, 253, 606

Gomez, M., Hartmann, L., Kenyon, S. J., & Hewett, R. 1993, AJ, 105, 1927

Goto, M., Usuda, T., Dullemond, C. P., Henning, T., Linz, H., Stecklum, B., & Suto, H. 2006, ApJ, 652, 758

Grady, C. A., Devine, D., Woodgate, B., Kimble, R., Bruhweiler, F. C., Boggess, A., Linsky, J. L., Plait, P., Clampin, M., & Kalas, P. 2000, ApJ, 544, 895

Greenberg, J. M. Interstellar Grains, ed. B. M. Middlehurst & L. H. Aller (the University of Chicago Press), 221–+

Guilloteau, S. & Dutrey, A. 1998, A&A, 339, 467

Gullbring, E., Hartmann, L., Briceno, C., & Calvet, N. 1998, ApJ, 492, 323

Habing, H. J. 1968, Bull. Astron. Inst. Netherlands, 19, 421

Hamidouche, M., Looney, L. W., & Mundy, L. G. 2006, ApJ, 651, 321

Hartmann, L., Calvet, N., Gullbring, E., & D'Alessio, P. 1998, ApJ, 495, 385

Hartmann, L., Hewett, R., Stahler, S., & Mathieu, R. D. 1986, ApJ, 309, 275

Hartmann, L., Hinkle, K., & Calvet, N. 2004, ApJ, 609, 906

Hartmann, L., Megeath, S. T., Allen, L., Luhman, K., Calvet, N., D'Alessio, P., Franco-Hernandez, R., & Fazio, G. 2005, ApJ, 629, 881

Herczeg, G. J., Wood, B. E., Linsky, J. L., Valenti, J. A., & Johns-Krull, C. M. 2004, ApJ, 607, 369

Hersant, F., Dubrulle, B., & Huré, J. 2005, A&A, 429, 531

Hildebrand, R. H., Davidson, J. A., Dotson, J. L., Dowell, C. D., Novak, G., & Vaillancourt, J. E. 2000, PASP, 112, 1215

Hildebrand, R. H. & Dragovan, M. 1995, ApJ, 450, 663

Ho, P. T. P., Moran, J. M., & Lo, K. Y. 2004, ApJ, 616, L1

Hoang, T. & Lazarian, A. 2008, MNRAS, 388, 117

—. 2009, ApJ, 697, 1316

Hoff, W., Henning, T., & Pfau, W. 1998, A&A, 336, 242

Hoffleit, D. & Jaschek, C. . 1991, The Bright star catalogue (New Haven, Conn.: Yale University Observatory, —c1991, 5th rev.ed., edited by Hoffleit, Dorrit; Jaschek, Carlos —v(coll.))

Hogerheijde, M. R. & van der Tak, F. F. S. 2000, A&A, 362, 697

Holland, W. S., Greaves, J. S., Zuckerman, B., Webb, R. A., McCarthy, C., Coulson, I. M., Walther, D. M., Dent, W. R. F., Gear, W. K., & Robson, I. 1998, Nature, 392, 788

Hollenbach, D., Johnstone, D., Lizano, S., & Shu, F. 1994, ApJ, 428, 654

Hubrig, S., Stelzer, B., Schöller, M., Grady, C., Schütz, O., Pogodin, M. A., Curé, M., Hamaguchi, K., & Yudin, R. V. 2009, A&A, 502, 283

Hughes, A. M., Andrews, S. M., Espaillat, C., Wilner, D. J., Calvet, N., D'Alessio, P., Qi, C., Williams, J. P., & Hogerheijde, M. R. 2009a, ApJ, 698, 131

Hughes, A. M., Wilner, D. J., Calvet, N., D'Alessio, P., Claussen, M. J., & Hogerheijde, M. R. 2007, ApJ, 664, 536

Hughes, A. M., Wilner, D. J., Cho, J., Marrone, D. P., Lazarian, A., Andrews, S. M., & Rao, R. 2009b, ApJ, 704, 1204

Hughes, A. M., Wilner, D. J., Kamp, I., & Hogerheijde, M. R. 2008a, ApJ, 681, 626

Hughes, A. M., Wilner, D. J., Qi, C., & Hogerheijde, M. R. 2008b, ApJ, 678, 1119

Igea, J. & Glassgold, A. E. 1999, ApJ, 518, 848

Ingleby, L. & Calvet, N. 2009, ApJ, submitted

Ireland, M. J. & Kraus, A. L. 2008, ApJ, 678, L59

Isella, A., Carpenter, J. M., & Sargent, A. I. 2009, ApJ, 701, 260

Isella, A., Testi, L., & Natta, A. 2006, A&A, 451, 951

Isella, A., Testi, L., Natta, A., Neri, R., Wilner, D., & Qi, C. 2007, A&A, 469, 213

Jewitt, D., Luu, J., & Trujillo, C. 1998, AJ, 115, 2125

Johansen, A. & Klahr, H. 2005, ApJ, 634, 1353

Johansen, A., Oishi, J. S., Low, M.-M. M., Klahr, H., Henning, T., & Youdin, A. 2007, Nature, 448, 1022

Jonkheid, B., Dullemond, C. P., Hogerheijde, M. R., & van Dishoeck, E. F. 2007, A&A, 463, 203

Jonkheid, B., Kamp, I., Augereau, J.-C., & van Dishoeck, E. F. 2006, A&A, 453, 163

Jura, M., Malkan, M., White, R., Telesco, C., Pina, R., & Fisher, R. S. 1998, ApJ, 505, 897

Jura, M., Zuckerman, B., Becklin, E. E., & Smith, R. C. 1993, ApJ, 418, L37+

Kalas, P., Graham, J. R., Chiang, E., Fitzgerald, M. P., Clampin, M., Kite, E. S., Stapelfeldt, K., Marois, C., & Krist, J. 2008, ArXiv e-prints

Kamp, I. & Bertoldi, F. 2000, A&A, 353, 276

Kamp, I. & Dullemond, C. P. 2004, ApJ, 615, 991

Kamp, I. & van Zadelhoff, G.-J. 2001, A&A, 373, 641

Kastner, J. H., Huenemoerder, D. P., Schulz, N. S., & Weintraub, D. A. 1999, ApJ, 525, 837

Kastner, J. H., Zuckerman, B., Weintraub, D. A., & Forveille, T. 1997, Science, 277, 67

Kenyon, S. J. & Hartmann, L. 1987, ApJ, 323, 714

—. 1995, ApJS, 101, 117

Kim, J. S., Hines, D. C., Backman, D. E., Hillenbrand, L. A., Meyer, M. R., Rodmann, J., Moro-Martín, A., Carpenter, J. M., Silverstone, M. D., Bouwman, J., Mamajek, E. E., Wolf, S., Malhotra, R., Pascucci, I., Najita, J., Padgett, D. L., Henning, T., Brooke, T. Y., Cohen, M., Strom, S. E., Stobie, E. B., Engelbracht, C. W., Gordon, K. D., Misselt, K., Morrison, J. E., Muzerolle, J., & Su, K. Y. L. 2005, ApJ, 632, 659

Kitamura, Y., Kawabe, R., & Saito, M. 1996, ApJ, 457, 277

Kitamura, Y., Momose, M., Yokogawa, S., Kawabe, R., Tamura, M., & Ida, S. 2002, ApJ, 581, 357

Koerner, D. W., Sargent, A. I., & Beckwith, S. V. W. 1993, Icarus, 106, 2

Köhler, R., Neuhäuser, R., Krämer, S., Leinert, C., Ott, T., & Eckart, A. 2008, A&A, 488, 997

Kraus, A. L. & Hillenbrand, L. A. 2008, ApJ, 686, L111

Krauss, O. & Wurm, G. 2005, ApJ, 630, 1088

Krejny, M., Matthews, T., Novak, G., Cho, J., Li, H., Shinnaga, H., & Vaillancourt, J. E. 2009, ArXiv e-prints

Krist, J. E., Stapelfeldt, K. R., Ménard, F., Padgett, D. L., & Burrows, C. J. 2000, ApJ, 538, 793

Lay, O. P., Carlstrom, J. E., & Hills, R. E. 1997, ApJ, 489, 917

Lay, O. P., Carlstrom, J. E., Hills, R. E., & Phillips, T. G. 1994, ApJ, 434, L75

Lazarian, A. 2007, Journal of Quantitative Spectroscopy and Radiative Transfer, 106, 225

Lazarian, A. & Hoang, T. 2007, ApJ, 669, L77

—. 2008, ApJ, 676, L25

Lee, H. M. & Draine, B. T. 1985, ApJ, 290, 211

Lin, D. N. C. & Papaloizou, J. 1986, ApJ, 309, 846

Lin, D. N. C. & Papaloizou, J. C. B. 1993, in Protostars and Planets III, ed. E. H. Levy & J. I. Lunine, 749–835

Looney, L. W., Mundy, L. G., & Welch, W. J. 2000, ApJ, 529, 477

Lubow, S. H. & D'Angelo, G. 2006, ApJ, 641, 526

Lynden-Bell, D. & Pringle, J. E. 1974, MNRAS, 168, 603

Mamajek, E. E. 2005, ApJ, 634, 1385

Mamajek, E. E. 2009, in American Institute of Physics Conference Series, Vol. 1158, American Institute of Physics Conference Series, ed. T. Usuda, M. Tamura, & M. Ishii, 3–10

Mannings, V. 1994, MNRAS, 271, 587

Mannings, V. & Sargent, A. I. 1997, ApJ, 490, 792

Marrone, D. P. 2006, PhD thesis, Harvard University

Marrone, D. P. & Rao, R. 2008, in Society of Photo-Optical Instrumentation Engineers (SPIE) Conference Series, Vol. 7020, Society of Photo-Optical Instrumentation Engineers (SPIE) Conference Series

Marsh, K. A. & Mahoney, M. J. 1992, ApJ, 395, L115

Marsh, K. A., Silverstone, M. D., Becklin, E. E., Koerner, D. W., Werner, M. W., Weinberger, A. J., & Ressler, M. E. 2002, ApJ, 573, 425

Martin-Zaïdi, C., Deleuil, M., Simon, T., Bouret, J.-C., Roberge, A., Feldman, P. D., Lecavelier Des Etangs, A., & Vidal-Madjar, A. 2005, A&A, 440, 921

Mathis, J. S., Rumpl, W., & Nordsieck, K. H. 1977, ApJ, 217, 425

Matsumura, S., Pudritz, R. E., & Thommes, E. W. 2009, ApJ, 691, 1764

McCaughrean, M. J. & O'Dell, C. R. 1996, AJ, 111, 1977

Merín, B., Montesinos, B., Eiroa, C., Solano, E., Mora, A., D'Alessio, P., Calvet, N., Oudmaijer, R. D., de Winter, D., Davies, J. K., Harris, A. W., Cameron, A., Deeg, H. J., Ferlet, R., Garzón, F., Grady, C. A., Horne, K., Miranda, L. F., Palacios, J., Penny, A., Quirrenbach, A., Rauer, H., Schneider, J., & Wesselius, P. R. 2004, A&A, 419, 301

Meyer, M. R., Hillenbrand, L. A., Backman, D., Beckwith, S., Bouwman, J., Brooke, T., Carpenter, J., Cohen, M., Cortes, S., Crockett, N., Gorti, U., Henning, T., Hines, D., Hollenbach, D., Kim, J. S., Lunine, J., Malhotra, R., Mamajek, E., Metchev, S., Moro-Martin, A., Morris, P., Najita, J., Padgett, D., Pascucci, I., Rodmann, J., Schlingman, W., Silverstone, M., Soderblom, D., Stauffer, J., Stobie, E., Strom, S., Watson, D., Weidenschilling, S., Wolf, S., & Young, E. 2006, PASP, 118, 1690

Mouillet, D., Larwood, J. D., Papaloizou, J. C. B., & Lagrange, A. M. 1997, MNRAS, 292, 896

Mulders, G. D., Dominik, C., & Min, M. 2010, ArXiv e-prints

Mundy, L. G., McMullin, J. P., Grossman, A. W., & Sandell, G. 1993, Icarus, 106, 11

Muzerolle, J., Briceño, C., Calvet, N., Hartmann, L., Hillenbrand, L., & Gullbring, E. 2000, ApJ, 545, L141

Najita, J. R., Strom, S. E., & Muzerolle, J. 2007, MNRAS, 378, 369

Natta, A., Testi, L., Neri, R., Shepherd, D. S., & Wilner, D. J. 2004, A&A, 416, 179

Nelson, R. P. & Papaloizou, J. C. B. 2003, MNRAS, 339, 993

—. 2004, MNRAS, 350, 849

Neuhäuser, R., Walter, F. M., Covino, E., Alcalá, J. M., Wolk, S. J., Frink, S., Guillout, P., Sterzik, M. F., & Comerón, F. 2000, A&AS, 146, 323

Nomura, H., Aikawa, Y., Tsujimoto, M., Nakagawa, Y., & Millar, T. J. 2007, ApJ, 661, 334

Owen, J. E., Ercolano, B., Clarke, C. J., & Alexander, R. D. 2010, MNRAS, 401, 1415

Padoan, P., Goodman, A., Draine, B. T., Juvela, M., Nordlund, Å., & Rögnvaldsson, Ö. E. 2001, ApJ, 559, 1005

Panić, O., Hogerheijde, M. R., Wilner, D., & Qi, C. 2008, A&A, 491, 219

Papaloizou, J. C. B. & Nelson, R. P. 2003, MNRAS, 339, 983

Papaloizou, J. C. B., Nelson, R. P., & Snellgrove, M. D. 2004, MNRAS, 350, 829

Pascucci, I., Hollenbach, D., Najita, J., Muzerolle, J., Gorti, U., Herczeg, G. J., Hillenbrand, L. A., Kim, J. S., Carpenter, J. M., Meyer, M. R., Mamajek, E. E., & Bouwman, J. 2007, ApJ, 663, 383

Pessah, M. E., Chan, C., & Psaltis, D. 2007, ApJ, 668, L51

Petit, J.-M., Holman, M. J., Gladman, B. J., Kavelaars, J. J., Scholl, H., & Loredo, T. J. 2006, MNRAS, 365, 429

Pety, J. 2005, in SF2A-2005: Semaine de l'Astrophysique Francaise, ed. F. Casoli, T. Contini, J. M. Hameury, & L. Pagani, 721–+

Piétu, V., Dutrey, A., & Guilloteau, S. 2007, A&A, 467, 163

Piétu, V., Guilloteau, S., & Dutrey, A. 2005, A&A, 443, 945

Pontoppidan, K. M., Blake, G. A., van Dishoeck, E. F., Smette, A., Ireland, M. J., & Brown, J. 2008, ApJ, 684, 1323

Qi, C., Ho, P. T. P., Wilner, D. J., Takakuwa, S., Hirano, N., Ohashi, N., Bourke, T. L., Zhang, Q., Blake, G. A., Hogerheijde, M., Saito, M., Choi, M., & Yang, J. 2004, ApJ, 616, L11

Qi, C., Wilner, D. J., Aikawa, Y., Blake, G. A., & Hogerheijde, M. R. 2008, ApJ, 681, 1396

Qi, C., Wilner, D. J., Calvet, N., Bourke, T. L., Blake, G. A., Hogerheijde, M. R., Ho, P. T. P., & Bergin, E. 2006, ApJ, 636, L157

Quillen, A. C. 2006, ApJ, 640, 1078

Ratzka, T., Leinert, C., Henning, T., Bouwman, J., Dullemond, C. P., & Jaffe, W. 2007, A&A, 471, 173

Reipurth, B. 2005, in Astronomical Society of the Pacific Conference Series, Vol. 341, Chondrites and the Protoplanetary Disk, ed. A. N. Krot, E. R. D. Scott, & B. Reipurth, 54–+

Rettig, T. W., Haywood, J., Simon, T., Brittain, S. D., & Gibb, E. 2004, ApJ, 616, L163

Rice, W. K. M., Armitage, P. J., Wood, K., & Lodato, G. 2006, MNRAS, 373, 1619

Rice, W. K. M., Wood, K., Armitage, P. J., Whitney, B. A., & Bjorkman, J. E. 2003, MNRAS, 342, 79

Roberge, A., Weinberger, A. J., & Malumuth, E. M. 2005, ApJ, 622, 1171

Rodmann, J., Henning, T., Chandler, C. J., Mundy, L. G., & Wilner, D. J. 2006, A&A, 446, 211

Rogstad, D. H., Lockhart, I. A., & Wright, M. C. H. 1974, ApJ, 193, 309

Sadakane, K. & Nishida, M. 1986, PASP, 98, 685

Salyk, C., Blake, G. A., Boogert, A. C. A., & Brown, J. M. 2007, ApJ, 655, L105

—. 2009, ApJ, 699, 330

Sano, T., Miyama, S. M., Umebayashi, T., & Nakano, T. 2000, ApJ, 543, 486

Schneider, G., Wood, K., Silverstone, M. D., Hines, D. C., Koerner, D. W., Whitney, B. A., Bjorkman, J. E., & Lowrance, P. J. 2003, AJ, 125, 1467

Scholl, H., Cazenave, A., & Brahic, A. 1982, A&A, 112, 157

Semenov, D., Wiebe, D., & Henning, T. 2006, ApJ, 647, L57

Shakura, N. I. & Syunyaev, R. A. 1973, A&A, 24, 337

Shu, F. H., Galli, D., Lizano, S., Glassgold, A. E., & Diamond, P. H. 2007, ApJ, 665, 535

Sicilia-Aguilar, A., Henning, T., & Hartmann, L. W. 2010, ApJ, 710, 597

Siess, L., Dufour, E., & Forestini, M. 2000, A&A, 358, 593

Simon, M., Dutrey, A., & Guilloteau, S. 2000, ApJ, 545, 1034

Simon, M. & Prato, L. 1995, ApJ, 450, 824

Sitko, M. L., Lynch, D. K., & Russell, R. W. 2000, AJ, 120, 2609

Skrutskie, M. F., Cutri, R. M., Stiening, R., Weinberg, M. D., Schneider, S., Carpenter, J. M., Beichman, C., Capps, R., Chester, T., Elias, J., Huchra, J., Liebert, J., Lonsdale, C., Monet, D. G., Price, S., Seitzer, P., Jarrett, T., Kirkpatrick, J. D., Gizis, J. E., Howard, E., Evans, T., Fowler, J., Fullmer, L., Hurt, R., Light, R., Kopan, E. L., Marsh, K. A., McCallon, H. L., Tam, R., Van Dyk, S., & Wheelock, S. 2006, AJ, 131, 1163

Skrutskie, M. F., Dutkevitch, D., Strom, S. E., Edwards, S., Strom, K. M., & Shure, M. A. 1990, AJ, 99, 1187

Song, I., Sandell, G., & Friberg, P. 2004, in ASP Conf. Ser. 324: Debris Disks and the Formation of Planets, ed. L. Caroff, L. J. Moon, D. Backman, & E. Praton, 250–+

Stapelfeldt, K. & The WFPC2 Science Team. 1997, in Science with the VLT Interferometer, ed. F. Paresce, 395–+

Stauffer, J. R., Hartmann, L. W., & Barrado y Navascues, D. 1995, ApJ, 454, 910

Stone, J. M., Hawley, J. F., Gammie, C. F., & Balbus, S. A. 1996, ApJ, 463, 656

Strom, K. M., Strom, S. E., Edwards, S., Cabrit, S., & Skrutskie, M. F. 1989, AJ, 97, 1451

Sylvester, R. J., Skinner, C. J., Barlow, M. J., & Mannings, V. 1996, MNRAS, 279, 915

Tamura, M., Hough, J. H., Greaves, J. S., Morino, J.-I., Chrysostomou, A., Holland, W. S., & Momose, M. 1999, ApJ, 525, 832

Tamura, M., Hough, J. H., & Hayashi, S. S. 1995, ApJ, 448, 346

The, P. S., de Winter, D., & Perez, M. R. 1994, A&AS, 104, 315

Thi, W. F., Blake, G. A., van Dishoeck, E. F., van Zadelhoff, G. J., Horn, J. M. M., Becklin, E. E., Mannings, V., Sargent, A. I., van den Ancker, M. E., & Natta, A. 2001a, Nature, 409, 60

Thi, W. F., van Dishoeck, E. F., Blake, G. A., van Zadelhoff, G. J., Horn, J., Becklin, E. E., Mannings, V., Sargent, A. I., van den Ancker, M. E., Natta, A., & Kessler, J. 2001b, ApJ, 561, 1074

Trilling, D. E., Koerner, D. W., Barnes, J. W., Ftaclas, C., & Brown, R. H. 2001, ApJ, 552, L151

Trujillo, C. A. & Brown, M. E. 2001, ApJ, 554, L95

Turner, N. J., Sano, T., & Dziourkevitch, N. 2007, ApJ, 659, 729

Uchida, K. I., Calvet, N., Hartmann, L., Kemper, F., Forrest, W. J., Watson, D. M., D'Alessio, P., Chen, C. H., Furlan, E., Sargent, B., Brandl, B. R., Herter, T. L., Morris, P., Myers, P. C., Najita, J., Sloan, G. C., Barry, D. J., Green, J., Keller, L. D., & Hall, P. 2004, ApJS, 154, 439

Uzpen, B., Kobulnicky, H. A., Semler, D. R., Bensby, T., & Thom, C. 2008, ApJ, 685, 1157

van den Ancker, M. E., de Winter, D., & Tjin A Djie, H. R. E. 1998a, A&A, 330, 145

—. 1998b, A&A, 330, 145

van Dishoeck, E. F., Thi, W., & van Zadelhoff, G. 2003, A&A, 400, L1

Varnière, P., Blackman, E. G., Frank, A., & Quillen, A. C. 2006, ApJ, 640, 1110

Velikhov, E. P. 1959, Soviet Phys. JETP, 36, 1398

Vrba, F. J., Coyne, G. V., & Tapia, S. 1993, AJ, 105, 1010

Wahhaj, Z., Koerner, D. W., & Sargent, A. I. 2007, ArXiv Astrophysics e-prints

Wang, Y., Jaffe, D. T., Graf, U. U., & Evans, II, N. J. 1994, ApJS, 95, 503

Wardle, M. 2007, Ap&SS, 311, 35

Weaver, W. B. & Jones, G. 1992, ApJS, 78, 239

Webb, R. A., Zuckerman, B., Platais, I., Patience, J., White, R. J., Schwartz, M. J., & McCarthy, C. 1999, ApJ, 512, L63

Weidenschilling, S. J. 1977, Ap&SS, 51, 153

—. Formation processes and time scales for meteorite parent bodies, ed. J. F. Kerridge & M. S. Matthews, 348–371

Weidenschilling, S. J., Spaute, D., Davis, D. R., Marzari, F., & Ohtsuki, K. 1997, Icarus, 128, 429

Weinberger, A. J., Becklin, E. E., Schneider, G., Chiang, E. I., Lowrance, P. J., Silverstone, M., Zuckerman, B., Hines, D. C., & Smith, B. A. 2002, ApJ, 566, 409

Weinberger, A. J., Becklin, E. E., Schneider, G., Smith, B. A., Lowrance, P. J., Silverstone, M. D., Zuckerman, B., & Terrile, R. J. 1999, ApJ, 525, L53

Weintraub, D. A., Sandell, G., & Duncan, W. D. 1989, ApJ, 340, L69

White, R. J. & Ghez, A. M. 2001, ApJ, 556, 265

Wilner, D. J., Bourke, T. L., Wright, C. M., Jørgensen, J. K., van Dishoeck, E. F., & Wong, T. 2003, ApJ, 596, 597

Wilner, D. J., D'Alessio, P., Calvet, N., Claussen, M. J., & Hartmann, L. 2005, ApJ, 626, L109

Wilner, D. J., Ho, P. T. P., Kastner, J. H., & Rodríguez, L. F. 2000, ApJ, 534, L101

Wolf, S. & D'Angelo, G. 2005, ApJ, 619, 1114

Wolf, S., Schegerer, A., Beuther, H., Padgett, D. L., & Stapelfeldt, K. R. 2008, ApJ, 674, L101

Wolk, S. J. & Walter, F. M. 1996, AJ, 111, 2066

Wright, C. M. 2007, Ap&SS, 311, 47

Youdin, A. N. & Shu, F. H. 2002, ApJ, 580, 494

Zuckerman, B. 2001, ARA&A, 39, 549

Zuckerman, B., Forveille, T., & Kastner, J. H. 1995, Nature, 373, 494